TÉCNICO LISBOA

UNIVERSIDADE DE LISBOA

INSTITUTO SUPERIOR TÉCNICO

Biomanufacturing of DNA-origami nanostructures for bio-imaging

Ana Rita da Silva Santos

Supervisor: Doctor Duarte Miguel de França Teixeira dos Prazeres

Co-Supervisor: Doctor Pedro Miguel Neves Ribeiro Paulo

Thesis approved in public session to obtain the PhD degree in

Biotechnology and Biosciences

Jury final classification: Pass with Distinction

2023

UNIVERSIDADE DE LISBOA

INSTITUTO SUPERIOR TÉCNICO

Biomanufacturing of DNA-origami nanostructures for bio-imaging

Ana Rita da Silva Santos

Supervisor: Doctor Duarte Miguel de França Teixeira dos Prazeres

Co-Supervisor: Doctor Pedro Miguel Neves Ribeiro Paulo

Thesis approved in public session to obtain the PhD degree in Biotechnology and Biosciences

Jury final classification: Pass with Distinction

Jury

Chairperson: Doctor João Pedro Estrela Rodrigues Conde, Instituto Superior Técnico, Universidade de Lisboa

Members of the Committee:

Doctor João Pedro Estrela Rodrigues Conde, Instituto Superior Técnico, Universidade de Lisboa

Doctor Duarte Miguel de França Teixeira dos Prazeres, Instituto Superior Técnico, Universidade de Lisboa

Doctor Ana Cecília Afonso Roque, Faculdade de Ciências e Tecnologia da Universidade Nova de Lisboa

Doctor Gabriel António Amaro Monteiro, Instituto Superior Técnico, Universidade de Lisboa

Doctor Ângela Maria Almeida de Sousa, Faculdade de Ciências da Saúde da Universidade da Beira Interior

Funding Institution: Fundação para a Ciência e Tecnologia

2023

RESUMO

As nanoestruturas de DNA-origami assentam na auto-organização de uma molécula de DNA de cadeia simples (ssDNA) longa (~ 10^3-10^4 bases) (*scaffold*) numa nanoestrutura alvo com a ajuda de oligonucleótidos curtos (agrafos). Os *scaffolds* são geralmente purificados por (i) extração do DNA genómico de fago produzido em *E. coli*, que tem limitações na sequência e levanta questões de segurança quanto à contaminação das culturas seguintes, limitando o potencial de escalabilidade e aplicações desta técnica, ou (ii) por extração de gel de agarose, que é uma técnica trabalhosa, demorada, limitada, não escalável, apresenta baixa recuperação com baixa qualidade e requer equipamentos específicos, tornando-a inadequada para aplicações farmacêuticas ou analíticas.

O principal objetivo deste trabalho é melhorar a recuperação e a qualidade dos *scaffolds*. Primeiramente, um método livre de fagos, infeção reversa em *E. coli*, foi usado para produzir *scaffolds* contendo sequências aleatórias recorrendo a um plasmídeo ajudante e partículas de fagemídeo. Este método permitiu a produção de altos títulos de partículas de fagemídeo incapazes de auto-replicação, ultrapassando as preocupações de segurança relacionadas com a produção de fagos. Por outro lado, a produção de *scaffolds* usando PCR assimétrico (aPCR) também foi explorada. Além de gerar as moléculas ssDNA alvo, a reação de aPCR contém DNA de cadeia dupla, dNTPs, excesso de primers e enzimas como contaminantes. Para purificar essas misturas foram testadas duas abordagens: (i) afinidade entre esferas magnéticas funcionalizadas e o ssDNA alvo e (ii) cromatografia de troca aniónica e multimodal como plataforma escalável para a purificação de dez misturas de aPCR. Uma ferramenta de cromatografia analítica baseada em cromatografia líquida de alta eficiência de fase reversa de pares de iões também foi desenvolvida para a quantificação de *scaffolds* de ssDNA. Finalmente, a aplicabilidade de tetraedros de DNA-origami para bioimagem e como modelo de entrega de drogas foi avaliada por técnicas de espectroscopia e microscopia óticas.

Palavras-chave: Nanotecnologia de DNA, DNA-origami, ssDNA *scaffold*, produção biotecnológica, processamento a jusante, HPLC analítico, espectroscopia óptica

ABSTRACT

DNA-origami nanostructures are emerging as components of nanomachines, nanopores, drug delivery systems and biosensors. They rely on the self-assembly of a long (~10^3–10^4 bases) single stranded (ssDNA) DNA molecule (the scaffold) into a target nanostructure with the assistance of short oligonucleotides (the staples). Scaffolds are usually purified by (i) extraction of phage genomic DNA, produced in *E. coli*, which has sequence limitations and raises safety concerns regarding contamination of following cultures, preventing the scalability potential of the technique and its applications, or (ii) by agarose gel extraction., which is a laborious, time consuming, limited and not scalable technique that presents low recovery, delivers low-quality products, and requires specific equipment, making it not suitable for pharmaceutical or analytical applications.

The main goal of this work is to improve the recovery and quality of ssDNA scaffolds. Firstly, a phage-free method, in *E. coli*, called reverse infection was used to produce ssDNA scaffolds containing random sequences based on the use of a helper plasmid and phagemid particles. This method allowed the generation of high titers of phagemid particles not capable of self-replicating, overcoming the safety concerns related with phage production. On the other hand, production of ssDNA scaffolds using asymmetric PCR (aPCR) was also explored. Besides generating the target ssDNA molecules, contaminants of aPCR comprise double stranded DNA, dNTPs, excess of primers and enzyme. To purify these mixtures two approaches were tested: (i) affinity between functionalized magnetic beads and the target ssDNA and (ii) anion-exchange and multimodal chromatography as a scalable platform for the purification of ten aPCR mixtures. An analytical chromatography tool based on ion-pair reverse phase high performance liquid chromatography was also developed for the quantification of ssDNA scaffolds. Finally, the applicability of DNA-origami tetrahedrons for bio-imaging and as a drug delivery model was evaluated by optical spectroscopy and microscopy techniques.

Keywords: DNA nanotechnology, DNA-origami, ssDNA scaffold, biotechnological production, downstream processing, analytical HPLC, optical spectroscopy

ACKNOWLEDGEMENTS

O meu primeiro agradecimento vai para o Professor Miguel Prazeres por todo o apoio, motivação e disponibilidade para discutir todos os resultados e dúvidas que surgiram, não só ao longo desta tese, como de todo o meu percurso científico. Um agradecimento especial também ao Professor Pedro Paulo pelo apoio e por tudo o que me ensinou com toda a paciência num tópico tão desafiante e tão fora da minha área de conforto. Tenho a certeza que graças aos dois serei uma melhor cientista.

I would like to also thank to Professor Hendrik Dietz for welcoming me at Dietz Lab in Technical University of Munich. I learned a lot about DNA-origami technology thanks to your insights and vast experience in the subject. A special thanks to everyone at Dietz's Lab members, namely to Max and Karl who introduced me to an amazing project and kindly guided me since day one.

Gostaria também de agradecer ao programa BIOTECnico, na pessoa da Professora Isabel Sá Correia, por me ter aceitado no programa e ter dado a oportunidade de explorar este desafio que foi o doutoramento. O meu sincero obrigada também aos membros da minha Comissão de Acompanhamento de Tese, Professora Ana Azevedo e Professor Gabriel Monteiro, que mais uma vez acompanharam este percurso e, apesar de não serem oficialmente orientadores, sempre se mostraram disponíveis a discutir e ajudar com qualquer tópico.

Um sincero obrigado ao iBB por me ter recebido não só ao longo destes 5 anos mas durante toda a minha curta carreira científica. Todos os que se cruzaram comigo nestes laboratórios têm um bocadinho seu nesta tese. Não só os que ainda continuam, como o Diogo Faria, a Cristiana, o Jorge ou o Ricardo Silva, mas também alguns que já partiram como a Maria João e a Sara Rosa. Obrigada por todas as discussões (científicas ou não) e parvoíces que tanto ajudaram a passar estes anos e a tornar o ambiente mais leve quando não se vê luz ao fundo do túnel.

Um agradecimento especial à Alexandra, à Clara, à Cláudia, à Sara Sousa Rosa e ao Davide que apesar de ter conhecido num ambiente de trabalho se tornaram muito mais que isso. Tornaram-se verdadeiros amigos com quem eu sei que poderei sempre contar, nos dias alegres e tristes. Um especial obrigada à Sara Sousa Rosa e ao Davide por nunca me deixarem

sozinha, por todas as noites enquanto estive longe em que me fizeram sentir um pouco mais perto de casa. Não há palavras para descrever e sabem que farei o mesmo por vocês.

Faltam aqueles que provavelmente ainda hoje não percebem bem do que se trata esta tese, e ainda assim nunca duvidaram de mim e apoiaram-me incondicionalmente.

Em primeiro lugar, um agradecimento aos amigos que me adotaram, Maria, Pedro Marçal, Ana Isabel, João, Ana Catarina, Pedro Domingos, Guilherme e Sara. À Maria e ao Pedro Marçal agradeço todas as viagens e férias quando mais precisei de me afastar do trabalho. A todos agradeço por me mostrarem, especialmente nestes últimos meses, que juntos somos mais fortes e que estaremos unidos em tudo o que acontecer. Um obrigada também ao Afonso que em tão pouco tempo marcou a vida de cada um de nós.

À minha amiga mais antiga, Catarina, que durante esta tese se tornou também afilhada. Obrigada por todo o apoio incondicional pessoal e profissional. Sei que juntas iremos alcançar todos os objetivos que desejamos.

A todos os amigos que levei da faculdade, Maria Ana, Marco, Merlin, Ana e Vanessa, foi convosco que começou o meu amor pela ciência e apesar de não o partilhar com nenhum de vocês sei que me apoiam incondicionalmente e que estão sempre a torcer por mim.

Esta tese também é muito da minha família. À Carla que sempre foi como uma mãe para nós e nos apoiou em todos os momentos. A toda a sua família, a Maria, o Aníbal, o Nuno, a Carina, o Vicente e o Tiago, que são família adquirida e que sempre estiveram presentes. Aos meus avós, Maria da Luz, António, Iria e Carlos, por, onde quer que estejam, continuarem a olhar por mim. À minha irmã que orgulhosamente decidiu seguir as minhas pisadas e que daqui a uns anos será ela a escrever uma tese. Ao meu pai por todos os conselhos e compreensão ao longo de toda a minha vida. E à minha mãe por todo o apoio, paciência e amor incondicional. Todos vocês fizeram de mim a pessoa que sou hoje.

Finalmente, um agradecimento especial ao Ricardo (e à Cookie). Por tudo. Cada deceção, vitória, frustração e descoberta foi partilhada contigo e sentida pelos dois. Por toda a atenção, cuidado e preocupação. Não teria sido a mesma coisa sem ti.

Esta tese é dedicada a cada uma destas pessoas mencionadas aqui. Todos vocês contribuíram para o meu desenvolvimento pessoal e profissional. Foram 5 anos difíceis mas convosco ao meu lado, tudo parece fácil e sinto-me capaz de enfrentar o que aí virá!

ABBREVIATIONS LIST

AFM	Atomic force microscopy
aPCR	Asymmetric polymerase chain reaction
bp	Base pair
CCα	Decision limit
CCβ	Detection capability
DNA	Deoxyribonucleic acid
dsDNA	Double stranded DNA
E. coli	*Escherichia coli*
EDC	1-ethyl-3-(3-dimethylaminopropyl)carbodiimide hydrochloride
EDTA	Ethylenediamine tetraacetic acid
FCS	Fluorescence correlation spectroscopy
FoB	Folding Buffer
FRET	Förster resonance energy transfer
GxP	Product of gene x
HPLC	High performance liquid chromatography
IPC	Ion-pair chromatography
IRF	Instrument response function
LiCl	Lithium chloride
LOD	Limit of detection
LOQ	Limit of quantitation
$MgCl_2$	Magnesium chloride
MOI	Multiplicity of infection
NaCl	Sodium Chloride

NaOH	Sodium hydroxide
nt	Nucleotide(s)
OD	Optical density
PCR	Polymerase chain reaction
PEG	Polyethylene glycol
pfhp	Phage-free helper plasmid
PS	Packaging signal
QD	Quantum dots
RCA	Rolling circle amplification
RP	Reverse phase
SEC	Size exclusion chromatography
ssDNA	Single stranded DNA
TCSPC	Time-correlated single photon counting
TEM	Transmission electron microscopy
TMPyP	*meso*-Tetra(*N*-methyl-4-pyridyl)porphine tetratosylate
Tris	Tris(hydroxymethyl)aminomethane
V_R	Retention volume

INDEX

THESIS SCOPE AND OUTLINE

This thesis was developed in the framework of BIOTECnico PhD program at Institute for Bioengineering and Biosciences in Instituto Superior Técnico (Lisbon, Portugal), and in Professor Hendrik Dietz's laboratory in Technical University of Munich (Munich, Germany). Also, optical spectroscopy experiments derived from a collaboration with Centro de Química Estrutural in Instituto Superior Técnico.

The goals of this project were (i) to develop scalable processes for the biomanufacturing of scaffolds and DNA-origami nanostructures, and (ii) to study the possibility of using fluorescently labelled DNA nanostructures in bio-imaging applications and as drug delivery agents. This thesis is thus divided in six chapters.

Chapter I presents a general introduction on DNA nanotechnology and DNA-origami technology. The manufacturing of DNA-origami nanostructures is assessed from the design to the several methods for single stranded DNA (ssDNA) scaffold production and the folding and purification of DNA-origami nanostructures. Finally, examples of possible applications of these nanostructures are presented.

The research work carried out during this thesis is presented in the following four chapters. Chapter II presents cell-based processes for the production of single-stranded DNA scaffolds. On a first approach, M13mp18 phage was used to infect *E. coli* cells, producing a ssDNA molecule equal do its genome. User-defined sequence phagemids were also used either with a strategy that relies on the co-transformation of *E. coli* cells with a helper plasmid and a phagemid, or by infection of *E. coli* cells previously transformed with the helper plasmid.

Chapters III and IV.1 describe two different strategies for the purification of ssDNA scaffolds from asymmetric PCR (aPCR) mixtures containing double stranded DNA (dsDNA) and excess of dNTPs and primers as contaminants. Chapter III reports the use of functionalized magnetic beads as affinity agents for the capture of ssDNA scaffolds. After removal of the impurities, ssDNA could then be recovered by heating and magnetic separation. Moreover, reusage of the magnetic beads was also evaluated. Chapter IV.1 shows the possibility of scaling up the purification of ssDNA scaffolds resorting to chromatography. In this chapter, anion-exchange

and multimodal chromatography were explored. Also, the effect of pore and bead size was evaluated.

Chapter IV.2 derives from the need of having accurate quantification methods that distinguish between different types of nucleic acids like ssDNA, dsDNA and small oligonucleotides or dNTPs. In this chapter, a method based on ion-pair reverse chromatography is described for the quantification of ssDNA either from aPCR mixtures or from *E. coli* phage infection production. High performance liquid chromatography (HPLC) parameters like the limit of detection (LOD) and limit of quantitation (LOQ) were determined for the ss and dsDNA coming from the aPCR reaction and for the M13mp18 phage genome.

Finally, Chapter V uses DNA-origami tetrahedrons as model for the evaluation of DNA-origami folding using optical spectroscopy. In a first approach, the hydrodynamic radius and diffusion time of single-labelled DNA tetrahedrons were assessed by fluorescence correlation spectroscopy (FCS). Also, single-molecule analysis was performed, and the fluorescence decays and on-off behavior of individual fluorophores were evaluated. Next, the tetrahedrons were dual-labelled with a Förster resonance energy transfer (FRET) pair in order to observe energy transfer as the folding process takes place by real-time PCR and FCS. Finally, the possibility to intercalate the cationic porphyrin meso-tetra(4-N-methylpyridyl)porphine (TMPyP), as a photosensitizer used in photodynamic therapy, was assessed.

Chapter VI presents the final remarks of this thesis by summing up and concluding the main achievements of this work and its future challenges.

CHAPTER I – GENERAL INTRODUCTION

Abstract

DNA nanotechnology is an emerging field that encompasses the self-assembly of nucleic acids into nanostructures by exploring Watson-Crick base pairing. These DNA nanostructures are expected to find application as components of nanomachines, nanopores, drug delivery systems and biosensors.

DNA nanostructures are often assembled using the "scaffolded DNA-origami" strategy, whereby a long (~10^3–10^4 bases) ssDNA molecule (the scaffold) is folded with the assistance of short oligonucleotides (the staples) into the target nanostructure. The scaffold can be either produced (i) biologically, by isolating the DNA of phages like M13mp18, (ii) enzymatically, by cutting out the target sequence from the phage genome, or (iii) by asymmetric PCR, using the phage genome as template and appropriate primers, followed by extraction from an agarose gel electrophoresis separation. The staple sequences required to assemble a target nanostructure from a specific ssDNA scaffold are designed using different computational algorithms and then synthesized chemically. The target ssDNA and the staple strands are subsequently assembled by slow thermal annealing under high magnesium concentrations. Next, nanostructures are purified from impurities (non-integrated staples, misfolded nanostructures, aggregates) using gel electrophoresis, centrifugal filters, rate-zonal centrifugation, and size exclusion chromatography. Finally, quality control using microscopy techniques such as atomic force microscopy or negative staining transmission electron microscopy is performed to evaluate the successful folding of a target structure.

Keywords: DNA nanotechnology, DNA-origami, scaffold, staples

I.1. DNA nanotechnology

DNA nanotechnology takes advantage of the physical and chemical properties of DNA to assemble synthetic structures [1]. Key features that make DNA a powerful tool for the assembly of nanostructures are: (i) its predictable and programmable interactions, (ii) its binding specificity, (iii) its thermodynamic stability, (iv) the fact that sequences can be user-defined and will reliably bind to their complementary counterparts, (v) its well-defined structure at the nanometer scale, (vi) its persistence length of ~50 nm, (vii) the rapid synthesis and modification and (viii) the existence of DNA-acting enzymes that allow further controlled modifications [1, 2].

The use of DNA nanotechnology was first demonstrated by Ned Seeman in 1982 and was based on the programmed assembly of branched DNA junctions [3]. Seeman took advantage of the self-recognition properties of DNA and developed rigid branched DNA motifs based on the complementary Watson-Crick base pairing between segments of a given set of oligonucleotides [1, 3, 4]. Despite several advances in this field for over 20 years, the resulting structures were always limited to assembly into discrete finite objects or infinite periodic lattices through sticky-end cohesion, which requires exact stoichiometric control and purification of the oligonucleotides or structures resulting in a process with yields of only 34%. Moreover, the complexity of the structures that can be produced by this strategy is limited to geometric shapes and to the repetition of building blocks [4, 5].

In 2006, this problem was overcome when Rothemund introduced the scaffold-based DNA-origami method [6]. In this technique, a long single stranded DNA (ssDNA) molecule (the scaffold) is folded with the assistance of short oligonucleotides (the staples) into the target nanostructure [4, 7]. Rothemund used the genome of the M13mp18 phage (a 7.25 kb circular ssDNA) and 200 staple strands to fold 100 nm, 2D structures shaped as squares, disks and five-pointed stars, with a spatial resolution of 6 nm [6]. The self-assembly process occurs by annealing the scaffold in the presence of 100-fold excess of staple strands for one hour and results in a yield of at least 70% of the target shape. Since in this case the staple strands hybridize with a common scaffold rather than with each other, their stoichiometric ratio is no longer relevant [4, 6].

The relatively weak resistance of single-layer DNA-origami nanostructures to mechanical stress led to development of 3D DNA objects [4, 8]. In 2009, Shih demonstrated the design and assembly of six 3D shapes – monolith, square nut, railed bridge, genie bottle, stacked cross, slotted cross – with dimensions ranging between 10 and 100 nm. In this case, shapes were formed as pleated layers of helices constrained to a honeycomb lattice [9].

Since then, many reports were published focusing on the development of new wireframes for DNA nanostructures. This goes from simply switching the wireframe to a square [10] or an hexagonal lattice [11], to creating objects with a custom curvature and twist [12] or even to creating two and three-dimensional wireframe objects with gridiron or polygonal mesh helix routing [13–16].

Summarizing, DNA nanostructures can be fabricated either by a top-down or a bottom-up approach. In the first case, the process starts with large structures and reduces their sizes to the required dimensions and patterns by removing or subtracting substances from bulk materials. Despite this standard manufacturing strategy was applied in early developments of DNA nanotechnology, its application is limited to reach molecular sizes. On the other hand, the bottom-up self-assembly approach relies on chemical assembly and molecular recognition to connect individual molecules, allowing the production of well-defined nanostructures with less than 100 nm, which is the target for DNA-origami technology [1, 2, 17].

In addition to the design of new nanostructures, the unlimited possibilities for site-specific integration of functional groups and organic and inorganic compounds into these objects has enabled their application in several fields of research [18, 19].

Figure I.1 shows the exponentially growing interest in the fields of DNA nanotechnology and DNA-origami [20]. Notably, a 10-fold increase in publications can be observed between 2007 and 2017.

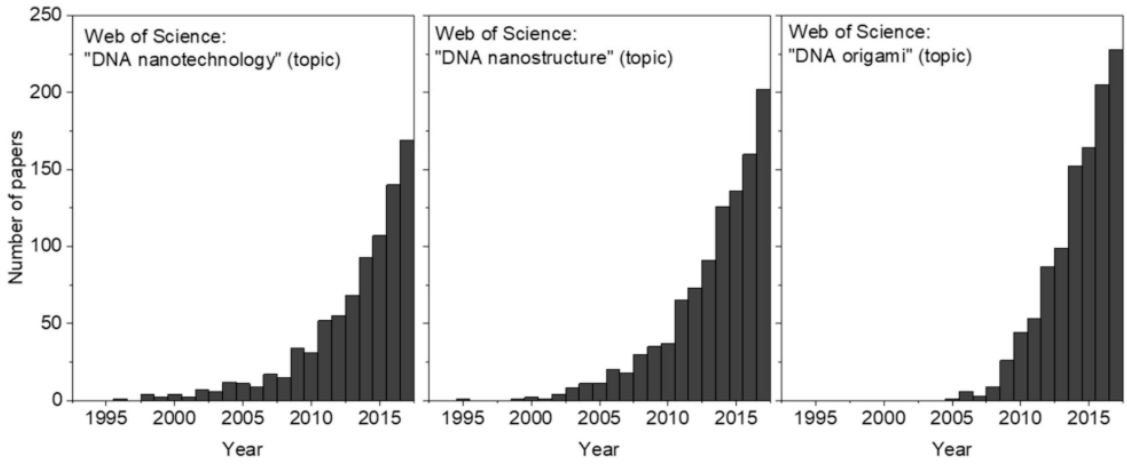

Figure I.1: Published papers in DNA nanotechnology. Source: [20].

Moreover, there are already two DNA nanotechnology-based companies that have DNA-origami products as their core technology: Tilibit nanosystems and GATTAquant [20].

Tilibit nanosystems [21] was founded in 2012 and is connected to the Technische Universität München, Germany. It provides origami materials, like ssDNA scaffolds and staple strands, and services on design, building and testing that aim to economically supply DNA-origami materials and assist with nanostructure preparation.

On the other hand, GATTAquant [22] was founded in 2014 and is connected to the Technische Universität Braunschweig, Germany. This company provides DNA nanorulers, which are DNA-origami based objects carrying fluorophores with a precisely defined separation. With this product, GATTAquant aims to quantify the resolution of super-resolution microscopes.

I.2. DNA-origami manufacturing

DNA-origami manufacturing comprises five main steps: (i) define the target shape, design the scaffold-staple layout and determine the sequence with a software program, (ii) prepare the scaffold and staple oligonucleotides, (iii) allow DNA to self-assembly though a temperature ramp at high salt buffer concentration, (iv) purify and functionalize the nanostructure, if desired, and (v) visualize and analyze the structure [7, 8] (Figure I.2).

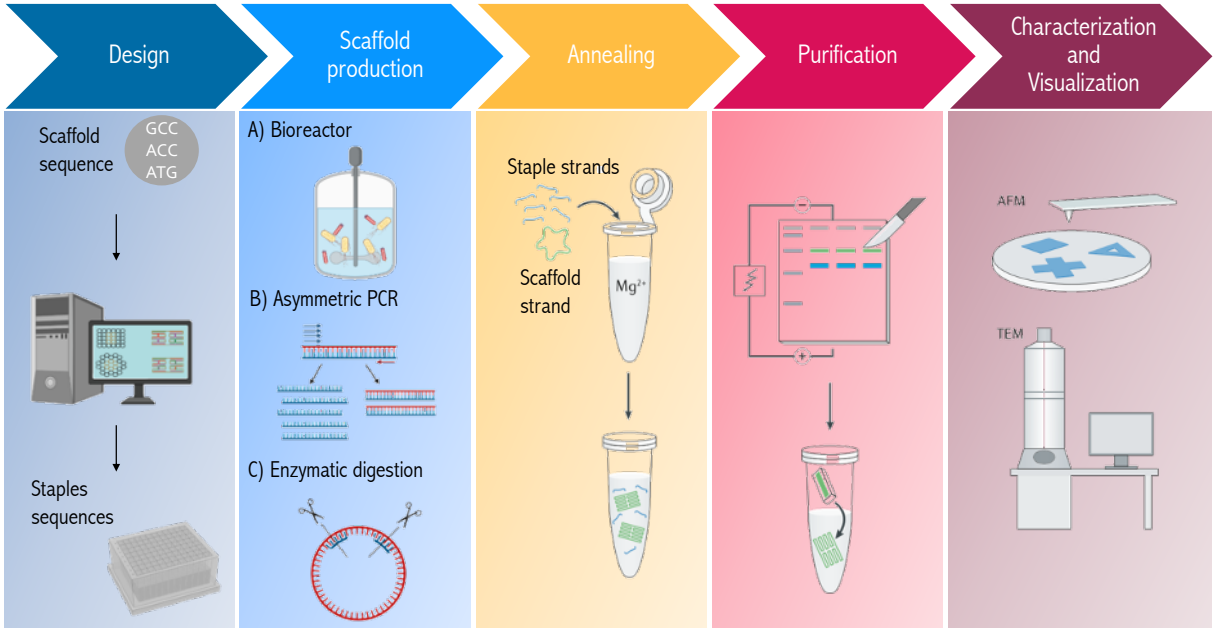

Figure I.2. Schematic representation of the DNA-origami manufacturing process. First, the desired target shape is inserted into a software that in combination with the desired scaffold sequence, retrieves the staple sequences required. Then, the scaffold is produced either in a bioreactor using E. coli cells, by asymmetric PCR or by enzymatic digestion. The scaffold can then be mixed with the staple strands under a defined magnesium concentration to allow the folding into the target nanostructure and it can be purified from agarose gel. In the end, the DNA-origami is visualized to characterize the final product in terms of folding quality. Adapted from [23].

I.2.1. Design of DNA-origami nanostructures

The main design principle of DNA-origami nanostructures is a Watson-Crick base pair stacked into double-helical DNA domains of defined length. DNA-origami consists of the folding of a scaffold into close-packed bundles of double-helical DNA domains with the use of staple strands. The high interest in this field led to development of several design software packages for the rapid prototyping of DNA-origami nanostructures [24]. First, the target shape is sketched using a graphical tool. Then, the initial 2D or 3D model is turned into a wireframe mesh that functions as a map for DNA strands. Depending on the used software, an algorithm is used to route the scaffold throughout the mesh in a way that each vertex and edge of the model is filled. Using the scaffold sequence as an input, the software determines the sequences of the staple strands required to assemble the target nanostructure [25].

The first software for the design of DNA-origami nanostructures is caDNAno [25, 26]. This package allows the design of structures at the megadalton scale using square or honeycomb

lattices that comprise closely packed cylinders, which represent adjacent and parallel double stranded DNA (dsDNA) [5], [19], [25]–[27]. Other first generation DNA-origami design tools include Tiamat [28], SARSE-DNA [29], oxView and Hex-Tiles [30], which also require manual scaffold routing and manual scaffold and staple crossover [23].

Even though caDNAno is still the most widely used by experts in the field, first generation software is limited to lattices and requires an experienced user to design the target objects. With the growing interest of using DNA-origami as a tool for multiple subjects, more automated and user friendly software packages are being developed [31], [32].

Second generation software like vHelix [15] allows a semi-automatic top-down polyhedral DNA rendering of user-defined 2D and 3D objects. In this case, the desired shape is created, made into a triangulated, polyhedral wireframe mesh, and processed in a way where a single stranded DNA scaffold is routed automatically along the edges of the mesh by an algorithm. The routing through the scaffold is performed in a way that the scaffold passes each edge of the mesh only once, and without crossing straight over any vertices. Next, the single stranded edges are supplemented with short, complementary staple strands to make the structure robust. By defining the scaffold sequence, the staple sequences can be exported, synthesized, and eventually folded with scaffold strand to form wireframe DNA nanostructure [15], [25].

DAEDALUS (DNA-origami Sequence Design Algorithm for User-defined Structures) [14] relies on a fully automated spanning-tree algorithmic framework that enables the top-down wireframe design and fabrication of 3D objects. With this software, Bathe and co-workers created numerous Platonic, Archimedean, Johnson, Catalan, asymmetric constructs and polyhedra with non-spherical topologies. In the DEADALUS workflow, a 3D graph and the spanning tree are computed for the meshed target shape, followed by the scaffold routing by the spanning tree algorithm and sequence design with a predicted atomic model. The wireframe motif is based on two interconnected DNA double helices allowing structural robustness. The user inputs are the target object and the scaffold sequence, whereas the software outputs are the list of staple strands needed and atomistic models of the designed structures [14], [25], [32].

A fully automated design of 2D nanostructures is also possible using the PERDIX (Programmed Eulerian Routing for DNA Design using X-overs) software [33]. PERDIX allows 2D free-form geometry design with the internal mesh geometry rendered automatically by the algorithm

that performs automatic scaffold and staple routings, converting each edge into two parallel DNA duplex edges of arbitrary length. In PERDIX, a 2D graph with meshes and corresponding double cross-edges are rendered for the target object to generate the loop-crossover structure and to enable assigning crossovers by computation of node-edge dual graph. Then, the scaffold is routed through the whole object, complementary staple strands are assigned, and an atomic model is predicted. This software allows the creation of structures with internal triangular, quadrilateral and N-polygonal meshes [25], [33].

In order to enhance mechanical stiffness, biological stability and resistance against nucleases, the TALOS (Three-dimensional, Algorithmically generated Library of DNA-origami Shapes) [34] software allows 2D and 3D wireframe sequences to be designed with six helix bundle motifs instead of dsDNA or double-cross molecules as edges. It also allows the use of mitered vertex (i.e. a three-way vertex crossover) in addition to the flat vertex (i.e. a single-vertex scaffold crossover between each pair of neighboring edges) used in DAEDALUS [25], [34].

In addition to PERDIX and TALOS, METIS (Mechanically Enhanced and Three-layered origami Structure) [35] can be used to enhance mechanical stiffness and fidelity of vertex angles in 2D wireframe objects. In contrast to PERDIX, which generates target objects having varying vertex types with single-layer/double cross-based wireframe motifs with or without internal mesh geometry, METIS generates lattice-based geometries by stacking three layers corresponding to a cross-section of six-helix bundle. This software allows the generation of triangular, quadrilateral and irregular letter-like mesh objects [25], [35].

Finally and more recently, ATHENA [31] was developed as a Graphical User Interface (GUI) to all the aforementioned software. ATHENA is a GUI that integrates 2D and 3D target wireframe geometry file input together with application of fully automated sequence design and visualization, allowing the user to design any king of wireframe structure with two or six helix bundle, flat or mitered vertex. In addition to staple sequence design, ATHENA produces output files including all-atom structures in Protein Data Bank (PDB) and caDNAno files for editing or modifying sequence designs for, for example, DNA-origami functionalization [25], [31].

Another third-generation software that provides a GUI and combines almost all first and second generation software is Adenita [36]. It can design lattice-based wireframes, multilayered structures, free-form tiles, and single-stranded tiles, and contains an integrated simulation platform to predict the stability of the designed structures in buffer after their

formation. Moreover, Adenita is the only software that accommodates other molecules such as proteins, lipids or drug molecules [23], [36].

Figure I.3 presents a decision-making flowchart to choose the right design software for designing DNA-origami nano-objects.

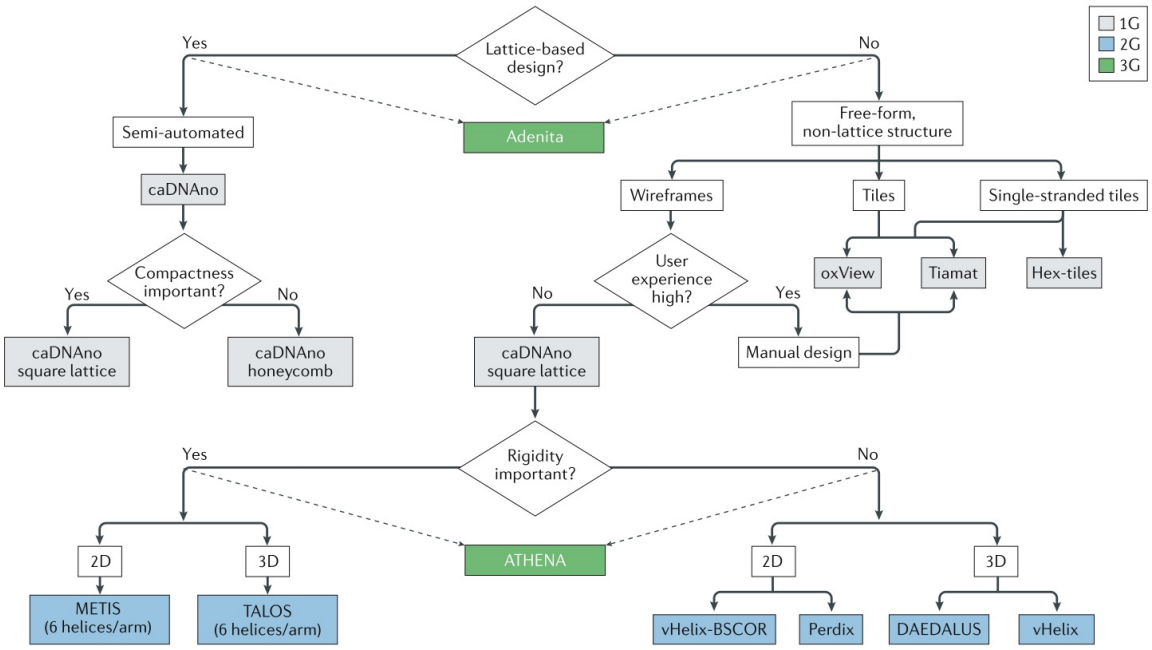

Figure I.3: Decision making flowchart for the selection of DNA-origami design software. The colored boxes, grey for first generation, blue for second and green for third, represent the software that are best suitable for a given task. Adapted from [23].

I.2.2. Production of ssDNA scaffolds

The fundamental units in a DNA-origami nanostructure are a ssDNA scaffold and a set of staple DNA oligonucleotides [7].

The production of scaffold DNA for DNA-origami is usually performed by (i) purifying phage-derived single-stranded genomic DNA, (ii) PCR-based methods or (iii) alternative enzymatic methods [7].

I.2.2.1. Phage-based ssDNA production

Scalable production of ssDNA for DNA-origami is commonly based on the M13 phage reproduction system. The produced DNA is mainly comprised of the 6407 nucleotides (nt) long M13 genome. The M13 genome includes 11 genes, which encode for all proteins necessary for the phage reproduction process, packaging of the genomic phage DNA and release of the

phage capsids from the host cell into the environment, and 2 non-coding sequences, a packaging signal where DNA encapsulation starts and the origin of replication which initiates the replication of single stranded and double stranded phage DNA. The phage DNA is encapsulated in a tube-like capsid by 2300 copies of protein pVIII. 5 copies of each pIII and pVI proteins can be found at the front of the capsid, which binds the host cell and initiates infection. Another 5 copies of each pVII and pIX proteins close the capsid at the rear. The remaining genes encode for proteins that aid replication (pII, pV and pX) or support phage assembly (pI, pIV, pXI) (Figure I.4) [37], [38].

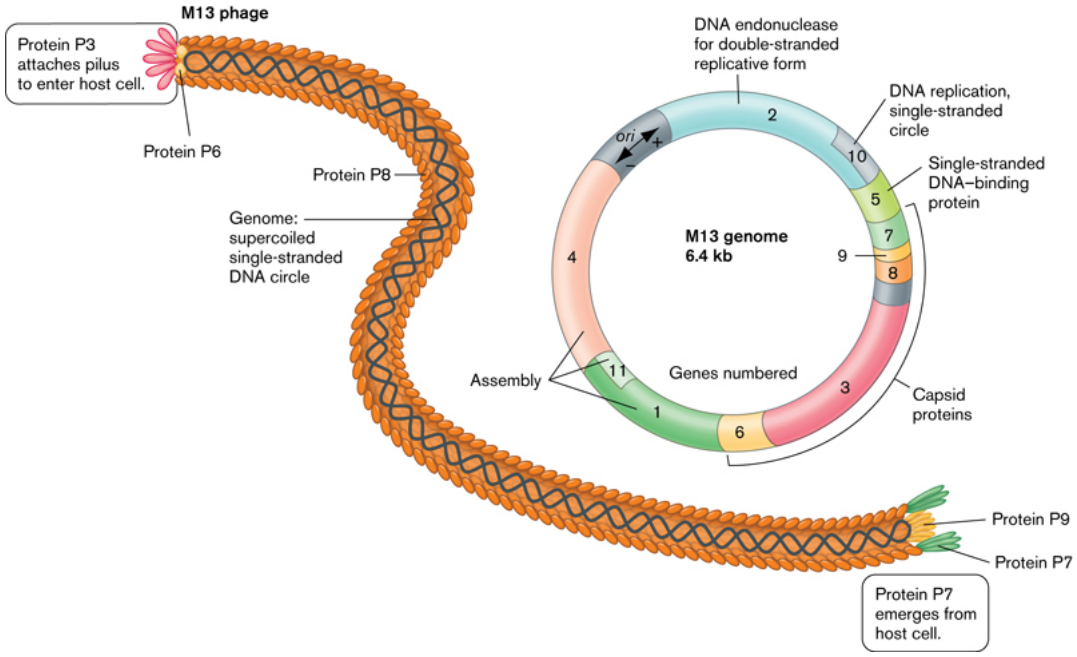

Figure I.4.Schematic representation of the M13 phage genome Adapted from [39].

The M13 phage infects *Escherichia coli* (*E. coli*) using a replication system called rolling circle amplification (RCA) that can be divided into three stages [40]. In the first stage, pIII binds to the F pili of *E. coli* cells, followed by the insertion of the single stranded phage scaffold DNA (+ strand) into the cytoplasm. Here, the ssDNA is converted into its replication form (RF), a dsDNA containing the (+) and (-) strands of DNA. In the second stage, *E. coli* DNA polymerase III binds to the RF DNA and separates the (+) strand from the (-) strand: (i) (-) strand acts as the template to form the RF DNA synthesizing of a new (+) strand, (ii) in early production stages, the (+) strand is also used as a template for DNA polymerase III to form new RF DNA that will be nicked by phage protein pII allowing the production of new (+) strand DNA, by pII circularization of displaced (+) strand, and RF DNA, by DNA polymerase III [40], [41]. Stage 2 continues until pV reaches a threshold concentration in the cytoplasm. At that point, pV

dimers bind the newly synthesized ssDNA preventing its conversion to RF DNA and exporting it as phage DNA [42]. The fact that M13 extrudes directly into the culture medium without causing bacterial lysis allows an easy recovery of its ssDNA genome and its subsequent use as DNA-origami scaffold [43] (Figure I.5a). Moreover, the development of an engineered version of the M13 ssDNA with a higher replication rate, the M13mp18, made it the first and most common source of ssDNA scaffold for DNA-origami assembly [43], [44]. Other M13 variants were developed by Douglas *et al.* ranging between 7560 and 8634 nt by replacement of a segment of M13mp18 by PCR-amplified fragments of bacteriophage λ [9].

The widespread use of these types of scaffolds led to the development of dedicated production processes. Originally, M13mp18 scaffolds were produced in shake flasks with ssDNA yields up to 10 mg/L culture [45]. However, further optimization of the production of M13 bacteriophages using bioreactors led to the maximization of the ssDNA yield. Kick and colleagues demonstrated the possibility of producing 410 mg/L of M13mp18 ssDNA using the XL1-Blue MRF' *E. coli* host and a fed-batch process in a stirred-tank bioreactor [46]. Moreover, the same group studied the importance of the specific growth rate and multiplicity of infection in M13 propagation and subsequent ssDNA production. They concluded that using a growth rate of 0.15 h^{-1} and a multiplicity of infection of 0.05 pfu cfu^{-1} in the fed-batch production process, the concentration of pure isolated M13 ssDNA could be enhanced by 54% to 590 mg/L [47]. In both cases, phages were recovered by polyethylene glycol (PEG) precipitation and ssDNA was extracted by combining alkaline lysis and ethanol precipitation [46], [47]. Continuous fermentation processes were also successfully used to produce M13mp18 ssDNA using *E. coli* JM109 as host organism, which lead to comparable results to the fed-batch process [48]. More recently, Lee and co-workers showed that by optimizing the pV untranslated region sequence in M13 phage, the ssDNA titer could improve 2.5 times [49].

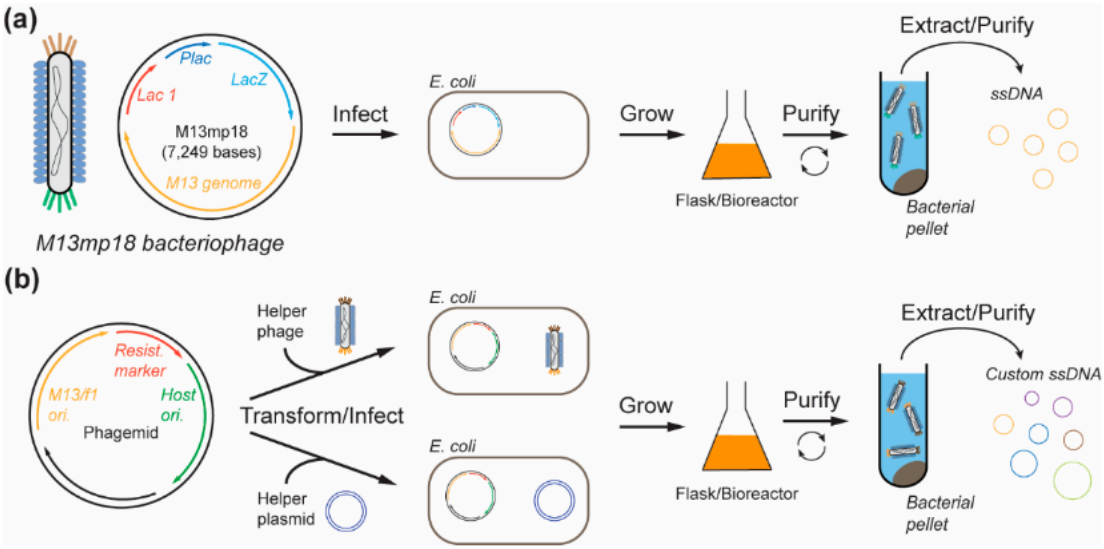

Figure I.5. Phage-based methods for ssDNA scaffold production. (a) M13mp18 infects E. coli, replicates and releases phage particles into the culture medium that can be extracted and purified yielding ssDNA scaffolds. (b) Custom-made ssDNA scaffolds and other essential genes for replication are encoded into a phagemid that is used to transform E. coli in the presence of a helper phage or a helper plasmid. The transformed or infected cells are grown, releasing the phagemid particles containing the target ssDNA scaffold that can then be extracted and purified. Source: [43].

Even though the M13mp18 scaffold can be produced at a large-scale, the final sequence and size of the ssDNA scaffold produced is always limited by the genes and regulatory sequences in the genome necessary for ssDNA replication, packaging, and extrusion into the culture medium This limitation led to the development of phagemids, which can be produced in a similar manner to M13 but have more flexibility in terms of the sequence. In this case, the only constrains of phagemids are the presence of i) two origins of replication, one dsDNA ori for plasmid replication and amplification of the phagemid, and one ssDNA ori for ssDNA phage replication, and of ii) a resistance marker for selection (Figure I.5b). Since the phagemid sequence does not encode for any M13 proteins, parallel infection with a helper phage is required to provide the components necessary to produce ssDNA-containing phage particles. Even though helper phages can replicate in *E. coli*, they preferentially package the ssDNA encoded by the phagemid [43]. This strategy was applied by Zadegan's [50] and Chen's [51] groups using the commercially available helper phage M13KO7 to produce 1983-nt and >10,000-nt long ssDNA scaffolds, respectively. To avoid possible contaminations with the ssDNA of the helper phage, helper plasmids coding for coat proteins but lacking the ssDNA origin of replication can be used. Brown *et al.* [52] transformed an *E. coli* strain with a helper plasmid and a 2404-nt ssDNA mini-M13, encoded by a deletion derivative of the pBluescript

KS(-) phagemid, yielding 0.2-0.4 mg/L. Nafisi *et al.* [53] produced scaffolds ranging between 1512 and 10,080 nt by using a helper plasmid and a phagemid derived from pUC18 containing specific restriction sites for insert cloning. An even larger circular ssDNA DNA scaffold was created by LaBean and colleagues using a λ/M13 hybrid. To create this 51,466-nt hybrid, a M13 phagemid DNA was cloned into double stranded λ DNA and used to infect *E. coli* cells previously transformed with a helper plasmid [54].

Although phagemid-based scaffold production is a scalable and cost-effective method, phagemids also contain a double-stranded origin of replication, required in earlier stages of phagemid production, which can lead to the co-production of dsDNA contaminants [43], [52]. To overcome this limitation, Shepherd and coworkers [55] designed two miniphages (i) a 1676-nt scaffold containing only an antibiotic resistance gene and a single-stranded f1 ori, and (ii) a 2529-nt scaffold equal to (i) plus a synthetic sequence to increase the size of the produced ssDNA scaffold. Using an *E. coli* strain transformed with a helper plasmid, it was possible to produce 0.5 mg/L, in shake flask scale, of the 1676-nt scaffold and 4 mg/L, in bioreactor, of the 2529-nt scaffold free from dsDNA contaminations.

Remarkably, Praetorius and coworkers developed a method that allows the simultaneous production of ssDNA scaffold and staples at the milligram scale. This technology uses phagemids to generate single-stranded precursor DNA that contains the target strand sequences interleaved with self-excising cassettes, each comprising two Zn^{2+}-dependent DNA-cleaving DNA enzymes. These self-excising DNAzyme cassettes can be cloned

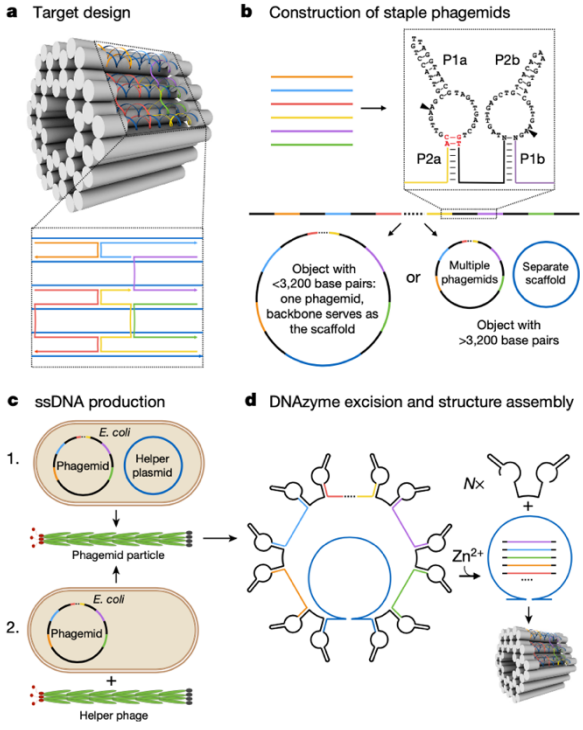

Figure I.6: Overview of the biotechnological mass production of DNA-origami. (a) Model of a DNA-origami nanostructure. Grey cylinders represent double helices, dark blue line represents the DNA scaffold and colored lines represent the staple strands. (b) Scheme of how staple sequences (colored) are interleaved with self-excising DNAzyme cassettes to generate the pseudogene to be cloned into a single or multiple phagemid backbones. (c) Two approaches for ssDNA production in (1) a single phagemid or (2) on a helper phage. (d) A single-stranded staple phagemid in which staples (colored) and scaffold (dark blue) are interleaved with DNAzyme sequences (black). Cleavage products can self-assemble into the target DNA-origami structure. Source: [56]

into a single phagemid backbone or distributed over multiple phagemid backbones. After digestion, backbone ssDNA can be removed by anion exchange chromatography and isopropanol precipitation, yielding 141 mg/L (Figure I.6) [43], [56]. The same group also reported a sequence design method that uses a split-ori phagemid to generate custom sequence-controlled scaffolds ranging between 1317 and 9072-nt. In this system, a full copy of the phage ori is placed upstream of the insert sequence, and a second, truncated copy of the phage ori is placed downstream of the insert. After transformation of *E. coli* cells with the phagemid and a suitable helper plasmid, the resulting ssDNA will comprise one phage ori and the insert sequence, but no backbone, minimizing the fixed-sequence to 234 bases and maximizing the freedom to design custom scaffold sequences [57].

I.2.2.2. PCR-based approaches

PCR techniques allow the amplification of target dsDNA sequences from various DNA templates, and hence the obtention of custom length defined scaffolds for DNA-origami. However, the double stranded nature of the amplified fragments requires additional steps of separation and purification to produce the ssDNA that will serve as a scaffold strand for DNA-origami folding [43].

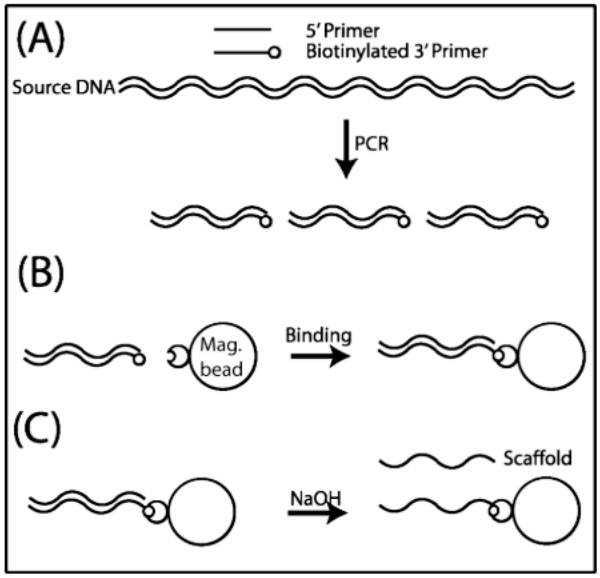

Figure I.7: Production of ssDNA scaffold. (A) PCR conditions, (B) Binding of PCR product to streptavidin-coated beads, (C) Denaturation of DNA strand and collection of the scaffold. Source: [33]

One approach for this isolation is to combine PCR amplification with strand separation via streptavidin-coated magnetic beads (Figure I.7). In this case, PCR is performed using either the lambda or M13mp18 phage DNA as template and a biotinylated 3' primer [58] or a dual-biotin group [59]. The PCR product is purified with a commercial kit and run in an agarose gel to allow isolation of the desired band from fragments resulting from unspecific amplification. Then, the PCR product is bound to streptavidin-coated magnetic beads. After being rinsed to remove any unbound DNA, the bead bound DNA product is denatured in

sodium hydroxide. The ssDNA product is finally purified using either a commercial kit or by ethanol precipitation, yielding 1100 ± 300 ng of ssDNA scaffold for a 2958 bp PCR product (Figure I.7). This method was used to generate linear scaffolds ranging between 756 and 4808 nucleotides (nt) in length [58]. The main drawbacks of this method are the harsh denaturation conditions, which can affect the streptavidin-biotin interactions, resulting in dsDNA contamination, and the cost, since an excess of biotinylated primers are used in the PCR reaction, which will saturate the magnetic beads, requiring the usage of high quantity of beads to capture all ssDNA strands [43].

Another alternative encompasses the use of a lambda exonuclease that binds to the dsDNA amplicon and selectively digests the unwanted DNA strand. For this to happen, this strand must bear a 5' terminal phosphate group, which is incorporated during PCR amplification by using modified primers [43]. Zhang and co-workers [60] used this strategy to produce a 26000-nt ssDNA scaffold from a PCR fragment amplified from the lambda phage genome. In another study, Han et al. [61] produced self-complementary ssDNA scaffolds ranging between 966 and 10682-nt for staple-free DNA assembly using commercially synthesized dsDNA as template. However, the cost of the enzyme required for this method, the fact that an extra purification step for removal of the enzyme (which can lead to ssDNA loss) is necessary and its relative ineffectiveness for separating residual dsDNA from ssDNA, limits the adoption of the method at large-scale [43].

A selective nascent polymer catch-and-release (SNAPCAR) technique was also used for the generation of ssDNA scaffolds ranging between 1650 and 7301 nt. This method relies on the reactivity of growing poly(acrylamide-co-acrylate) chains to capture acrylamide-modified dsDNA in PCR reactions. After NaOH addition, dsDNA is denatured, and the non-anchored target strand is released. The copolymer can then be precipitated on demand to enable extraction of the target ssDNA strand [43], [62]. This method was further developed into methanol-responsive polymer PCR to enable the subsequent extraction of the anchored ssDNA strand. In this case, an uracil base was included in the acrylamide-modified primer allowing its cleavage and extraction by precipitation of the polymer anchor [63].

Another approach uses asymmetric PCR (aPCR) to generate ssDNA scaffolds [14], [64], [65] by reducing the amount of the primer that amplifies the strand complementary to the target scaffold strand. This approach minimizes the excess of ssDNA in the final structure, which may

result in non-specific object aggregation, interfere with folding or with downstream chemical functionalization. Veneziano and co-workers used this methodology to synthesize linear ssDNA ranging between 450 and 3400 nt, either by using the M13mp18 phage genome or dsDNA fragments as templates. aPCR samples were then run in an agarose electrophoresis gel and the desired ssDNA fragment was excised yielding 1.5-4.5 pmol ssDNA per 50 μL reaction [14], [64].

PCR amplification of plasmids in combination with enzymatic digestion was also used for ssDNA production. Shih and colleagues generated long circular ssDNA molecules from dsDNA plasmid using the nicking endonuclease *Nb.BsrDI*, which site-specifically cleaves the phosphodiester bond of only one strand of dsDNA plasmids. Then, the nicked strand was fully digested using the combined action of T7 and Lambda exonucleases [9]. Despite the fact that large amounts of dsDNA plasmids can be produced through bacterial cultivation, disadvantages of this method includes the fact that plasmids may (i) not have the desired length, (ii) contain unnecessary or lack necessary nucleotide sequences stretches, such as genetic regulatory elements or protein encoding genes, or (iii) not possess the necessary nicking endonuclease restriction site [66]. To overcome these limitations, Niemeyer et al. developed a method for tailored length ssDNA scaffolds from given plasmids taking advantage of a combination of site- and ligation-independent cloning protocols. In this method, two PCR primers flanking the region of interest are designed, leading to its amplification. Both primers contain 5' extensions complementary to each other, such that PCR amplification generates amplicons with homologous ends, which mediate circularization in bacteria and enable the introduction of a nicking enzyme *Nb.BbvCI* recognition site. The resulting PCR mixture is then treated with *DpnI*, which cleaves the ubiquitous sequence GATC when it is methylated at the adenine base, as it is the case after *E. coli* propagation, digesting the template plasmid. The PCR product is then used to transform *E. coli* in which the linear PCR products are circularized, repaired, propagated, and can be obtained after fermentation by subsequent plasmid isolation strategies. The isolated plasmids are transformed into ssDNA by nicking with *Nb.BbvCI* and subsequent T7-exonuclease digestion. The resulting ssDNA plasmids were collected by sodium acetate precipitation and analyzed by agarose gel electrophoresis yielding 150 pmol of ssDNA that can be used as DNA-origami scaffold (Figure I.8) [66].

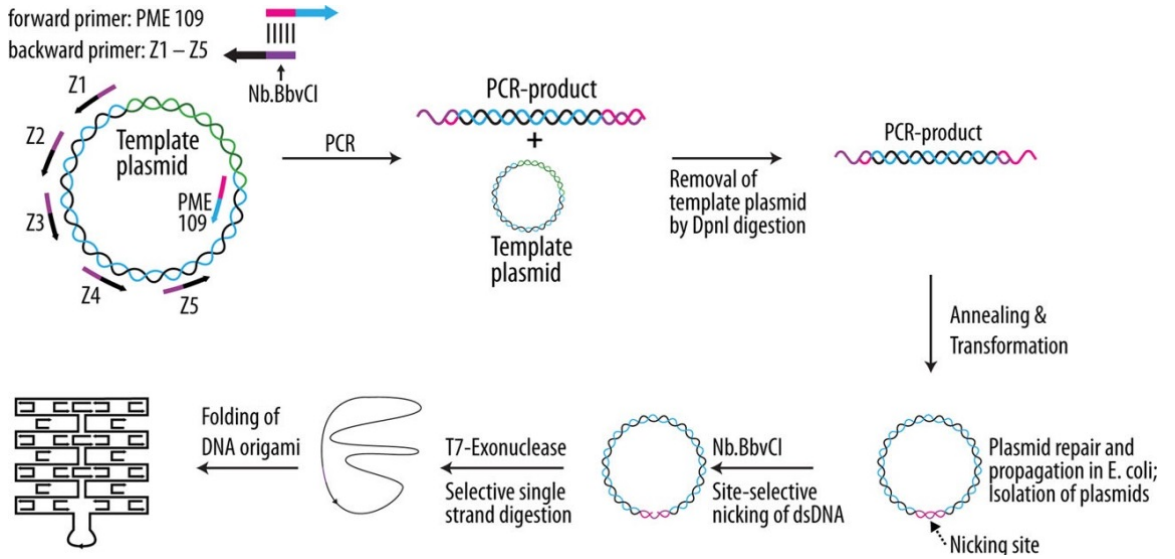

Figure I.8: Schematic overview of ssDNA scaffold preparation for DNA-origami by combination of site-directed mutagenesis and site- and ligation-independent cloning. Source: [66]

I.2.2.3. Enzymatic Methods

Although PCR-based approaches have the advantage of delivering custom scaffold DNA sequences, they are usually limited to the analytical microgram scale. For this reason, a number of alternative enzymatic methods were developed [7].

One example was the one used by Richert to prepare a 704 nt linear or cyclic scaffold. In this method, the authors excised the desired fragment from the M13mp18 genomic ssDNA with the aid of two 20 nt cleavage-inducing oligonucleotide sequences complementary to the limits of the desired fragment, and restriction endonucleases *EcoRI* and *BglII*. Following digestion, samples were run on agarose gel electrophoresis and the desired band was excised with an extraction kit yielding 12.4 pmol ssDNA [67].

Another approach uses rolling circle amplification (RCA), which enables the isothermal amplification of long ssDNA concatemers up to several nucleotides long, containing from ten to a few hundred tandem repeats complementary to the template sequence. This method requires a circularized ssDNA template, a single primer and a polymerase with strand displacement capabilities, usually Phi29, and consists of the polymerase extension of the primer around a circular template strand to form a complementary strand. Once the starting point is reached, the polymerase begins to displace the 5'-end of the newly synthesized strand, permitting the polymerase to continually synthesize the concatemeric ssDNA [43]. This method was used by Ma [68] to produce scaffolds around 8,000 and 19,000-nt long from 96 and 144-nt circle templates, respectively. Despite the high yield achieved with this technique,

the use of concatemeric ssDNA scaffolds makes it limited to nanostructures that include repeated motifs [43].

Hamblin and colleagues [69] developed an alternative method that uses time, or order of addition, to assemble ssDNA scaffold ranging between 480 and 1058-nt from 42 and 101-bp dsDNA building blocks, respectively. In this approach, each of the dsDNA building blocks was synthesized with 10-nt single-stranded sticky overhangs programmed at their 5' or 3' ends to anneal with a complementary sticky overhang of the subsequent building block and ligated with T4 DNA ligase to produce a long linear dsDNA strand. The termination building block exhibits blunt-ends to allow PCR amplification of the fragment that can then be separated by streptavidin-biotin magnetic beads [69]. Even though this method offers the ability to produce a scaffold with an arbitrary sequence, it requires multiple steps and a subsequent PCR-based approach to produce high yields of ssDNA [43].

I.2.3. Production of ssDNA staple strands

The staple strands needed to assemble DNA-origami nanostructures can be bought from commercial providers of solid-phase-synthesized DNA or produced by enzymatic amplification of chip-synthesized DNA, or custom DNA oligonucleotides, through digestion with restriction endonucleases from a long single strand [7].

Shih et al. showed the possibility of producing, amplifying and purifying subsets of hundreds or thousands of ssDNA with different lengths in a multistep one-pot procedure based on three rounds of RCA, producing nanomolar amounts of ssDNA oligonucleotides [70].

Another approach to generate staples is the monoclonal stoichiometric (MOSIC) method (Figure I.9). Here, a MOSIC pseudogene containing (i) the desired staple sequences and (ii) sequences that can form hairpins in between, is computer-generated and produced by sequence-verified gene synthesis. Then, assembly PCR is used to form a long double-stranded construct followed by cloning into *E. coli*, where the construct replicates as a plasmid that is subsequently sequenced until a colony with the plasmid with the right sequence is found. After obtention of the right plasmid, the DNA can be amplified in single-stranded form *in vitro* by excision of the pseudogene followed by recircularization and nicking to create templated for rolling-circle amplification or by cloning into a phagemid vector and subsequent

production of ssDNA via rescue by helper phage. Finally, the long ssDNA can be cut using restriction enzymes due to the presence of hairpins [71].

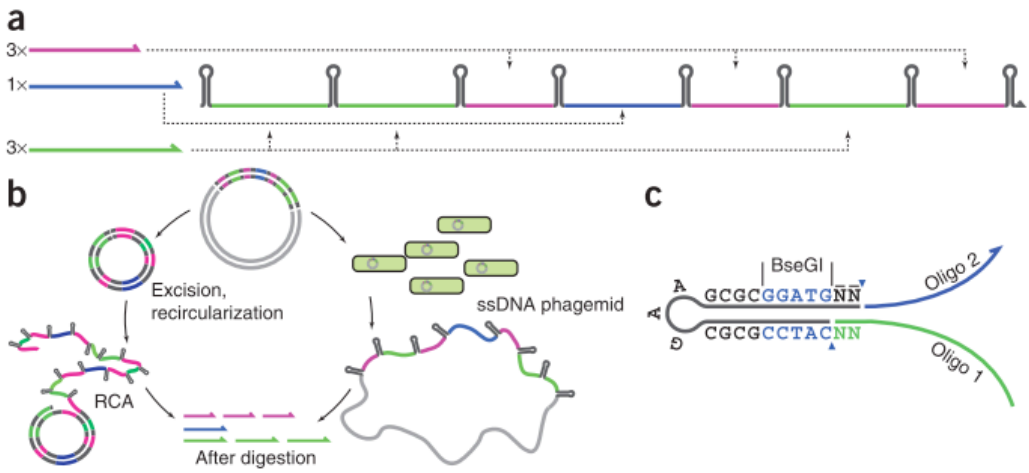

Figure I.9: Schematic overview of the monoclonal stoichiometric oligonucleotide production method. (a) Schematic of oligonucleotides with their relative stoichiometry (3x magenta, 1x blue, 3x green). Dashed lines indicate how the pseudogene is assembled in random order. (b) Illustration of in vitro rolling circle amplification (left) or helper phage rescue (right). (c) Schematic of the hairpin. Source: [71]

I.2.4. Folding and purification of DNA-origami nanostructures

Folding of DNA-origami nanostructures is usually performed in one-pot self-assembly reaction mixtures. Apart from the target object, these reactions also produce misfolded objects and/or aggregates depending on the assembly conditions [7]. Optimal self-assembly conditions include a perfectly controlled temperature interval [72] and the presence of calibrated amounts of cations [73]. A screen of folding conditions, namely temperature and salt concentration, is helpful for determining the requirements for an efficient self-assembly of a target DNA-origami nanostructure in terms of yield, occurrence of side-products and reaction duration. This screen allows a rationalization to refine assembly conditions to reduce the emergence of undesired side products, which can be further reduced by iterative cycles of design and folding conditions. Because of the sensitivity of folding DNA-origami on temperature and increased aggregation tendency at high scaffold DNA concentrations, folding reactions are typically carried out in less than 1 mL volumes with scaffold DNA concentrations below 100 nM. In addition, the cation concentrations in the assembly reaction should be kept between 10 to 25 mM of magnesium depending on the overall shape of the object [7].

Once folded, DNA-origami structures are stable under a wider range of solution conditions, including physiological conditions [74], [75], drying [76], [77] and washing with organic solvents [77].

Despite the finding of the optimal folding conditions, the final assembly reaction will still contain excess DNA staple strands and some assembly side-products, making it necessary to introduce a step for the purification and/or enrichment of the target DNA-origami structure. Several methodologies are implemented to separate and/or enrich a DNA-origami containing solution, namely (i) precipitation, (ii) gel extraction, (iii) filter purification, (iv) size-exclusion chromatography (SEC) and (iv) ultracentrifugation [7]. Figure 10 gives an overview of these separation and/or enrichment methods, either in terms of separation ability (A) and quantitative and qualitative properties (B).

The first approach relies on the use of depleting agents such as PEG to separate folded objects from excess staple strands. PEG precipitation is a rapid method that allows to concentrate and change the buffer of the final sample. However, it introduces residual PEG molecules [7], [76], [78]. More recently, salting-out of DNA-origami nanostructures in the presence of ammonium sulfate was demonstrated. Even though this methodology showed to be able to concentrate the DNA-origami sample and also to purify it from double stranded genomic DNA, it is not clear if it is suitable for purification from staple strands and multimers [79].

Agarose gel electrophoresis allows the separation of different species based on their electrophoretic mobilities, allowing the extraction of a target band by excising the corresponding gel slice and extracting the molecules/nanostructures from the gel matrix [7], [9]. Dietz et al. developed a gel extraction protocol that allows the recovery of 20-40 % intact particles in just 10 minutes. However, high centrifugal forces can lead to increased accumulation of agarose residuals in the filtrate [7]. In order to improve the yield, electro-elution of target species into a sucrose pool might be used instead of physical extraction [80].

A residual-free separation of reaction products can be accomplished using ultrafiltration. This approach relies on the use of membranes with a specific molecular weight cut-off. However, scalability is limited due to the restrictions imposed by the pore sizes of the filtration membrane. Dietz et al. tested different small-scale molecular weight cut-off filter types, with 10, 30, 50 and 100 kDa cut-offs. Both the 50 and 100 kDa filters efficiently separated the high-molecular weight DNA-origami structures from the low-molecular weight excess staple

strands when multiple cycles of buffer exchange and filtration were used. Moreover, the ionic strength of the sample solution played an important role on recovery yields, with the presence of low magnesium concentration (5 mM) giving yields above 90%, whereas use of greater magnesium concentrations reduced the yield [7].

A)

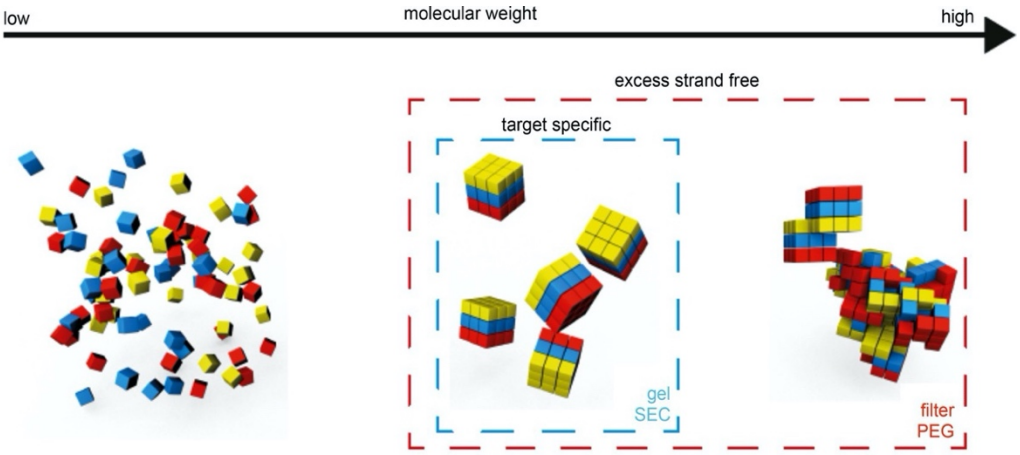

	PEG precipitation	Gel purification	Filter purification	SEC	Ultracentrifugation
Analyze sample composition	✖	✔	✖	✔	✖
High-pass/low-pass molecular weight separation	✔	✖	✔	✖	✔
Band-pass molecular weight separation	✖	✔	✖	✔	✖*
Enrich target species	✔	✖	✔	✖	✔

B)

	PEG precipitation	Gel purification	Filter purification	SEC	Ultracentrifugation
Yield	> 90 %	< 30 %	~90 %	70-90 %	> 90 %
Duration	1 h	4 h	0.5 h	3 h	1 h
Volume limitation	✖	✔	✖	✔	✖
Dilution	✖	✔	✖	✔	✖
Residual-free	✖	✖	✔	✔	✔
Damage	✖	✖	✖	✖	✖

Figure I.10: Overview of properties of PEG precipitation, gel purification, filter purification, size exclusion chromatography (SEC) and ultracentrifugation as methods for separation and enrichment. (A) Schematic overview of the several components of a folding reaction: low molecular-weight staple strands, correctly folded DNA-origami nanostructures, and misfolded DNA objects. Dashed boxes show the possibility of gel, SEC, filter and PEG purification for separating desired DNA-origami from excess staple strands (red) and/or higher ordered DNA-origami objects (blue). The table below compares the methods based on their capacity to achieve the listed goals. A green check mark indicates that the purification fulfils the goals and a red cross that it does not. Red star indicates that the criteria can be fulfilled if, for example, density gradient ultracentrifugation, is used. (B) Comparison of the purification methods based on yield, duration, volume limitation, dilution, residual-free and damage properties. Duration refers to 100 mL sample. Source: [7]

SEC can also be employed to selectively purify DNA-origami nanostructures not only from excess staple strands but also from higher-molecular weight structures such as dimers, trimers and other oligomers. SEC separates particles according to their size due to differences in effective path lengths during fluid passage through columns packed with a porous resin. Smaller particles experience longer paths due to diffusive excursions into the pores of the resin [7]. The first report of this technology used low pressures and fast flow rates to isolate DNA-origami nanostructures from excess staple strands, but failed to discriminate monomeric from dimeric DNA-origami [81]. More recently, Dietz et al. demonstrated that by using a 200 nm pore size resin it is possible to isolate the monomeric target nanostructure not only from PEG and excess staple strands but also from dimers or trimers. This shows that SEC-HLPC is an attractive alternative to agarose gel electrophoresis when it comes to selectively purifying DNA-origami objects. SEC is a scalable technique, free from contamination with agarose residues. However, since SEC dilutes the sample, it should be combined with other methods like PEG precipitation or filtration [7].

Finally, ultracentrifugation using of a glycerol gradient has yielded recoveries of 40-80% [82]. Also, the use of an iodixanol gradient in rate-zonal centrifugation proved to be efficient to separate free DNA-origami nanostructures from DNA-origami objects bound to gold nanoparticles [83]. However, both processes take longer than two hours to complete, were conducted in non-native sample buffers and were not tested for the possibility of creating dense DNA-origami solutions. To overcome this limitations, Dietz et al. developed a protocol for sedimentation by ultracentrifugation using centrifugal forces above 50 000 g at which DNA nanostructures accumulate in the bottom of a test tube in 15-30 min, achieving a 98 % recovering yield [7].

I.2.5. Quality control of DNA-origami nanostructures

After completion of the biomanufacturing process, it is necessary to evaluate the correct folding of the resulting DNA-nanostructures. As a first approach, gel electrophoresis, UV-visible and fluorescence spectroscopy, and circular dichroism can be used. These techniques provide the average chemical or physical characteristics of the molecules in solution, since they can differentiate between groups of molecules with similar properties. However, they are not suitable for single-molecule analysis [23].

Gel electrophoresis is the method of choice to assess self-assembly performance and relies on the application of an electric field to evaluate the electrophoretic mobility of components of the DNA-origami solution. The technique allows one to draw conclusions regarding the overall folding quality, through indicators such as band sharpness and migration distance, and to distinguish between the correct folded structure and multimers of multiple orders, as well as misfolded and/or partially assembled intermediates [7], [23]. DNA is visualized by staining the gel with an intercalating UV-fluorescent dye, and products are quantified using fluorescent gel scanners. Alternatively, identification and isolation of the product of interest can be done using fluorescent dyes that are incorporated into the DNA nanostructure by substitution of selected staple strands [23]. Wagenbauer and colleagues [84] developed a photometric method that examines the remaining content of ssDNA motifs in the folded DNA-origami structures with a fluorescent probe by combining gel electrophoresis and fluorescent probes. Also, photoactive compounds capable of Förster resonance energy transfer (FRET) can be used to monitor dynamic processes of structural reconfiguration in real time. Since the distance and number of fluorophores are fully predictable, structural conformations that imply a change in their spatial configuration can be monitored and quantified by FRET spectroscopy [23]. One practical example, is the work developed by Dietz´s group [85] that resorted to the Cy3-Cy5 FRET dye pair to measure the folding kinetics of every staple strand and its two terminal segments during constant-temperature assembly of a multiplayer DNA-origami object.

Another approach involves the use of UV-visible and circular dichroism spectroscopy. In this case, the DNA-origami nanostructures are coupled with metal nanoparticles allowing the determination of DNA concentration-dependent properties [86] and identification of the final compound chiral signature [87].

Even though the aforementioned techniques are suitable to obtain a general picture of the assembly process, they lack spatial-temporal detail. This detail can be obtained by using single-molecule techniques, such as transmission electron microscopy (TEM) [7], [24], atomic force microscopy (AFM) [14] or cryo-electron microscopy [14], single-molecule fluorescence microscopy [88] or single-molecule force measurements [89].

AFM relies on the sensing of the intramolecular forces occurring between the AFM tip and the sample, allowing the obtention of the height profile of the sample deposited on an atomically

flat surface with a lateral resolution of 1-2 nm. This technique has been mainly employed on the characterization of 2D structures since the deformation caused by the AFM tip during scanning makes it difficult to obtain the complete topography of surface features in low-rigidity structures like 3D or multilayered DNA-origami [23], [90], [91].

For the characterization of 3D DNA objects, TEM and cryo-EM are preferred. In TEM, uranyl salts are usually used to produce negatively stain contrast in TEM micrographs, since they are excluded from the densely packed DNA structures, and the result is a bright image of the sample on a dark background. Processing of the resulting images allows the assessment of the heterogeneity of DNA-origami, the identification of structural flaws, and the reconstruction of 3D models from TEM images of a single structure. However, the high vacuum and dehydration conditions associated with TEM imaging may result in flattening and distortion of structures that display inner cavities [23], [90]. In these cases, cryo-EM conditions are preferred since they allow imaging in fully hydrated cryogenic conditions. Moreover, the acquisition of large sets of individual particle images and post-processing using sophisticated post-imaging software tools results in a large increase of the signal to noise ratio, enabling the full reconstruction of the 3D structure with near atomic resolution [23], [90], [91].

Another alternative is the use of fluorescence-based techniques, which provide an indirect characterization of local molecular events occurring near dye molecules attached to the DNA surface. Examples are the use of single-molecule FRET and super-resolution microscopy. While FRET relies on the distance-dependent energy transfer between a donor and an acceptor photoactive probe, super-resolution imaging is the consecutive switching of fluorescent molecules between an on and off state [23]. One example of super-resolution spectroscopy that allows the reconstruction of DNA-origami structures is DNA-PAINT (DNA-point accumulation for imaging in nanoscale topography). This method is based on specific, transient binding of short fluorescent DNA oligonucleotides to single-stranded docking strands expanded from the DNA-origami structure. Upon binding of a fluorescently labeled strand from solution, its fluorescence emission is detected, allowing the description of conformational dynamics and kinetics of diffusion processes [88], [90].

Finally, another alternative is the use of single-molecule force spectroscopy based on optical tweezers, which use a highly focused laser beam to hold and move the DNA-origami objects in a manner similar to tweezers. This technique has been employed in the observation of small

DNA-origami domains and promises to be an essential tool for the investigation of dynamic events at the single-molecule level [23], [89].

I.3. Applications

DNA-origami technology has been used in many fields of research as a tool for a wide range of applications [7], [19], [92]–[96]. Table 1 shows examples of fields of research and gives a brief description of potential applications.

Table I.1: Examples of several fields of studies and reports describing DNA-origami technology applications.

Structural Biology	
Use of nanotubes for NMR structure determination of membrane proteins	[78], [97]
Biophysics	
Transporting mechanisms coordinated by cytoplasmic dynein and kinesin-1 microtubule-based motors to eukaryotic cells	[98]
Study of small DNA secondary structures using rigid DNA linkers for high-resolution single-molecule mechanical experiments	[99]
Use of DNA-PAINT, a transient binding of short fluorescently labeled oligonucleotides, for super-resolution imaging of *in vitro* synthetic DNA structures	[100]
Use of gatekeeper nanoplates to convert nanopores in solid-state membranes into a biosensing device for label-free and sequence-specific detection of DNA	[101]
DNA-origami as a transmembrane channel in lipid bilayers to detect single-DNA molecules	[102]
Use of DNA-origami nanostructures in combination with high-speed atomic force microscopy for single-molecular dynamics of proteins	[103]
Quantification of DNA strand breaks in 2-fluoroadenine-containing nucleotides, a therapeutic agent used in cancer radiotherapy, upon irradiation with low-energy electrons	[104]
Therapeutics	
Developing of a DNA nanorobot, controlled by an aptamer-encoded logic gate, capable of transporting molecular payloads to cells, sensing	[105]

cell surface inputs for conditional, triggered activation and reconfiguring its structure for payload delivery	
A dual-functional imaging and photodynamic therapy nanosystem loaded with BMEPC, an imaging agent and photosensitizer, to promote tumor apoptosis	[106]
DNA-origami as doxorubicin, an anti-cancer drug, carrier through intercalation showed a high level of drug loading efficiency and prominent cytotoxicity not only to regular human breast cancer adenocarcinoma cancer cells but also to doxorubicin-resistance cancer cells by increasing cellular internalization of doxorubicin	[107]
A DNA-origami tube decorated with 62 cytosine-phosphate-guanine (CpG)-containing oligonucleotides was able to trigger a strong immune response, characterized by cytokine production and immune cell activation	[108]
Photonics	
Directed self-assembly of DNA-origami onto lithographically patterned binding sites for controlled coupling of molecular emitters to photonic crystal cavities	[109]
Use of a rectangular DNA-origami labelled with fluorophores at specific positions was used as a nanoscopic ruler allowing super-resolution microscopy to optically resolve two fluorophores separated by 90 nm	[110]
Functionalized DNA-origami nanotubes for the fabrication of streptavidin-conjugated quantum dot arrays	[111]
Self-assembled nanoantennas, prepared by attaching one or two gold nanoparticles to DNA-origami structures, to enhance 117-fold the fluorescence intensity for a dye molecule positioned in the 21 nm gap between 100 nm gold nanoparticles	[112]
Plasmonics	
DNA-origami as a self-assembly platform to construct reconfigurable 3D plasmonic nanostructures sensitive to conformational changes manifested into a controlled shift of the plasmonic resonance peak	[113]
DNA-origami for high-yield production of plasmonic structures that contain nanoparticles arranged in nano-meter-scale helices	[114]
Use of DNA-origami to custom-tune plasmonic metamolecules in order to study plasmonic features like electric and magnetic resonances at visible frequencies	[115], [116]

Two gold nanoparticles linked by a three-layered DNA-origami block were used to enhance spectroscopic signals	[117]

Electronics

Synthetic polymer wires containing short oligonucleotides that extend from each repeat can be made to assemble arbitrary routes using both 2 and 3-D DNA-origami templates	[118]
A transistor-like behavior was observed when mixing a rectangular DNA-origami template with carbon nanotubes that can sequence-specific bind to the DNA structure	[119]
Directed assembly of 5 nm gold nanoparticles into large-area, spatially ordered, 2D arrays through the site-selective deposition of DNA-origami onto lithographically patterned substrates.	[120]

I.4. References

[1] N. C. Seeman and H. F. Sleiman, "DNA nanotechnology," *Nat. Rev. Mater.*, vol. 3, 2017.

[2] F. Zhang, J. Nangreave, Y. Liu, and H. Yan, "Structural DNA nanotechnology: State of the art and future perspective," *J. Am. Chem. Soc.*, vol. 136, no. 32, pp. 11198–11211, 2014.

[3] N. C. Seeman, "Nucleic acid junctions and lattices," *J. Theor. Biol.*, vol. 99, no. 2, pp. 237–247, 1982.

[4] B. Saccà and C. M. Niemeyer, "DNA-origami: The art of folding DNA," *Angew. Chemie - Int. Ed.*, vol. 51, no. 1, pp. 58–66, 2012.

[5] A. Kuzuya and M. Komiyama, "DNA-origami: Fold, stick, and beyond," *Nanoscale*, vol. 2, no. 3, pp. 310–322, 2010.

[6] P. W. K. Rothemund, "Folding DNA to create nanoscale shapes and patterns," *Nature*, vol. 440, no. 7082, pp. 297–302, 2006.

[7] K. F. Wagenbauer *et al.*, "How We Make DNA-origami," *ChemBioChem*, vol. 18, no. 19, pp. 1873–1885, 2017.

[8] F. Hong, F. Zhang, Y. Liu, and H. Yan, *DNA-origami: Scaffolds for Creating Higher Order Structures*, vol. 117, no. 20. 2017.

[9] S. M. Douglas, H. Dietz, T. Liedl, B. Högberg, F. Graf, and W. M. Shih, "Self-assembly of DNA into nanoscale three-dimensional shapes," *Nature*, vol. 459, no. 7245, pp. 414–418, 2009.

[10] Y. Ke *et al.*, "Multilayer DNA-origami packed on a square lattice," *J. Am. Chem. Soc.*, vol. 131, no. 43, pp. 15903–15908, 2009.

[11] Y. Ke, N. V. Voigt, K. V. Gothelf, and W. M. Shih, "Multilayer DNA-origami packed on hexagonal and hybrid lattices," *J. Am. Chem. Soc.*, vol. 134, no. 3, pp. 1770–1774, 2012.

[12] H. Dietz, S. M. Douglas, and W. M. Shih, "Folding DNA into twisted and curved nanoscale shapes," *Science*, vol. 325, no. 5941, pp. 725–730, 2009.

[13] D. Han *et al.*, "DNA gridiron nanostructures based on four-arm junctions," *Science*, vol. 339, no. 6126, pp. 1412–1415, 2013.

[14] R. Veneziano *et al.*, "Designer nanoscale DNA assemblies programmed from the top

down," *Science*, vol. 352, no. 6293, 2016.
[15] E. Benson *et al.*, "DNA rendering of polyhedral meshes at the nanoscale," *Nature*, vol. 523, no. 7561, pp. 441–444, 2015.
[16] F. Zhang *et al.*, "Complex wireframe DNA-origami nanostructures with multi-arm junction vertices," *Nat. Nanotechnol.*, vol. 10, no. 9, pp. 779–784, 2015.
[17] N. C. Seeman, "DNA in a material world," *Nature*, vol. 421, no. 6921, pp. 427–431, 2003.
[18] Y. R. Yang, Y. Liu, and H. Yan, "DNA Nanostructures as Programmable Biomolecular Scaffolds," *Bioconjug. Chem.*, vol. 26, no. 8, pp. 1381–1395, 2015.
[19] P. Wang, T. A. Meyer, V. Pan, P. K. Dutta, and Y. Ke, "The Beauty and Utility of DNA-origami," *Chem*, vol. 2, no. 3, pp. 359–382, 2017.
[20] K. E. Dunn, "The business of DNA nanotechnology: Commercialization of origami and other technologies," *Molecules*, vol. 25, no. 2, 2020.
[21] "Tilibit nanosystems." [Online]. Available: https://www.tilibit.com.
[22] "GATTAquant." [Online]. Available: http://www.gattaquant.com.
[23] S. Dey *et al.*, "DNA-origami," *Nat. Rev. Methods Prim.*, vol. 1, no. 1, pp. 1–24, 2021.
[24] C. E. Castro *et al.*, "A primer to scaffolded DNA-origami," *Nat. Methods*, vol. 8, no. 3, pp. 221–229, 2011.
[25] P. Piskunen, S. Nummelin, B. Shen, M. A. Kostiainen, and V. Linko, "Increasing Complexity in Wireframe DNA Nanostructures," *Molecules*, vol. 25, no. 1823, 2020.
[26] S. M. Douglas, A. H. Marblestone, S. Teerapittayanon, A. Vazquez, G. M. Church, and W. M. Shih, "Rapid prototyping of 3D DNA-origami shapes with caDNAno," *Nucleic Acids Res.*, vol. 37, no. 15, pp. 5001–5006, 2009.
[27] T. Delaveau, G. Charvin, J. Uhlendorf, S. Bottani, P. Hersen, and G. Batt, "Computer-Aided Design of DNA-origami Structures," vol. 1244, pp. 277–285, 2015.
[28] S. Williams, K. Lund, C. Lin, P. Wonka, S. Lindsay, and H. Yan, "DNA Computing Vol. 5347." Springer, New York, 2009.
[29] E. S. Andersen *et al.*, "DNA-origami design of dolphin-shaped structures with flexible tails," *ACS Nano*, vol. 2, no. 6, pp. 1213–1218, 2008.
[30] M. Matthies, N. P. Agarwal, E. Poppleton, F. M. Joshi, P. Šulc, and T. L. Schmidt, "Triangulated Wireframe Structures Assembled Using Single-Stranded DNA Tiles," *ACS Nano*, vol. 13, no. 2, pp. 1839–1848, 2019.
[31] H. Jun, X. Wang, W. P. Bricker, S. Jackson, and M. Bathe, "Rapid Prototyping of Wireframe Scaffolded DNA-origami using ATHENA," *bioRxiv*, no. 2, 2020.
[32] V. Linko and M. A. Kostiainen, "Automated design of DNA-origami," *Nat. Biotechnol.*, vol. 34, no. 8, pp. 826–827, 2016.
[33] H. Jun *et al.*, "Autonomously designed free-form 2D DNA-origami," *Sci. Adv.*, vol. 5, no. 1, pp. 1–9, 2019.
[34] H. Jun *et al.*, "Automated sequence design of 3D polyhedral wireframe DNA-origami with honeycomb edges," *ACS Nano*, vol. 13, no. 2, pp. 2083–2093, 2019.
[35] H. Jun, X. Wang, W. P. Bricker, and M. Bathe, "Automated sequence design of 2D wireframe DNA-origami with honeycomb edges," *Nat. Commun.*, vol. 10, no. 1, pp. 1–9, 2019.
[36] E. De Llano *et al.*, "Adenita: interactive 3D modelling and visualization of DNA nanostructures," *Nucleic Acids Res.*, vol. 48, no. 15, pp. 8269–8275, 2020.
[37] J. Sambrook, E. Fritsch, and T. Maniatis, *Molecular Cloning A Laboratory Manual*, 3rd Editio. New York NY: Cold Spring Harbor Laboratory Press, 2001.
[38] N. D. Zinder and J. D. Boeke, "The filamentous phage (Ff) as vectors for recombinant

DNA- a review," *Gene*, vol. 19, no. 1, pp. 1–10, 1982.
[39] J. Slonczewski and J. Foster, *Microbiology: An Evolving Science*. New York NY: W.W. Norton & Company, 2011.
[40] J. Rakonjac, N. J. Bennett, J. Spagnuolo, D. Gagic, and M. Russel, "Filamentous bacteriophage: biology, phage display and nanotechnology applications.," *Curr. Issues Mol. Biol.*, vol. 13, no. 2, pp. 51–76, 2011.
[41] K. Horiuchi, "Initiation mechanisms in replication of filamentous phage DNA," *Genes to Cells*, vol. 2, no. 7, pp. 425–432, 1997.
[42] W. Fulford and P. Model, "Bacteriophage f1 DNA replication genes," *J. Mol. Biol.*, vol. 203, no. 1, pp. 39–48, 1988.
[43] J. Bush, S. Singh, M. Vargas, E. Oktay, C. H. Hu, and R. Veneziano, "Synthesis of DNA-origami scaffolds: Current and emerging strategies," *Molecules*, vol. 25, no. 15, pp. 1–18, 2020.
[44] C. Yanisch-Perron, J. Vieira, and J. Messing, "Improved M13 phage cloning vectors and host strains: nucleotide sequences of the M13mp18 and pUC19 vectors," *Gene*, vol. 33, pp. 103–119, 1985.
[45] P. Reddy and K. McKenney, "Improved method for the production of M13 phage and single-stranded DNA for DNA sequencing," *Biotechniques*, vol. 20, no. 5, pp. 854–860, 1996.
[46] B. Kick, F. Praetorius, H. Dietz, and D. Weuster-Botz, "Efficient Production of Single-Stranded Phage DNA as Scaffolds for DNA-origami," *Nano Lett.*, vol. 15, no. 7, pp. 4672–4676, 2015.
[47] B. Kick, S. Hensler, F. Praetorius, H. Dietz, and D. Weuster-Botz, "Specific growth rate and multiplicity of infection affect high-cell-density fermentation with bacteriophage M13 for ssDNA production," *Biotechnol. Bioeng.*, vol. 114, no. 4, pp. 777–784, 2017.
[48] B. Kick, K. L. Behler, T. S. Severin, and D. Weuster-Botz, "Chemostat studies of bacteriophage M13 infected Escherichia coli JM109 for continuous ssDNA production," *J. Biotechnol.*, vol. 258, no. January, pp. 92–100, 2017.
[49] B. Lee, J. Lee, D. J. Ahn, S. Lee, and M. Oh, "Optimizing protein V untranslated region sequence in M13 phage for increased production of single-stranded DNA for origami," pp. 1–8, 2021.
[50] R. M. Zadegan *et al.*, "Construction of a 4 Zeptoliters switchable 3D DNA box origami," *ACS Nano*, vol. 6, no. 11, pp. 10050–10053, 2012.
[51] X. Chen, Q. Wang, J. Peng, Q. Long, H. Yu, and Z. Li, "Self-Assembly of Large DNA-origami with Custom-Designed Scaffolds," *ACS Appl. Mater. Interfaces*, vol. 10, no. 29, pp. 24344–24348, 2018.
[52] S. Brown *et al.*, "An easy-to-prepare mini-scaffold for DNA-origami," *Nanoscale*, vol. 7, no. 40, pp. 16621–16624, 2015.
[53] P. M. Nafisi, T. Aksel, and S. M. Douglas, "Construction of a novel phagemid to produce custom DNA-origami scaffolds," *Synth. Biol.*, vol. 3, no. 1, pp. 1–8, 2018.
[54] A. N. Marchi, I. Saaem, B. N. Vogen, S. Brown, and T. H. Labean, "Toward larger DNA-origami," *Nano Lett.*, vol. 14, no. 10, pp. 5740–5747, 2014.
[55] T. R. Shepherd, R. R. Du, H. Huang, E. C. Wamhoff, and M. Bathe, "Bioproduction of pure, kilobase-scale single-stranded DNA," *Sci. Rep.*, vol. 9, no. 1, pp. 1–9, 2019.
[56] F. Praetorius, B. Kick, K. L. Behler, M. N. Honemann, D. Weuster-Botz, and H. Dietz, "Biotechnological mass production of DNA-origami," *Nature*, vol. 552, no. 7683, pp. 84–87, 2017.

[57] F. A. S. Engelhardt *et al.*, "Custom-Size, Functional, and Durable DNA-origami with Design-Specific Scaffolds," *ACS Nano*, vol. 13, no. 5, pp. 5015–5027, 2019.
[58] E. Pound, J. R. Ashton, H. A. Becerril, and A. T. Woolley, "Polymerase chain reaction based scaffold preparation for the production of thin, branched DNA-origami nanostructures of arbitrary sizes," *Nano Lett.*, vol. 9, no. 12, pp. 4302–4305, 2009.
[59] M. Yuce, H. Kurt, and H. Budak, "Characterization of a dual biotin tag for improved single stranded DNA production," *Anal. Methods*, vol. 6, no. 2, pp. 548–557, 2014.
[60] H. Zhang, J. Chao, D. Pan, H. Liu, Q. Huang, and C. Fan, "Folding super-sized DNA-origami with scaffold strands from long-range PCR," *Chem. Commun.*, vol. 48, no. 51, pp. 6405–6407, 2012.
[61] D. Han *et al.*, "Single-stranded DNA and RNA origami," *Science*, vol. 358, no. 6369, 2017.
[62] E. Krieg and W. M. Shih, "Selective Nascent Polymer Catch-and-Release Enables Scalable Isolation of Multi-Kilobase Single-Stranded DNA," *Angew. Chemie*, vol. 130, no. 3, pp. 722–726, 2018.
[63] D. Minev *et al.*, "Rapid in vitro production of single-stranded DNA," *Nucleic Acids Res.*, vol. 47, no. 22, pp. 11956–11962, 2019.
[64] R. Veneziano, T. R. Shepherd, S. Ratanalert, L. Bellou, C. Tao, and M. Bathe, "In vitro synthesis of gene-length single-stranded DNA," *Sci. Rep.*, vol. 8, no. 1, pp. 1–7, 2018.
[65] C. I. Wooddell and R. R. Burgess, "Use of asymmetric PCR to generate long primers and single-stranded DNA for incorporating cross-linking analogs into specific sites in a DNA probe," *Genome Res.*, vol. 6, no. 9, pp. 886–892, 1996.
[66] M. Erkelenz *et al.*, "A facile method for preparation of tailored scaffolds for DNA-origami," *Small*, vol. 10, no. 1, pp. 73–77, 2014.
[67] H. Said, V. Schuller, F. J. Eber, C. Wege, T. Liedl, and C. Richert, "M1.3 - A Small Scaffold for DNA-origami Full," *Nanoscale*, vol. 5, no. 1, pp. 284–290, 2013.
[68] Y. Ma *et al.*, "RCA strands as scaffolds to create nanoscale shapes by a few staple strands," *J. Am. Chem. Soc.*, vol. 135, no. 8, pp. 2959–2962, 2013.
[69] G. D. Hamblin, J. F. Rahbani, and H. F. Sleiman, "Sequential growth of long DNA strands with user-defined patterns for nanostructures and scaffolds," *Nat. Commun.*, vol. 6, no. May, 2015.
[70] T. L. Schmidt *et al.*, "Scalable amplification of strand subsets from chip-synthesized oligonucleotide libraries," *Nat. Commun.*, vol. 6, pp. 1–7, 2015.
[71] C. Ducani, C. Kaul, M. Moche, W. M. Shih, and B. Högberg, "Enzymatic production of 'monoclonal stoichiometric' single-stranded DNA oligonucleotides," *Nat. Methods*, vol. 10, no. 7, pp. 647–652, 2013.
[72] J. P. J. Sobczak, T. G. Martin, T. Gerling, and H. Dietz, "Rapid folding of DNA into nanoscale shapes at constant temperature," *Science*, vol. 338, no. 6113, pp. 1458–1461, 2012.
[73] T. G. Martin and H. Dietz, "Magnesium-free self-assembly of multi-layer DNA objects," *Nat. Commun.*, vol. 3, 2012.
[74] D. Wang *et al.*, "Stability study of tubular DNA-origami in the presence of protein crystallisation buffer," *RSC Adv.*, vol. 5, no. 72, pp. 58734–58737, 2015.
[75] S. Ramakrishnan, G. Krainer, G. Grundmeier, M. Schlierf, and A. Keller, "Structural stability of DNA-origami nanostructures in the presence of chaotropic agents," *Nanoscale*, vol. 8, no. 19, pp. 10398–10405, 2016.
[76] E. Stahl, T. G. Martin, F. Praetorius, and H. Dietz, "Facile and scalable preparation of pure and dense DNA-origami solutions," *Angew. Chemie - Int. Ed.*, vol. 53, no. 47, pp.

12735–12740, 2014.
[77] H. Kim, S. P. Surwade, A. Powell, C. O'Donnell, and H. Liu, "Stability of DNA-origami nanostructure under diverse chemical environments," *Chem. Mater.*, vol. 26, no. 18, pp. 5265–5273, 2014.
[78] G. Bellot, M. A. McClintock, J. J. Chou, and W. M. Shih, "DNA nanotubes for NMR structure determination of membrane proteins," *Nat. Protoc.*, vol. 8, no. 4, pp. 755–770, 2013.
[79] M. Hanke, N. Hansen, R. Chen, G. Grundmeier, K. Fahmy, and A. Keller, "Salting-Out of DNA-origami Nanostructures by Ammonium Sulfate," *Int. J. Mol. Sci.*, vol. 23, no. 5, 2022.
[80] G. Bellot, M. A. McClintock, C. Lin, and W. M. Shih, "Recovery of intact DNA nanostructures after agarose gel-based separation," *Nat. Methods*, vol. 8, no. 3, pp. 192–194, 2011.
[81] A. Shaw, E. Benson, and B. Högberg, "Purification of functionalized DNA-origami nanostructures," *ACS Nano*, vol. 9, no. 5, pp. 4968–4975, 2015.
[82] C. Lin, S. D. Perrault, M. Kwak, F. Graf, and W. M. Shih, "Purification of DNA-origami nanostructures by rate-zonal centrifugation," *Nucleic Acids Res.*, vol. 41, no. 2, 2013.
[83] S. H. Ko *et al.*, "High-speed, high-purity separation of gold nanoparticle-DNA-origami constructs using centrifugation," *Soft Matter*, vol. 10, no. 37, pp. 7370–7378, 2014.
[84] K. F. Wagenbauer, C. H. Wachauf, and H. Dietz, "Quantifying quality in DNA self-assembly," *Nat. Commun.*, vol. 5, pp. 1–7, 2014.
[85] F. Schneider, N. Möritz, and H. Dietz, "The sequence of events during folding of a DNA-origami," *Sci. Adv.*, vol. 5, no. 5, pp. 1–11, 2019.
[86] L. Opherden, J. Oertel, A. Barkleit, K. Fahmy, and A. Keller, "Paramagnetic decoration of DNA-origami nanostructures by Eu3+ coordination," *Langmuir*, vol. 30, no. 27, pp. 8152–8159, 2014.
[87] R. Schreiber *et al.*, "Chiral plasmonic DNA nanostructures with switchable circular dichroism," *Nat. Commun.*, vol. 4, pp. 1–6, 2013.
[88] R. Jungmann, C. Steinhauer, M. Scheible, A. Kuzyk, P. Tinnefeld, and F. C. Simmel, "Single-molecule kinetics and super-resolution microscopy by fluorescence imaging of transient binding on DNA-origami," *Nano Lett.*, vol. 10, no. 11, pp. 4756–4761, 2010.
[89] M. C. Engel *et al.*, "Force-Induced Unravelling of DNA-origami," *ACS Nano*, vol. 12, no. 7, pp. 6734–6747, 2018.
[90] R. Jungmann, M. Scheible, and F. C. Simmel, "Nanoscale imaging in DNA nanotechnology," *Wiley Interdiscip. Rev. Nanomedicine Nanobiotechnology*, vol. 4, no. 1, pp. 66–81, 2012.
[91] V. Birkedal *et al.*, "Single molecule microscopy methods for the study of DNA-origami structures," *Microsc. Res. Tech.*, vol. 74, no. 7, pp. 688–698, 2011.
[92] A. R. Chandrasekaran, N. Anderson, M. Kizer, K. Halvorsen, and X. Wang, "Beyond the Fold: Emerging Biological Applications of DNA-origami," *ChemBioChem*, pp. 1081–1089, 2016.
[93] A. Udomprasert and T. Kangsamaksin, "DNA-origami applications in cancer therapy," *Cancer Sci.*, vol. 108, no. 8, pp. 1535–1543, 2017.
[94] B. R. Madhanagopal, S. Zhang, E. Demirel, H. Wady, and A. R. Chandrasekaran, "DNA Nanocarriers: Programmed to Deliver," *Trends Biochem. Sci.*, vol. 43, no. 12, pp. 997–1013, 2018.
[95] A. Kuzyk, R. Jungmann, G. P. Acuna, and N. Liu, "DNA-origami Route for

Nanophotonics," *ACS Photonics*, vol. 5, no. 4, pp. 1151–1163, 2018.
[96] N. Liu and T. Liedl, "DNA-Assembled Advanced Plasmonic Architectures," *Chem. Rev.*, vol. 118, no. 6, pp. 3032–3053, 2018.
[97] M. J. Berardi, W. M. Shih, S. C. Harrison, and J. J. Chou, "Mitochondrial uncoupling protein 2 structure determined by NMR molecular fragment searching," *Nature*, vol. 476, no. 7358, pp. 109–113, 2011.
[98] N. D. Derr, B. S. Goodman, R. Jungmann, A. E. Leschziner, W. M. Shih, and S. L. Reck-Peterson, "Tug-of-war in motor protein ensembles revealed with a programmable DNA-origami scaffold," *Science*, vol. 338, no. 6107, pp. 662–665, 2012.
[99] E. Pfitzner *et al.*, "Rigid DNA beams for high-resolution single-molecule mechanics," *Angew. Chemie - Int. Ed.*, vol. 52, no. 30, pp. 7766–7771, 2013.
[100] R. Jungmann, M. S. Avendaño, J. B. Woehrstein, M. Dai, W. M. Shih, and P. Yin, "Multiplexed 3D cellular super-resolution imaging with DNA-PAINT and Exchange-PAINT," *Nat. Methods*, vol. 11, no. 3, pp. 313–318, 2014.
[101] R. Wei, T. G. Martin, U. Rant, and H. Dietz, "DNA-origami Gatekeepers for Solid-State Nanopores," *Angew. Chemie*, vol. 124, no. 20, pp. 4948–4951, 2012.
[102] M. Langecker *et al.*, "Synthetic lipid membrane channels formed by designed DNA nanostructures," *Science*, vol. 338, no. 6109, pp. 932–936, 2012.
[103] A. Rajendran, M. Endo, and H. Sugiyama, "State-of-the-art high-speed atomic force microscopy for investigation of single-molecular dynamics of proteins," *Chem. Rev.*, vol. 114, no. 2, pp. 1493–1520, 2014.
[104] J. Rackwitz *et al.*, "Sensitizing DNA Towards Low-Energy Electrons with 2-Fluoroadenine," *Angew. Chemie*, vol. 128, no. 35, pp. 10404–10408, 2016.
[105] S. M. Douglas, I. Bachelet, and G. M. Church, "A Logic-Gated Nanorobot for Targeted Transport of Molecular Payloads," *Science*, vol. 335, no. February, pp. 831–834, 2012.
[106] X. Zhuang *et al.*, "A Photosensitizer-Loaded DNA-origami Nanosystem for Photodynamic Therapy," *ACS Nano*, vol. 10, no. 3, pp. 3486–3495, 2016.
[107] Q. Jiang *et al.*, "DNA-origami as a carrier for circumvention of drug resistance," *J. Am. Chem. Soc.*, vol. 134, no. 32, pp. 13396–13403, 2012.
[108] V. J. Schüller *et al.*, "Cellular immunostimulation by CpG-sequence-coated DNA-origami structures," *ACS Nano*, vol. 5, no. 12, pp. 9696–9702, 2011.
[109] A. Gopinath, E. Miyazono, A. Faraon, and P. W. K. Rothemund, "Engineering and mapping nanocavity emission via precision placement of DNA-origami," *Nature*, vol. 535, no. 7612, pp. 401–405, 2016.
[110] C. Steinhauer, R. Jungmann, T. L. Sobey, F. C. Simmel, and P. Tinnefeld, "DNA-origami as a nanoscopic ruler for superresolution microscopy," *Angew. Chemie - Int. Ed.*, vol. 48, no. 47, pp. 8870–8873, 2009.
[111] H. Bui *et al.*, "Programmable periodicity of quantum dot arrays with DNA-origami nanotubes," *Nano Lett.*, vol. 10, no. 9, pp. 3367–3372, 2010.
[112] G. P. Acuna, F. M. Möller, P. Holzmeister, S. Beater, B. Lalkens, and P. Tinnefeld, "Fluorescence enhancement at docking sites of DNA-directed self-assembled nanoantennas," *Science*, vol. 338, no. 6106, pp. 506–510, 2012.
[113] P. Zhan *et al.*, "Reconfigurable Three-Dimensional Gold Nanorod Plasmonic Nanostructures Organized on DNA-origami Tripod," *ACS Nano*, vol. 11, no. 2, pp. 1172–1179, 2017.
[114] A. Kuzyk *et al.*, "DNA-based self-assembly of chiral plasmonic nanostructures with tailored optical response," *Nature*, vol. 483, no. 7389, pp. 311–314, 2012.

[115] E. M. Roller, C. Argyropoulos, A. Högele, T. Liedl, and M. Pilo-Pais, “Plasmon-Exciton Coupling Using DNA Templates,” *Nano Lett.*, vol. 16, no. 9, pp. 5962–5966, 2016.
[116] E. M. Roller, L. K. Khorashad, M. Fedoruk, R. Schreiber, A. O. Govorov, and T. Liedl, “DNA-assembled nanoparticle rings exhibit electric and magnetic resonances at visible frequencies,” *Nano Lett.*, vol. 15, no. 2, pp. 1368–1373, 2015.
[117] P. Kühler, E. M. Roller, R. Schreiber, T. Liedl, T. Lohmüller, and J. Feldmann, “Plasmonic DNA-origami nanoantennas for surface-enhanced Raman spectroscopy,” *Nano Lett.*, vol. 14, no. 5, pp. 2914–2919, 2014.
[118] J. B. Knudsen *et al.*, “Routing of individual polymers in designed patterns,” *Nat. Nanotechnol.*, vol. 10, no. 10, pp. 892–898, 2015.
[119] H. T. Maune *et al.*, “Self-assembly of carbon nanotubes into two-dimensional geometries using DNA-origami templates,” *Nat. Nanotechnol.*, vol. 5, no. 1, pp. 61–66, 2010.
[120] A. M. Hung, C. M. Micheel, L. D. Bozano, L. W. Osterbur, G. M. Wallraff, and J. N. Cha, “Large-area spatially ordered arrays of gold nanoparticles directed by lithographically confined DNA-origami,” *Nat. Nanotechnol.*, vol. 5, no. 2, pp. 121–126, 2010.

CHAPTER II – PHAGE AND PHAGE-FREE SINGLE STRANDED DNA PRODUCTION WITH *ESCHERICHIA COLI*

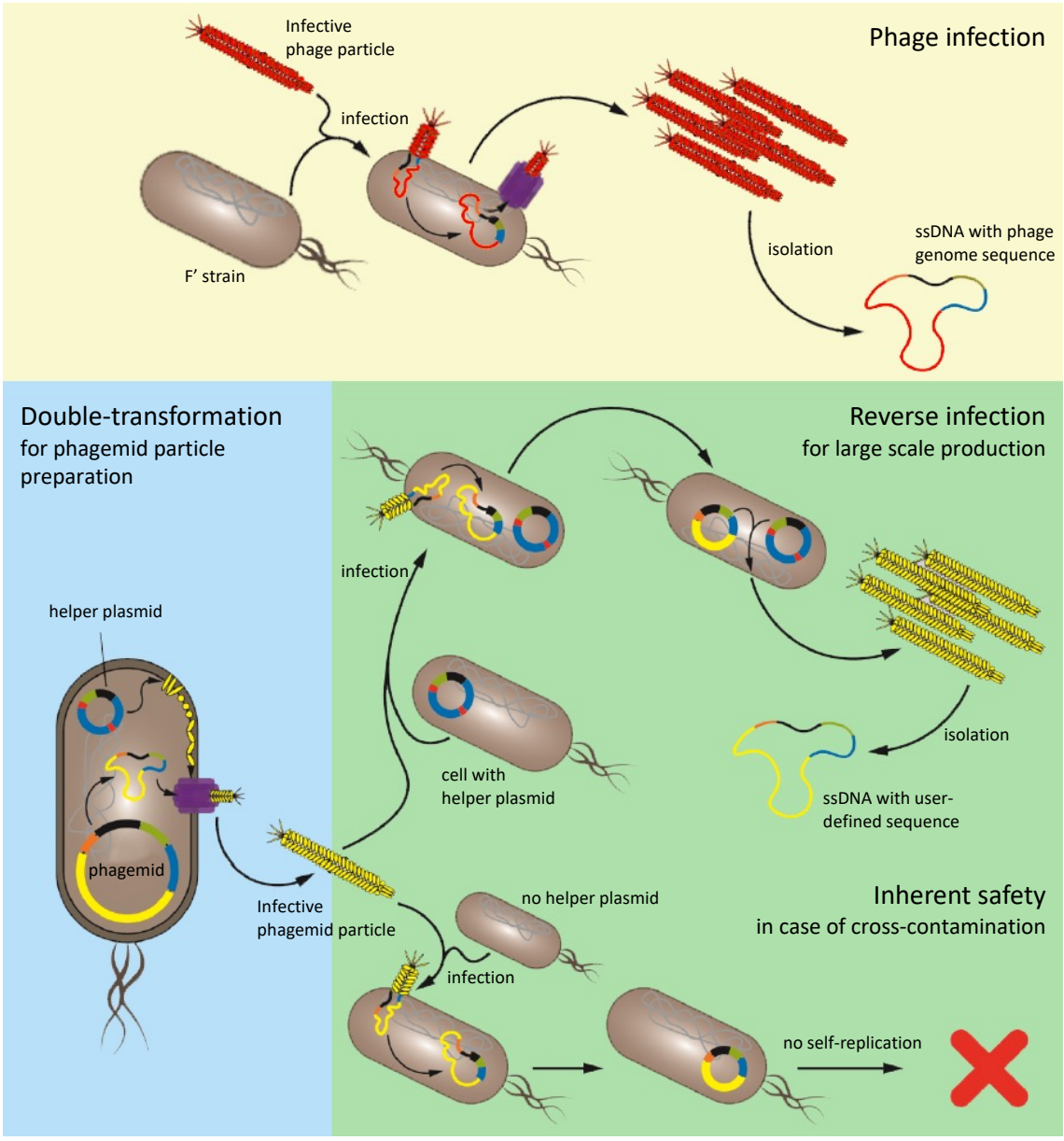

Phage infection experiments were part of the work developed by Berke Santos to 1st Cycle Integrated Project in Biomedical Engineering.

Double transformation and reverse infection experiments contributed to: Behler, K. L., Honemann, M. N., Silva-Santos, A. R., Dietz, H., & Weuster-Botz, D. (2022). Phage-free production of artificial ssDNA with Escherichia coli. *Biotechnology and Bioengineering*, 1–12.

Abstract

Artificial single stranded DNA (ssDNA) that lengths up to the kilobase range is increasingly needed in mass quantities to realize the potential of emerging technologies such as genome editing and DNA-origami. One alternative to produce this type of molecules is the infection of an *E. coli* host cell with a bacteriophage like the M13mp18. Even though, this method produces a circular single stranded DNA molecule of 7249 nucleotides with the sequence of the M13mp18 genome with high yields, the need for ssDNA scaffolds with user defined sequences and the fact that it requires dedicated, and thus costly, fermentation infrastructure, because of the risk of cross-contaminating manufacturer plants with self-replicating phages, led to the development of alternative strategies to produce long ssDNA molecules.

Our system utilizes a designed phagemid and an optimized helper plasmid. The phagemid encodes one gene of the M13 phage genome and a freely chosen custom target sequence, while the helper plasmid encodes the other genes of the M13 phage. The phagemid particles produced are not capable of self-replication in the absence of the helper plasmid. This enables cross-contamination-free biotechnological production of ssDNA at any contract manufacturer. We compared the standard phage infection protocol, that yields up to 3.5 mg/L of media of ssDNA, with a double transformation protocol where the phagemid and the helper plasmid are co-transformed into the *E. coli* cells, and developed a method called reverse infection, which allows the growth of *E. coli* cells before phagemid production, with a 1.5 to 3-fold increase in ssDNA production compared to double transformation method.

Keywords: ssDNA, phage, phagemid, DNA-origami, biotechnological production

II.1. Introduction

Single stranded DNA (ssDNA) occurs in nature commonly only in viruses or in a transient state when double-stranded DNA (dsDNA) is replicated. Lately, ssDNA came into scientific focus as a useful biopolymer for various applications. For example, in CRISPR/Cas based genomic editing, long ssDNA donor strands with a length of 0.5-2 kb lead to higher insertion efficiencies [1], [2]. In nanotechnology, ssDNA is used as a building material for DNA-origami, which is a bottom-up method for the construction of two- and three-dimensional nanoparticles with user-defined shapes [3]–[5]. DNA-origami nanoparticles are already used in many scientific fields [6]–[11] and are currently being explored for applications such as drug delivery systems or as direct therapeutic agents for virus neutralization [12]–[16]. These and other future applications will ultimately require mass quantities of ssDNA.

Single stranded DNA can be chemically synthesized or produced *in vitro* by enzymatic processes [17]–[23], but these methods can be costly and may not easily be amenable to scale up. To satisfy the need for scalable mass production of custom sequence ssDNA, biotechnological processes have been developed [24], [25]. Genetically engineered M13-phages are produced in a high cell density cultivation and their ssDNA-genome is isolated for further use. However, this approach has limitations with respect to the length of the user-defined sequence that can be inserted [26]. To overcome the limitations of the M13 genome itself, Zinder and Boeke [27] developed a so-called phagemid, a phage-plasmid-hybrid. This phagemid consists of a plasmid backbone, the M13 origin of replication, and its packaging signal (PS), leaving ample space for inserts with user-defined sequence. The phagemid can be produced as ssDNA and packaged into M13 phage hulls as it is recognized by the cell and phage machinery. To add the phage machinery to the cells, a helper phage or a helper plasmid is needed. The helper phage is an M13 phage with an impaired M13-ori (leading to less phage ssDNA) [28], whereas the helper plasmid is a plasmid comprised of the M13 genes and a plasmid backbone but without any regulatory sequences of the M13 phage [29]. However, common methods using the helper plasmid provide limited yields of ssDNA up to 2 mg per liter [30]. With the use of helper phages, the cells produce phagemid-particles that contain the desired ssDNA in addition to complete helper phages that contaminate the product [25]. Nevertheless, the presence of the self-replicating helper phages is undesirable because it

precludes running the aforementioned biotechnological processes by contract manufacturers. This is because of risk of cross-contaminating subsequent processes, since phages may not be cleaned from the fermentation equipment with 100% certainty by standard cleaning and sterilization procedures [31].

To enable the scalable production of high amounts of ssDNA without the use of self-replicating particles, a new method called “reverse infection” was developed. Here, *E. coli* cells are first transformed with a helper plasmid, thus becoming a production strain. This strain can then be cultivated in shake flask or in a scalable high cell density cultivation process in a controlled stirred-tank bioreactor. Upon reaching the proper cell density, the cells are infected with phagemid particles – i.e. phage hulls containing only the phagemid as ssDNA. After infection, cells produce and package high amounts of the desired phagemid ssDNA as phagemid particles, which are not self-replicating by themselves. To make this reverse infection setup possible, we designed a suitable set of phagemid and helper plasmid, since, as already described in the literature, *E. coli* cells that carry a helper plasmid normally develop a resistance to infection [32]–[34]. The developed method was tested for the production of two different size ssDNA scaffolds: the CSF1 (4843 nt) and the CSMB (3254 nt) that only differ in the length of the user-defined sequence. Moreover, titer production of these new scaffolds was compared with the standard production of M13mp18 ssDNA genome by phage infection and with the double transformation procedure based on co-transformation of *E. coli* cells with a helper plasmid and either the CSF1 or CSMB phagemid. Fig. II.1. shows a workflow of the three different strategies used for ssDNA production using *E. coli* cells.

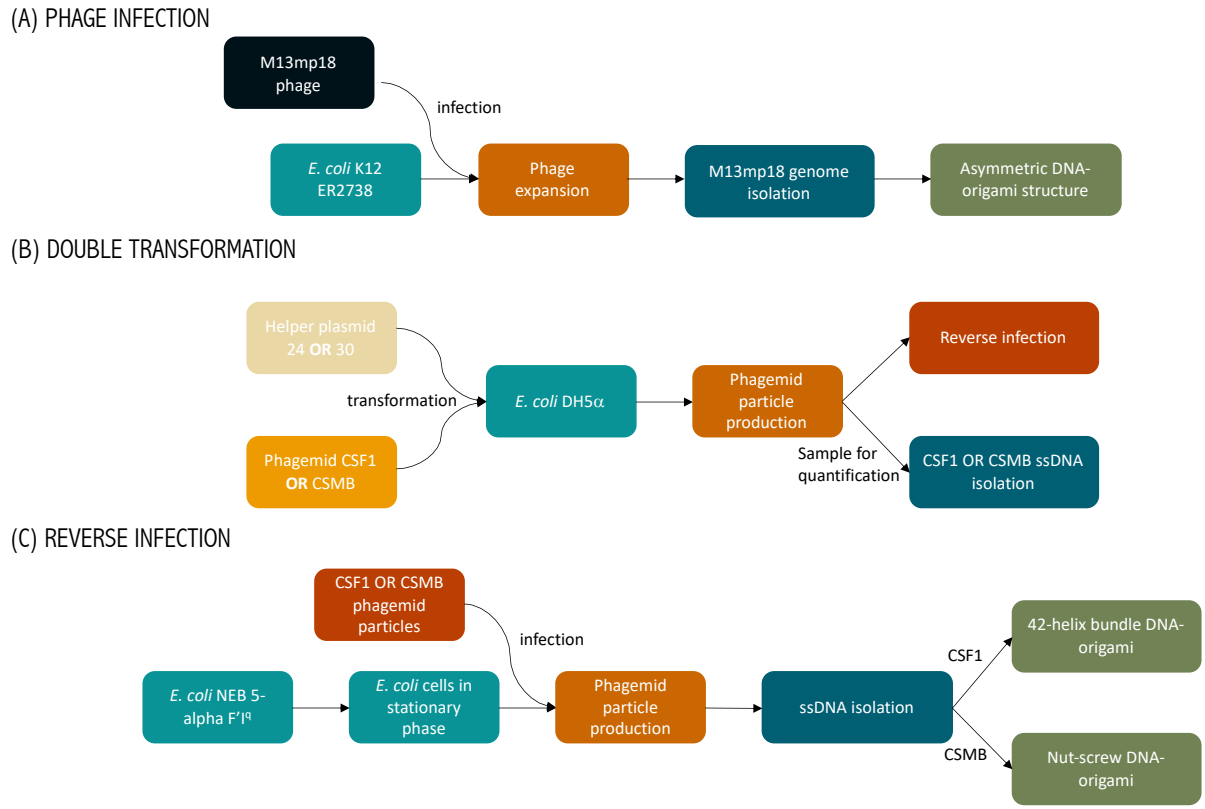

Figure II.1. Workflow of the three strategies used for the production of ssDNA scaffolds using E. coli cells. (A) Standard procedure using E. coli infection with phages like the M13mp18. (B) Double transformation of E. coli cells with a helper plasmid and a phagemid, resulting in the production of phagemid particles containing a ssDNA genome equal to the phagemid sequence. (C) Reverse infection protocol developed that allows cell growth before infection with the phagemid particles. Once again, the produced phagemid particles contain a ssDNA molecule with a sequence equal to the phagemid.

II.2. Materials and Methods

II.2.1. Materials

The producer *E. coli* strain K12 ER2738 and M13mp18 RF I DNA were from New England Biolabs (Massachusetts, USA). *E. coli* strains DH5α and NEB® 5-alpha F'I^q were from Invitrogen (Massachusetts, USA) and New England Biolabs (Massachusetts, USA), respectively. All salts used were of analytical grade.

II.2.2. Phage production

E. coli K12 ER2738 were transformed with M13mp18 RF I DNA according to manufacturer's protocol [35]. After transformation, a blue plaque was selected, and phage expansion was

performed by infecting a pre-culture of *E. coli* at an optical density (OD) of 0.5 in 5 mL complex medium (2xYT) supplemented with tetracycline (10 μg/mL) and 5 mM $MgCl_2$. After 2 h at 37 °C, 250 rpm, the culture was transferred to 750 mL of 2xYT medium supplemented with tetracycline and magnesium and incubated overnight. Following this phage expansion step, the cells were centrifuged for 30 min at 4700 g and the supernatant was mixed with 3 % PEG-8000/3 % NaCl for 30 min at room temperature to precipitate the phages. After centrifugation (20 min, 4000 g), phages were resuspended in TE buffer, centrifuged (15 min, 15000 g) to remove remaining debris and filtered through a 0.22 μm syringe filter. Phage particles quantification was performed according to [36].

II.2.3. Phagemid particle production

To preproduce phagemid particles, chemically competent E. coli DH5α were double transformed, at the same time, with a helper plasmid and a phagemid developed at Dietz Laboratory. Cells were plated on LB agar plates containing the respective antibiotics for the selection of both plasmids. Colonies were then picked and grown in pre-culture tubes in 2 mL of 2xYT also containing both antibiotics and 5 mM of $MgCl_2$ at 37 °C while shaking at 250 rpm. After 6 to 8h, precultures were completely passaged to 3 L baffled shaking flasks (DURAN® Baffled Flask, DWK Life Sciences GmbH, Wertheim, Germany) containing 750 mL of fresh medium (2xYT + 5 mM $MgCl_2$ + antibiotics). Shaking flask cultivations were kept at 37 °C and 250 rpm in a shaking incubator overnight. Then, cultures were centrifuged for 30 min at 47000 g and the supernatant containing the preproduced phagemid particles was mixed with 3 %(w/v) PEG 8000 and 3 %(w/v) NaCl for 30 min at room temperature. After precipitation, the mixture was centrifuged for 30 min at 4000 g and phagemid particles were resuspended in 3.5 mL Tris-EDTA (TE) buffer (10 mM Tris, 1 mM EDTA, pH 8). To remove remaining cellular debris, the solution was centrifuged for 15 min at 15000 g and the supernatant was kept and stored at 4 °C. Phagemid particle quantification was performed by determination of the amount of ssDNA contained in 200 μL of sample and considering that each DNA molecule corresponds to a phagemid particle.

II.2.4. Reverse infection

NEB® 5-alpha F'I^q was transformed with a helper plasmid and cells were plated on LB agar plates containing the respective antibiotic. Colonies were then picked and grown in pre-culture tubes in 2 mL of 2xYT also containing antibiotic and 5 mM of $MgCl_2$ at 37 °C while shaking at 250 rpm. After 6 to 8h, precultures were passaged to 100 mL baffled shaking flasks containing 50 mL EnPresso B medium (Sigma-Aldrich, Missouri, USA). Cultivations were kept at 37 °C and 250 rpm in a shaking incubator overnight. Then, OD was measured, and the culture was infected with phagemid particles at a multiplicity of infection (MOI) of 100 tfu/cfu. Subsequently, the cultures were further incubated overnight at 30 °C. Following phagemid production, the cells were centrifuged for 30 min at 4700 g and the supernatant was mixed with 3 % PEG-8000/3 % NaCl for 30 min at room temperature to precipitate the phagemid particles. After centrifugation (30 min, 4000 g), phages were resuspended in TE buffer, centrifuged (15 min, 15000 g) to remove remaining debris.

II.2.5. Isolation of ssDNA

Phages and phagemid particles were lysed through the addition of 8 mL lysis buffer (200 mM NaOH, 1% SDS) and 7.5 mL neutralization buffer (3 M potassium acetate, pH 5.5). After 15 minutes of incubation on ice, samples were centrifuged again for 10 min at 13000 g. Supernatants were mixed with freeze cold absolute ethanol at a ratio of 1:1 and incubated on ice for 30 minutes. After another round of centrifugation for 10 min at 13000 g, the pellets were incubated with cold 75% ethanol for 10 min. After centrifuging as before, the ssDNA pellets were resuspended in 1 mL TE buffer. ssDNA concentration was determined by UV-adsorption at 260 nm and mass concentrations were calculated from the respective extinction coefficients which were calculated from the ssDNA sequence (7.12×10^7 $M^{-1}cm^{-1}$ for M13mp18, 4.61×10^7 $M^{-1}cm^{-1}$ for ssDNA from phagemid particles) [37].

II.2.6. Agarose gel electrophoresis

Agarose gel electrophoresis was performed in 2% agarose gels containing 0.5x Tris-Borate EDTA (TBE) buffer (10x TBE, Carl Roth, Karlsruhe, Germany or Invitrogen, Massachusetts, USA)

and 5.5 mM $MgCl_2$ pre-stained with ethidium bromide. The working voltage was 90 V for 1-2 hours. The gels were imaged using a Axygen Gel Documentation System (Axygen Inc, Union City, USA) or a Typhoon 9500 FLA Laser scanner (GE Healthcare Biosciences AB, Upsala, Sweden). Ladders used were NZYDNA ladder III (NZYTech, Lisbon, Portugal) and 1kb Plus DNA ladder from NEB (New England Biolabs, Massachusetts, USA). Gels were loaded with samples pre-mixed with a 6× loading buffer (40% (w/v) sucrose, 0.25 %(w/v) bromophenol blue).

II.2.7. Folding of DNA-origami nanostructures

To confirm the correct sequence identity and quality of the scaffolds, an asymmetric structure, a brick-shaped 42 helix bundle and a nut-screw were folded. Objects were designed using caDNAno v.02 [38]. The full list of oligonucleotides and design diagram are in Supplementary Information. Chemically synthesized oligonucleotides were ordered from Tilibit nanosystems (Munich, Germany) for the asymmetric structure and Integrated DNA Technologies (IDT, San José, USA) for the 42-helix bundle and nut-screw. To determine the optimal folding condition, an initial folding screen was performed according to [39]. For the asymmetric structure, a temperature ramp was performed between 60 and 40 °C for the scaffold to staple ratio and magnesium concentration screen at a rate of 1 °C/h. After selection of the best folding condition, folded structures were purified using PEG precipitation and analyzed with agarose gels and negative staining transmission electron microscopy (TEM).

II.2.8. Imaging

TEM grids were prepared by incubation of 5 μL of the purified samples on formvar-supported carbon-coated Cu400 grids (Electron Microscopy Sciences, Hatfield, USA) for 30-40 s. Excess sample was then blotted away and the grids were fixed with an aqueous 2% uranyl formate solution for 30 s. After drying, the grids were imaged using a transmission electron microscope (JEOL JEM-1400, JEOL Lda. Tokyo, Japan or FEI Tecnai 120, FEI, Hillsboro, USA), operated at 120 kV, and a magnification of 30000x, resulting in a final pixel size of 3.56 Å per pixel. Images were acquired using the SerialEM software [40] and analyzed in the Software Fiji (open source, fiji.sc).

II.3. Results and Discussion

II.3.1. Phage production

The easiest and most straightforward approach for the large production of ssDNA scaffolds is the infection of *E. coli* cells with phages. In this case, an *E. coli* strain containing a F' is chosen that is infected with a phage plaque during exponential growth. After phage expansion and purification, the phages can be lysed releasing ssDNA molecules with a sequence identical to the genome of the infectious phage. The most used phage is the M13mp18, an engineered version of the bacteriophage M13 with a higher replication rate [34], [41]. After expansion in *E. coli* K12 ER2738, a total of (2.5 ± 0.5) x 10^{14} phages/mL could be obtained. To recover the ssDNA scaffold, phages were submitted to alkaline lysis, resulting in 3.5 mg/L of media of ssDNA scaffold (Fig. II.2).

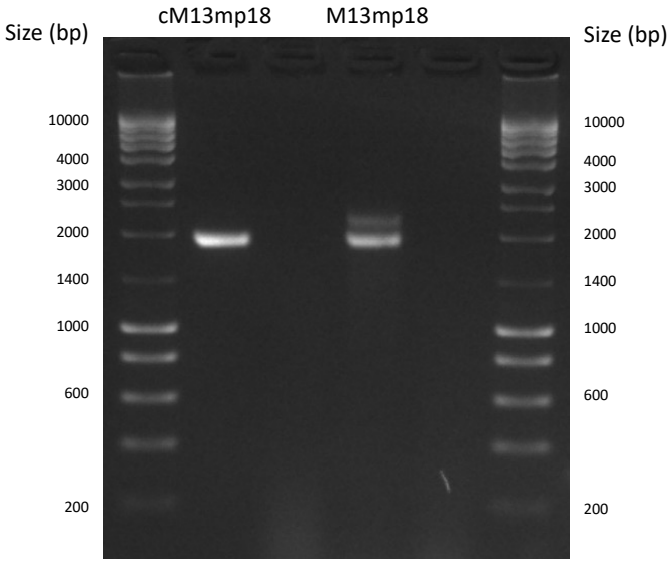

Figure II.2. Production of M13mp18 ssDNA. Agarose gel electrophoresis of M13mp18 ssDNA after infection of an F' E. coli. cM13mp18 represent ssDNA control using commercially available M13mp18 ssDNA from New England Biolabs.

The recovered ssDNA scaffold could be used as template for asymmetric PCR reactions required to produce different size ssDNA scaffolds used in the following chapters of this thesis.

II.3.1.1 Asymmetric structure folding

To evaluate the quality of the produced ssDNA scaffold, an object with an asymmetric design was folded. The initial folding screen is shown in Fig. II.3A. Since the range of the temperature folding screen did not allow the folding of the correct structure, the temperature ramp was extended from what is reported in the literature [39] to 40 °C. Magnesium concentration screen led to the conclusion that the lowest magnesium condition at which less by-products were formed and a sharp band could be obtained was 20 mM. For this reason, this condition was chosen, the folding was repeated, objects were purified, and negative TEM was performed (Fig. II.3B).

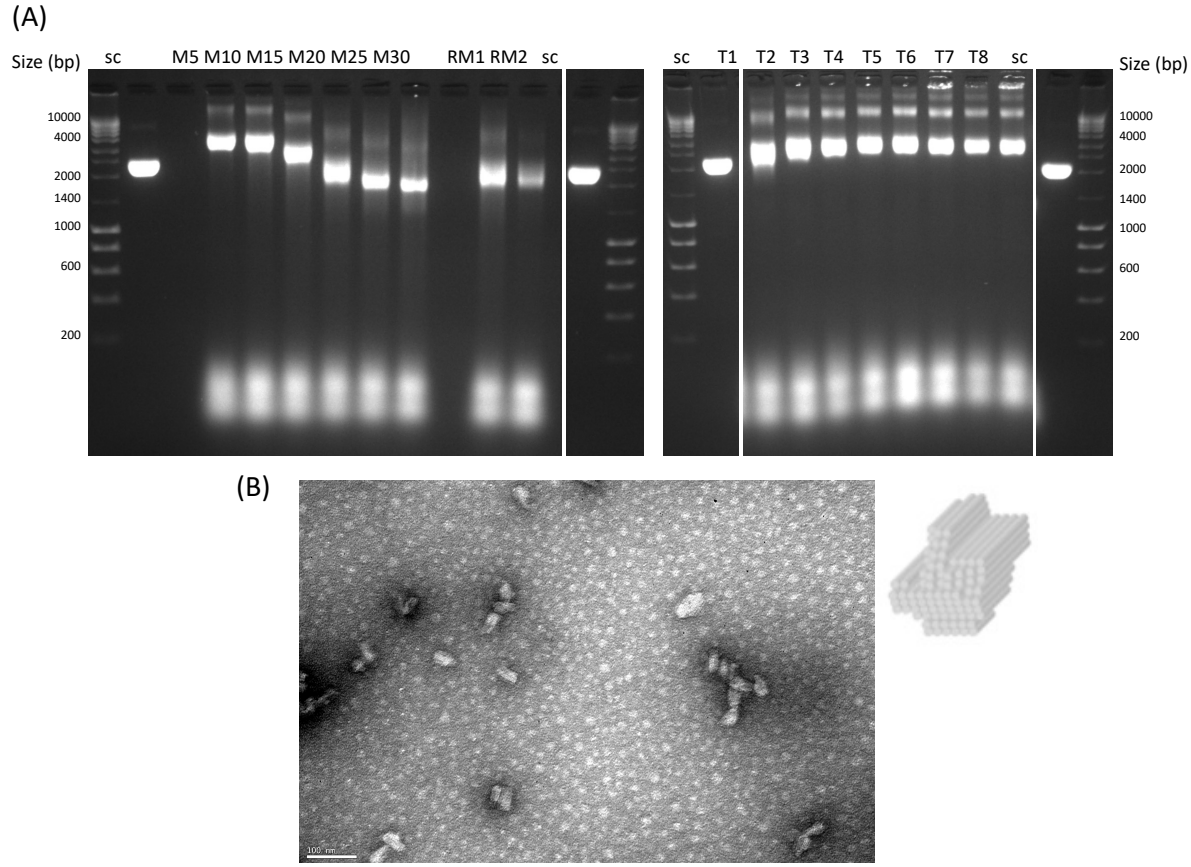

Figure II.3. Initial folding screen and TEM visualization of asymmetric structure. (A) Agarose gel electrophoresis of M13mp18 ssDNA folding into an asymmetric structure under several folding conditions. sc – scaffold, M – magnesium concentration screen; folding buffer (5 mM Tris Base, 1 mM EDTA, 5 mM NaCl) with (i) 5 –5 mM $MgCl_2$, (ii) 10 – 10 mM $MgCl_2$, (iii) 15 – 15 mM $MgCl_2$, (iv) 20 –20 mM $MgCl_2$, (v) 25 –25 mM $MgCl_2$, (vi) 30 –30 mM $MgCl_2$, RM – scaffold to staple ration screen; 1- 50 nM scaffold, 200 nM staples; 2 – 20 nM scaffold, 200 nM staples, T – general temperature interval screen; 1 – folding interval (50 ℃-47 ℃), 2 – folding interval (52 ℃-49 ℃), 3 – folding interval (54 ℃-51 ℃), 4 – folding interval (56 ℃-53 ℃), 5 – folding interval (58 ℃-55 ℃), 6 – folding interval (60 ℃-57 ℃), 7 – folding interval (62 ℃-59 ℃), 8 – folding interval (64 ℃-61 ℃). (B) TEM field view of the folded DNA-origami from M13mp18 scaffold under M20 conditions. Scale bar is 100 nm.

Negative staining TEM analysis reveals a well and uniform folded structure with the presence of some aggregates like it was predicted by agarose gel analysis. Overall, this supports the idea of a good quality scaffold production with special relevance on the correct produced sequence making it suitable for use in further experiments.

II.3.2. Phagemid production by double transformation

To preproduce phagemid particles, a methodology already reported in the literature was used [25] where *E. coli* cells were double transformed with a helper plasmid and the target phagemid. On a first approach, the CSF1 phagemid (4843 bp) (Fig. II.4D) was co-transformed with the phage free helper plasmid No. 27 (pfhp27) (Fig. II.4A), a helper plasmid derived from M13KO7 where the M13 origin of replication was replaced by the *rmB1* terminator but else all the M13 genes are present in their natural order and regulation. Developed phagemids carry a substantial amount of user-defined sequence (random De Brujin sequence of 5^{th} order) which can be used as a scaffold for DNA-origami.

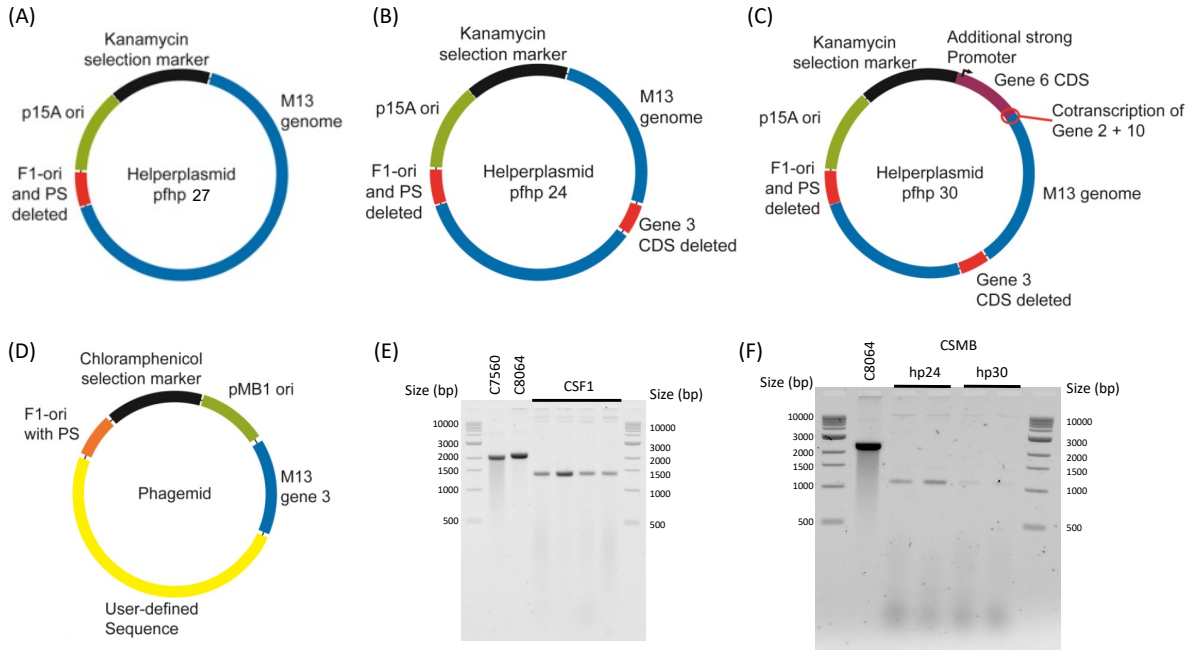

Figure II.4. Development of helper plasmid and phagemid and phagemid particle preparation. (A) Schematic representation of the helper plasmid (phage free helper plasmid No. 27: pfhp 27) derived from helper phage M13KO7. Here, the M13 origin of replication is replaced by the rmB1 terminator. Else all M13 genes are present in their natural order and regulation. (B) Schematic representation of the helper plasmid no. 24 (pfhp 24) based on pfhp 27. The coding sequence of gene 3 is deleted. (C) Schematic representation of the helper plasmid no. 30 (pfhp 30) based on pfhp 24. Here, a second gene 6 copy was placed downstream of an additional strong promoter directly upstream of the M13 genome. This will most likely result in co-transcription of genes 2 and 10 starting from the additional strong promoter. (D) The phagemid has a plasmid-ori (pMB1) to be propagated independently of the helper plasmid. Apart from the user-defined sequence, the phagemid contains the replication origin of the M13 phage including its packaging signal (PS) as well as the complete natural expression cassette of the M13 phage for its gene 3. (E) Agarose gel electrophoresis of the product of double-transformation of CSF1 phagemid plasmid and pfhp 27. C7560 and C8064 represent ssDNA controls with 7560 and 8064-nt respectively. (F) Agarose gel electrophoresis of the product of double-transformation of CSMB phagemid plasmid and pfhp 24 and pfhp 30. C8064 represent a ssDNA control with 8064-nt.

Agarose gel electrophoresis analysis of the ssDNA of the phagemid particles produced (Fig. II.4E), shows that, in fact, the production of a ssDNA molecule with the sequence of the CSF1 phagemid is possible, without significant contamination from the helper plasmid. Moreover, this method led to the generation of (5.5 ± 1.9) x 10^{10} phagemid particles and 0.23 ± 0.08 mg/L of media of ssDNA.

Since the produced phagemid particles are intended to be used for *E. coli* infection, changes on the helper plasmid were required for this purpose and the possibility of using them for double transformation protocol was also evaluated. Resistance to M13 phage infection of *E.*

coli cells due to the overexpression of gene 3 has already been described in the literature [32]. The product of gene 3 (G3P) is considered the head of the phage hull and is responsible for the infection of *E. coli* [42]. How the product of gene 3 induces an infection resistance remains in the dark. Based on this, a combination of helper plasmid and phagemid that exploits the infection resistance caused by gene 3 was developed. For this purpose, the coding sequence of gene 3 was first deleted from the pfhp 24. Secondly, the expression cassette for gene 3 of the M13 phage was integrated into the sequence of the phagemids (Fig. II.3D). In this case, *E. coli* cells carrying the helper plasmid are not resistant to infection and the set of M13 genes is only completed upon infection so that new particles can be assembled. Even though in the case of double transformation protocol the production of gene 3 and phagemid assemble occurs simultaneously, this split is extremely important to assure the safety of the process and prevent cross-contaminations when the reverse infection protocol is being used.

To evaluate this combination CSMB (3254 bp) phagemid was used and agarose gel electrophoresis analysis (Fig. II.3E) shows that it is possible to produce phagemid particles ($(5.2 \pm 0.4) \times 10^{10}$) and 0.14 ± 0.01 mg/L of media of ssDNA using the double transformation protocol, even though the gene that codes for G3P is absent from the helper plasmid.

Moreover, overexpression of genes 2 and 10 coded in the helper plasmid prior to infection can lead to increased productivity in *E. coli* cells since the product of gene 2 (G2P) plays an important role in the replication of viral ssDNA and the product of gene 10 (G10P) protects the nascent ssDNA from hydrolysis [42]. Thus, an increased amount of G2P and G10P in *E. coli* positively affects the amount of ssDNA formed by the cell after infection with M13 phages. Having this in mind, an additional helper plasmid No. 30 (pfhp30) that overexpresses genes 2 and 10 was designed. For this purpose, a strong constitutive promoter and a second copy of gene 6 were added upstream of genes 2 and 10. Thus co-transcribing genes 6, 2 and 10 with the strong promoter, should result in higher protein concentration. The expression of gene 6 was increased, as this gene product is necessary for proper termination of the phage hull [43].

Double transformation of CSMB phagemid and pfhp 30 was also evaluated and agarose gel electrophoresis analysis (Fig. II.4E) shows that it is also possible to produce phagemid particles ($(6.5 \pm 1.7) \times 10^{10}$) and 0.18 ± 0.04 mg/L of media of ssDNA using this combination. Even though the yield with helper plasmid 30 is higher, agarose gel electrophoresis analysis reveal

that the amount of ssDNA produced is lower. This discrepancy is probably due to the method of quantification (UV260nm) and probably means that the sample from the double transformation with helper plasmid 30 has more contaminants, overestimating the amount of DNA produced. For this reason, the phagemid particles used for reverse infection were the ones produced with helper plasmid 24.

II.3.3. Phagemid production by reverse infection

The efficient production of biomolecules in microorganisms relies on the separation of biomass and product formation. This separation allows the microorganisms to grow to high cell density without the metabolic burden of product formation. For M13 phages especially, the positive effect of the decoupling has been shown [44]. Additionally, bacterial cells infected with M13 phages stop phage production after a while [45]. Therefore, it is important that the cells are only infected when a high amount of biomass has been produced. The reverse infection method described here separates the production of biomass and product, by first growing cells transformed with a helper plasmid that contains most of the phage genes. After sufficient biomass production, the cells are then infected with phagemid particles, that provide the missing gene, regulatory sequences, and the user-defined DNA sequence and allow for product formation.

Having this is mind, *E. coli* cells transformed with pfhp24 and grown until stationary phase were infected with the target phagemid particle at a MOI of approximately 100 phagemid particles per cell (tfu/cfu). The growth media used was specially developed for expressing protein in bacteria, which should lead to higher protein production and, consequently, increase the phagemid particle titer. After approximately 16 h, cells were harvested, phagemid particles in the supernatant were purified and the ssDNA from phagemid particles was isolated.

Agarose gel electrophoresis analysis (Fig. II.5) shows that it was possible to produce both CSF1 and CSMB ssDNA using this strategy with a yield increase of 1.5 to 3-fold compared to double transformation protocol. In fact, 0.3 mg/L of media of CSF1 and 0.43 mg/L of media of CSMB could be produced with high quality.

Moreover, the production of CSMB by reverse infection of an *E. coli* cell previously transformed with pfhp 30 was also evaluated. The results showed that the changes made in the helper plasmid in fact affect the ssDNA produced with a 2-fold production increase (0.38 mg/L of media) compared to the double transformation protocol using the same combination (Fig. II.5B).

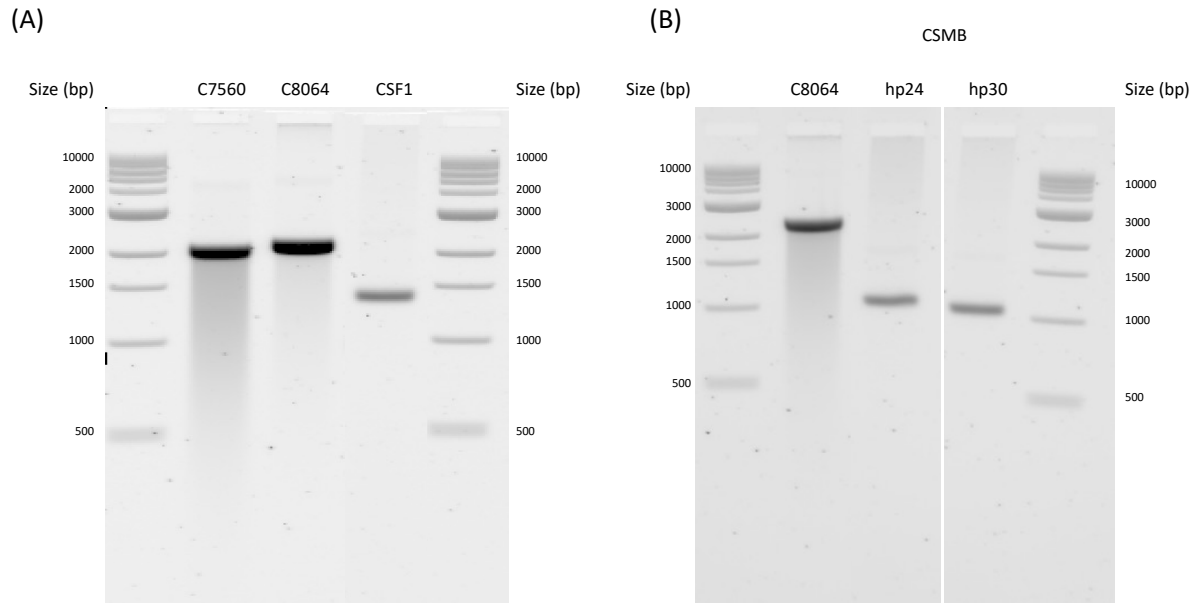

Figure II.5. Production of ssDNA using the reverse infection protocol. (A) Agarose gel electrophoresis of CSF1 ssDNA after reverse infection of an E. coli transformed with pfhp24 with a CSF1 phagemid particle. C7560 and C8064 represent ssDNA controls with 7560 and 8064-nt respectively. (A) Agarose gel electrophoresis of CSMB ssDNA after reverse infection of E. coli transformed with pfhp24 or pfhp 30, respectively, with a CSMB phagemid particle. C8064 represents ssDNA control with 8064-nt.

These results were used as base for a study on fed-batch production of ssDNA in a bioreactor. In fact, it was possible to recover 83 mg/L of media of CSF1 in a 2.5 L bioreactor after 16 to 17 hours production using *E. coli* JM109 WT cells pre-transformed with pfhp30 (results not shown) [46].

II.3.3.1 42-helix bundle and nut-screw folding

To verify the quality of the ssDNA produced, two different DNA-origami structures were folded. For the CSF1 scaffold, a 42-helix bundle was designed, and an initial folding screen was performed (Fig II.6A). According to the initial folding screen, the structure seems to give an overall good quality, except for the higher temperature ramps and lowest magnesium

concentration. On the first case it might be due the fact that the temperatures studied are above the melting temperature of several oligonucleotides, preventing them from hybridization with the scaffold DNA. In the case of magnesium concentration screening, lower concentrations do not stabilize the DNA enough for the folding to occur. Moreover, when the concentration goes above 20 mM, more aggregates start to form, which can be seen in the pockets in Fig. II.6A, lanes M25 and M30.

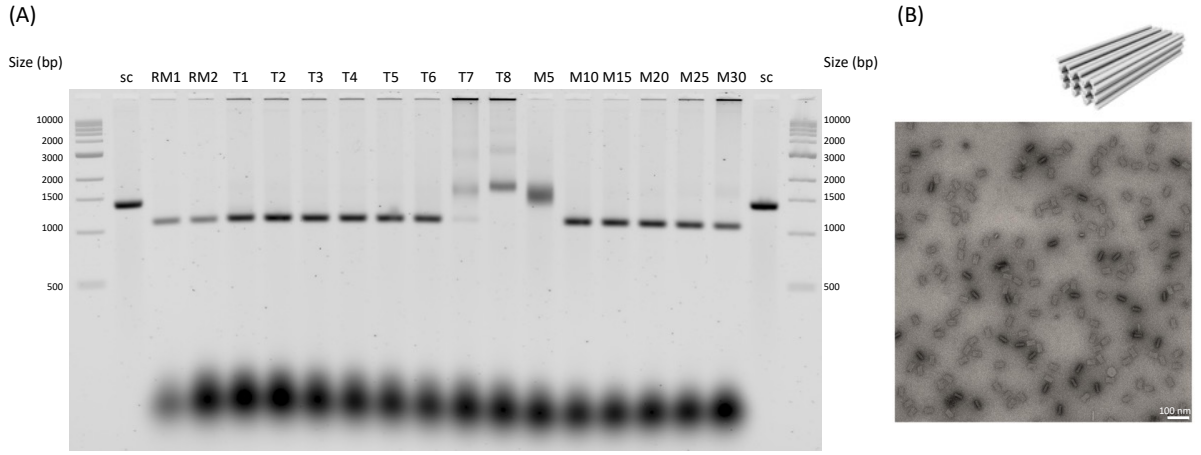

Figure II.6. Initial folding screen and TEM visualization of 42-helix bundles. (A) Agarose gel electrophoresis of CSF1 ssDNA folding into 42-helix bundle under several folding conditions. sc – scaffold, RM – scaffold to staple ration screen; 1- 50 nM scaffold, 200 nM staples; 2 – 20 nM scaffold, 200 nM staples, T – general temperature interval screen; 1 – folding interval (50 ℃-47 ℃), 2 – folding interval (52 ℃-49 ℃), 3 – folding interval (54 ℃-51 ℃), 4 – folding interval (56 ℃-53 ℃), 5 – folding interval (58 ℃-55 ℃), 6 – folding interval (60 ℃-57 ℃), 7 – folding interval (62 ℃-59 ℃), 8 – folding interval (64 ℃-61 ℃), M – magnesium concentration screen; folding buffer (5 mM Tris Base, 1 mM EDTA, 5 mM NaCl) with (i) 5 –5 mM $MgCl_2$, (ii) 10 – 10 mM $MgCl_2$, (iii) 15 – 15 mM $MgCl_2$, (iv) 20 –20 mM $MgCl_2$, (v) 25 –25 mM $MgCl_2$, (vi) 30 –30 mM $MgCl_2$. (B) TEM field view of the folded DNA-origami from CSF1 scaffold under M20 conditions. Scale bar is 100 nm.

Negative staining TEM analysis (Fig. II.6B) under 20 mM magnesium shows that in fact the target structure was folded, with good quality and no presence of aggregates, confirming the quality of the produced scaffold.

For the CSMB scaffold, a nut-screw was designed. Initial folding screen (Fig. II.7A) shows that the designed structure has a high tendency to form double and higher order structures. However, it was possible under 10 mM of magnesium to obtain a single, sharp band of folded structure. Negative staining analysis (Fig. II7B) confirms that the structure is prone to aggregation but still it was possible to observe folding of the CSMB scaffold into the desired nut-screw structure, confirming it's quality and correct sequence.

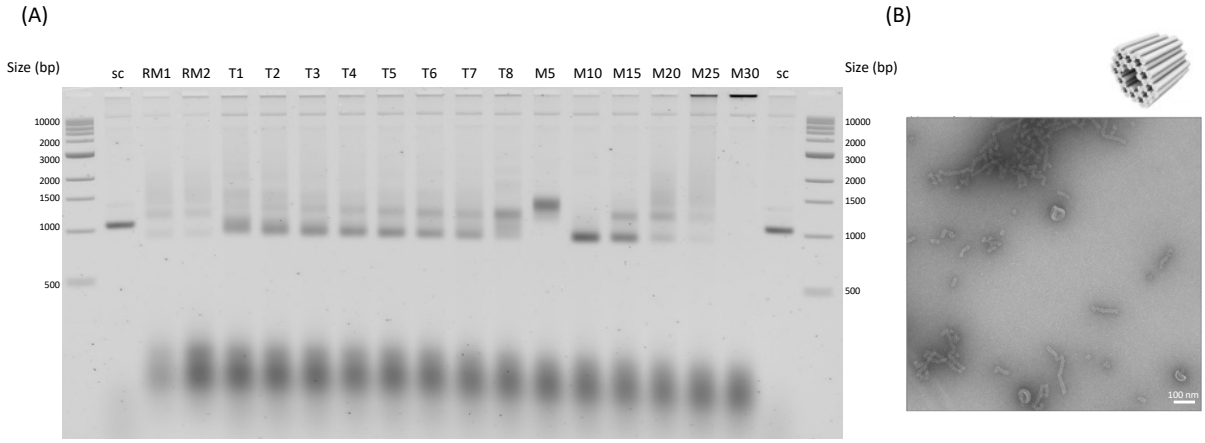

Figure II.7. Initial folding screen and TEM visualization of nut-screw DNA-origami. (A) Agarose gel electrophoresis of CSMB ssDNA folding into a nut screw under several folding conditions. sc – scaffold, RM – scaffold to staple ration screen; 1- 50 nM scaffold, 200 nM staples; 2 – 20 nM scaffold, 200 nM staples, T – general temperature interval screen; 1 – folding interval (50 ℃-47 ℃), 2 – folding interval (52 ℃-49 ℃), 3 – folding interval (54 ℃-51 ℃), 4 – folding interval (56 ℃-53 ℃), 5 – folding interval (58 ℃-55 ℃), 6 – folding interval (60 ℃-57 ℃), 7 – folding interval (62 ℃-59 ℃), 8 – folding interval (64 ℃-61 ℃), M – magnesium concentration screen; folding buffer (5 mM Tris Base, 1 mM EDTA, 5 mM NaCl) with (i) 5 –5 mM $MgCl_2$, (ii) 10 – 10 mM $MgCl_2$, (iii) 15 – 15 mM $MgCl_2$, (iv) 20 –20 mM $MgCl_2$, (v) 25 –25 mM $MgCl_2$, (vi) 30 –30 mM $MgCl_2$. (B) TEM field view of the folded DNA-origami from CSMB scaffold under M10 conditions. Scale bar is 100 nm.

II.4. Conclusion

Even though the use of phages is the most straightforward approach for the biotechnological mass production of ssDNA molecules that can be used in DNA-origami techniques, safety issues, like possible cross-contamination of large reactors, and the desire for having user-defined sequence scaffolds, make its use limited. For this purpose, reverse infection method showed to be a great promise, allowing the efficient and scalable production of artificial ssDNA with *E. coli*. The produced phagemid particles used are not self-replicating even though they can infect *E. coli* cells that were previously transformed with a helper plasmid. Large scale production has been feasible at any contract manufacturer as remaining, unwanted phagemid particles after cleaning and sterilization are of no consequence to other following processes with *E. coli*. Moreover, this method showed to be more efficient and resulted in a 1.5 to 3-fold yield increase compared to the previous double transformation method reported [25]. The produced ssDNA was free of contaminating DNA species that could interfere with downstream applications such as DNA-origami folding.

II.5. References

[1] R. M. Quadros *et al.*, "Easi-CRISPR: A robust method for one-step generation of mice carrying conditional and insertion alleles using long ssDNA donors and CRISPR ribonucleoproteins," *Genome Biol.*, vol. 18, no. 1, pp. 1–15, 2017.

[2] H. Bai *et al.*, "CRISPR/Cas9-mediated precise genome modification by a long ssDNA template in zebrafish," *BMC Genomics*, vol. 21, no. 1, pp. 1–12, 2020.

[3] P. W. K. Rothemund, "Folding DNA to create nanoscale shapes and patterns," *Nature*, vol. 440, no. 7082, pp. 297–302, 2006.

[4] S. M. Douglas, H. Dietz, T. Liedl, B. Högberg, F. Graf, and W. M. Shih, "Self-assembly of DNA into nanoscale three-dimensional shapes," *Nature*, vol. 459, no. 7245, pp. 414–418, 2009.

[5] H. Dietz, S. M. Douglas, and W. M. Shih, "Folding DNA into twisted and curved nanoscale shapes," *Science*, vol. 325, no. 5941, pp. 725–730, 2009.

[6] S. M. Douglas, J. J. Chou, and W. M. Shih, "DNA-nanotube-induced alignment of membrane proteins for NMR structure determination," *Proc. Natl. Acad. Sci. U. S. A.*, vol. 104, no. 16, pp. 6644–6648, 2007.

[7] R. Jungmann, C. Steinhauer, M. Scheible, A. Kuzyk, P. Tinnefeld, and F. C. Simmel, "Single-molecule kinetics and super-resolution microscopy by fluorescence imaging of transient binding on DNA-origami," *Nano Lett.*, vol. 10, no. 11, pp. 4756–4761, 2010.

[8] N. D. Derr, B. S. Goodman, R. Jungmann, A. E. Leschziner, W. M. Shih, and S. L. Reck-Peterson, "Tug-of-war in motor protein ensembles revealed with a programmable DNA-origami scaffold," *Science*, vol. 338, no. 6107, pp. 662–665, 2012.

[9] M. Langecker *et al.*, "Synthetic lipid membrane channels formed by designed DNA nanostructures," *Science*, vol. 338, no. 6109, pp. 932–936, 2012.

[10] E. Pfitzner *et al.*, "Rigid DNA beams for high-resolution single-molecule mechanics," *Angew. Chemie - Int. Ed.*, vol. 52, no. 30, pp. 7766–7771, 2013.

[11] A. Shaw *et al.*, "Spatial control of membrane receptor function using ligand nanocalipers," *Nat. Methods*, vol. 11, no. 8, pp. 841–846, 2014.

[12] E. S. Andersen *et al.*, "Self-assembly of a nanoscale DNA box with a controllable lid," *Nature*, vol. 459, no. 7243, pp. 73–76, 2009.

[13] S. M. Douglas, I. Bachelet, and G. M. Church, "A Logic-Gated Nanorobot for Targeted Transport of Molecular Payloads," *Science*, vol. 335, no. February, pp. 831–834, 2012.

[14] Y. X. Zhao, A. Shaw, X. Zeng, E. Benson, A. M. Nyström, and B. Högberg, "DNA-origami delivery system for cancer therapy with tunable release properties," *ACS Nano*, vol. 6, no. 10, pp. 8684–8691, 2012.

[15] S. Li *et al.*, "A DNA nanorobot functions as a cancer therapeutic in response to a molecular trigger in vivo," *Nat. Biotechnol.*, vol. 36, no. 3, pp. 258–264, 2018.

[16] C. Sigl *et al.*, "Programmable icosahedral shell system for virus trapping," *Nat. Mater.*, vol. 20, no. 9, pp. 1281–1289, 2021.

[17] C. Ducani, C. Kaul, M. Moche, W. M. Shih, and B. Högberg, "Enzymatic production of 'monoclonal stoichiometric' single-stranded DNA oligonucleotides," *Nat. Methods*, vol. 10, no. 7, pp. 647–652, 2013.

[18] J. Y. Kishi, T. E. Schaus, N. Gopalkrishnan, F. Xuan, and P. Yin, "Programmable autonomous synthesis of single-stranded DNA," *Nat. Chem.*, vol. 10, no. 2, pp. 155–164, 2018.

[19] T. Notomi *et al.*, "Loop-mediated isothermal amplification of DNA," *Nucleic Acids Res.*, vol. 28, 2000.

[20] S. Kosuri and G. M. Church, "Large-scale de novo DNA synthesis: Technologies and applications," *Nat. Methods*, vol. 11, no. 5, pp. 499–507, 2014.

[21] P. M. Lizardi, X. Huang, Z. Zhu, P. Bray-Ward, D. C. Thomas, and D. C. Ward, "Mutation detection and single-molecule counting using isothermal rolling-circle amplification," *Nat. Genet.*, vol. 19, no. 3, pp. 225–232, 1998.

[22] G. T. Walker, M. S. Fraiser, J. L. Schram, M. C. Little, J. G. Nadeau, and D. P. Malinowski, "Strand displacement amplification - an isothermal, in vitro DNA amplification technique," *Nucleic Acids Res.*, vol. 20, no. 7, pp. 1691–1696, 1992.

[23] R. Veneziano, T. R. Shepherd, S. Ratanalert, L. Bellou, C. Tao, and M. Bathe, "In vitro synthesis of gene-length single-stranded DNA," *Sci. Rep.*, vol. 8, no. 1, pp. 1–7, 2018.

[24] F. A. S. Engelhardt *et al.*, "Custom-Size, Functional, and Durable DNA-origami with Design-Specific Scaffolds," *ACS Nano*, vol. 13, no. 5, pp. 5015–5027, 2019.

[25] F. Praetorius, B. Kick, K. L. Behler, M. N. Honemann, D. Weuster-Botz, and H. Dietz, "Biotechnological mass production of DNA-origami," *Nature*, vol. 552, no. 7683, pp. 84–87, 2017.

[26] B. Kick, F. Praetorius, H. Dietz, and D. Weuster-Botz, "Efficient Production of Single-Stranded Phage DNA as Scaffolds for DNA-origami," *Nano Lett.*, vol. 15, no. 7, pp. 4672–4676, 2015.

[27] N. D. Zinder and J. D. Boeke, "The filamentous phage (Ff) as vectors for recombinant DNA- a review," *Gene*, vol. 19, no. 1, pp. 1–10, 1982.

[28] J. Vieira and J. Messing, "Production of Single-Stranded Plasmid DNA," in *Selected Methods in Enzymology*, R. Wu, L. Grossman, and K. B. T.-R. D. N. A. M. Moldave, Eds. San Diego: Academic Press, 1989, pp. 225–233.

[29] L. Chasteen, J. Ayriss, P. Pavlik, and A. R. M. Bradbury, "Eliminating helper phage from phage display," *Nucleic Acids Res.*, vol. 34, no. 21, pp. 1–11, 2006.

[30] T. R. Shepherd, R. R. Du, H. Huang, E. C. Wamhoff, and M. Bathe, "Bioproduction of pure, kilobase-scale single-stranded DNA," *Sci. Rep.*, vol. 9, no. 1, pp. 1–9, 2019.

[31] S. D. Branston, E. C. Stanley, J. M. Ward, and E. Keshavarz-Moore, "Determination of the survival of bacteriophage M13 from chemical and physical challenges to assist in its sustainable bioprocessing," *Biotechnol. Bioprocess Eng.*, vol. 18, no. 3, pp. 560–566, 2013.

[32] J. D. Boeke, P. Model, and N. D. Zinder, "Effects of bacteriophage f1 gene III protein on

the host cell membrane," *MGG Mol. Gen. Genet.*, vol. 186, no. 2, pp. 185–192, 1982.

[33] A. K. Brödel, A. Jaramillo, and M. Isalan, "Engineering orthogonal dual transcription factors for multi-input synthetic promoters," *Nat. Commun.*, vol. 7, p. 13858, 2016.

[34] C. Yanisch-Perron, J. Vieira, and J. Messing, "Improved M13 phage cloning vectors and host strains: nucleotide sequences of the M13mp18 and pUC19 vectors," *Gene*, vol. 33, pp. 103–119, 1985.

[35] N. E. Biolabs, "M13mp18 RF I DNA." [Online]. Available: https://www.neb.com/products/n4018-m13mp18-rf-i-dna#Product Information.

[36] L. A. Day and R. L. Wiseman, "A comparison of DNA packaging in the virions of fd, Xf, and Pf1," *Single-Stranded DNA Phages*, pp. 605–625, 1978.

[37] A. V. Tataurov, Y. You, and R. Owczarzy, "Predicting ultraviolet spectrum of single stranded and double stranded deoxyribonucleic acids," *Biophys. Chem.*, vol. 133, no. 1–3, pp. 66–70, 2008.

[38] S. M. Douglas, A. H. Marblestone, S. Teerapittayanon, A. Vazquez, G. M. Church, and W. M. Shih, "Rapid prototyping of 3D DNA-origami shapes with caDNAno," *Nucleic Acids Res.*, vol. 37, no. 15, pp. 5001–5006, 2009.

[39] K. F. Wagenbauer *et al.*, "How We Make DNA-origami," *ChemBioChem*, vol. 18, no. 19, pp. 1873–1885, 2017.

[40] D. N. Mastronarde, "Automated electron microscope tomography using robust prediction of specimen movements," *J. Struct. Biol.*, vol. 152, no. 1, pp. 36–51, 2005.

[41] J. Bush, S. Singh, M. Vargas, E. Oktay, C. H. Hu, and R. Veneziano, "Synthesis of DNA-origami scaffolds: Current and emerging strategies," *Molecules*, vol. 25, no. 15, pp. 1–18, 2020.

[42] A. Mai-Prochnow, J. G. K. Hui, S. Kjelleberg, J. Rakonjac, D. McDougald, and S. A. Rice, "'Big things in small packages: The genetics of filamentous phage and effects on fitness of their host,'" *FEMS Microbiol. Rev.*, vol. 39, no. 4, pp. 465–487, 2015.

[43] J. Rakonjac, N. J. Bennett, J. Spagnuolo, D. Gagic, and M. Russel, "Filamentous bacteriophage: biology, phage display and nanotechnology applications.," *Curr. Issues Mol. Biol.*, vol. 13, no. 2, pp. 51–76, 2011.

[44] B. Kick, K. L. Behler, T. S. Severin, and D. Weuster-Botz, "Chemostat studies of bacteriophage M13 infected Escherichia coli JM109 for continuous ssDNA production," *J. Biotechnol.*, vol. 258, no. January, pp. 92–100, 2017.

[45] S. W. Smeal, M. A. Schmitt, R. R. Pereira, A. Prasad, and J. D. Fisk, "Simulation of the M13 life cycle II: Investigation of the control mechanisms of M13 infection and establishment of the carrier state," *Virology*, vol. 500, pp. 275–284, 2017.

[46] K. L. Behler, M. N. Honemann, A. R. Silva-Santos, H. Dietz, and D. Weuster-Botz, "Phage-free production of artificial ssDNA with Escherichia coli," *Biotechnol. Bioeng.*, no. January, pp. 1–12, 2022.

Supplementary Material

II.S1: Design scheme of the asymmetric structure

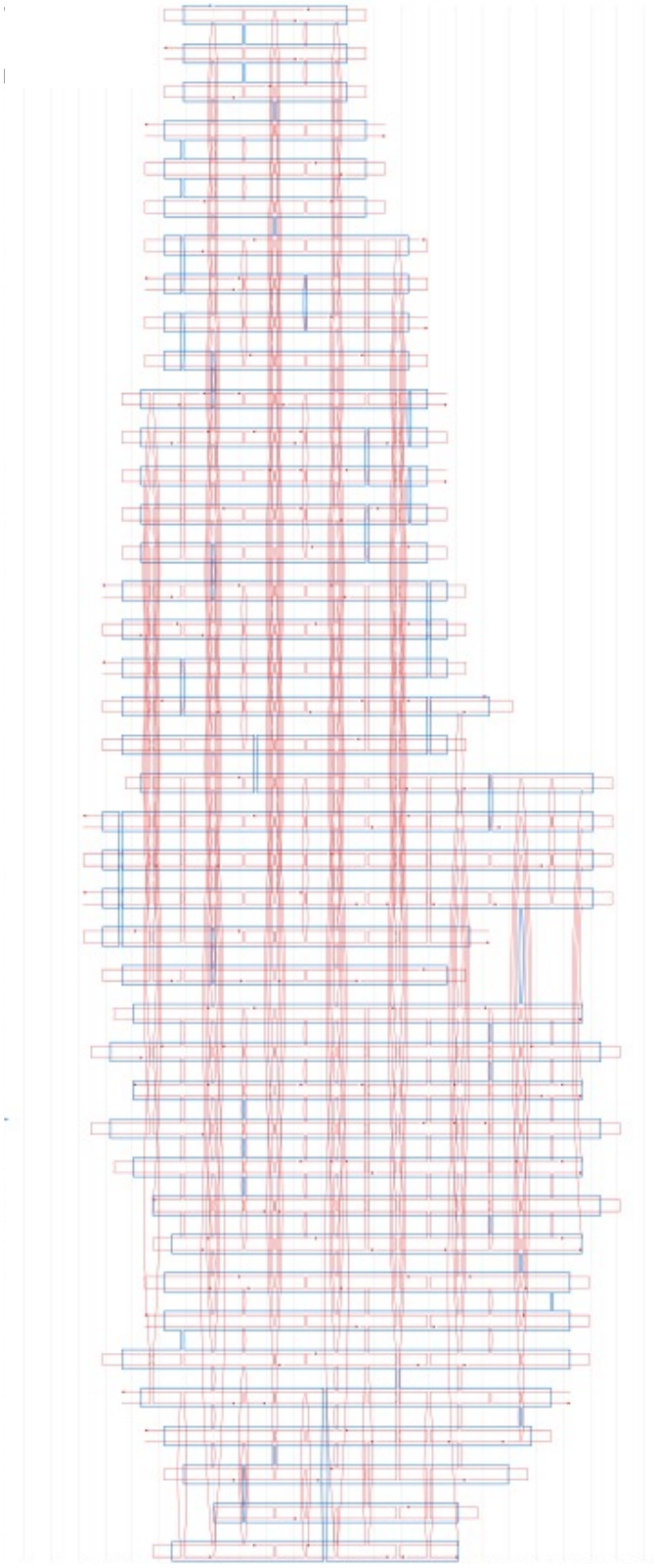

Figure II.S1. Scaffold/staple layout of the asymmetric structure. Generated with caDNAno v0.2.

II.S2: Staple sequences for asymmetric design

Table II.S1: Staple sequences for the folding of asymmetric structure.

Staple	**Sequence**
0[79]22[78]	CAAAGGGCGGGTGCCTCGCTCACTGCTTAATGTTGCATGCGGTCACGTTG
1[78]23[77]	ATTGTTGTTCCGGCCAACCAGGGTGGTGCCAAGCGACAGGAAGCCGGA
3[43]14[38]	TTTTTTTTTTGGGTGAGACGGGCGAGTTTTTTTTTTAAAGGGTCGTGCCGAGGATCCCCGGGTTTTT
3[78]21[74]	AGCGAAATCGCCTGGCCCTTGCCCCAGAGTAAAATAACATCACTT
4[69]16[86]	AAAATCAGCCCCCGGCAGGCGAAAATCCTGACGCTGGTTGAGAGAGGG
5[62]6[38]	GGGCCGTAAAGCACTAAATTTTTTTTTTTCGGAACCGGAAAGCCGGCGATTTTT
6[100]8[82]	TTTTTAGCGGTCCTTTTTTTTTTTTTTGATGGTGGTTCAATAGCCCTTGGGC
7[38]22[54]	TTTTTACGTGGCAACAGCTGAGAAGTTTTCCTTTTTTTTTTCAGTCACGACGTTGT
8[81]32[82]	GCGCGCGGGGACGTGCTTCGCCGCTACAGCTTTCAATAGGAATTGCGG
9[90]10[86]	AGGCGGTTTTTTTTTTTTTGCGTAGAGTTTTTTTTTTATAGGGTTGAGTAAAGAACTT
10[52]13[53]	AACCTAAGGGTTTTTTTTTTAAGAAAGCGAAAGGTCACGCTAGCTCTTTTTTTTTTGAATTCGTAAT
10[85]30[86]	GCGTTGAATGAGTGTAAAGTGTAATTGTTAAGGAAGATGATAATCATG
12[65]3[77]	AACCCGCCGCGCCCGCTTTAATGAATCAGTTTGGCCTTATAAATCAAA
12[109]32[106]	TTTAACTCGCGTCTTTTTTTTTTTGAAATGGATCACCATCAACTGTTTTTTTTTTATAGCAAACAT
13[54]51[45]	CAAAACGTTAAAACTAGCTTGAGAGATCTGGAGCTCATTGAATCCCCCTCGAATCG
14[61]10[53]	ACTCTAAGCTGCATTCCAGTCGCGTGAACCGTCTATCAGGGCGATGTTTTTTTTTTGCCCACTAGGA
15[38]33[53]	TTTTTTACCGGCGCGTAAACAACCCGAAATTTTTTAAAAATTCTGAGT
15[62]1[77]	CAGTGTAGCGGAGCGGGCGCTAGGGCGAAAAACCAACAAGAGTCCACT
16[85]44[86]	ATTTTATCCTCGTTCGTGCATCTGGTGTAGCACCAGCACTCAGAGCAA
16[111]36[106]	TTTTTAACCAGAGGAATTTTTTTTTTAAACGCTCCATCACCTCATTAG
18[64]20[53]	GAGTAGAAGGTTGGGTAACGCCTTTTTTTTTTAGGGTGTTTTTATCCA
18[93]37[81]	TCTTTGATTAGTAAGAGTCTGTGGGCGATCCCAGGCAACAATAACCCA
20[52]56[54]	GCTGGCAGCTTTCGCGCGAGCAACACCGCTCCTGATTTAGAACCTGA
20[61]2[43]	ATTACGAATCAGTGCAGAATCCTGATTGCCTTCACCAGGTCGAGGTATCACCCAAATCAAGTTTTTT
20[116]41[106]	TTTTTGCAACGCTAGTTTGACATATCTTTTTTTTTTTGGTCAGTTGGCACCG
21[48]59[53]	GCGATTAATAGCTCAACTGGAAGTCTTTTGATCTATTATACCATCCTAGTCCTG
21[75]60[86]	GCTGGTAATATCCGAATTGAGCCAATTCTAGGTCAGGAAAAAGATGC
22[53]52[54]	ATCGGCCGGCGGATTCAGTATTGGCAAAGAGATGATGATTAACAATAA
22[65]5[61]	GACTTCTGGTCGGTACGCAGGCCACCATTTAGAGCTTGACGGCTAAAG
22[77]63[73]	CCAGTTCTGAGAGCTGTTTAGCATTGCATCATTAGAGAAA
23[46]64[54]	GCCGAAAGGGTACGGTGTCATGTTTTGCGGATGGCTTAGAGCTT
23[78]64[82]	AAGGTGCGGGGTTGATTCGAAGGTTACTTTAGGAGCACTAACGTTTTA
23[102]21[116]	TTAGGAGGCCCAAATTAACCGTTTTTTTTTTTTGCAGCCATTTTTTT
24[69]4[70]	AATGTGATGGGATACTGCAGGTACGGCCAGTTTTTCTTCTTCACCGGC
24[77]60[78]	CAACATAATAAAGCGAAGATAATTGCACGTGATGATGGCATCGGAAGT

24[89]0[80]	GCCAGGGCGCCGGAAGCAAGCTAACTTTTTTTTTTTCACATTAAGTGTTTTTTTTTTGACTCCAACGT
24[116]42[106]	TTTTTTCAATCGTTGTACCAACCTAATTTTTTTTTTTAACATCGCCATTAAGATTTTCGAGCGG
26[57]24[78]	GTTGGTCATAGCTGTTTCCTGTGTGAAAAGCCTGTTTTAACCAT
26[77]56[78]	TATAAGCAAAAGGGGAAGCCTTTTTTTAATATTTCAATCATATGCGGG
26[97]25[116]	ACAAAATAATATACGAGCGTACTATGGTTTTTTTTTTTTGCTTTTGACGCTTTTT
27[90]12[110]	CCATCACCAAAAACTCCGCTCACAATTCCACACTTTTTTT
28[80]46[78]	GGCCAACAGATACGTGGTAATGCCGGGGAAGAAGG
28[105]47[101]	CGATTAGTCTTTAATTTTTTTTTTTTGCGCGAATATGATAACGGAACTGACGAGAAACACCAGTCAATA
30[61]31[45]	CTATTTATGTCAATCCCTTCTGAAACAAGAGAATCGATCCTGAG
30[85]51[73]	ATAAATCACAGACACCACATTCAACTAATGAT
31[27]32[46]	TTTTTGGTCATTGGAATTTTTTTTTTCGGTAATCGTAATATTTTGTGCAATGCTT
31[46]46[22]	AGTCTACAAAAAGAACTGTTGTGAATTACCTTATAGAAATTTTT
31[91]28[106]	TTTTTGAATGGCTACCAGTAAATTGGCAGATTCACCATTTTTTTTTTGTCACA
32[45]56[35]	TAGAACAATTACATAACAAACAATCATAATAGTACCGACAAAA
32[81]51[93]	GATGAGAAAGGTAAATTGAAATCTACAAAAGAAGAGCAACACTATCAT
32[105]58[110]	TATGTGAGTGAAGTTACAAGCCAACGATTTAACATAAATTGTAA
33[38]45[41]	AATTATTTTTTTTTTAAATTCGCATTTCGGATTCACAGGCAATAGCATTAGG
33[54]51[63]	AATTTAATCAGCTCATTAAATGTTTAATAAATATAAAGGAAT
35[27]36[42]	TTTTTTAAATCATTCCTTTTTTTTTTGTGGGAACAAACTCAGGAAAATAGTAGTGAAAA
36[41]65[53]	GGTACCCTGAAAGAGGTCTAAACCAATTATTTTTTTTTTAATCAAGAT
36[93]9[89]	AATGGTAGCGCCATATCGTAACAGAATCAGCACGTATAAG
36[105]65[116]	ATAGACTTCAACCAGACCACCGCGCCTCCGGTATCTAACGAGCGTCT
37[58]15[61]	GCAACATGAGGCGGTGACCGTAAGCGAGTACCACCA
37[82]80[80]	GCAGCAGATTATCAAAAACAGATAGGCAGATTATACAAGACCTAAACTATATGTATCAATAG
37[122]56[118]	CAAATATTTTTTTTTTTTTCAAACCCTCAATCATGCTGAACACCAGAAGAGGTTTAAAT
38[92]7[100]	GAAAGAGAACAATGTTGGGAACCATCACGGATTAAAGTTGCAGCATTTTT
40[39]21[47]	ATTTTTTTTTTTTTAAATATGCTTTTTTTTTTAACTAAAGGGATTTTTTTTTTTGTGCTGCAAG
40[61]14[62]	TTGCTCTTCATTCCCATTTGGGCGGCACCGCGACGACAGTAAAACGCG
41[107]69[113]	TCAATAGATAATAAAGGCTTACAATAGCAGCGAATAAACAGCTTGATAATAAGTA
41[122]58[118]	TTTGAGTCGAGCTTCAAAGCGAAATATCGCCTGAGGCTACTAAAGAAG
41[152]60[146]	AACTTTTTTTTTTAATTCGACAACTTTTAAAACATCGC
42[65]18[65]	ATCAAAGCGGTATATTTTATATAACACCTCTTCGCTATCGGCCTTGCCT
42[105]66[106]	AACTTTGAGGTGCAGGGATTTCTTAATAATTTTTAAAGTCAGATTTAT
43[22]23[45]	TTTTTAAAATCAGGTCTTTGGCATCATTTTTTTTTTATTCTACTGATTTTTTTTTTTTCGCACTCCA
43[98]18[94]	CCCGAAACATTTCGGTAGATTTGCGCAACTATTACCGCTAGCAATACT
43[131]65[151]	CGAACGTTATTAATCGTATTATAAACAACTGAATTTTGTCGTCTTTCCAGACG
43[152]56[146]	GTTTTTTTTTTTTGAGTAACATTTACCTTTTGAGGCG
44[85]71[73]	TTATTCGGAAACAGTTAGATTAAGACGCTGTTATATAATTTAATGGGG
45[42]62[40]	AAGGGTGTTTGGATATAGATAAATTTACGAGCATGTTTTTTTTTTTAGAAACCAATCAACGGGTAT

45[58]26[58]	CATATCCAAAAGAAATTAGCAACGCAAGGAGTTAAATCTAAATT
45[142]67[137]	AGATCATTTTTTTCCATTACGCATAACGACAATGTAGAAAGGAG
45[152]54[138]	ACATTTTTTTTTTTCGGGAGAAACTCATTACCGTAATCTTGACAAGAACTGACCTTGTACAG
46[77]24[70]	CTTGAGATGGTTTAAATTACCTTATTTCAAAATTAAGCTA
47[22]33[37]	TTTTTACGAGACAAAATTCCTCATATTTTTTTTTTTATTTTA
47[94]28[81]	AAAACGAGTAGCCGGAGAGTTCTAGCGAAAAGCCTAAAAGGGACATTCT
47[102]17[111]	TATGACCCTGAAATCGGTCTGGCCTTACCTACATTTGACGAGAGCGGGAGCTATTTTT
47[114]71[109]	TAACCTTCCCTTAGAATCCTTGCCAATCGCATATTTTAAGTACC
47[130]57[141]	AATCGTCCGGATATAATAACGGACTGACCAGACGGTCAGTTACT
47[152]47[129]	CAATTTTTTTTTTATCAACGTAACAAAGCTGCTCATTCAGTA
48[34]30[27]	CTTTAAACTTTTTTTTTTAGTTCGCGATTTTGGCTATCATTTTT
48[61]26[78]	ACGCCAACCTGAAAGCGTAAGAAGATAGAACATATGTACCCCGGTTTG
48[127]50[110]	TTTTTAGGTAGAAAGATTCATCAGTACCAGACGACGATTTTTTTTTTTAAAAAC
50[109]31[90]	CAAAATAGCGAGAGGCTTTTGCGTTAATAATAGGAATAATA
51[46]48[35]	TCGACTGGATAGCGTCCATTTTTTTTTTATACTGCGAAATG
51[64]12[66]	TACGAGGCCAGATACAAGGACGTTGAGAGGGTTAAAGATTCAAATATTAGCTCATTGCTGGC
51[74]48[62]	AGTAAGTTTTGCCAGAGGGGGTAATAGTAATACCAGTCTA
51[94]26[98]	AACCCTCGTTTTGAGATTAACGAACTATTCAACCCAGTCAAATTATTT
52[53]54[42]	TTTATCAAAATCATAGGTCTTTTTTTTTTTGAGAGACTACCTATAAGG
52[65]22[66]	GTTTTAGTATTACCTGAGAAAATTATAACAGAGGGTGCCACGTGAGGG
52[101]23[101]	AACATACAGTATAAAAATCGCGAATTGCGTAAAATACCATCTAAAGATGGAAATTCGCCA
52[125]49[127]	TAATTTTGCTTCTGTGAATAAGGCTTGCCCAACATTATTACTTTTT
53[120]45[141]	GAACGCGATAGGCTGGCGCTATTAGGAACCGAATTCGCCTGAATATACAGTAAC
54[41]74[38]	CGAACGCAATAAGTTACCTTTGGGAATTAGAGCCTTAGCGTTTGCCATTTTT
54[57]30[62]	CGAAAGCCTGCAATAGTGTTCATTTGATTTCAACTGTGTAGGAG
54[137]73[148]	ACTGATATAAGTATATTTTTTTTTTGCCCGGAATAGGTAGGCTGAGTTTTT
55[38]34[27]	GATCAAGAAAAATGATTTTTTTTTTCCATATGAATAATACATCCAATTTTT
56[53]72[32]	ATATAATACTAGAATGTGATAATTTTAACCCAAAGACAAAATTTTTTTTTTGGGACCGACTTGAG TTTTT
56[77]67[65]	CATTTTAAAGTACACAGCGATTCCCATGTATACCGAAGCCCTTTTTGA
56[93]27[89]	GTAATTAATAAAGACAGAGGCGATAAAGCTTAATACTTCG
56[117]81[105]	CGCCATCTCAACAGTTTCAAATAAGACAAAAAGACACCACGGAATAAT
56[145]53[151]	CAACTTTGAAAGAGGTTTTTTTTTTTACAGATGAACGGTCATCAAGA
57[35]42[22]	GGTAAAGTAATTCGCTAATGCAGAACGCGCCTTTTTTTTTTTGTTTATCAACATATACTTCAATCA TTTTT
57[142]68[136]	TAACGAAGGCACAGCCCTCATAGTTTTTTTTTTTTAGCCCCACAAG
58[109]65[97]	GAATACGTACAAACAGCAAGAAACAATGAACCCTGAACTCACGTTGTA
58[117]81[119]	AGGCAAGTCGAAATGAGGTTTAGCGGATAATAGCGGGGGAAACGCA
58[125]47[113]	AACGAACTTTTTCAAATTGAGACGTCAGATGATTGCTTTGAATACCAA
59[54]81[55]	AACATGTTCATGTCCAGACTCATTTTAATAACGGTCACCGTCCGACATTC
60[77]66[62]	CACCCTGTATCGGTAGGCTCCATTAGACGGTGTTTAACGTCAAAAATG
60[85]70[82]	GGGATCCGAGGGTATTGACCCCACGGAGATCCCTCA

60[89]24[90]	TTTAAGAGGAATATTCCTAATGAAAAGAACGAACATGGGCGCCCTGTA
60[133]64[146]	GATATAGATTTTGCAATCCTTTGATTTAGAAGTATTAGACTTTACATTAGTA
60[145]57[151]	CCAAACGGGTAAAATTTTTTTTTTTTACGTAATGCCACTGCCGGAAC
61[98]38[93]	GGTGAAGTTAAAGGGAATCATTGGAAGCAAGATTAGAGAATCAACAGTT
63[70]20[62]	GCGTACCTTTTGAAATATTCTAAATATAATGCTGAACTCAAACT
63[74]67[89]	GCCGTTGAACCTCCCAGCTACAATTTTATCCGATTTTTGAGAATTAAC
64[53]68[38]	GAAGCCGTACCGCATTCCAAGAATAATCGGTAAGCAGATAGCCTTTTT
64[81]69[93]	GCTTTATTTTCAAAAAAATTATCAGCAGCTATCTCCGTAACACTGAGT
64[145]61[151]	AATTTCAACAGTTTCTTTTTTTTTTAGCGGAGTGAGAAACAACAAC
65[54]67[55]	TAGCAGCCTTTACAGTTTTTTTTTTAGAGAATAACATA
65[98]36[94]	CCAACGTCTAAGAACGCGAGGCAACTAATAACTCCAACGCGAACGACA
65[117]58[126]	TTCGCCATATTAGGGTAATTGAGCGCTTAAGCCCAATACCGATAA
66[61]37[57]	AAAATAGTTGCTATCCTTATCACTCATCGAATAATATCGTCAGAAGCAATATAACT
66[105]60[90]	CCCAATCCAAATAAGAAACTGAATCTAAAATCTCCATCGTAGCCGCTT
66[121]37[121]	CACAGAGCCTAAGGAATTAGCAAATCTTCGGTCGGTTTTAATAAGAAACCCT
67[56]45[57]	AAAACAGGAAGAAAAGCTGTCTTTATAAACAACAAGAAAATAATAAGAAC
67[66]40[62]	AGCGCAAAAGGAGCTTTGCACCCGACTTGCGGGAGGTTTTAATTGCAA
67[90]56[94]	TGAACAATAGCAATTTGCTTTCACTCATCTGCAACGGCAT
67[138]66[122]	AGATAAGTAACTTTTTTTTTTGATCTAAAGTTTTAGTTACAAAATAAA
68[135]41[121]	AATTGAGTAATATCAGAACAACTAAATTTGCCCTGTATGGAGATATAGCA
69[38]54[58]	TTTTTGAACACAGGGATAGCAAGCCCCCACCACCCGACGACAACCGAC
69[94]47[93]	TTAACCGCCATTGTATCACATCTTCTATTCTTACGCGATAGCTACATA
69[114]52[126]	CAACGCCTGTAGCAGTACTCAGCCGCGACCGAAAACTTTAGGGCTTAT
70[81]79[77]	GATAAGACTCATAGACGGATATTCATGAGCCGCCGCCAGCATCGCCTC
71[74]76[86]	CATGATACCGCCACGCACCATTACCATTAGTTTCATCGTAAACAGTGT
71[110]75[117]	AGGTACCGCCACCAATGAAACCATCGAAGTTTGCCCTATT
71[122]43[130]	GCCGTCGAGAGGGTCAGGCGCATGCTCCATATCATAAGTGAGGAAGGCGGAACAGCC
72[148]71[121]	TTTTTACTCCTCAATTTTTTTTTTTTAAGCAGTAGCGACAGAATCATAGCAGCATTAGGATGT
73[32]55[37]	TTTTTCCAAGAAGGAATTTTTTTTTTACCGAGGATTAAATAAGAATTTTTTTTTTTAAACACCG
73[62]52[66]	ATGTGAATTAAATACCCAACCAGCGCTCCGGCTTAGGTTGGGAGAAGA
73[70]63[69]	TACCTCAGAGAATAGGAAATACCAAGCTTTAATTCAGCAGCGGAACAA
74[89]52[102]	GTCAAGGCCGCGTAGAAACTTATTACTTGTCACAAAATGCTGATGCAAATAA
75[38]77[61]	TTTTTTCTTTTCATAATCCCTTGATATTTTTTTTTTTTCACAAACAAATA
75[98]61[97]	TGCCTATTAGCAAAGAAACGTCACCCTCAGCGTCACCAACTAAAACGA
75[118]78[106]	ATGAGTGTACAGAGCCACTTTTTTTTTTCACCCTCAGAGCCG
75[132]60[134]	AAGTAGAGAAGGACCGTAATGTATCACCTTCCACAGACCAACCTAGTTGCGCCC
76[85]75[97]	GCCTTGTCAGAGCCGCCACCCTCAGAACCGACCAGAACCC
77[62]80[66]	AAACGATTGGAAAATCACGGTTGAGGAACCGATTGAGGGAGGTATGGT
77[84]81[101]	GAAAGCGCAGTCCGGGGTCATAATGCCCCACCACCAACATAAAGGTGGCA
77[122]75[131]	CATACATGGCTTTTTTTTTTTTTTGATGATACAGTCTGAAACATGA
78[105]74[90]	CCCCACCCTCTGGTAATAAGTTTTAATCTGAATTTCAGACTGTAGCGC

79[56]73[69]	CAGGTCAGACCGGAACTGACAGGACGGAACCACATTAAAGCACCAG
79[78]73[61]	CCAGTAACAGGAGCCACCTCCTCATTGGTCATAGCCCCCTTAAGCAAA
80[65]42[66]	TTAAAGAACTTTTGAAATCGCGAAACCGAGCCAGAAAGACAGCAATTC
80[79]77[83]	AAAATTCAGAAGGTAAAAATTATTTGCCCGTAGCATTTTCAAAGCCAGAATG
81[102]43[97]	ACAGTTTATTGCAGTATGGTTAATTTTCGCCTGAACGCCAACTACAGAGGTTATCATCAG
81[106]77[121]	ATAAAATTTTGCTCTTTCGGAACTTTAGCGTACCGTTCCAGTAAGCGT

II.S3: Design scheme of the 42-helix bundle

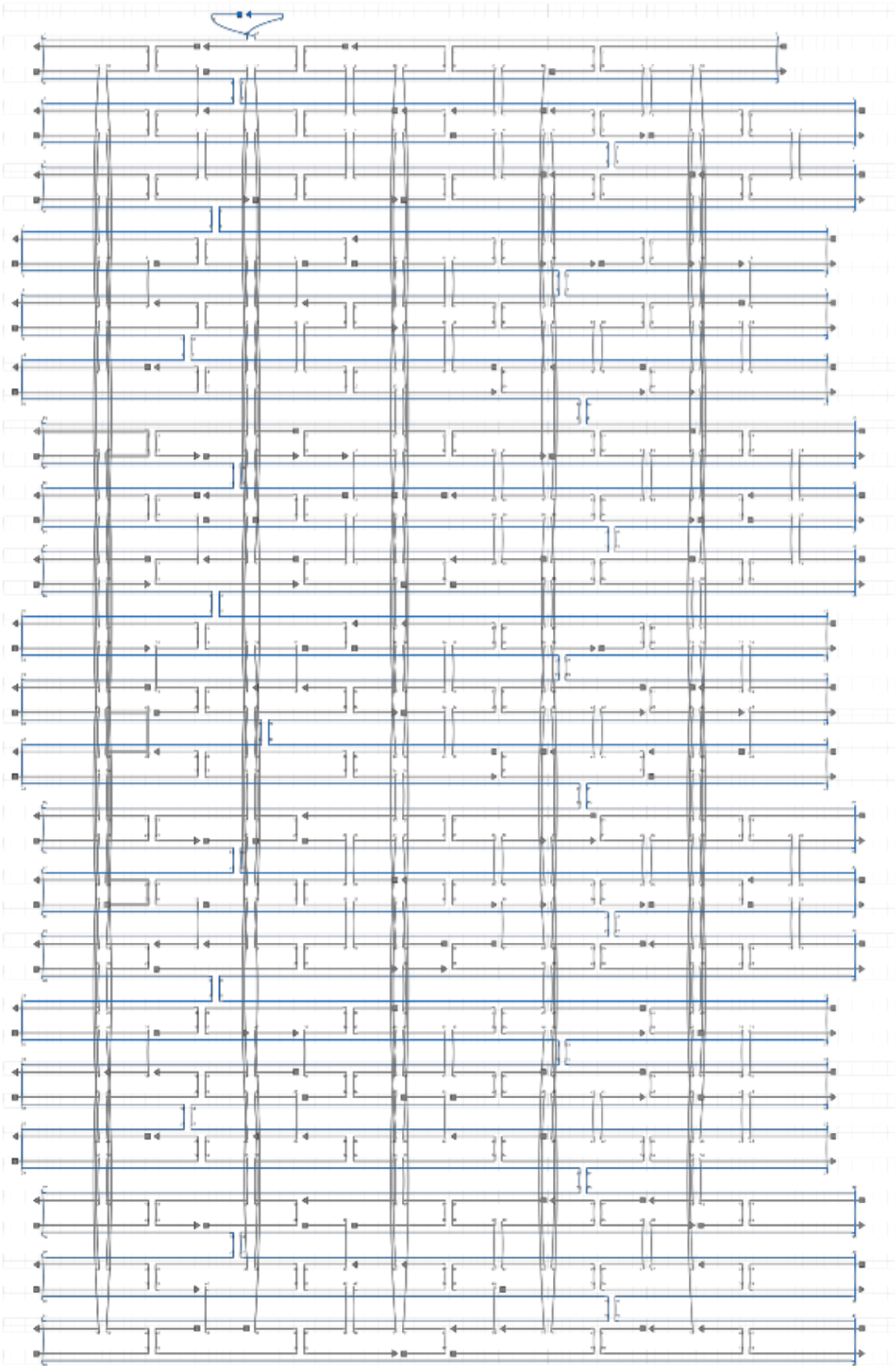

Figure 0.S2: Scaffold/staple layout of the 42-helix bundle. Generated with caDNAno v0.2.

II.S4: Staple sequences for 42-helix bundle

Table II.S2: Staple sequences for the folding of 42-helix bundle.

Staple	Sequence
Pass Oligo 1	TGA ATC GCG ACG TGC GTC CCG TCG ACC TCG TAC TAT ATA GCT TCT TTT T
Pass Oligo 2	TTT TTT ATA ATG AGT AGC AAA CGT AGT TTT T
Pass Oligo 3	TTT TTC GTG AGC AAT CCC TCG TGT TTT T
Pass Oligo 4	TTT TTC CCT CAG AGC CGC CAC ACC CTC AGA GCC ACC ATT TTT
Pass Oligo 5	TTT TTG CTA CAC TAG AAG AAC AGT TCT CAA GGC TCA GTG TAA CAC
Pass Oligo 6	TTT TTT CCA AAA AAG GTG AAT TTT TTT T
Pass Oligo 7	TTT TTA CCC TTC TTC TAC GCT AAG ACT TTT T
Pass Oligo 8	TTT TTA GGA TCT TCT ACT GGA TCT TTT T
Pass Oligo 9	GAG TAA CTA TTT CGG AGG CTG AGA CTC CTC AAG TTT TT
Pass Oligo 10	TTT TTC CAC AGA CAG CCC TCA TAG ATA ATT TCC AAA AGA AGT GGT AGG ATT A
Pass Oligo 11	TTT TTT GAG ACG AAA AAG CCA CAT CTT GCT TTT T
Pass Oligo 12	TTT TTG TTA ATG CCC CCT GCC AGT GCC CGT ATA AAC ATT TTT
Pass Oligo 13	TTT TTC GAT AAA ATT TGT TGA CGG GGT TTT T
Pass Oligo 14	TTT TTT CAT TAA GCA TTC CAG GGA TTG GCT TTT T
Pass Oligo 15	TTT TTC GTA AAG CAC GAA AAC TTA AAT TTT T
Pass Oligo 16	TTT TGG TTC CTT TTA ACT CAC CTG CCG AAA ATA CGC CCG GTT TTT
Pass Oligo 17	TTT TTA GAT TGT ACT CGA AGT TCT TTT TTT T
Pass Oligo 18	AAC TCT GCG GGT ATG AAT TGC AGG TAG GAA GTC TAA ACG TAG TTT TTT T
Pass Oligo 19	TTT TTT TCT ACG GGT TAT CAA AAT TTT T
Pass Oligo 20	TTT TTT AGT GAT CTT ATT TCA TTA TGG TGA ACT CGA TAA ACT GAC GCT TCT T
Pass Oligo 21	TTT TTT GCC CCG GGA GTG TGC AGC TCT TTT T
Pass Oligo 22	TTT TTC CTG TTA AGT GTG CAG CTT TCT TTT T
Pass Oligo 23	TTT TTG CAG ACA CGA CTA ATG CAC TTT TTT T
Pass Oligo 24	AGG AGC TAA CTA AGA TCA CTG ATC TAG TGG TTT TT
Pass Oligo 25	TTT TTC GTT CAA TTA GGC TAA TAG ACT TTT T
Pass Oligo 26	TTT TTT CGG AAA GAA TTA GCC CGT TAT TTT T
Pass Oligo 27	CTG TAG GAG TTC TGA GCG AGC ATC GCA GTA CTG TTG TAA TTT TTT
Pass Oligo 28	TTT TTT GTG AAT AAA ATA TCC AGT TTT T
Pass Oligo 29	CTT TCG AAA AGG CTT TTC ACG TTG AAA ATC TTT TT
Pass Oligo 30	TTT TTG AAT ATA TGT GTA GAA ACT AGC ATT CAT AAA AC
Pass Oligo 31	TTT TTC CCC CTT ATT AGC GTT GCA TTT TTG ATC GGA GTT ACT
Pass Oligo 32	TTT TTT CAT AGC TCA CGC CAC TGG CAG CAT TTT T
Pass Oligo 33	TTT TTA AAG CCG GCT CCT CTC CAT GAT TTT T
Pass Oligo 34	TTT TTT CGC GAT AAC CGC GGT CAT AGT TTT T
Pass Oligo 35	TTT TTA ATT AGA GCC AGC AAA ACT TGA GAA GAC TCC TTA TTC GCT CCT T
Pass Oligo 36	CAT GAG AGT CTG ACA AGA TCC TTT GAT CTT TTT TT
Pass Oligo 37	TTT TTT TGT TAT CTT AAC CCA AAA GAT TTT T

Pass Oligo 38	TTT TTA CGA TTG GCC TTG ATA GGT TGA GGC AGG TCA GTT TTT
Pass Oligo 39	TTT TTT AGC AAG CCC AAG CCT GTA GCA TTT TTT T
Pass Oligo 40	TTT TTA CGG AAA TTA TTC ATT GGG AAG GTA AAG GTG GCA ACA TAT ACG C
Pass Oligo 41	TTT TTT ATC AAC AGG AGT CCA AGG TCA TAC CTA GA
Pass Oligo 42	GCA TCG CGG TTA CTA GAT GGC CAA CGG ACT AAA TCT TTG GGG TCG AGG TGC TTT TT
Pass Oligo 43	TTT TTT TGG ACC GAG ATA GGG TTG AGT GTT GAT GGG CA
Pass Oligo 44	TTT TTA GAA GGA TTA GGC ATT TTC AGG GAT TTT T
Pass Oligo 45	TTT TTA ACA GTA GCA CCT CGT CCG AGT TTT T
Pass Oligo 46	TTT TTC TGA ACG GTC TGG TTA AGG CCG TAG GCC GGA TCA GGC GGG CAA GAA TTT TT
Pass Oligo 47	TTT TTC CCA CTA GAC TAC TGC GCT GGT TTT T
Pass Oligo 48	CCA CCC TAT TAG CGT TCC CCC CCC TGC CCG GGA AGC GTG GCG CTT TCT TTT T
Pass Oligo 49	TTT TTG CCA CTG GTA ACG GCC TAA CTA CGT TTT T
Pass Oligo 50	TTT TTC GCT CTC CTG TTC CGA TGG AAG CAA GGC CA
Pass Oligo 51	TTT TTA AAA TAC ATA CAT AAA TAT TGT TTT T
Pass Oligo 52	TTT TTA CTG GCA TGA TTC CAT TTG GGT TTT T
Core 1	TAC GTG GAC CCT CAC CAG AAT TAA TAA GTT TTA ACG AGA AAA
Core 2	TGG TCT GGC GAA AGC CGC TAC CTG GTA GCG GTG GTA AGA GTT
Core 3	CCA AGC TAA CTA TCG ATT TCT GGG ATT CGT TAC CTT CGG AAA
Core 4	AGT ATG TAA TAA CAC CCT GCC ACG GTC TTC CAA CAC ATC CAG
Core 5	CTA CAA CTA GGA ACC AGC TTG GCA AAA GCT TAT CG
Core 6	AAC CGC CTC AAT GAT TTA CAA CTT TCC AGA CGT TAC GGA GTG
Core 7	ACC ATA CGT GAC GGG CTT GTG CGC TAG GGC GCT GGA CAC CCG
Core 8	GAG ACC CGA ACG TGT TAG AGC TTT CAC AAA AAG AAC ATG TGG
Core 9	GTT TAG TCG TAT GAT GAT GGA AAT TTT CTG TAT GGG GTT TTA TTC TTC A
Core 10	GTT CTG ACG GGC GAA AAA CCG TCT ATC AGG CGG CAT AAA GTA
Core 11	CAT ATT CTT TAA AAT AGG TAC ATT GAG CAC TCA AAC ATG GAA GCC ACT C
Core 12	ACA AAA ACG TTT AGG GTA CCA CAT ACG CAA CCC CCC GTT CTT CTT GGA T
Core 13	AAC CAC CCA AGT GTG TCA TAT GTC TTG AGC GTT GCC CGA CAG
Core 14	GTA TTT AAG AAT AGA AAG GAA TTG TCG TGG AGT CTC AGT AGC
Core 15	AAG TAG GAA CGG GTT GAC GAG TTA GCC CGA CCG CTA CTC ATC
Core 16	TTC ATA TGG TTT ACG TAC TGG GGA AAG CAC CAA TGG ACA GAA
Core 17	TAT CGG TCT TGC GTT TCC AGT CCC TAA TCA AGT TTG GAA CCC
Core 18	TCG ATA TCA AAT TAA CAA ATC AAA TGA AAC CAC GTT AAG GGA
Core 19	GGC TTT TTA CCG TTA TTA GCA AGC GTC AAT CAC CGG AAC CAG
Core 20	CTC CCT TGC TTA CCG GAT ACC AAG ATA CAC CGT AAT TGT ATC
Core 21	GCC ATT GTT TTC TCG CGG CAT CAC TAT TGG CCC ACT ACG TGA TCT CAC C
Core 22	TGA GTT GTC CTG AAC ATT TAC GCG AAA CTG GCG TTA ACC AAG
Core 23	GAT GAT ACA GGA GTC AGC GCC ATA AGT TTA TTT TGT GCC GTC
Core 24	GGT TTA TCC ATG TAA GAG CCA ACG AAT GGT GCC TT
Core 25	CCC CGA TGC GAG AAT CCG AGG CTC TTA GGG AAC AAA CCA CCG
Core 26	TAT ATG AAG AAG TTA TCG CCA CAT TTT ACG ATC AAG GTT CCG

Core 27	GTT CGC TCG CAA TAC ACA GTC CGC CTT TGT TCG GTC CGG TAA
Core 28	CCG TAA CAC TGA GAG CTA AGT AAA GGC CGT CCA ACG TAG GTC
Core 29	CCT CAA ATA GCT CCC ATG ATG CCA ACG TCA AAG CCC CGC CCT
Core 30	TGA AAA TAG TTG GAA CCT CTT ACG TGC CGC TTC CTA TGT TCT
Core 31	AAC CTG AGT CCA TAG GGC GAA ACA TGC GGA GCG ATG AAA ACG TTT CAG T
Core 32	GCT GAC ACC AGT GAC GCT TAC TGG ACC GCG GAG GCC AAA CCT AGT AAC A
Core 33	TTT GCA AGC AGC AGG AAG CCA AGG CGG CTA AGC CAT CGT ATG
Core 34	ACC GGA ACC GCC TCC CTC AGA CCG TAA TCA GTT TCG TCA CCA
Core 35	AGG AAG GCG GCA CGG GCC CTA CAA GGA TAC TCC GTA AAT GCG ATT TAT T
Core 36	GAG CCC AGC CGC CAC CCT CAG AAC CGC CCA GAA CC
Core 37	TAC GGT CTC AAT AAC TGG TGA AAA TTA ACA GAT GGT ATC TCA
Core 38	GCA TAA GTC CTT GCT CTG TAT TTG GCC AAT CAA TCA CCG AGC
Core 39	GCA GAG CGA CAC GAG CCA GGA CAG GCG TGG GTT TTG TAT TAA GAA CCT A
Core 40	ATC TGA GTC ACC TGT CAG AAG TGT GAA GAC GCC GCG GTT TGG
Core 41	TTA TTC TGG GGT CAG ATC CTC AGG CCG CCA GCA TTG ACA GGA TTC ACA A
Core 42	GCC AGG TAT CGT CGT GGT ATT TGC CAT ATG TCG TT
Core 43	TTC ATC GTG CCA TCT TTT CAT AAT CAA AGA CTG TAA GAT TGT
Core 44	GAG GTA TGT AGG TAA GCG GTC GTT TTA ACG TTT AAC AAA CGG
Core 45	AAA CCA TCG ATA GCA TTA AAG GAA CCG CAC CAG GCG ACT ATA
Core 46	ATT GGT GAG TTA AAA CCG TAC GCT CAC CGT CAC CGA TCA CCA
Core 47	AGG GTG ACG CGT ATC TTG GTC TCG AGT AAC GAG AGT ATT TGC GAG GAG C
Core 48	AAC GAT CTA AAG TTC AAC TAA CGC AGA CCA CGG TG
Core 49	GAT GCT AGG TAG CTC TTG ATC CGG CAA CCT GTC AAA ATA GTA
Core 50	GAA GAA AAC AGC TCC CAT GGT TTG TCG CAT ATC CAT TCC CCG GGT GAG T
Core 51	AGC CAC CTC AAG TTT AGT CAG AGT CTG TAT AGG CAT TTC CAT
Core 52	CGG ATG TTA ATG CGG AGC GGG CCT TTT GGC GCC TT
Core 53	CCG ACA GTT GCT CAT GGA AAA CGG TGC GCT CAG CCT CAG CGA
Core 54	CCG GTT CTA ACT TTT GTA ACG GCG GTG GAC CGC CAC TGA ATT
Core 55	ACC ATC ATT GGA ACA AGA GTC CAG CAC CGA AAA CGG TGT AAC
Core 56	ATA GAA CCG GCC CAG CAT TGG TCC GTT ATT CTG TGT GGA AGG
Core 57	GTA AAC TAA TAA AAG TGC ACG GCA GTT TGT AAT CCC TTA TTA
Core 58	GGA TAA GTC ACA ATC AAT AAA CAT GAA AGC TCA GTC ACC CTC
Core 59	TTG TGC TTA TTT GGC GAA ATT CCG GAT GGC CGG AAT TTC ACC
Core 60	CCC TCA GGA GAG GGA GAG GTG CTT CAT GTT CCG CTA TCC TAA
Core 61	AAT TAG TCA TAC ATG ACA TTC GAA ACG CAA AGA CAA AGT ATA
Core 62	AGG CTC CTC AAG TCT TGA TAT CCA CGG AAA AGA CAA AAG GGC
Core 63	CTA CAG AAT CTG CGC TCT GCT ATT ACG CTG CGC GTA AAA TAG
Core 64	TAA AGG GAA TTC TAA CCA TTC TAT ACC CGC ACA CCC TCG TAA
Core 65	GAG ATT CAT AGG TGT ATA AAA AAC CGA TTG AGG GAA AAG GTG
Core 66	GAA ATA TGC AGG GTT CAC CGT CTT TCA TCA CTC CAG GCT GCA
Core 67	GAG CCT TTA ATT CCA GGA ATT GCG AAT ATT AGC GTG TAC AAA ACC ACC A

Core 68	GCG CGT TGT AGC ACC ATT ACC CCA GTA ATC AGG AGG CCC GGA
Core 69	AGG GCG CGG CTT TGC CAA AGT AAT CTC TTC AAC GGT GTC TCA
Core 70	ATC CGG TGG GCT GTA ACG CCC GGG CGA TAA AGA ACG TGG ACT
Core 71	TTT TTT GCC GCG CTT CCC AGG CGA TGA CGG ATC AAT TAC GAT
Core 72	TCG ACG CGC CCC CCC GTA CGC GTC TTA CTT CAA CAG TTT CAG
Core 73	GGA ACG AAA ACT GCG CAG AAA AAA AGG AAT TTG GTG TTC TTG
Core 74	GTA AAT GGC TGG AGT GCC TTT AGG CCG GAA ACG TCG CAG TCT
Core 75	GCC ATC AAT CAA AAA CCC TTT AGG GAT GGA GCC TCT GAA ATG
Core 76	CGC ACA TGT GAT TTG GAT ATA ATG TAG AAG TCC ACA CAC TAT CCC ATA T
Core 77	CAC CAG CCG CCC ATC ATT ATC ACC GAA TCA AGC GTG GGG CGA
Core 78	AGT AGA CGC TGC TAA ACA ACT AAA TGT ACT GGG TTG GCG CCA

II.S5: Design scheme of the nut-screw

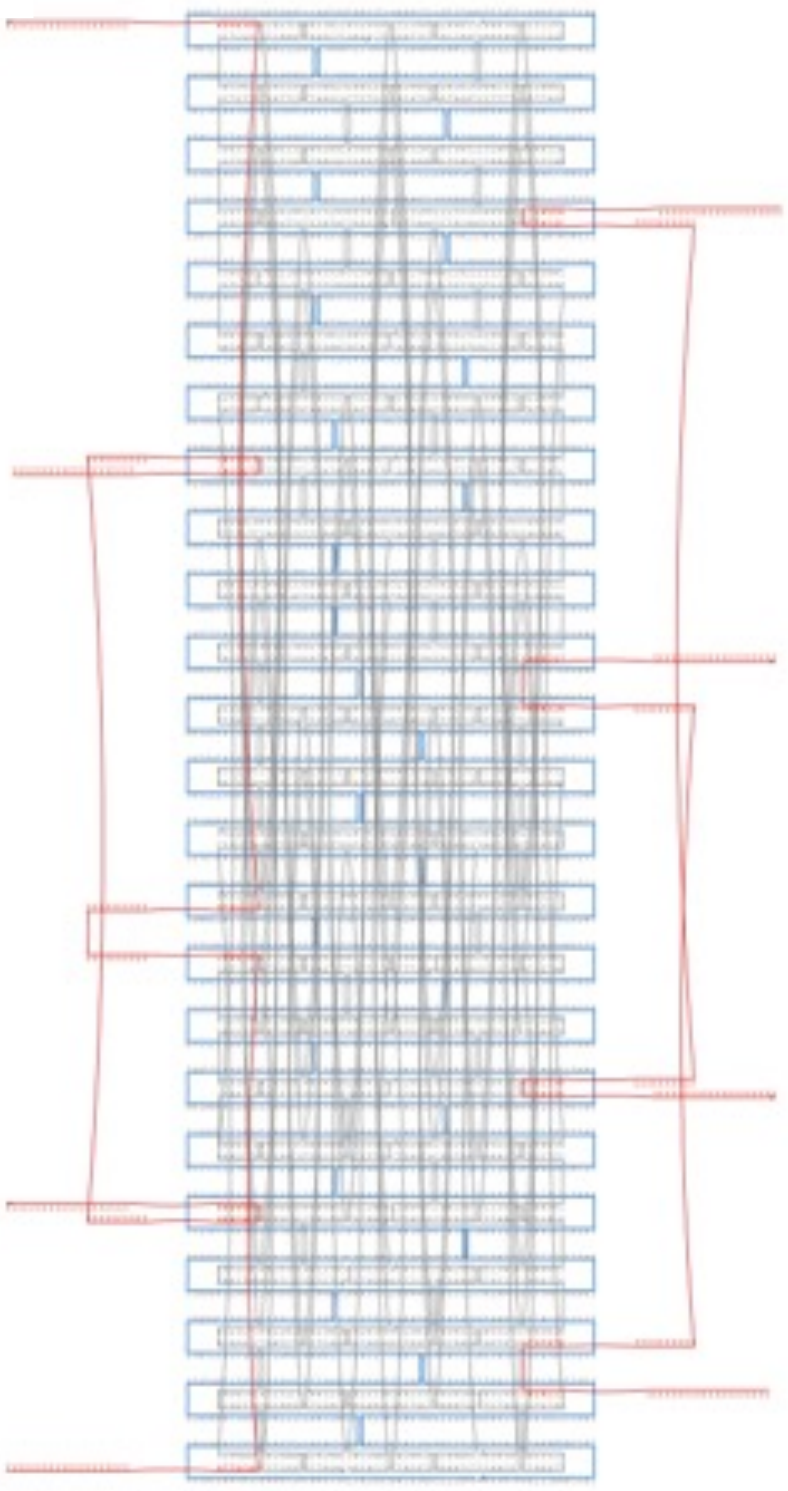

Figure II.S3: Scaffold/staple layout of the nut-screw structure. Generated with caDNAno v0.2.

II.S6: Staple sequences for nut-screw

Table II.S3: Staple sequences for the folding of nut-screw structure.

Staple	**Sequence**
Oligo 1	ACG AAC CCC CCG TTC GTT CGC TGA AAG AGG TCC AGC GTT TTA GTT TCC CAC CTG TC
Oligo 2	TTC GCA CGA AGA TCC GAA GTT AGA GCA TGT ACC TTA CGC TGG GGG AAT AAA GAC AC
Oligo 3	CAA CGG TGT GTG GGA GTT CGG TCA TAG CTC ACG CTT GTG TTC CGA CCC TGC CGC TTC GCT TTC
Oligo 4	TGT AGG TCA GCC CGG AGT CCA TGA ATT ATG CAA TTG ACA TCG GTA ACT ATC GTC TTA CCG CTG
Oligo 5	GCG AAA CGC TCC CTG CGT AGC ATT TTC GTT CCG CTG ATT GAT AAT ACG TCT TAA CAC ACG ATT
Oligo 6	ACC GGG CAA TGA AAG TTT GGA ACA AGA GCA GGG CGT GGC ATC GTA AAA CAA AAA ATT TGA GTT
Oligo 7	CGC CTT AGT ATC TCG TTT GGC TTC CAG CGA GGG TCC GTG CGC TCT CCA AAA GTG AAG GCA ATG
Oligo 8	ATC GAG ACT GGG TGT TAA AGA CAT TCA CCG TAT GAT AAA GGC AAA AAG GGT AGC GGT GGT TTT
Oligo 9	GTC GAG GAC CTA TAT AAG CAC AAG TTT TTA TTC ACG AAA GCG GCT AGG GAC CAC CAT TAA TGC CCC CCT G
Oligo 10	ATT CCA CAG GCA TCC CCG TGC GCC AGG CGC GCG TAC GCT GGC AAG TGT AAG AAA GGA GCC CCC AGT TGG G
Oligo 11	CAT GCC GTT TGT AAG AGT TGG ACC GCT GAT CTC AAG TAA GAG GTT CCT TTC ACC AGC GCA GAA GGT TGA G
Oligo 12	GCT GAT GAT ACG CAC CCG TTT TAT GGA CAG AAT ATT TCC CTA GTG TTA CGG TGA AAC TAC ACA ACC TCC GTG ATC CA
Oligo 13	TCA CCA TTG CCC TTT TAA ATC CAC TGC TGA ATG CTC GAT TCA GGT TCA TTT TGT TTG CAA GGC AAA TAT TCC GCT GGT AAT GAA
Oligo 14	CCC CCG CAG CTT GAC GGG GCG TTG CCA TCC CCT CCC CAC GTC AAA GGG CAT TTC CGT CGC TCT GGA GTG ACG TTC AGT AGT CAA
Oligo 15	AAG ACC GTA AGA TGA ATC GTG GCG GCA TAG CTG CTC CAT AGT CCG TGA AAG CCG GCG AAG CTC ATC CGG AAT TAG GCC TTT TTA
Oligo 16	CCG GAG CTT TCT CAC TGG ATA TTA CGT GGT TTT CAG CAG TTT ACA AGG AAG CTA AAA TGG AGA CAC GAC GGA AAA ACT CCG CTT
Oligo 17	GGG TCT GAT CGC CTA CAC AAT GTG AGA CAA ACC TGA AGT CGA CGT TAA CGA TTA CGT GTC ACG ACA GTA AGT GCG CCT TGG CGA
Oligo 18	TTG GTG CCA CCC CCT GGG GGT GGA TTG AAT CAG CGT CTA CGG ATT GAG GTT CGT ATG GGA CTC AAG GTT GCG AAA ACG TCG CGA
Oligo 19	ATG GCC CAT CAC CCT AAT CAA GTT TTT CCG TCT ATT CCA CTA AGA ACT TTC ACC ATG TAT TTT CAC TGG ATA TAC CAA TCC CAA
Oligo 20	CGT ACA GTC GAA GAA TAT TAG CAA ACG TCA TAA ATG GTT GTT AGT ATT CTT CCC GGA TCA AGG GTC GCC AGC TAA ACA GAG TCA
Oligo 21	TTT TCA GGA GCT CTG GCC TAT GTT CTT TCA GAT CCC CCC GCC TGA ACC CGG ACG ACG GCA GCA GAT TAC GTT TTG ATC CAA TCC
Oligo 22	AAA CTG ATG TAC CTC ACT GGT GTA TAA GAG TTC TTG AAC AGT ATT TGG TCT TCG GAA AGT ACG CTT TCG ACC GAG ATA GGG TTG
Oligo 23	GGG CGG GGC GTA TAC GGC TAC GTC GGC AAG CCG TCG AAG GTC CCG CCA GAC GTG GAC TCC ATT GTG TCA GTT AAA CGT GGC CAA
Oligo 24	ACC CAT GGA ACT GTA ACA GGA GCT ACA GCT TCT TCT ATC GAG CTA GCA CCA ACC CAA AGA TGG CTT CCA TAC TAG AAG AAG TGG
Oligo 25	CCT CGT AGT ATT TGG GTT GGC GTG TAA CAT TGG GTG GGT ATT GGC GGA ATG AGC TGG CGT TTT TCC ATA GAG TCA GAT TCA TCC
Oligo 26	GAT TTA GCC TCA CTG ACC CAA GTT CCA GAT AAA ACC ATC GGG CTC GTT CAA GAT AGC CCG CAA ATC ACC GCC CGG GAT TCC GAG
9390_MH	TGT TCG GAA TGG TTG GCT TAC GTC ACA ATC GAT GCG TAA CAA AAA GGC GAA GAC ACT GAT TTT CCG CAG AAC GAC ACG GCT ATT AAC TTG CTG TCG CT

9391_MH	CCC GCC TAG AAA AAA CCA GAC ATG AAC ATT TTG AGG CAT TTC TCA ATG TTG CCG TAG GAA CCC TTC CAC CAG GGA TGA AAC GAC AAA ATC GGA CTA TA
9392_MH	AGC GTG GAC CGG ATC CTG GAA CCG ACA GAC GCT CAG CTC CGC GCC GCT ACA GGG CGT CAC GCT CGA TCG GTC CTC CCC CCT CAC TAA AGG GAA GGG AAA TTC TTG
9393_MH	CCT CCC TCC CTT TGT TGT TAC TGG TGA TAT GGG ATT CGT ATG ACT GTA ATC GCG ACC GCT AAC AGT CTC CGC CAT CTG GCT ATT GTT GTT CTA TAA GTA GGA TTT
9394_MH	ACA AAC CTA GCT CTC AGT TAC ATC TGC GAG GCG GTT TAG CAG CTG GCA GCA GCC ACA CCC GGT GCA AAC AGA ATG CGA ATA AAA ACG TTC GTC CAA GCT TCG GGA
9395_MH	AGT GGC ATT ACA ACA TCC TCG GAT ATT CCC GCT TCT CCC CCT CTT CGG ATA TAT TCG AGC AAA CTG AAA CTT CAC CCT TAG CAT TTC TCA TCG GCA TTG CGT CGG GCA ATG A
9396_MH	CCC ACC GGT CGG AGA GTA GGC GTC GTA CTA CCC TGA CTC TTT GTT GCC GAA GTC AAC AGG CCC GAA GAA ATG GCC TAT TGA GCT AGG ACT GAG TGA AAG GCG CAG TCG CGA A

CHAPTER III – AFFINITY-BASED MAGNETIC PARTICLES FOR THE PURIFICATION OF SINGLE STRANDED DNA SCAFFOLDS FOR BIOMANUFACTURING DNA-ORIGAMI NANOSTRUCTURES

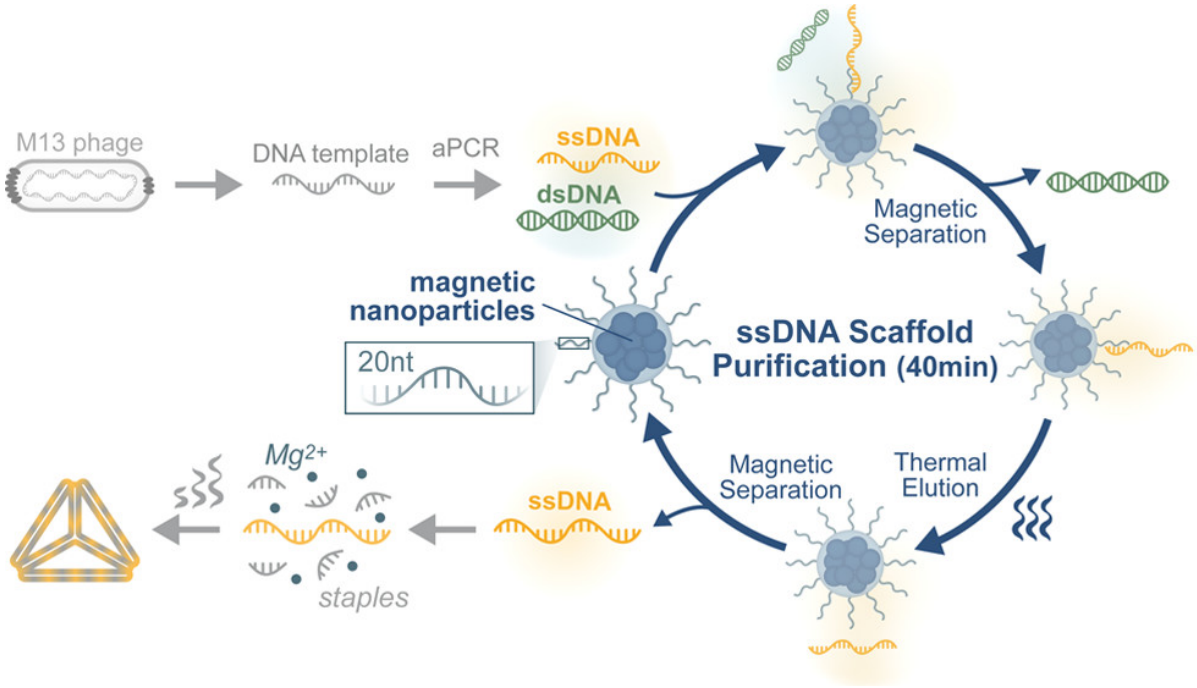

This chapter has been published as: Silva-Santos, A. R., Oliveira-Silva, R., Sousa Rosa, S., Paulo, P. M., & Prazeres, D. M. F. (2021). Affinity-Based Magnetic Particles for the Purification of Single-Stranded DNA Scaffolds for Biomanufacturing DNA-Origami Nanostructures. *ACS Applied Nano Materials*, *4*(12), 14169-14177.

Abstract

DNA nanotechnology encompasses the self-assembly of nucleic acids into complex nanostructures via Watson–Crick base pairing. Asymmetric PCR (aPCR) is often used to generate 500-3500 nucleotide (nt) long, object-specific, single-stranded DNA (ssDNA) scaffolds from DNA templates, which can then be assembled into nano-objects by the DNA-origami technique. One crucial step in ssDNA scaffold preparation is purification. Scaffolds are usually purified by agarose gel extraction, a laborious, time consuming, limited and not scalable technique that presents low recovery yields, delivers low-quality products, and requires specific equipment. To overcome such pitfalls, we present a simple, fast, and potentially scalable affinity-based method comprising magnetic particles and a simple magnet. The system was used to purify ssDNA scaffolds from aPCR mixtures. Scaffolds with 449 nt and 1000 nt were synthesized by aPCR alongside with double-stranded DNA (dsDNA) using the genome of the M13mp18 phage as template. Magnetic particles were functionalized with a 20-nt oligonucleotide complementary to the 3' end of the ssDNA scaffolds. Hybridization between the ssDNA scaffolds in the aPCR mixture and the affinity beads was promoted, which allowed (i) the removal of the dsDNA and (ii) subsequent recovery of ssDNA upon melting to denaturing temperatures. The purified scaffolds were used to assemble 31 and 63-bp edge length tetrahedra using site-specific short oligonucleotide, thermal annealing, and high magnesium concentrations. The resulting DNA-origami structures showed high assembly yield and purity, as observed using agarose gel electrophoresis. In conclusion, the method enabled the purification of 550 ng of 449-nt and 880 ng of 1000-nt ssDNA fragments per aPCR reaction (50 μL), demonstrating its potential as a helpful and versatile tool in the production of DNA-origami nanostructures.

Keywords: DNA nanotechnology; DNA-origami; magnetic separation; nanoparticle functionalization; nucleic acids immobilization; ssDNA scaffold purification.

III.1. Introduction

DNA nanotechnology involves the molecular self-assembly of nucleic acids into nanostructures [1–3]. The method explores Watson–Crick base pairing to construct complex nanostructures [1, 2], including 2D-arrays [4] and 3D-shapes such as cubes [5], octahedrons [6] and a variety of polyhedrons [7]. These nanostructures are often assembled using the 'scaffolded DNA-origami' strategy, whereby a long (~10^3–10^4 nt) single stranded DNA (ssDNA) molecule (the scaffold) is folded with the assistance of short oligonucleotides (the staples) into the target shape [6–9]. The specificity of this technique, which allows the site-specific introduction of functional groups, is very appealing in an increasing number of fields of study, with applications ranging from nanomachines [10], solid-state nanopores [11], drug delivery systems [12, 13], biosensors [14], protein crystallization [15], molecular logic gates and computing [16], among others [17, 18]. Due to its particular features, the potential of scaffolded DNA-origami technologies is undeniable. Nevertheless, the real widespread usability and/or applications of DNA-origami can be strongly hampered by scalability and preparation/assembly problems.

The production of scaffold DNA for DNA-origami is usually performed by (i) purification of phage-derived single-stranded genomic DNA [19–21], (ii) PCR [22] or asymmetric PCR from DNA templates [7, 19] or (iii) enzymatic single-strand digestion of double-stranded DNA [19, 23, 24]. The most expedite way of obtaining a ssDNA scaffold is to use native or recombinant phage genomic DNA, which can be purchased or produced and purified from phage cultures using standard laboratory techniques. Conventional PCR can be used to amplify scaffolds from the phage genomic DNA, which is used as a template. After amplification, the target ssDNA scaffold is obtained from the dsDNA amplicon by selective enzymatic digestion, using for example a lambda exonuclease [25]. Scaffolds can also be synthesized by the enzymatic digestion of double-stranded DNA using two different strategies. The first strategy involves the annealing of two oligonucleotides at locations within the phage genome that flank the target region so that specific double stranded restriction sites are formed. Upon addition of the corresponding restriction enzymes, the DNA is cleaved, generating the target scaffold [7, 24]. The second strategy involves the enzymatic single-strand digestion of PCR-amplified double-stranded DNA where molecular biology techniques are used to introduce a nicking

endonuclease site in a plasmid that can be produced *in vivo* in *E. coli* [19, 23]. Finally, Veneziano *et al.* described the use of asymmetric PCR to generate 500-3500 nt, object-specific scaffolds using DNA from the M13 phage as template [7, 27]. The technique relies on the use of one primer (the forward primer) in molar excess over the second primer (the reverse primer) in order to preferentially amplify the ssDNA target over its complementary strand. The size limitations of this approach have recently been overcome by using a highly-processive polymerase to achieve scaffolds with more than 15000 nt lengths [19].

Once the ssDNA scaffolds are produced, they must be purified to obtain a highly quality product. Purification is a crucial step that currently imposes a major limitation in the preparation of suitable raw materials in quantities and with a quality compatible with the self-assembly of the target nanostructures. For example, after aPCR production, the mixture not only contains the ssDNA scaffolds, as well the unused primers, template DNA and dsDNA fragments formed by the scaffold and its complementary strand. Purification can be accomplished by agarose gel electrophoresis separation of nucleic acids followed by band excision and physical extraction from the gel matrix, which typically yields 1-5 pmol per 50 µL reaction depending on the fragment size and sequences [7]. While this well-established method is the gold standard for scaffold purification, it is laborious, operator dependent, not scalable and yields scaffolds with agarose gel residues [27]. Another approach described by Stahl *et al.* is the use of polyethylene (PEG) precipitation. In this case, purified DNA 7249-8064 nt scaffolds derived from the genome of bacteriophage M13 by polyethylene (PEG) precipitation were obtained and used to assemble various DNA shapes [22]. However, the Achilles heel of this strategy is that it is not suitable to assemble smaller structures that require scaffolds significantly shorter than the full phage genome. While small targets might still self-assemble by using the full phage genome, excess scaffold that is not part of the object is likely to interfere with the folding and posterior functionalization or lead to non-specific aggregation [7]. Additionally, this method is not selective enough to be used with other production approaches.

Pound *et al.* separated the amplicon strands via streptavidin-coated magnetic beads. In this case, PCR is performed using phage DNA as template and a biotinylated 3’ primer. After purification of the PCR product, binding to streptavidin-coated magnetic beads is promoted

and the bead-bound DNA product is denatured in diluted sodium hydroxide. Following bead separation, the desired ssDNA, which is found in the supernatant, is purified with a commercial kit or by ethanol precipitation, yielding 1.2 pmol of scaffold per 100 µL reaction for a 2958 bp PCR product [28]. Apart from the low yield, the main disadvantages are the cost of biotinylated primers and of streptavidin-coated magnetic beads, which cannot be re-used.

With this work we aim to develop an alternative purification method to obtain ssDNA scaffolds with high yield and high quality that can overcome the hurdles of established methods. More specifically, we describe a scalable, rapid, cost-efficient, reproducible, and versatile affinity-based method that uses magnetic oligo beads as the solid phase, that can virtually be applied to any DNA sequences/structures. Affinity separation is a well-known method, routinely used in the separation of biomolecules such as antibodies [29, 30], AAV virus [30], and more recently, mRNA [31]. In this case, primer sequences that hybridized with ssDNA are immobilized in the magnetic beads, which are used to capture the ssDNA scaffolds. Magnetic separation is already established for a number of processes that include separation of nucleic acids, such as hybridization assays [32–35], isolation of specific DNA and mRNA molecules from cells [36–38], and recovery of viral mRNA genome [39, 40]. However, to the best of our knowledge have not been used in the context of DNA scaffold isolation. Herein, magnetic beads modified with short oligonucleotides complementary to the 3’ end of the target scaffolds were used to isolate 449-nt and 1000-nt ssDNA from aPCR reaction mixtures. Table III.1 summarizes the advantages of disadvantages of the proposed purification method compared to what is reported in the literature.

Table III.1. Comparison between the proposed purification method and others reported in the literature.

Purification method	Advantages	Disadvantages	Reference
PEG and ethanol precipitation	• Well established method • High yields • Suitable for all production methods	• Limited to large scaffolds that are not suitable for smaller structures • Non-selective	[19-21]
Streptavidin-coated magnetic beads	• Fast • Specific	• Cost of biotinylated primers and streptavidin-coated magnetic beads that cannot be re-used • Not suitable for all production methods	[28]
Agarose gel extraction	• Affordable • Selective • Well established method • Suitable for all production methods	• Low yield • Not scalable • User-dependent • Agarose residues can co-purify • Intercalating dyes on the scaffold	[7]
Carboxyl-modified magnetic beads	• Fast • Specific • Scalable • Re-usable • Suitable for all production methods	• Primer design • Cost of magnetic beads and modified primers	-

The recovered ssDNA was further used to assemble tetrahedrons by an origami folding strategy with appropriate staples to yield nanostructures with 31 and 63-bp edge length. Overall, a simple and robust method suitable for the purification of ssDNA scaffolds intended for the DNA-origami assembly of nanostructures was conceived.

III.2. Materials and Methods

III.2.1. Materials

Sera-Mag SpeedBead carboxylate-modified magnetic particles (hydrophobic) were obtained from GE Healthcare (Uppsala, Sweden). All salts used were of analytical grade. The producer *E. coli* strain K12 ER2738 and M13mp18 RF I DNA were from New England Biolabs (Massachusetts, USA) and Accustart™ Taq DNA Polymerase HiFi was from Quantabio (Massachusetts, USA). Primers, oligonucleotides, and staple sequences were from Stab Vida (Caparica, Portugal).

III.2.2. M13mp18 genomic DNA production and purification

E. coli K12 ER2738 were transformed with M13mp18 RF I DNA (GenBank: X02513.1) according to manufacturer's protocol [41]. After transformation, a blue plaque was selected, and phage expansion was performed by infecting a pre-culture of *E. coli* at an optical density of 0.5 in 5 mL LB medium supplemented with tetracycline (10 μg/mL). After 2 h at 37 °C, 250 rpm, the culture was transferred to 500 mL of LB medium supplemented with tetracycline and incubated overnight. Following this phage expansion step, the cells were centrifuged for 10 min at 3,200 g and the supernatant was mixed with 4 % PEG-8000/3 % NaCl for 10 min at 37 °C, 250 rpm, and then placed on ice for 45 min to precipitate the phages. After centrifugation (20 min, 8,100 g), phages were resuspended in storage buffer (1 % BSA, 15 % glycerol and 1× PBS), centrifuged (5 min, 8,100 g) to remove remaining debris and filtered through a 0.22 μm syringe filter. This master stock of M13mp18 phages was used as a starting material for the extraction of genomic ssDNA. The extraction was performed according to [42] after a new precipitation step of 1 mL of the master phage stock with 4 % PEG-8000/3 % NaCl for 30 min at room temperature to change from the storage buffer to TE (10 mM Tris-HCl, 1 mM EDTA, pH 8.5).

III.2.3. Single stranded DNA scaffold generation by asymmetric PCR

The target 449 nt and 1000 nt scaffolds (see sequences in Supplementary Material) were synthesized by aPCR according to [7, 27]. Briefly, a forward primer concentration of 1 μM

(GTCGTCGTCCCCTCAAACT for 449 nt and GTCTCGCTGGTGAAAAGAAA for 1000 nt), a reverse primer concentration of 20 nM (ATTAATGCCGGAGAGGGTAG), 30 ng of phage genomic ssDNA template, 200 mM deoxynucleotide triphosphates (dNTPs) and 1 unit of Accustart Taq DNA polymerase were mixed in a final volume of 50 μL. The aPCR program included a 1 min step at 94 °C for initial denaturation, followed by 30 cycles of 94 °C at 20 s; 55 °C at 30 s; 68 °C at 90 s per kilobase of amplification target. PCR products were cleaned-up from excess of primers, oligonucleotides and enzyme using a QIAquick PCR Purification Kit (Qiagen), with TE as the final buffer.

III.2.4. Functionalization of magnetic beads

One mg of Sera-Mag SpeedBead carboxylate-modified magnetic particles (hydrophobic) (20 μL) was mixed with 5 μL 0.5 M MES, pH 5.5, filled with 25 μL of MilliQ water up to a volume of 50 μL and equilibrated at 37 °C. Next, 4 nmol of a 20-nt oligonucleotide complementary to the 3' terminal of the 449 and 1000 nt-long ssDNA scaffolds (ATTAATGCCGGAGAGGGTAG) and modified with an amine in the 5' terminal (40 μL) was added to the magnetic bead mixture. Functionalization was then promoted by adding 10 μL of 10 % (w/v) 1-ethyl-3-(3-dimethylaminopropyl)carbodiimide hydrochloride (EDC) in water, prepared immediately before use to avoid degradation [43]. The mixture was then placed in a lab shaker overnight at 37 °C. Finally, the magnetic beads were washed three times with PBS in order to remove unbound oligonucleotide strands.

III. 2.5. Functionalization assessment and characterization

The surface charge of the magnetic nanoparticles before and after modification was measured to monitor the oligonucleotide functionalization, the binding of complementary targets and reuse. The particles were suspended in the appropriate buffer (100 μg in 1 mL) and measured using a Zetasizer Nanoseries from Malvern Instruments. The buffers used were 10 mM citrate buffer for pH3, 10 mM acetate buffer for pH 4 and 5, 10 mM MES for pH 6 and 10 mM Tris-HCl for pH 7, 8 and 9.

To confirm and determine the degree of functionalization of the magnetic beads, hybridization with 1 μM of a fully complementary oligonucleotide sequence modified with a fluorescein molecule at the 5' terminal was promoted for 5 min at 65 °C in 1x SSC (150 mM NaCl, 15 mM trisodium citrate, pH 7) hybridization buffer. After separation from solution using a standard magnet, the magnetic beads were re-suspended in 100 μL of TE buffer and heated to 80 °C for 2 min to denature the hybridized oligonucleotides. Supernatant samples collected before and after thermal denaturation were analyzed in a Cary Eclipse Fluorescence Spectrophotometer (Agilent) against a calibration curve prepared with standards of the modified oligonucleotide with concentrations ranging between 0.125 and 1 μM. The binding capacity of the functionalized magnetic beads was (2.8 ± 0.5) x 10^{-5} μmol/mg.

III.2.6. Affinity-based single stranded DNA purification

To disrupt secondary structures, samples obtained after clean-up of an aPCR reaction mixture (~50 μL) were heated to 65 °C for 2 min and immediately placed on ice prior to use. 100 μg of functionalized magnetic beads (*see* Supplementary Material S3) were washed and equilibrated with binding buffer (20 mM Tris-HCl, pH 7.5, 1 M LiCl, 2 mM EDTA). The volume of cleaned-up aPCR reaction was adjusted to 100 μL with TE buffer and an equal volume of binding buffer was added to the beads. Hybridization between the nanoparticles (NPs) and the ssDNA was promoted by incubating the 200 μL mixture on a shaker for 5 min at room temperature. Then, magnetic particles were sorted from solution using a standard magnet and the supernatant containing the products that did not hybridize was removed. To eliminate un-specifically bound products, beads were washed twice with 200 μL of washing buffer (10 mM Tris-HCl, pH 7.5, 150 mM LiCl, 2 mM EDTA). Elution of ssDNA scaffolds from the magnetic beads was performed by addition of 50 μL of TE buffer, incubation at 80 °C for 2 min and magnetic separation. The concentration of the eluted DNA was measured by UV spectroscopy using a NanoDrop instrument (ThermoFischer).

III.2.7. Design, folding and purification of DNA-origami objects

Design of staple strands required to fold 31-bp and 63-bp edge length tetrahedrons (see Supplementary material S4) was performed with the DAEDALUS software [7] by inputting the sequences of the 449-nt and 1000-nt ssDNA scaffolds, respectively. DNA-origami assembly and purification was performed using the methods described in [7, 28] with minor adaptions. Briefly, 5 to 40 nM of scaffold strand was mixed with 40 nM of a mix of staple strands in 50 μL of Tris-acetate EDTA-$MgCl_2$ buffer (40 mM Tris, 20 mM acetic acid, 2 mM EDTA, 12 mM MgCl2, pH 8). Annealing was performed in a thermal cycler according to the following sequence: 95 °C for 5 min, cooling from 80 to 75 °C at 1 °C per 5 min, cooling from 75 to 30 °C at 1 °C per 15 min and cooling from 30 to 25 °C at 1 °C per 10 min. Tetrahedron-containing solutions were purified with an Amicon Ultra-0.5 mL centrifugal filter with a molecular weight cut-off of 100 kDa by diafiltrating 5 times with 5 mM Mg^{2+} buffer to remove excess of staple strands.

III.2.8. Gel electrophoresis

Agarose gels for scaffold purification assessment were prepared with 1% (w/v) agarose (Fisher Scientific, Waltham, MA, US) in TAE buffer (40 mM Tris base, 20 mM acetic acid and 1 mM EDTA, pH 8). Gels were loaded with samples pre-mixed with a 6× loading buffer (40% (w/v) sucrose). NZYDNA ladder III (NZYTech, Lisbon, Portugal) was used as a molecular weight marker. Electrophoresis was performed in TAE buffer at 100 V for 60 minutes. Gels were stained in a 1× SYBR Safe (Thermo Fisher Scientific, Massachusetts, USA) and images were obtained with a TruBlu™ blue light transilluminator (Edvotek). For densitometry analysis, gels were imaged with a Axygen Gel Documentation System (Axygen, Inc, Union City, USA) and the intensity of the bands was analysed using ImageJ.

For DNA-origami analysis, gels were prepared with 2% (w/v) agarose (Fisher Scientific, Waltham, MA, US) in 0.5x TBE buffer (44.5 mM Tris-borate, 1 mM EDTA, pH 8.3) and 5.5 mM $MgCl_2$. Gels were loaded with samples pre-mixed with a 6× loading buffer (40% (w/v) sucrose). NZYDNA ladder III (NZYTech, Lisbon, Portugal) was used as a molecular weight marker. Electrophoresis was performed in 0.5x TBE buffer and 5.5 mM $MgCl_2$ at 90 V for 120 minutes. Gels were pre-stained with ethidium bromide (Thermo Fisher Scientific, Massachusetts, USA)

and images were obtained with a Axygen Gel Documentation System (Axygen, Inc, Union City, USA).

III.2.9. Fluorescence Correlation Spectroscopy

FCS measurements were performed on a Microtime 200 setup from PicoQuant GmbH (Germany). The excitation source used was a pulsed diode laser emitting at 482 nm with a repetition rate of 20 MHz (LDH-P-C-485, PicoQuant GmbH). The laser beam was focused 10 μm inside the sample by means of a water immersion objective of N.A. 1.2 (UPlanSApo 60×, Olympus). Fluorescence emission was collected by the same objective and cleaned by a dichroic filter (485DRLP, Omega) and by a bandpass filter with transmission range between ca. 528 and 562 nm (545AF35, Omega). Out-of-focus light was rejected by means of a 50 μm pinhole. The collected emission was detected by single-photon avalanche diode detectors (SPCM-AQR-13, Perkin Elmer). Data acquisition and preliminary analysis were performed on SymPhoTime software (PicoQuant GmbH). The tetrahedron nanostructures were singly labelled with a fluorescein dye (FAM) for the FCS measurements.

III.3. Results and Discussion

III.3.1. Conceptual design of method

Synthesis of ssDNA scaffolds by aPCR is accompanied by generation of dsDNA fragments formed by hybrids of the scaffold and of its complementary strand. In the context of DNA-origami production, these dsDNA fragments must be removed alongside with unused primers, template DNA and polymerase to prevent interference during the subsequent assembling of nanostructures. As discussed previously, this separation is often performed by agarose gel electrophoresis followed by band excision and gel extraction. Despite being highly adopted, gel electrophoresis is cumbersome and relatively inefficient. Here we present an alternative ssDNA scaffold purification method that relies on affinity-based magnetic particles (Figure III.1). The underlying concept is to specifically fish the target scaffold (ssDNA) strands from the aPCR mixture by using beads modified with complementary short oligonucleotides, while leaving the dsDNA fragments in solution. Following magnetic separation of the solid phase

from the impurity-containing solution, beads are re-suspended in buffer and subjected to a temperature increase to melt the scaffold-ligand hybrids. The solution with purified scaffolds is then recovered via magnetic separation (Figure III.1).

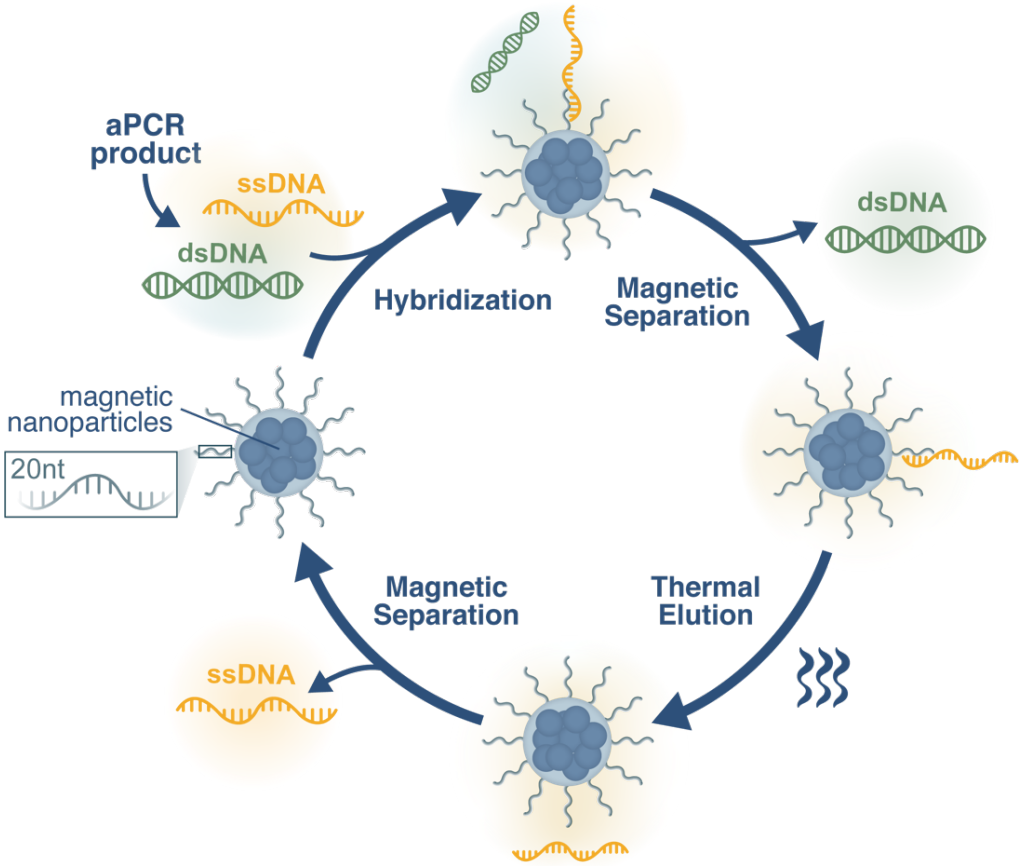

Figure III.1. Schematic representation of the method used to purify ssDNA scaffolds from aPCR mixtures. Affinity magnetic nanoparticles are added to the aPCR reaction mixture to selectively fish out ssDNA scaffolds from the solution via hybridization of an immobilized 20-nt ligand and the 3' end of scaffolds. The scaffold-loaded nanoparticles are separated from the solution that contains unbound dsDNA impurities by magnetic separation. Bound scaffolds are thermally eluted and recovered after removing nanoparticles by magnetic separation.

III.3.2. Magnetic bead functionalization

A 20-nt long oligonucleotide that is complementary to the 3' end of the two target ssDNA scaffolds tested in this study (see supplementary data) was immobilized to the Sera-Mag SpeedBead Carboxylate-modified superparamagnetic particles through the formation of an amide bond. The particles contain two layers of magnetite encapsulated in a polymer and

display irregular shapes with sizes of the order of 1 μm, as seen by scanning electron microscopy (Figure III.2).

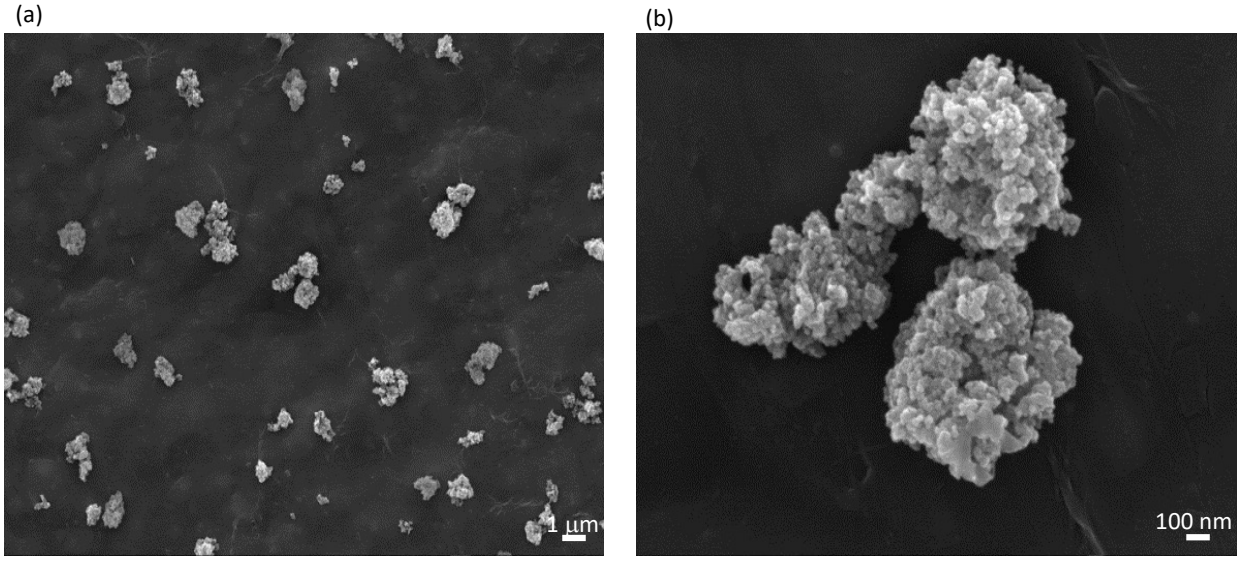

Figure III.2. SEM analysis of Sera-Mag SpeedBead Carboxylate-modified magnetic particles functionalized with a 20-nt oligonucleotide. Scale bar is 1 μm for the left image and 100 nm for the right image.

Zeta potential measurements is often used in materials characterization since it provides a pH-dependent tool to quickly assess the surface charge of particles in a non-destructive fashion during functionalization and immobilization steps [44]. Herein, the technique was used to probe surface charge of the magnetic beads before and after DNA loading over a pH range from 3 to 9. Analyzing Figure III.3 it is possible to observe that, for pH values of 5 and above, there is no expressive difference across the surface. This is due to the fact that under these conditions the DNA and the functional groups present in the NPs surface contribute negatively to the overall charge, therefore making the differences less expressive. Notwithstanding, under acidic conditions (pH 3 and 4), the zeta potential of the bare (unfunctionalized) beads displayed an overall positive charge of 20 and 11.0 ± 4.1 mV (Figure 3, blue bars), respectively. Despite the negative or utmost neutral nature of the carboxyl groups used to immobilize the DNA probe, the positive charge can be conferred by the presence of other functional groups present in the coating (e.g., amines). This was not confirmed since the exact composition of the magnetic nanoparticles was not disclosed by the manufacturer. After immobilization of the 20-nts strand DNA probe, a decrease of the overall charge to 11.7 ± 0.6 (pH 3) and 5.1 ± 2.3 mV (pH 4) was observed. This corroborates the immobilization of the fishing probe strands onto the nanoparticles surface due to the

contribution of the negative charges from the phosphate backbone of DNA. Furthermore, when target ssDNA sequences with 449 and 1000-nt were introduced an extra decrease of the overall surface charge was observed, which indicates that additional DNA strands are binding to the surface of the magnetic nanoparticles. Therefore, the zeta surface results concur with a successful immobilization of the ssDNA fishing probe and hybridization with the target scaffolds.

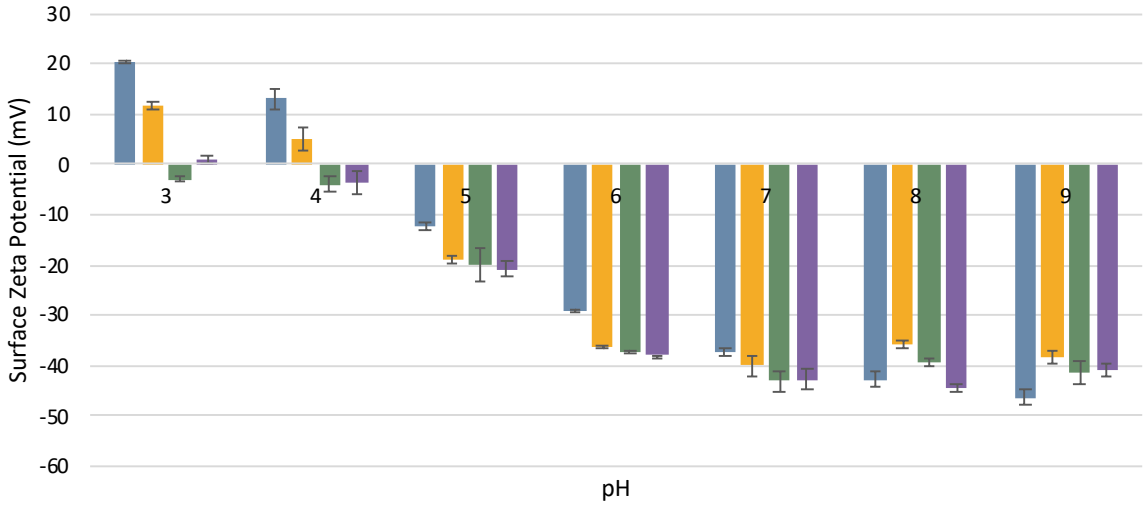

Figure III.3. Capture of ssDNA scaffolds via hybridization with magnetic particles functionalized with oligonucleotides. Sera-Mag particles were functionalized with 20-nt long oligonucleotides and subsequently used to capture 449-nt and 1000-nt ssDNA scaffolds. The pH influence on zeta potential was evaluated with the appropriate buffers. Blue bars- non-functionalized magnetic particles; yellow bars- particles functionalized with a 20-nt oligonucleotide; green and purple bars - magnetic particles after hybridization with the 449 and the 1000-nt scaffold, respectively.

To estimate the DNA binding capacity of the functionalized magnetic particles, hybridization with a fully complementary fluorescein-modified oligonucleotide was promoted (see Materials and Methods section). The binding capacity was equal to (2.8 ± 0.5) x 10^{-5} μmol/mg, a figure that can be translated into a maximum ability to capture 3.8 ± 0.7 μg/mg and 8.5 ± 1.6 μg/mg of the 449 and 1000 nt-long ssDNA scaffolds, respectively.

III.3.3. Single-stranded DNA scaffold purification

Purified genomic ssDNA of the M13mp18 phage was used as a template for the aPCR synthesis of the 449-nt and 1000-nt ssDNA scaffolds (see sequences in Supplementary Material) that are required to assemble tetrahedra with 31 and 63-bp edge length,

respectively (Figure III.4b). The sequence of the shorter scaffold matches entirely with the final 449 nucleotides of the 1000-nt scaffold, as shown in Figure III.4a.

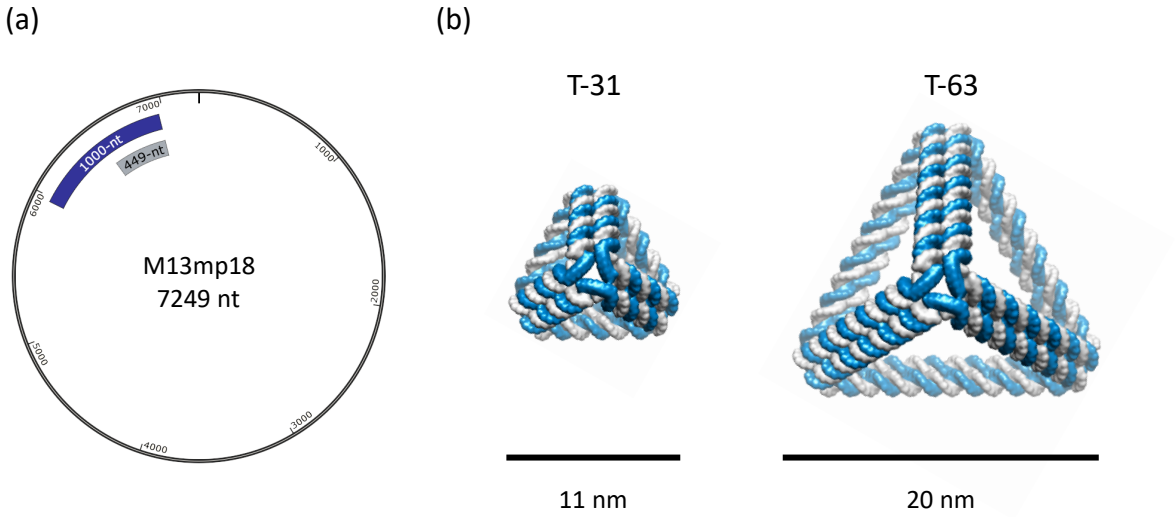

Figure III.4. (a) Schematic representation of the 449 and 1000-nt scaffolds position on the M13mp18 genome. (b) Atomic models of the folded 31 (T-31) and 63-bp (T-63) edge length tetrahedra.

The resulting PCR mixtures were pre-purified with a commercial kit to remove excess of primers and thus prevent unspecific hybridization with the magnetic beads in subsequent steps. At this stage, the mixtures contain essentially the ssDNA scaffolds and dsDNA impurities, as can be judged by the agarose gel electrophoresis analysis shown in Figure III.5. The SYBR dye when excited with blue light illumination (497 nm) enabled DNA fragments visualization in the gel making it possible to discern between ssDNA (orange band) and dsDNA (green band). Orange and green bands are clearly observable in the case of the 449-nt scaffold (lane F of the gel in Figure III.5a). In this specific case, the ssDNA band migrated less than the dsDNA, probably due to formation of secondary structures. In the case of the larger 1000-nt scaffold, discrimination between ssDNA and dsDNA was not possible, with evidence showing that under the electrophoresis conditions used the two fragments co-migrate as a single green band (lane F of the gel in Figure III.5b). In this case, a fast-migrating band is also seen, which probably corresponds to products of incomplete amplification.

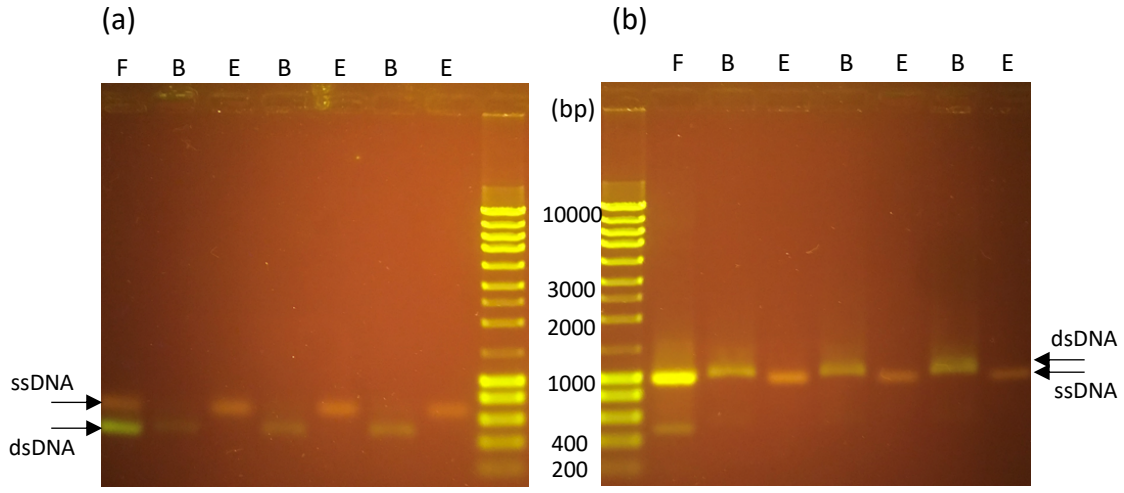

Figure III.5. Agarose gel electrophoresis analysis of the purification of 449-nt (a) and 1000-nt (b) ssDNA scaffolds from aPCR mixtures using magnetic beads. Lane F corresponds to the pre-purified aPCR product. Hybridization between magnetic beads and aPCR products was promoted and, after magnetic separation, the solution with unbound dsDNA was recovered (lanes B). After washing and resuspending the beads in a buffer, the solution was heated to denaturing temperatures, followed by magnetic separation. Eluted ssDNA scaffolds were collected in the supernatant and analyzed (lanes E). The same beads were used three times in each case to assess reusability of the system.

The pre-purified aPCR products containing ssDNA and dsDNA were then mixed with the functionalized magnetic beads (100 µg per 50 µL aPCR mix) and hybridization between the ssDNA and the 20-nt immobilized ligand was promoted. The hybridized ssDNA-beads were magnetically separated from the solution containing unbound products. An analysis of the separated solution shows that dsDNA was isolated from ssDNA, as can be observed by the presence of a single green band in lanes B of the gel corresponding to the 449-nt fragment (Figure III.5a). In the case of the 1000-nt fragment, the solution separated from the beads also contains a single green band of dsDNA (see lanes B in Figure III.5b).

To elute the bound scaffolds, the magnetic beads were heated to 80 °C, a temperature that is higher than the melting temperature of the hybrid (57 C°). After removing beads by magnetic separation, the solution containing ssDNA was analyzed by gel electrophoresis. Results clearly showed the presence of single orange bands corresponding to the ssDNA scaffolds (lanes E in Figure 5a and 5b). DNA quantitation in the recovered solutions indicated a recovery of 550 ± 160 ng (4.0 ± 1.1 pmol) and 890 ± 220 ng (2.9 ± 0.7 pmol) per 50 µL aPCR reaction for the 449-nt and 1000-nt scaffolds, respectively. Densitometry analysis of five independent purification runs revealed an ssDNA yield of 92± 3 % and 89 ± 5 % of the 449-nt and 1000-nt scaffolds, respectively. No dsDNA was detected by this method in any of the runs analyzed.

Purification was also performed using the standard agarose gel extraction procedure, which resulted in recoveries of 424 ± 40 ng and 552 ± 75 ng per 50 µL aPCR reaction for the 449-nt and 1000-nt scaffolds, respectively. Veneziano *et al.* obtained a slightly larger amount of 695 ± 35 ng when using gel extraction to purify an equivalent 1000 nt scaffold fragment from a 50 µL aPCR mixture [19]. This difference might be justified by the operator-dependence of this type of procedure. Overall, the amount of recovered ssDNA obtained with the magnetic bead hybridization method was higher for both scaffolds.

The data in Figure 5 further shows that the beads can be re-used for at least three times without losing ssDNA binding capacity. This indicates that the oligonucleotide ligand is not sensitive to thermal degradation under the tested conditions. Preliminary experiments show that significant loss of recovery yield (30%) occurs only from the 8^{th} reutilization on (results not shown). This can be explained by the loss of beads during the washing steps, since no ssDNA is observed in the unbound fraction.

Furthermore, we confirmed that the same ligand could be used to purify ssDNA scaffolds with different lengths because they shared the same 20 nt at the 3' terminal (Figure 5). Purification experiments were also conducted using amounts of beads per 50 µL of aPCR other than 100 µg, in the range 10-400 µg. The results show that yields decrease with amounts lower than 100 µg or stabilize/decrease with amounts higher than 100 µg (see Supplementary Material III.S3).

III.3.4. Assembly of DNA-origami nanostructures

The purified 449-nt and 1000-nt ssDNA chains were used as scaffolds to assemble 31-bp and 63-bp edge length tetrahedra, respectively. The target 3D tetrahedron geometry was rendered as a scaffolded DNA-origami nanoparticle by the software DAEDALUS using the sequences of the 449-nt and 1000-nt ssDNA scaffolds as an input [7]. Staples sequences (*see* Supplementary material) and atomic models (Figure III.4b) were obtained as an output. Folding of the scaffolds into the desired nanostructures was promoted under high magnesium concentration using a slow temperature decrease ramp. Following assembly, ultracentrifugation with a centrifugal filter with a molecular cut-off of 100 kDa was used to remove excess staple strands and concentrate the nano-objects. Agarose gel electrophoresis

analysis (Figure III.6a) of the solutions obtained after folding no longer shows the presence of original scaffold band. Instead, a newer, sharp band is found that migrated less than the ssDNA scaffold. This result is consistent with a good overall folding quality [7]. Furthermore, the analysis indicates that excess staple strands were successfully removed.

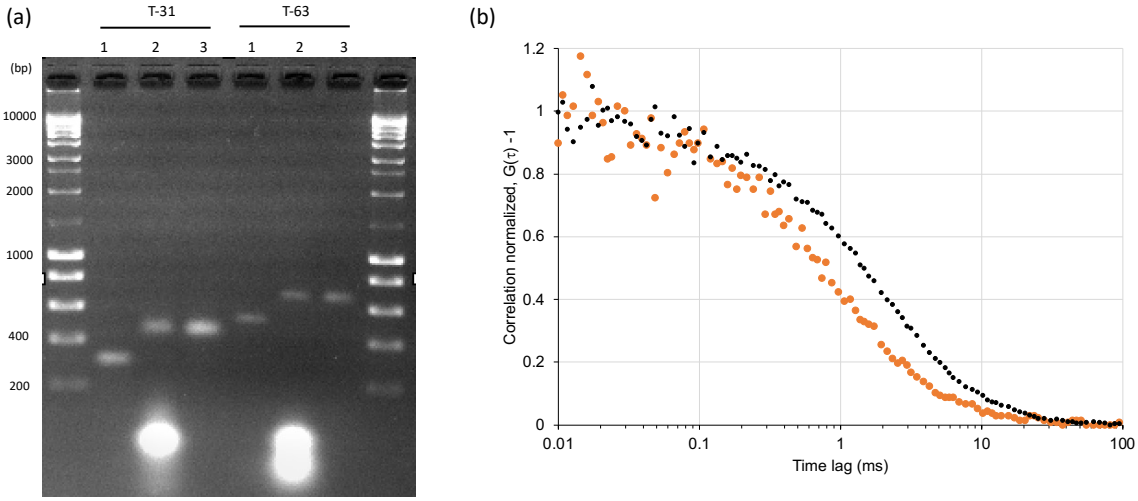

Figure III.6. Folding of DNA-origami nanostructures. The purified 449-nt and 1000-nt ssDNA scaffolds were used to fold 31-bp (T-31) and 63-bp (T-63) edge length tetrahedra under high magnesium concentrations. The folding products were purified by ultracentrifugation with a 100-kDa molecular weight cut-off filter and five times diafiltered with 5 mM Mg2+ buffer to remove excess staple strands. (a) Agarose gel electrophoresis analysis. Legend: lane 1 – purified ssDNA scaffolds; lane 2- solutions obtained after folding; lane 3- solutions obtained after folding and staple removal. (b) Fluorescence correlation spectroscopy analysis of the T-31 (orange dots) and T-63 (black dots) tetrahedron in aqueous medium.

Furthermore, the purified tetrahedra were characterized by fluorescence correlation spectroscopy (FCS). The diffusion coefficients obtained for the 31-bp and 63-bp edge length tetrahedron in aqueous medium were equal to 56 and 27 $\mu m^2\ s^{-1}$, respectively. These coefficients correspond to hydrodynamic diameters of around 8.8 and 18.4 nm, which are consistent with the simulated dimensions of the DNA-origami nanostructures (Figure III.4).

III.4. Conclusion

DNA-origami technology has spurred a growing interest over the past few years. Nevertheless, current techniques used to produce ssDNA scaffolds are cumbersome and most of the times not compatible with pharmaceutical or analytical applications. In particular, they often rely on agarose gel electrophoresis extraction for scaffold purification, a methodology that is laborious, not scalable, requires specialized equipment and personnel and yields scaffolds

with agarose gel residues. In this work, a process based on complementary oligonucleotide probes attached to magnetic beads was developed that allows the isolation of ssDNA scaffolds from asymmetric PCR mixtures. To do so, a 20-nt oligo was coupled to carboxylate-modified magnetic beads allowing the hybridization between the beads and 449 and 1000-nt ssDNA scaffolds generated by aPCR. Following bead separation and elution, 550 ± 160 ng of 449-nt ssDNA and 890 ± 220 ng of 1000-nt ssDNA, virtually free from dsDNA contaminants, could be recovered per 50 µL aPCR reaction. Additionally, this method showed better results than the established agarose gel purification method. The purification process was complete in less than 1 hour, which is substantially less than the 3 hours required using the standard agarose gel electrophoresis extraction. Furthermore, the beads were re-used without loss of binding capacity for at least three cycles. Lastly, beads modified with a given probe, as shown here, can be used to purify ssDNA scaffolds with different lengths as long as they share the same 3' region. Purification of other scaffolds will require coupling different probes to the beads.

Overall, the ssDNA scaffold purification strategy proposed is versatile and overcomes the limitations of agarose gel electrophoresis separation and extraction, as it deliver a highly purified product, it can be applied to virtually any known scaffold sequence, and to any production scale.

III.5. References

[1] N. C. Seeman and P. S. Lukeman, "Bottom up control of Geometry on the Nanoscale," *Rep. Prog. Phys.*, vol. 68, no. 1, pp. 237–270, 2005.

[2] P. W. K. Rothemund, "Folding DNA to create nanoscale shapes and patterns," *Nature*, vol. 440, no. 7082, pp. 297–302, 2006.

[3] F. Zhang, J. Nangreave, Y. Liu, and H. Yan, "Structural DNA nanotechnology: State of the art and future perspective," *J. Am. Chem. Soc.*, vol. 136, no. 32, pp. 11198–11211, 2014.

[4] A. Chworos *et al.*, "Building programmable jigsaw puzzles with RNA," *Science*, vol. 306, no. 5704, pp. 2068–2072, 2004.

[5] J. Chen and N. C. Seeman, "Synthesis from DNA of a molecule with the connectivity of a cube," *Nature*, vol. 354, pp. 56–58, 1991.

[6] W. M. Shih, J. D. Quispe, and G. F. Joyce, "A 1.7-kilobase single-stranded DNA that folds into a nanoscale octahedron," *Nature*, vol. 427, no. 6975, pp. 618–621, 2004.

[7] R. Veneziano *et al.*, "Designer nanoscale DNA assemblies programmed from the top down," *Science*, vol. 352, no. 6293, 2016.

[8] S. M. Douglas, A. H. Marblestone, S. Teerapittayanon, A. Vazquez, G. M. Church, and W. M. Shih, "Rapid prototyping of 3D DNA-origami shapes with caDNAno," *Nucleic*

Acids Res., vol. 37, no. 15, pp. 5001–5006, 2009.

[9] C. E. Castro *et al.*, "A primer to scaffolded DNA-origami," *Nat. Methods*, vol. 8, no. 3, pp. 221–229, 2011.

[10] P. Ketterer, E. M. Willner, and H. Dietz, "Life Sciences: Nanoscale rotary apparatus formed from tight-fitting 3D DNA components," *Sci. Adv.*, vol. 2, no. 2, pp. 1–9, 2016.

[11] A. B. Farimani, P. Dibaeinia, and N. R. Aluru, "DNA-origami-graphene hybrid nanopore for DNA detection," *ACS Appl. Mater. Interfaces*, vol. 9, no. 1, pp. 92–100, 2017.

[12] S. M. Douglas, I. Bachelet, and G. M. Church, "A Logic-Gated Nanorobot for Targeted Transport of Molecular Payloads," *Science*, vol. 335, no. February, pp. 831–834, 2012.

[13] J. Yan, C. Hu, X. Liu, J. Zhong, G. Sun, and D. He, "Recent Developments of New DNA-origami Nanostructures for Drug Delivery," *Curr. Pharm. Des.*, vol. 21, no. 22, pp. 3181–3190, 2015.

[14] H. Pei *et al.*, "A DNA nanostructure-based biomolecular probe carrier platform for electrochemical biosensing," *Adv. Mater.*, vol. 22, no. 42, pp. 4754–4758, 2010.

[15] B. Zhang *et al.*, "DNA-origami as Seeds for Promoting Protein Crystallization," *ACS Appl. Mater. Interfaces*, vol. 10, no. 51, pp. 44240–44246, 2018.

[16] Y. Amir, E. Ben-Ishay, D. Levner, S. Ittah, A. Abu-Horowitz, and I. Bachelet, "Universal computing by DNA-origami robots in a living animal," *Nat. Nanotechnol.*, vol. 9, no. 5, pp. 353–357, 2014.

[17] H. T. Maune *et al.*, "Self-assembly of carbon nanotubes into two-dimensional geometries using DNA-origami templates," *Nat. Nanotechnol.*, vol. 5, no. 1, pp. 61–66, 2010.

[18] E. M. Roller, L. K. Khorashad, M. Fedoruk, R. Schreiber, A. O. Govorov, and T. Liedl, "DNA-assembled nanoparticle rings exhibit electric and magnetic resonances at visible frequencies," *Nano Lett.*, vol. 15, no. 2, pp. 1368–1373, 2015.

[19] S. M. Douglas, H. Dietz, T. Liedl, B. Högberg, F. Graf, and W. M. Shih, "Self-assembly of DNA into nanoscale three-dimensional shapes," *Nature*, vol. 459, no. 7245, pp. 414–418, 2009.

[20] B. Kick, F. Praetorius, H. Dietz, and D. Weuster-Botz, "Efficient Production of Single-Stranded Phage DNA as Scaffolds for DNA-origami," *Nano Lett.*, vol. 15, no. 7, pp. 4672–4676, 2015.

[21] A. N. Marchi, I. Saaem, B. N. Vogen, S. Brown, and T. H. Labean, "Toward larger DNA-origami," *Nano Lett.*, vol. 14, no. 10, pp. 5740–5747, 2014.

[22] E. Stahl, T. G. Martin, F. Praetorius, and H. Dietz, "Facile and scalable preparation of pure and dense DNA-origami solutions," *Angew. Chemie - Int. Ed.*, vol. 53, no. 47, pp. 12735–12740, 2014.

[23] M. Erkelenz *et al.*, "A facile method for preparation of tailored scaffolds for DNA-origami," *Small*, vol. 10, no. 1, pp. 73–77, 2014.

[24] H. Said, V. Schuller, F. J. Eber, C. Wege, T. Liedl, and C. Richert, "M1.3 - A Small Scaffold for DNA-origami Full," *Nanoscale*, vol. 5, no. 1, pp. 284–290, 2013.

[25] H. Zhang, J. Chao, D. Pan, H. Liu, Q. Huang, and C. Fan, "Folding super-sized DNA-origami with scaffold strands from long-range PCR," *Chem. Commun.*, vol. 48, no. 51, pp. 6405–6407, 2012.

[26] R. Veneziano, T. R. Shepherd, S. Ratanalert, L. Bellou, C. Tao, and M. Bathe, "In vitro synthesis of gene-length single-stranded DNA," *Sci. Rep.*, vol. 8, no. 1, pp. 1–7, 2018.

[27] K. F. Wagenbauer *et al.*, "How We Make DNA-origami," *ChemBioChem*, vol. 18, no. 19,

pp. 1873–1885, 2017.

[28] E. Pound, J. R. Ashton, H. A. Becerril, and A. T. Woolley, “Polymerase chain reaction based scaffold preparation for the production of thin, branched DNA-origami nanostructures of arbitrary sizes,” *Nano Lett.*, vol. 9, no. 12, pp. 4302–4305, 2009.

[29] P. Füglistaller, “Comparison of immunoglobulin binding capacities and ligand leakage using eight different protein A affinity chromatography matrices,” *J. Immunol. Methods*, vol. 124, no. 2, pp. 171–177, 1989.

[30] W. Chu *et al.*, “Peptides and pseudopeptide ligands: a powerful toolbox for the affinity purification of current and next-generation biotherapeutics,” *J. Chromatogr. A*, vol. 1635, p. 461632, 2021.

[31] S. Bancel, W. J. Issa, J. G. Aunins, and T. Chakraborty, “Manufacturing methods for production of RNA transcripts.” Google Patents, 27-Nov-2018.

[32] H. Li and Z. He, “Magnetic bead-based DNA hybridization assay with chemiluminescence and chemiluminescent imaging detection,” *Analyst*, vol. 134, no. 4, pp. 800–804, 2009.

[33] S. A. M. Martins, D. M. F. Prazeres, L. P. Fonseca, and G. A. Monteiro, “Application of central composite design for DNA hybridization onto magnetic microparticles,” *Anal. Biochem.*, vol. 391, no. 1, pp. 17–23, 2009.

[34] J. M. Nam, S. I. Stoeva, and C. A. Mirkin, “Bio-Bar-Code-Based DNA Detection with PCR-like Sensitivity,” *J. Am. Chem. Soc.*, vol. 126, no. 19, pp. 5932–5933, 2004.

[35] S. Dubus, J. F. Gravel, B. Le Drogoff, P. Nobert, T. Veres, and D. Boudreau, “PCR-free DNA detection using a magnetic bead-supported polymeric transducer and microelectromagnetic traps,” *Anal. Chem.*, vol. 78, no. 13, pp. 4457–4464, 2006.

[36] B. I. Haukanes and C. Kvam, “Application of magnetic beads in bioassays,” *Bio/Technology*, vol. 11, no. 1, pp. 60–63, 1993.

[37] M. R. Green and J. Sambrook, “Isolation of poly(A)+ messenger RNA using magnetic oligo(dT) beads,” *Cold Spring Harb. Protoc.*, vol. 2019, no. 10, pp. 711–714, 2019.

[38] N. M. Adams, H. Bordelon, K. K. A. Wang, L. E. Albert, D. W. Wright, and F. R. Haselton, “Comparison of three magnetic bead surface functionalities for RNA extraction and detection,” *ACS Appl. Mater. Interfaces*, vol. 7, no. 11, pp. 6062–6069, 2015.

[39] L. Fabiani *et al.*, “Magnetic beads combined with carbon black-based screen-printed electrodes for COVID-19: A reliable and miniaturized electrochemical immunosensor for SARS-CoV-2 detection in saliva,” *Biosens. Bioelectron.*, vol. 171, no. October 2020, 2021.

[40] L. F. Huergo *et al.*, “Magnetic Bead-Based Immunoassay Allows Rapid, Inexpensive, and Quantitative Detection of Human SARS-CoV-2 Antibodies,” *ACS Sensors*, vol. 6, no. 3, pp. 703–708, 2021.

[41] N. E. Biolabs, “M13mp18 RF I DNA.” [Online]. Available: https://www.neb.com/products/n4018-m13mp18-rf-i-dna#Product Information.

[42] B. Kick, S. Hensler, F. Praetorius, H. Dietz, and D. Weuster-Botz, “Specific growth rate and multiplicity of infection affect high-cell-density fermentation with bacteriophage M13 for ssDNA production,” *Biotechnol. Bioeng.*, vol. 114, no. 4, pp. 777–784, 2017.

[43] J. P. da Costa, R. Oliveira-Silva, A. L. Daniel-da-Silva, and R. Vitorino, “Bionanoconjugation for Proteomics applications - An overview,” *Biotechnol. Adv.*, vol. 32, no. 5, pp. 952–970, 2014.

[44] R. Oliveira-Silva, J. P. Da Costa, R. Vitorino, and A. L. Daniel-Da-Silva, “Magnetic

chelating nanoprobes for enrichment and selective recovery of metalloproteases from human saliva," *J. Mater. Chem. B*, vol. 3, no. 2, pp. 238–249, 2015.

Supplementary Material

Sequences of scaffolds

The sequences of the two scaffolds synthesized by asymmetric PCR are shown below. The 20 nucleotides at the 3' end of the scaffolds used as targets for hybridization with the complementary 20-nt long oligonucleotide ligand (ATTAATGCCGGAGAGGGTAG) in the magnetic beads are underlined.

III.S1: 449-nt scaffold sequence (5'->3')

GTCGTCGTCCCCTCAAACTGGCAGATGCACGGTTACGATGCGCCCATCTACACCAACGTAAC
CTATCCCATTACGGTCAATCCGCCGTTTGTTCCCACGGAGAATCCGACGGGTTGTTACTCGC
TCACATTTAATGTTGATGAAAGCTGGCTACAGGAAGGCCAGACGCGAATTATTTTTGATGGC
GTTCCTATTGGTTAAAAAATGAGCTGATTTAACAAAAATTTAACGCGAATTTTAACAAAATA
TTAACGTTTACAATTTAAATATTTGCTTATACAATCTTCCTGTTTTTGGGGCTTTTCTGATT
ATCAACCGGGGTACATATGATTGACATGCTAGTTTTACGATTACCGTTCATCGATTCTCTTG
TTTGCTCCAGACTCTCAGGCAATGACCTGATAGCCTTTGTAGATCTCTCAAAAATAGCTACC
CTCTCCGGCATTAAT

III.S2: 1000-nt scaffold sequence (5'->3')

GTCTCGCTGGTGAAAAGAAAAACCACCCTGGCGCCCAATACGCAAACCGCCTCTCCCCGCGC
GTTGGCCGATTCATTAATGCAGCTGGCACGACAGGTTTCCCGACTGGAAAGCGGGCAGTGAG
CGCAACGCAATTAATGTGAGTTAGCTCACTCATTAGGCACCCCAGGCTTTACACTTTATGCT
TCCGGCTCGTATGTTGTGTGGAATTGTGAGCGGATAACAATTTCACACAGGAAACAGCTATG
ACCATGATTACGAATTCGAGCTCGGTACCCGGGGATCCTCTAGAGTCGACCTGCAGGCATGC
AAGCTTGGCACTGGCCGTCGTTTTACAACGTCGTGACTGGGAAAACCCTGGCGTTACCCAAC
TTAATCGCCTTGCAGCACATCCCCCTTTCGCCAGCTGGCGTAATAGCGAAGAGGCCCGCACC
GATCGCCCTTCCCAACAGTTGCGCAGCCTGAATGGCGAATGGCGCTTTGCCTGGTTTCCGGC
ACCAGAAGCGGTGCCGGAAAGCTGGCTGGAGTGCGATCTTCCTGAGGCCGATACGGTCGTCG
TCCCCTCAAACTGGCAGATGCACGGTTACGATGCGCCCATCTACACCAACGTAACCTATCCC
ATTACGGTCAATCCGCCGTTTGTTCCCACGGAGAATCCGACGGGTTGTTACTCGCTCACATT
TAATGTTGATGAAAGCTGGCTACAGGAAGGCCAGACGCGAATTATTTTTGATGGCGTTCCTA
TTGGTTAAAAAATGAGCTGATTTAACAAAAATTTAACGCGAATTTTAACAAAATATTAACGT
TTACAATTTAAATATTTGCTTATACAATCTTCCTGTTTTTGGGGCTTTTCTGATTATCAACC
GGGGTACATATGATTGACATGCTAGTTTTACGATTACCGTTCATCGATTCTCTTGTTTGCTC
CAGACTCTCAGGCAATGACCTGATAGCCTTTGTAGATCTCTCAAAAATAGCTACCCTCTCCG
GCATTAAT

III.S3: Magnetic beads capacity screening

A screening on the mass of beads necessary to successfully capture the target single stranded DNAs was performed using asymmetric PCR samples.

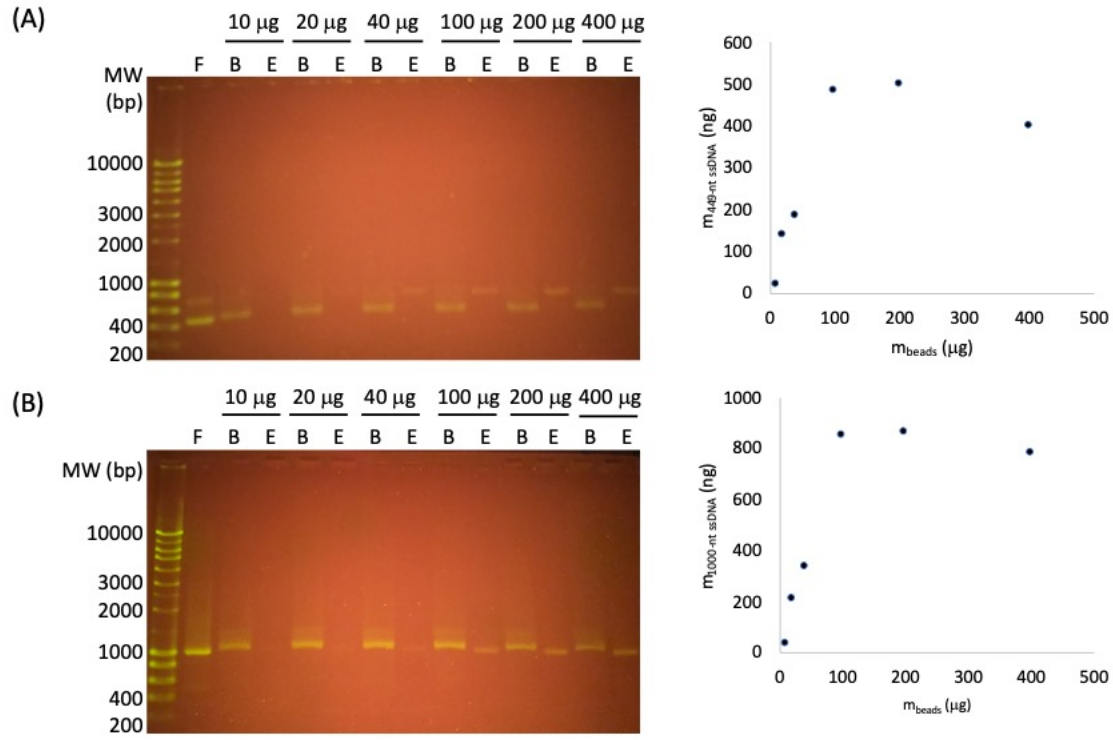

Figure III.S7: Screening of the mass of magnetic beads to be used. Agarose gel electrophoresis and spectrophotometric analysis of the purification of 449-nt (A) and 1000-nt (B) ssDNA scaffolds from asymmetric PCR mixtures for different amounts of magnetic beads. Lane F corresponds to the pre-purified aPCR product. Hybridization between magnetic beads and aPCR products was promoted and, after magnetic separation, the solution with un-bound dsDNA was recovered (lanes B). After washing and re-suspension in a buffer, the magnetic beads were heated to denaturing temperatures. Following magnetic separation, the solution with eluted ssDNA scaffolds was collected and analyzed (lane E). The same beads were used three times in each case.

III.S4: staple sequences and characteristics

Table III.S1: Staple sequences and characteristics to fold the 31-bp edge length tetrahedron from the 449-nt scaffold.

NAME	SEQUENCE	%GC	TM (°C)
T31_1-98-E	ACAACCCGTCCTGCCCCTGA	65	73.3
T31_2-237-V	AACGTTTTTTTAATATTTTGAACATTAAATGTTTTTTGAGCGAGTAGAGTCTGGAGCTTTTTAAACAAGAGAATTGTA	26.9	80
T31_2-346-E	ATCGATGAACAAATATTTAA	20	51.3
T31_3-284-E	AAAGCTTTTTGCTCACCCAA	40	63.5
T31_4-206-V	ATTTTTTTTTTGTTAAATCATAACCAATAGGTTTTTAACGCCATCAGCGTCTGGCCTTTTTTTCCTGTAGCCCGTTAA	34.6	85.5
T31_4-222-E	TTAAAATTCGAGCTTTCATC	30	56.1
T31_5-299-V	CGGTTTTTTTGATAATCAGAAAACAGGAAGATTTTTTTGTATAAGCGGTAATCGTAATTTTTAACTAGCATGGTACCC	30	56.1
T31_5-315-E	TCAATTAGATTGGTGCATAT	30	54.5
T31_6-51-V	TGGGATTTTTTAGGTTACGTGGGCGCATCGTTTTTTAACCGTGCATGGATTCTCCGTTTTTTGGGAACAAACCCGTAA	43.6	91.5
T31_6-67-E	GGCGGAATTCAAAATATTGA	35	61.2

Table III.S2: Staple sequences and characteristics to fold the 63-bp edge length tetrahedron from the 1000-nt scaffold.

NAME	SEQUENCE	%GC	TM (°C)
T63_1-212-E	GTGAAATTGTCGCCAGGGTGGTTATTTTTGTCTGTTTCCTGT	42.9	81.1
T63_1-191-E	AATTCCACACAGAGGCGGTTTGCGTATTGGGTATCCGCTCAC	52.4	85.6
T63_2-516-V	AAGATCGCACTTTTTTCCAGCCAGCTAATTCGTAATCTTTTTATGGTCATAGTAAATCAGCTCTTTTTATTTTTTAAC	30.8	81.6
T63_2-716-E	CCATCAAAAAGACGACCGTATCGGCCTCAGGCAATAGGAACG	52.4	85.1
T63_2-695-E	TGGCCTTCCTCATCTGCCAGTTTGAGGGGACTAATTCGCGTC	54.8	86.6
T63_3-398-E	CTATTACGGGGCGATCGGTGCGGGAGGTTACG	62.5	82.9
T63_3-587-E	TTGGTGTATTGACCGTAATGGGATCCTCTTCG	46.9	76.4
T63_3-390-E	CCAGCTGGCGCTGTTGGGAA	65	74.8
T63_4-453-V	TTCGCCATTCATTTTTGGCTGCGCAAAAAGGGGGATGTTTTTTGCTGCAAGGCGGCCAGTGCCTTTTTAAGCTTGCAT	47.4	94.9
T63_4-484-E	CTTCTGGTGCGATCCCCGGGTACCGAGCTCGTTCCGGCACCG	69	93.3
T63_4-463-E	CAAAGCGCCAGCCTGCAGGTCGACTCTAGAGCGGAAACCAGG	61.9	88.9
T63_5-632-V	TCCGTGGGAACTTTTTAAACGGCGGAGATGGGCGCATTTTTTCGTAACCGTGGTAGCCAGCTTTTTTTTCATCAACAT	44.9	92
T63_5-73-E	TCGTGCCACCCGCTTTCCAGTCGGACAACCCG	65.6	88.5
T63_5-640-E	TCGGATTCTAAATGTGAGCGAGTAGAAACCTG	43.8	73.3
T63_5-65-E	GCTGCATTAAGCGCTCACTG	55	66
T63_6-128-V	CTAACTCACATTTTTTTAATTGCGTTTGAATCGGCCATTTTTACGCGCGGGGAACATACGAGCTTTTTCGGAAGCATA	41	89.7
T63_6-325-E	CACGACGTGGGTAACGCCAGGGTTGTGCCTAA	59.4	83.1
T63_6-136-E	TGAGTGAGAAGTGTAAAGCCTGGGTTCCCAGT	50	76.3
T63_6-317-E	TGTAAAACGACGATTAAGTT	30	54

CHAPTER IV – CHROMATOGRAPHIC ISOLATION OF SINGLE STRANDED DNA SCAFFOLDS FOR BIOMANUFACTURING DNA-ORIGAMI NANOSTRUCTURES

CHAPTER IV.1. – SCALABLE PURIFICATION OF SINGLE STRANDED DNA SCAFFOLDS FOR BIOMANUFACTURING DNA-ORIGAMI NANOSTRUCTURES: EXPLORING ANION-EXCHANGE AND MULTIMODAL CHROMATOGRAPHY

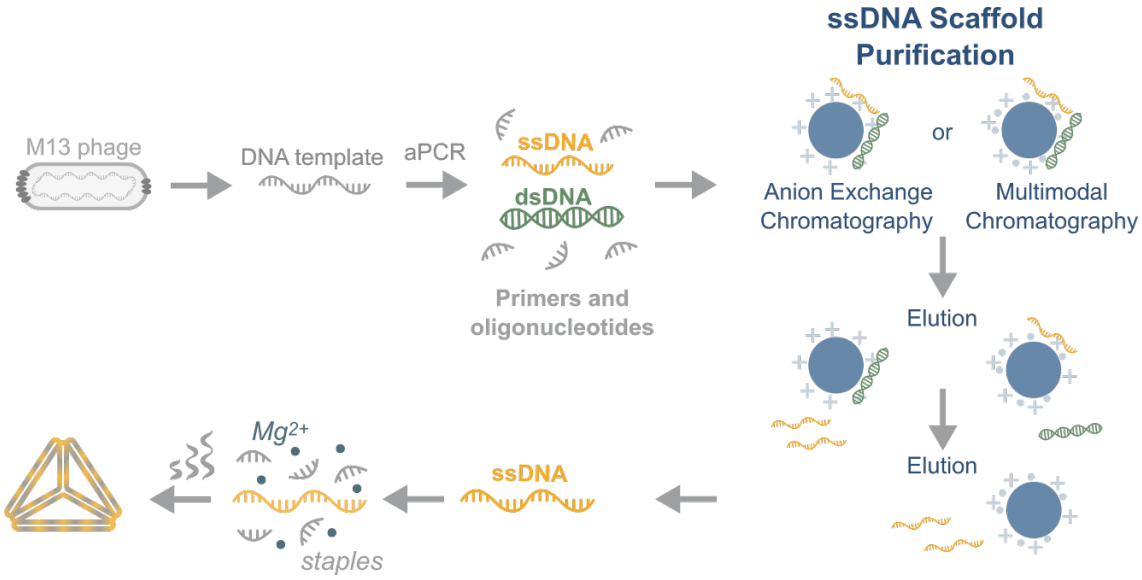

This chapter has been published as: Silva-Santos, A. R., Paulo, P. M., & Prazeres, D. M. F. (2022). Scalable purification of single stranded DNA scaffolds for biomanufacturing DNA-origami nanostructures: exploring anion-exchange and multimodal chromatography. *Separation and Purification Technology*, 121623.

Abstract

DNA-origami biomanufacturing relies in many cases on the use of asymmetric PCR (aPCR) to generate 500-3500 base, object-specific, single-stranded DNA (ssDNA) scaffolds. Each scaffold is usually purified by agarose gel extraction, a technique that is laborious, limited, not scalable, presents low recovery yields and a low-quality product. Alternatively, we present a chromatography-based method to purify ssDNA scaffolds from aPCR mixtures, which can be used in the context of DNA-origami techniques.

aPCR was performed to generate single and double-stranded DNA (dsDNA) from the M13mp18 genome. To isolate the target ssDNA from dsDNA and other PCR impurities, anion-exchange (Q-ligand) and multimodal chromatography (Capto^{TM} adhere ImpRes) were explored using stepwise gradients with increasing NaCl concentrations. In anion exchange chromatography, the less-charged ssDNA eluted before the dsDNA. In multimodal chromatography, however, the elution pattern was reversed, highlighting the importance played by hydrophobicity. In either case, collected ssDNA-containing fractions were homogeneous and impurity free.

Finally, 8.4 μg of a 1000-nt ssDNA fragment was purified and used alongside with site-specific short oligonucleotides (staples) to assemble 63-bp edge length tetrahedrons. Gel electrophoresis showed high assembly yield and purity, whereas fluorescence correlation spectroscopy confirmed that the tetrahedrons had a diffusion coefficient (26.7 $\mu m^2\ s^{-1}$) consistent with the expected size (20 nm).

Keywords: anion exchange chromatography, DNA-origami scaffold, multimodal chromatography, purification, single-stranded DNA.

IV.1.1. Introduction

DNA nanotechnology relies on Watson-Crick base pairing to self-assemble nucleic acids into complex nanostructures [1-3]. These nanostructures can be assembled using the "scaffolded DNA-origami" strategy, where a long single stranded DNA (ssDNA) molecule (the scaffold) is folded into the target shape with the assistance of short oligonucleotides (the staples) [4]–[7]. The versatility of this technique makes it very appealing in an increasing number of fields of study, with applications ranging from nanomachines [8], solid-state nanopores [9], drug delivery systems [10]–[13], biosensors [14], among others [15], [16].

One crucial step in DNA-origami is the scaffold preparation and purification. Veneziano *et al.* described the use of asymmetric PCR (aPCR) to generate 500-3500 nt, object-specific scaffolds using DNA from the M13 phage as template [5], [17]. The technique relies on the use of a molar excess of one primer (the forward primer) over the second primer (the reverse primer) to preferentially amplify the ssDNA target over its complementary strand. Once synthesized, the ssDNA scaffold in the aPCR mixture must be purified from unused primers, template DNA and dsDNA fragments formed by the scaffold and its complementary strand. This is usually accomplished by agarose gel electrophoresis separation of nucleic acids followed by band excision and physical extraction from the gel matrix, which typically yields 1-5 pmol per 50 µL reaction depending on the fragment size and sequences [5]. Although agarose gel electrophoresis is the gold standard for ssDNA scaffold purification, it is laborious, not scalable and yields scaffolds with agarose gel residues [18]. Alternatively, magnetic beads functionalized with oligonucleotides were used for the purification of ssDNA scaffolds from aPCR mixtures. Even though a good recovery and quality of the final product were obtained, the method is difficult to scale-up and requires the use of oligonucleotide ligands specific for each scaffold of interest [19].

Liquid chromatography, which is the primary tool for nucleic acid separation and purification, could potentially be used to purify ssDNA scaffolds [20]. Different types of chromatography were used for the purification of DNA fragments [21], [22], plasmid DNA [20], [23]–[25] and minicircles [26], [27] intended for uses in gene therapy or DNA vaccination. DNA chromatography matrices rely mainly on two different types of interactions between the solutes in the feed stream and the ligand in the solid phase: electrostatic and hydrophobic

interactions. At neutral pH, the sugar-phosphate backbone of nucleic acids is negatively charged, and thus anion-exchange chromatography is the preferred modality [28]. Factors like ligand density, chromatographic matrix, size, conformation and structure of the target nucleic acid molecule influence their access and diffusion through the pores of the chromatographic bead particles [21], [24]. The hydrophobic properties of nucleic acids were also explored in hydrophobic interaction chromatography [29]–[33]. More recently, studies with multimodal chromatography further showed that the combination of both electrostatic and hydrophobic interactions on the same ligand, results on an improved selectivity and specificity of the chromatographic process [21], [23], [27], [34], [35].

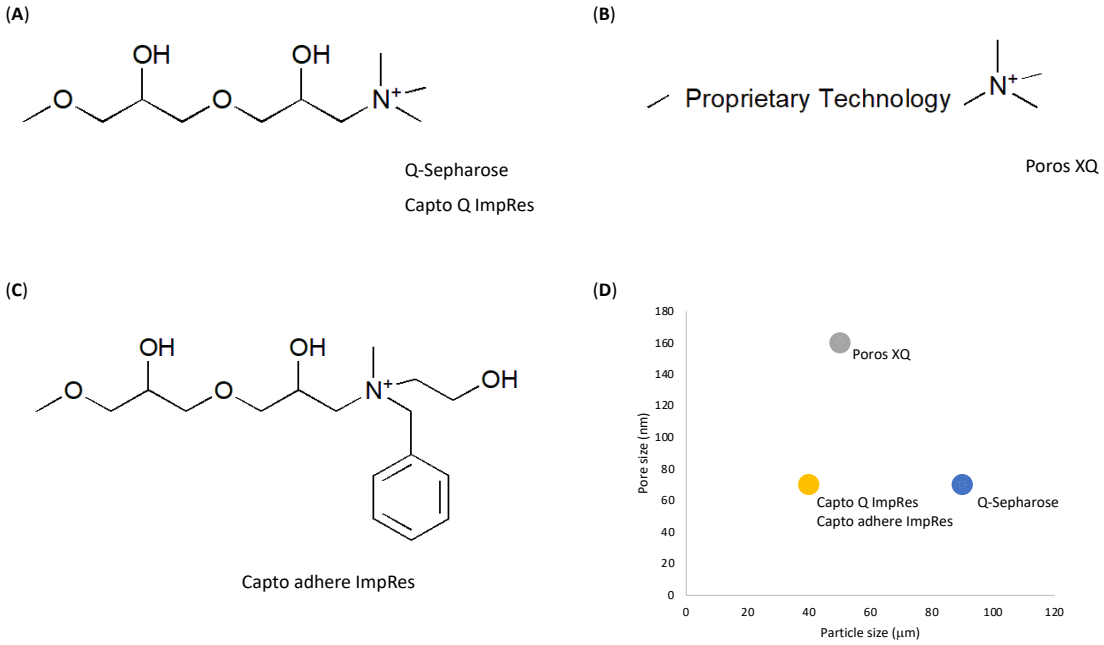

Figure IV.1.8. Anion exchange and multimodal ligands used for ssDNA scaffold purification. (A) Q-Sepharose, Capto Q ImpRes and (B) Poros XQ are quaternary amines that allow the establishment of electrostatic interactions between the solutes and the ligand through the charged nitrogen. (C) The Capto adhere ImpRes ligand (N-benzyl-N-methyl ethanolamine) allows the establishment of anion-exchange (charged nitrogen), hydrogen bonding (hydroxyls) and hydrophobic (phenyl ring) interactions. (D) Summary of the differences between the resins in terms of particle and pore size.

In this work, 1000 and 449 nt-long ssDNA scaffolds generated by aPCR were purified directly from the reaction mixtures using innovative, efficient, and reproducible processes based either on anion-exchange or multimodal chromatography (Fig. IV.1.1). Moreover, the purified 1000 nt-long ssDNA scaffold was used to successfully assemble a 63-bp edge length tetrahedron. This demonstrates that chromatography is compatible with the purification of

ssDNA scaffolds. Furthermore, as a scalable technique, chromatography is likely to play a crucial role in the scaling-up of DNA-origami technology.

IV.1.2. Materials and Methods

IV.1.2.1. Materials

Capto adhere ImpRes, Capto Q and Q Sepharose Fast Flow resins were from GE Healthcare (Uppsala, Sweden). POROS XQ resin was from Thermo Fisher (Massachusetts, USA). All salts used were of analytical grade. The producer *E. coli* strain K12 ER2738 and M13mp18 RF I DNA were from New England Biolabs (Massachusetts, USA) and Accustart^{TM} Taq DNA Polymerase HiFi was from Quantabio (Massachusetts, USA). Primers, oligonucleotides, and staple sequences were from Stab Vida (Caparica, Portugal).

IV.1.2.2. M13mp18 genomic DNA production and purification

E. coli K12 ER2738 cells were transformed with M13mp18 RF I DNA (GenBank: X02513.1) according to manufacturer's protocol [36]. Phage expansion and precipitation was performed according to [19]. Briefly, after transformation, a blue plaque was used to infect an *E. coli* pre-culture at an optical density of 0.5 in 5 mL medium supplemented with 10 μg/mL tetracycline. Phages were expanded overnight in 500 mL LB medium supplemented with tetracycline at 37 °C, 250 rpm. After expansion, supernatant was separated from the cells by centrifugation and phages were precipitated with 4 % PEG-8000 / 3 % NaCl, resuspended in TE buffer (10 mM Tris-HCl, 1 mM EDTA, pH 8.5) and further purified by filtration with a 0.22 μm syringe filter.

Extraction of genomic ssDNA was performed according to [37]. 400 μL lysis buffer (200 mM NaOH, 1 %(w/v) SDS) and 300 μL neutralization buffer (3 M potassium acetate, pH 5.5) were added to 200 μL of the phage solution and the mixture was placed on ice for 15 min. After centrifugation (10 min, 13,000 g), the supernatant was collected and mixed with ice cold ethanol at a 1:1 ratio and incubated on ice for 30 min. The precipitated ssDNA was centrifuged (10 min, 13,000 g), the pellet was washed with 75 % ice cold ethanol and centrifuged again.

Finally, the supernatant was discarded, and the precipitated ssDNA dissolved and diluted to a concentration of 6 ng/μL in TE buffer.

IV.1.2.3. Single stranded DNA scaffold generation by asymmetric PCR

The target scaffolds (*see* sequences in Supplementary Material) were synthesized by aPCR according to [5], [17]. Briefly, a forward primer concentration of 1 μM (GTCGTCGTCCCCTCAAACT for 449 nt and GTCTCGCTGGTGAAAAGAAA for 1000 nt), a reverse primer concentration of 20 nM (ATTAATGCCGGAGAGGGTAG), 30 ng of the extracted M13 ssDNA template, 200 mM deoxynucleotide triphosphates (dNTPs) and 1 unit of Accustart Taq DNA polymerase were mixed in a final volume of 50 μL. The aPCR program starts with and initial denaturation of 1 min, 94 °C, and is followed by 30 thermal cycles, with each one consisting of 94 °C, 20 s; 55 °C, 30 s; 68 °C, 90 s per kilobase for amplification.

IV.1.2.4. Anion-exchange chromatography

Anion-exchange chromatography was performed using either: (i) a pre-packed 1 mL HiTrap Q-Sepharose Fast Flow column; (ii) a Tricorn 5/50 column packed with 1 mL of Capto Q ImpRes resin, or; (iii) a Tricorn 5/50 column packed with 1 mL of Poros XQ resin connected to an ÄKTA purifier 10 system. Samples were prepared by pooling together ten asymmetric PCR reaction mixtures (10 × 50 μL). The mobile phase consisted of mixtures of low salt buffer A (10 mM Tris-HCl, 1 mM EDTA, pH 8) and high salt buffer B (2 M NaCl in buffer A). The absorbance of the eluate was continuously measured at 260 nm using a UV detector located at the column outlet and the system was operated at 1 mL/min. The column was equilibrated with 10 column volumes (CV) of 27% buffer B ($\kappa \approx$ 49.5 mS/cm). Then, 500 μL of aPCR sample was injected into the column by washing the injection loop with 1.5 mL of 27% buffer B. All unbound material was washed out of the column with 2 CV of 27% buffer B. The elution of bound species was accomplished with two steps: (i) 5 CV of 36.5% B ($\kappa \approx$ 64 mS/cm) and (ii) 5 CV of 40% B ($\kappa \approx$ 69.8 mS/cm). The eluate was collected (fractions of 500 μL) during the chromatographic run in 1.5 mL eppendorf tubes with a fraction collector.

IV.1.2.5. Multimodal chromatography

Multimodal chromatography was performed using a Tricorn 5/50 column packed with 1 mL of Capto adhere ImpRes resin connected to an ÄKTA purifier 10 system. Samples were prepared by pooling together ten asymmetric PCR reaction mixtures (10 × 50 μL). The mobile phase consisted of mixtures of buffer A and buffer B. The absorbance of the eluate was continuously measured at 260 nm and the system was operated at 1 mL/min. The column was equilibrated with 25% buffer B ($\kappa \approx$ 46.5 mS/cm) for 10 CV. Next, 500 μL of sample was injected by washing the injection loop with 1.5 mL of 25% buffer B. Two CV of buffer B at the same percentage were then used to wash unbound material. The elution of bound species was accomplished with two steps: (i) 7 CV of 80% B ($\kappa \approx$ 124 mS/cm) and (ii) 5 CV of 100% B ($\kappa \approx$ 147 mS/cm). During the run, eluate fractions of 500 μL were continuously collected in 1.5 mL microcentrifuge tubes with a fraction collector.

IV.1.2.6. ssDNA concentration

Peak fractions containing the ssDNA scaffold were concentrated using passivated 30 kDa Amicon Ultra-4 mL centrifugal filter (Merck). Centrifugal filters were filled with 5 %(v/v) Tween20 overnight at room temperature for passivation. Then, the devices were thoroughly rinsed with water and spun with milliQ water. Prior to concentration, centrifugal filters were equilibrated with TE buffer. After equilibration the samples were applied and diafiltrated three times with TE buffer. All spinning's were performed at 5,000 g, 10 min in a fixed-angle rotor at room temperature.

Recovery of ssDNA quantification was performed by UV-adsorption at 260 nm using a NanoDrop One (Thermo Scientific, Massachusetts, USA).

IV.1.2.7. Agarose gel extraction

Agarose gel was prepared with 1.5% (w/v) agarose (Fisher Scientific, Waltham, MA, US) in TAE buffer (40 mM Tris base, 20 mM acetic acid and 1 mM EDTA, pH 8) prestained with 1x SYBR Safe (Thermo Fisher Scientific, Massachusetts, USA). Gels were loaded with 10 aPCR reactions of each scaffold size pre-mixed with a 6x loading buffer (40% (w/v) sucrose). Electrophoresis

was performed in TAE buffer at 90 V for 60 minutes. The ssDNA bands were extracted and purified using QIAquick Gel Extraction Kit (Qiagen, Germany) according to manufacturer's protocol. The ssDNA concentration was estimated using a NanoDrop One spectrophotometer (Thermo Scientific, Massachusetts, USA).

IV.1.2.8. Design, folding and purification of DNA-origami objects

Design of staple strands to fold 63-bp edge length tetrahedra (see Supplementary material S3) was performed with the DAEDALUS software [5] using a 1000-nt ssDNA scaffold. DNA-origami assembly and purification was performed by slightly adapting the methods described in [5], [18]. Briefly, 40 nM scaffold strand was mixed with 400 nM of a mix of staple strands in 50 μL of Tris-acetate EDTA-$MgCl_2$ buffer (40 mM Tris, 20 mM acetic acid, 2 mM EDTA, 12 mM $MgCl_2$, pH 8). Annealing was performed in a thermal cycler according to the following sequence: 95 °C for 5 min, 80 to 75 °C at 1 °C per 5 min, 75 to 30 °C at 1 °C per 15 min, 30 to 25 °C at 1 °C per 10 min. The final tetrahedra solution was purified with an Amicon Ultra-0.5 mL centrifugal filter with a molecular weight cut-off of 100 kDa by diafiltrating 5 times with 5 mM Mg^{2+} buffer to remove excess of staple strands.

IV.1.2.9. Fluorescence correlation spectroscopy

FCS measurements were performed on a Microtime 200 setup from PicoQuant GmbH (Germany). The excitation source used was a pulsed diode laser emitting at 482 nm with a repetition rate of 20 MHz (LDH-P-C-485, PicoQuant GmbH). The laser beam was focused 10 μm inside the sample by means of a water immersion objective of N.A. 1.2 (UPlanSApo 60×, Olympus). Fluorescence emission was collected by the same objective and cleaned by a dichroic filter (485DRLP, Omega) and by a bandpass filter with transmission range between ca. 528 and 562 nm (545AF35, Omega). Out-of-focus light was rejected by means of a 50 μm pinhole. The collected emission was detected by single-photon avalanche diode detectors (SPCM-AQR-13, Perkin Elmer). Data acquisition and preliminary analysis were performed on SymPhoTime software (PicoQuant GmbH). The tetrahedron nanostructure and the 1000-nt

scaffold were singly labelled with a fluorescein dye or with Atto-488 dye for FCS measurements.

IV.1.2.10. Gel electrophoresis

Agarose gels were prepared with 1% (w/v) agarose (Fisher Scientific, Waltham, MA, US) in TAE buffer (40 mM Tris base, 20 mM acetic acid and 1 mM EDTA, pH 8). Gels were loaded with samples pre-mixed with a 6x loading buffer (40% (w/v) sucrose). NZYDNA ladder III (NZYTech, Lisbon, Portugal) was used as a molecular weight marker. Electrophoresis was performed in TAE buffer at 120 V for 90 minutes. Gels were stained in a 1x SYBR Safe (Thermo Fisher Scientific, Massachusetts, USA) and images were obtained with a TruBlu^{TM} blue light (497 nm) transilluminator (Edvotek).

IV.1.3. Results and discussion

aPCR reaction mixtures used to generate ssDNA scaffold also contain dsDNA, unspecific amplified fragments, excess primers and excess dNTPs. Here, we investigated whether anion-exchange or multimodal column chromatography could be used to separate the target ssDNA scaffolds from the other components in the mixture.

IV.1.3.1. Anion-exchange chromatography

Different strong anion exchange resins were tested for the isolation and purification of a ssDNA strand using 1 mL chromatographic columns. The selected matrices – Q-Sepharose, Capto Q ImpRes and Poros XQ - can mediate electrostatic interactions with the solutes in the feed stream through the charged nitrogen of the corresponding quaternary amine ligands (Fig IV.1.1D). The matrices further differ in particle (40 to 90 μm) and pore size (70 and 160 nm). The columns were pre-equilibrated with 27% buffer B (540 mM NaCl, ≈ 49.5 mS/cm). Ten aPCR reactions used to generate a 1000 nt-long scaffold (*see* sequence in Supplementary Material) were then pooled and the resulting 500 μL mixture was injected. Runs were performed at 1 mL/min, unbound material was washed with 2 CV of 27% B (540 mM, ≈ 49.5 mS/cm) and

elution was accomplished using two steps with increasing salt concentration, the first with 5CV of 36.5% B (≈ 64 mS/cm) and the second with 5CV of 40% B (≈ 69.8 mS/cm).

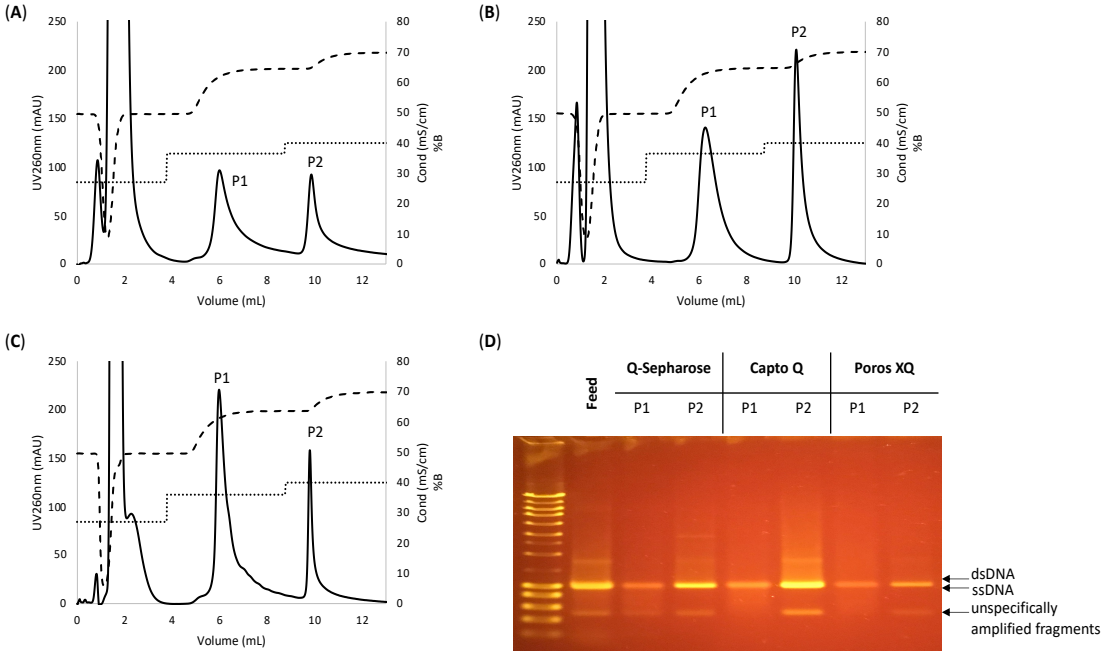

Figure IV.1.9. Anion exchange chromatography purification of a 1000-nt ssDNA scaffold produced by aPCR from double stranded DNA, unspecific amplification products, dNTPs and excess primers. A feed stream corresponding to a pool of ten aPCR reactions (500 μL) was injected into 1 mL (A) Q-Sepharose, (B) Capto Q ImpRes and (C) Poros XQ columns pre-equilibrated with 540 mM NaCl buffer (27% buffer B, ≈ 49.5 mS/cm). Unbound material was washed with 2 CV of 27 %B, and stepwise elution was performed with 5 CV of 36.5% B (≈ 64 mS/cm) and 5 CV of 40% B (≈ 69.8 mS/cm). Continuous line: absorbance at 260 nm (mAU); dashed line: conductivity (mS/cm); dotted line: percentage of buffer B (%B). (D) Agarose gel electrophoresis analysis of fractions collected during the chromatographic runs. Fractions collected during the chromatographic runs are marked P1 (step 1, correspondent to ssDNA) and P2 (step 2, correspondent to dsDNA). When excited with blue light illumination (497 nm) the SYBR dye makes it possible to discern between ssDNA (orange band) and dsDNA (yellow/green band).

The chromatograms obtained in the three columns are characterized by a major flowthrough peak and two, baseline-separated peaks, one for each elution step (Fig. IV.1.2 (A-C)). The retention volume of these two peaks was essentially the same across the three resins tested. The corresponding fractions were analysed by agarose gel electrophoresis alongside with the feed (Fig. IV.1.2 (D)). Under the electrophoresis conditions used, the ssDNA and dsDNA fragments in the aPCR mixture co-migrate as a single yellowish band (lane Feed in Fig. IV.1.2 (D)). Excess dNTPs and primers (19-20 nt long) eluted in the flowthrough due to their low charge density. Although these molecules cannot be observed in the agarose gel due to their

small size, preliminary experiments (see Supplementary material S4), which involved running mixtures of primers and dNTPs in the Q-Sepharose reference column, confirmed that they do not bind to the columns.

The analysis of the other fractions collected (Fig. IV.1.2 (D)) confirms that the peak eluting at 36.5% B (≈ 64 mS/cm) with a retention volume of ~6 mL contains the target ssDNA scaffold, whereas the second peak eluting at 40% B (≈ 69.8 mS/cm) with a retention volume of 10 mL, contains the dsDNA. This can be ascertained because in SYBR Safe stained gels, ssDNA shows up as an orange band (see lanes P1 in Fig. IV.1.2(D)), whereas dsDNA shows up as a bright green/yellow band (see lanes P2 in Fig. IV.1.2 (D)). Fractions of the second peak also contain DNA fragments that result from unspecific amplification.

The difference between the retention time of single and double stranded DNA species can be explained based on their charge density. At the working pH of 8, the two molecules are negatively charged and, thus, will bind to the strong anion exchangers. However, since dsDNA has double of the structural charges of ssDNA, its interaction with the charged nitrogen atom of the ligand is stronger, allowing it to remain bound to the column at higher salt concentrations [38].

Quantitation of DNA in the ssDNA fractions showed that 8.4 ± 1.3 μg of target ssDNA scaffold could be recovered from the 500 μL of aPCR pool from the Q-Sepharose column, 10.7 ± 1.7 μg from the POROS XQ and 9.0 ± 1.4 μg from the Capto Q ImpRes. Even though the chromatographic method was equally efficient for the three strong-anion exchange resins tested in terms of the mass recovered, peak resolution and shape varied between Q-Sepharose and Capto Q ImpRes and Poros XQ. Peaks obtained with PorosXQ and Capto Q were sharper, with minimal tailing observed for Capto Q. The Q Sepharose resin produced shorter peaks with larger trailing. This can be attributed to increased axial dispersion due to the large bead size of Q-Sepharose (90 nm) vs Poros XQ (50 nm) and Capto Q (40 nm). Even though the peak height is different across the studied resins, the ratio between the ssDNA and dsDNA peak areas is constant and approximately 1.5.

Additional experiments were performed that showed that the anion-exchange separation was reproducible (see Supplementary Material S5). Moreover, peak resolution was unaltered when double the feed volume was used (see Supplementary Material S6), showing that anion-

exchange chromatography can be used as a scale-up method for purification of ssDNA scaffolds.

Standard agarose gel extraction was performed and a recovery of 1.98 μg was achieved when applying 10 aPCR reactions into a gel pocket. This corresponds to a 4.2 to 5.4 -fold decrease when compared with the recovery obtained with the anion-exchange chromatographic method proposed. Moreover, the scalability of agarose gel extraction is limited, the purity of the recovered product might not be suitable for all uses since agarose residues can co-purify with the target ssDNA, and the use of intercalation dyes might compromise downstream applications.

IV.1.3.2. Multimodal chromatography

Multimodal chromatography was tested next as a potential alternative to anion-exchange chromatography. Multimodal separations rely on the use of stationary phases modified with small synthetic organic ligands that explore more than one type of interaction with the solutes in the feed stream. Here we tested a chromatographic column packed with the multimodal ligand resin, Capto adhere ImpRes (Fig. IV.1.1 (C)). Besides the ability to mediate anion-exchange interactions through the charged nitrogen, similarly to anion-exchange chromatography, the ligand is also able to engage in hydrophobic interactions via its phenyl ring.

The 1 mL column was pre-equilibrated with 25% buffer B (250 mM, ≈ 46.5 mS/cm). As before, ten aPCR reactions were pooled and the 500 μL mixture was injected in the column and the unbound material was washed at 1mL/min using 2 CV of the same buffer (25% B, 250 mM, ≈ 46.5 mS/cm). The elution of bound species was accomplished using two steps with increasing salt concentration, the first with 7 CV of 80% B (≈ 124 mS/cm) and the second with 5 CV of 100% B (≈ 147 mS/cm).

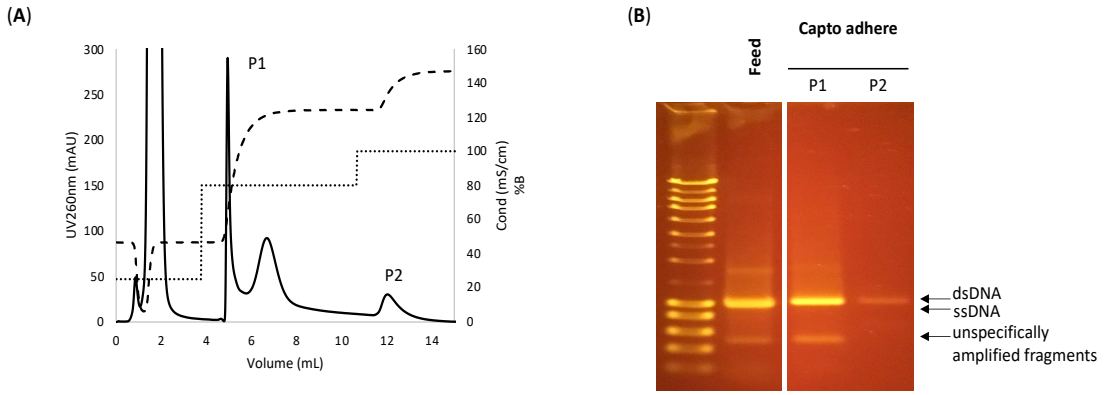

Figure IV.1.10. Multimodal chromatography purification of a 1000-nt ssDNA scaffold produced by aPCR from double stranded DNA, unspecific amplification products, dNTPs and excess primers. A feed stream corresponding to a pool of ten aPCR reactions (500 µL) was injected into a Tricorn 5/50 column packed with Capto adhere ImpRes resin pre-equilibrated with 500 mM NaCl buffer (25% buffer B, ≈46.5 mS/cm). Unbound material was washed with 2 CV of 25 %B, and stepwise elution was performed with 7 CV of 80% B (≈ 124 mS/cm) and 5 CV of 100% B (≈ 147 mS/cm). Continuous line: absorbance at 260 nm (mAU); dashed line: conductivity (mS/cm); dotted line: percentage of buffer B (%B). (B) Agarose gel electrophoresis analysis of fractions collected during the chromatographic run. Fractions collected during the chromatographic run are marked P1 (step 1, correspondent to dsDNA) and P2 (step 2, correspondent to ssDNA). When excited with blue light illumination (497 nm) the SYBR dye makes it possible to discern between ssDNA (orange band) and dsDNA (yellow/green band).

The chromatogram obtained is characterized by three groups of peaks, one for each elution step (Fig. IV.1.3(A)). As in the case of the anion exchange separation, excess dNTPs and primers eluted in the flowthrough due to their low charge density. An agarose gel electrophoresis analysis further showed that the two partially resolved peaks eluting at 80% B (and pooled as fraction P1), with a retention volume of ~6 mL, contain dsDNA (yellow/green band) and unspecific amplified fragments (Fig. IV.1.3(B)). The second, shorter peak eluting at 100% B with a retention volume of ~12 mL, contains the target ssDNA scaffold (orange band) (Fig. IV.1.3(B)). This corresponds to an inversion of the elution order of ssDNA and dsDNA obtained with anion-exchange chromatography.

As in anion-exchange chromatography, both the dsDNA and ssDNA can bind to the ligand. The interaction involved results most likely from a combination of electrostatic interactions of the charged nitrogen with the negatively charged sugar-phosphate backbone, and of hydrophobic interactions between the phenyl ring and DNA bases. Compared with the anion-exchange separation, the interactions established with the multimodal ligand are more tolerant to higher salt concentration, as judged by the fact that a conductivity of 124 mS/cm was required

to elute the first species compared to 64 mS/cm. As for the inversion of the elution order, this can be ascribed to the presence of the phenyl ring combined with the higher exposure of bases in the target ssDNA scaffold compared to dsDNA. Hydrophobic interactions are thus responsible for the binding of ssDNA to the ligand at very high salt concentrations. The fact that the nucleic acids with higher single strand content bind more strongly to multimodal resins compared to double stranded DNA has been previously reported for the case of plasmid and minicircle separations [23], [27]. Quantitation of DNA in the ssDNA fractions showed that ~8.2 ± 2.0 μg of target ssDNA scaffold could be recovered from the 500 μL of aPCR pool, a value that is comparable to the one obtained by anion exchange chromatography.

IV.1.3.3. Effect of scaffold size

The ability of the anion-exchange and multimodal chromatography columns to purify a smaller (449-nt) ssDNA scaffold from an aPCR mixture was evaluated next. Ten aPCR reactions were pooled and injected into the four chromatographic matrices tested using the same stepwise elution schemes as previously.

An agarose gel electrophoresis analysis of this pool (Figure 4(E)) shows that it contains essentially the ssDNA scaffold (orange band) and dsDNA impurities (yellow band). Here the ssDNA band migrated less than the dsDNA, probably due to secondary structure formation [19].

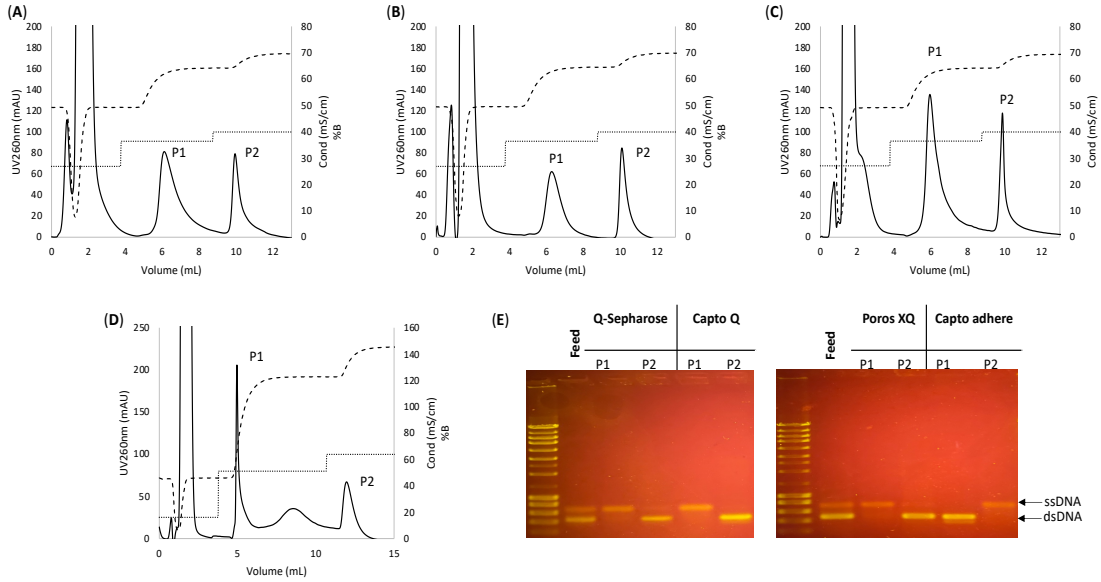

Figure IV.1.11. Anion-exchange and multimodal chromatography purification of a 449-nt ssDNA scaffold produced by aPCR from excess dNTPs and primers, single and double stranded DNA and unspecific amplification products. Chromatograms are shown for the purification using (A) Q-Sepharose, (B) Capto Q ImpRes, (C) Poros XQ and (D) Capto adhere ImpRes resin of ten aPCR pooled reactions containing dsDNA, the target ssDNA scaffold and excess of primers and dNTPs. Letters over peaks correspond to collected fractions. Continuous line: absorbance at 260 nm (mAU); dashed line: conductivity (mS/cm); dotted line: percentage of buffer B (%B). (E) Agarose gel electrophoresis analysis of pooled and concentrated peak samples during the chromatographic runs.

The chromatographic profiles obtained for the 449-nt ssDNA fragment were almost identical to the ones obtained for the 1000-nt ssDNA (Fig. IV.14(A-D)). Separation by anion-exchange with Q-Sepharose, Capto Q ImpRes and Poros XQ (Fig. IV.1.4(A-C)) produced a flowthrough peak, a first peak of ssDNA (V_R~6 mL) and a final peak of dsDNA (V_R~10 mL). The smaller size of the species involved here (449 nt and 2×449 nt) did not significantly affect the conductivity at which the ssDNA an dsDNA peaks were eluted, which were identical to the ones obtained with the 1000 nt and 2×1000 nt species (Fig. IV.1.2(A-C)). This highlights the versatility of the developed method and the importance of the ionic interactions in this type of chromatography. A gel electrophoresis analysis (Fig. IV.1.4(E)) confirmed that, as before, peak P1 contains ssDNA (orange band) and peak P2 dsDNA (yellow band).

Separation with the multimodal Capto adhere ImpRes resin produced a chromatogram with a flowthrough peak, partially resolved peaks of dsDNA eluting at ≈ 124 mS/cm, and a final peak of ssDNA eluting at≈ 147 mS/cm (Figure 4(D)). Gel electrophoresis analysis (Figure IV.1.4(E)) confirmed that peak P1 contains dsDNA (yellow band) and peak P2 ssDNA (orange band).

Quantitation of DNA in the ssDNA fractions showed that for this fragment it was possible to recover 4.6 ± 0.4 μg, 5.3 ± 0.9 μg and 6.2 ± 0.8 μg with Q-Sepharose, POROS XQ and Capto Q ImpRes anion-exchangers, respectively, and 4.3 ± 1.1 μg with the multimodal resin.

Once again, standard agarose gel extraction was performed and a recovery of 2.33 μg was achieved when applying 10 aPCR reactions into a gel pocket. This corresponds to a 1.8-2.7-fold decrease when compared with the recovery obtained with the chromatographic methods used. Although the differences in recovery are not so striking as in the case of the 1000-nt ssDNA fragment, the benefits of the proposed chromatographic processes and the limitations of recovery by gel extraction remain.

IV.1.3.4. Assembly of DNA-origami nanostructures

The purified 1000-nt ssDNA was used as scaffold to assemble 63-bp edge length tetrahedra, according to Veneziano *et al.* [5]. The target geometry was rendered as a scaffolded DNA-origami structure using the DAEDALUS software with the 1000-nt sequence as in input. Staple sequences (see Supplementary information) and atomic models (Figure 5 (B)) were obtained as an output. Folding of the scaffolds was promoted under high magnesium concentration (12 mM) using a slow temperature decrease ramp between 80 to 25 °C. After assembly, the excess of staple strands was removed by ultracentrifugation with a centrifugal filter of 100 kDa molecular weight cut-off and the sample was concentrated. Agarose gel electrophoresis analysis (Figure 5 (A)) of the solutions obtained after folding show a slight upward shift of the original scaffold band. This newer band migrates less than the original scaffold band, which is consistent to what is described in the literature [5]. The band sharpness is also consistent with a good overall folding quality [18], [39]. The post-folding removal of the excess staple strands by the centrifugal filter was efficient as judged by the absence of smear in the bottom of the gel. The slight decrease in migration observed for the nano-tetrahedra band after staple removal can be explained by the use of a diafiltration step with a buffer with lower salt concentration.

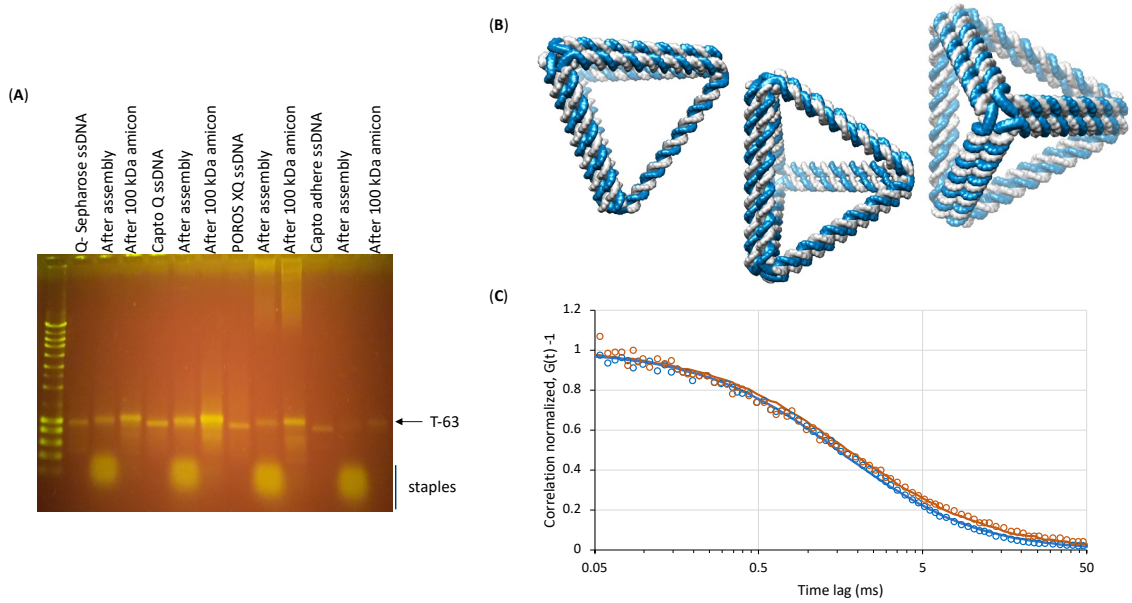

Figure IV.1.12. (A) Folding of DNA-origami nanostructures. The purified 1000-nt ssDNA scaffold was used to fold 63-bp edge length tetrahedra under high magnesium concentrations. The folding products were purified by ultracentrifugation with a 100-kDa molecular weight cut-off filter and five times diafiltered with 5 mM Mg^{2+} buffer to remove excess staple strands. (B) Atomic model of the 20 nm 63-bp edge length tetrahedra. (C) Fluorescence correlation spectroscopy analysis of the 1000-nt ssDNA scaffold (orange) and T-63 tetrahedron (blue) in an aqueous medium.

Further studies on the folding of T-63 tetrahedron were performed using fluorescence correlation spectroscopy (FCS). The diffusion coefficients obtained for the 1000-nt scaffold and the 63-edge length tetrahedron in the aqueous medium were equal to 19.6 and 26.7 $\mu m^2 s^{-1}$, respectively. The tetrahedron diffusion coefficient corresponds to a hydrodynamic diameter of 18.4 nm, which is consistent with the simulated dimensions of the DNA-origami nanostructure (20 nm edge) (Fig. IV.1.5).

IV.1.4. Conclusions

Even though DNA-origami technology has been used over the past few years for a wide range of applications, the current techniques used for ssDNA scaffold production and purification are cumbersome and most of the times not suitable for pharmaceutical or analytical applications since they often rely on agarose gel electrophoresis extraction. This type of methodology is laborious, not scalable and yields scaffolds that may be contaminated with agarose gel residues. In this work, anion-exchange and multimodal chromatography were

used to purify ssDNA scaffolds in 500 μL pools of ten aPCR reactions mixtures containing target ssDNA of 449-nt or 1000 nt, dsDNA, from dsDNA, fragments resulting from unspecific aPCR amplification, excess of primers and dNTPs. Both types of chromatography allowed the purification of between 8.4 μg and 10.7 μg of the 1000-nt ssDNA, virtually free from other impurities. Overall, we show that chromatography could play an important role in scaling-up the purification of ssDNA scaffold that is intended for biomanufacturing DNA-origami nanostructures.

IV.1.5 References

[1] N. C. Seeman and H. F. Sleiman, "DNA nanotechnology," *Nat. Rev. Mater.*, vol. 3, 2017.
[2] P. W. K. Rothemund, "Folding DNA to create nanoscale shapes and patterns," *Nature*, vol. 440, no. 7082, pp. 297–302, 2006.
[3] F. Zhang, J. Nangreave, Y. Liu, and H. Yan, "Structural DNA nanotechnology: State of the art and future perspective," *J. Am. Chem. Soc.*, vol. 136, no. 32, pp. 11198–11211, 2014.
[4] W. M. Shih, J. D. Quispe, and G. F. Joyce, "A 1.7-kilobase single-stranded DNA that folds into a nanoscale octahedron," *Nature*, vol. 427, no. 6975, pp. 618–621, 2004.
[5] R. Veneziano *et al.*, "Designer nanoscale DNA assemblies programmed from the top down," *Science*, vol. 352, no. 6293, 2016.
[6] S. M. Douglas, A. H. Marblestone, S. Teerapittayanon, A. Vazquez, G. M. Church, and W. M. Shih, "Rapid prototyping of 3D DNA-origami shapes with caDNAno," *Nucleic Acids Res.*, vol. 37, no. 15, pp. 5001–5006, 2009.
[7] C. E. Castro *et al.*, "A primer to scaffolded DNA-origami," *Nat. Methods*, vol. 8, no. 3, pp. 221–229, 2011.
[8] P. Ketterer, E. M. Willner, and H. Dietz, "Life Sciences: Nanoscale rotary apparatus formed from tight-fitting 3D DNA components," *Sci. Adv.*, vol. 2, no. 2, pp. 1–9, 2016.
[9] A. B. Farimani, P. Dibaeinia, and N. R. Aluru, "DNA-origami-graphene hybrid nanopore for DNA detection," *ACS Appl. Mater. Interfaces*, vol. 9, no. 1, pp. 92–100, 2017.
[10] S. M. Douglas, I. Bachelet, and G. M. Church, "A Logic-Gated Nanorobot for Targeted Transport of Molecular Payloads," *Science*, vol. 335, no. February, pp. 831–834, 2012.
[11] J. Yan, C. Hu, X. Liu, J. Zhong, G. Sun, and D. He, "Recent Developments of New DNA-origami Nanostructures for Drug Delivery," *Curr. Pharm. Des.*, vol. 21, no. 22, pp. 3181–3190, 2015.
[12] A. Udomprasert and T. Kangsamaksin, "DNA-origami applications in cancer therapy," *Cancer Sci.*, vol. 108, no. 8, pp. 1535–1543, 2017.
[13] B. R. Madhanagopal, S. Zhang, E. Demirel, H. Wady, and A. R. Chandrasekaran, "DNA Nanocarriers: Programmed to Deliver," *Trends Biochem. Sci.*, vol. 43, no. 12, pp. 997–1013, 2018.
[14] H. Pei *et al.*, "A DNA nanostructure-based biomolecular probe carrier platform for electrochemical biosensing," *Adv. Mater.*, vol. 22, no. 42, pp. 4754–4758, 2010.
[15] Y. Amir, E. Ben-Ishay, D. Levner, S. Ittah, A. Abu-Horowitz, and I. Bachelet, "Universal

computing by DNA-origami robots in a living animal," *Nat. Nanotechnol.*, vol. 9, no. 5, pp. 353–357, 2014.

[16] E. M. Roller, L. K. Khorashad, M. Fedoruk, R. Schreiber, A. O. Govorov, and T. Liedl, "DNA-assembled nanoparticle rings exhibit electric and magnetic resonances at visible frequencies," *Nano Lett.*, vol. 15, no. 2, pp. 1368–1373, 2015.

[17] R. Veneziano, T. R. Shepherd, S. Ratanalert, L. Bellou, C. Tao, and M. Bathe, "In vitro synthesis of gene-length single-stranded DNA," *Sci. Rep.*, vol. 8, no. 1, pp. 1–7, 2018.

[18] K. F. Wagenbauer *et al.*, "How We Make DNA-origami," *ChemBioChem*, vol. 18, no. 19, pp. 1873–1885, 2017.

[19] A. Rita Silva-Santos, R. Oliveira-Silva, S. Sousa Rosa, P. M. R. Paulo, and D. Miguel F. Prazeres, "Affinity-Based Magnetic Particles for the Purification of Single-Stranded DNA Scaffolds for Biomanufacturing DNA-Origami Nanostructures," *ACS Appl. Nano Mater.*, vol. 4, no. 12, pp. 14169–14177, Nov. 2021.

[20] M. M. Diogo, J. A. Queiroz, and D. M. F. Prazeres, "Chromatography of plasmid DNA," *J. Chromatogr. A*, vol. 1069, no. 1, pp. 3–22, 2005.

[21] T. Matos, J. A. Queiroz, and L. Bülow, "Binding and elution behavior of small deoxyribonucleic acid fragments on a strong anion-exchanger multimodal chromatography resin," *J. Chromatogr. A*, vol. 1302, pp. 40–44, 2013.

[22] T. Matos, G. Silva, J. A. Queiroz, and L. Bülow, "Preparative isolation of polymerase chain reaction products using mixed-mode chromatography," *Anal. Biochem.*, vol. 489, pp. 73–75, 2015.

[23] A. R. Silva-Santos, C. P. A. Alves, D. M. F. Prazeres, and A. M. Azevedo, "A process for supercoiled plasmid DNA purification based on multimodal chromatography," *Sep. Purif. Technol.*, vol. 182, pp. 94–100, 2017.

[24] A. Eon-Duval and G. Burke, "Purification of pharmaceutical-grade plasmid DNA by anion-exchange chromatography in an RNase-free process," *J. Chromatogr. B Anal. Technol. Biomed. Life Sci.*, vol. 804, no. 2, pp. 327–335, 2004.

[25] C. M. Ongkudon and M. K. Danquah, "Anion exchange chromatography of 4.2 kbp plasmid based vaccine (pcDNA3F) from alkaline lysed E. coli lysate using amino functionalised polymethacrylate conical monolith," *Sep. Purif. Technol.*, vol. 78, no. 3, pp. 303–310, 2011.

[26] C. P. A. Alves, M. Šimčíková, L. Brito, G. A. Monteiro, and D. M. F. Prazeres, "Development of a nicking endonuclease-assisted method for the purification of minicircles," *J. Chromatogr. A*, vol. 1443, pp. 136–144, 2016.

[27] A. R. Silva-Santos, C. P. A. Alves, G. Monteiro, A. M. Azevedo, and D. M. F. Prazeres, "Multimodal chromatography of supercoiled minicircles: A closer look into DNA-ligand interactions," *Sep. Purif. Technol.*, vol. 212, no. November 2018, pp. 161–170, 2019.

[28] P. Tiainen, I. Galaev, and P. O. Larsson, "Plasmid adsorption to anion-exchange matrices: Comments on plasmid recovery," *Biotechnol. J.*, vol. 2, no. 6, pp. 726–735, 2007.

[29] M. M. Diogo, J. A. Queiroz, and D. M. F. Prazeres, "Assessment of purity and quantification of plasmid DNA in process solutions using high-performance hydrophobic interaction chromatography," *J. Chromatogr. A*, vol. 998, no. 1–2, pp. 109–117, 2003.

[30] H. Bo *et al.*, "Using a single hydrophobic-interaction chromatography to purify pharmaceutical-grade supercoiled plasmid DNA from other isoforms," *Pharm. Biol.*, vol.

51, no. 1, pp. 42–48, 2013.

[31] S. S. Freitas, J. A. L. Santos, and D. M. F. Prazeres, “Plasmid purification by hydrophobic interaction chromatography using sodium citrate in the mobile phase,” *Sep. Purif. Technol.*, vol. 65, no. 1, pp. 95–104, 2009.

[32] J. Urthaler, W. Buchinger, and R. Necina, “Industrial scale cGMP purification of pharmaceutical grade plasmid-DNA,” *Chem. Eng. Technol.*, vol. 28, no. 11, pp. 1408–1420, 2005.

[33] S. Cardoso, U. Černigoj, N. Lendero Krajnc, and A. Štrancar, “Chromatographic purification of plasmid DNA on hydrophobic methacrylate monolithic supports,” *Sep. Purif. Technol.*, vol. 147, pp. 139–146, 2015.

[34] T. Matos, J. A. Queiroz, and L. Bülow, “Plasmid DNA purification using a multimodal chromatography resin,” *J. Mol. Recognit.*, vol. 27, no. 4, pp. 184–189, 2014.

[35] T. Matos, E. T. Mohamed, J. A. Queiroz, and L. Bülow, “Capto™ Resins for Chromatography of DNA: A Minor Difference in Ligand Composition Greatly Influences the Separation of Guanidyl-Containing Fragments,” *Chromatographia*, vol. 79, no. 19–20, pp. 1277–1282, 2016.

[36] N. E. Biolabs, “M13mp18 RF I DNA.” [Online]. Available: https://www.neb.com/products/n4018-m13mp18-rf-i-dna#Product Information.

[37] B. Kick, S. Hensler, F. Praetorius, H. Dietz, and D. Weuster-Botz, “Specific growth rate and multiplicity of infection affect high-cell-density fermentation with bacteriophage M13 for ssDNA production,” *Biotechnol. Bioeng.*, vol. 114, no. 4, pp. 777–784, 2017.

[38] G. S. Manning, “Limiting laws and counterion condensation in polyelectrolyte solutions I. Colligative properties,” *J. Chem. Phys.*, vol. 51, no. 3, pp. 924–933, 1969.

[39] S. Dey *et al.*, “DNA-origami,” *Nat. Rev. Methods Prim.*, vol. 1, no. 1, pp. 1–24, 2021.

Supplementary Material

Sequences of scaffolds

The sequences of the two scaffolds synthesized by asymmetric PCR are shown below.

IV.1.S1: 449-nt scaffold sequence (5'->3')

GTCGTCGTCCCCTCAAACTGGCAGATGCACGGTTACGATGCGCCCATCTACACCAACGTAAC
CTATCCCATTACGGTCAATCCGCCGTTTGTTCCCACGGAGAATCCGACGGGTTGTTACTCGC
TCACATTTAATGTTGATGAAAGCTGGCTACAGGAAGGCCAGACGCGAATTATTTTTGATGGC
GTTCCTATTGGTTAAAAAATGAGCTGATTTAACAAAAATTTAACGCGAATTTTAACAAAATA
TTAACGTTTACAATTTAAATATTTGCTTATACAATCTTCCTGTTTTTGGGGCTTTTCTGATT
ATCAACCGGGGTACATATGATTGACATGCTAGTTTTACGATTACCGTTCATCGATTCTCTTG
TTTGCTCCAGACTCTCAGGCAATGACCTGATAGCCTTTGTAGATCTCTCAAAAATAGCTACC
CTCTCCGGCATTAAT

IV.1.S2: 1000-nt scaffold sequence (5'->3')

GTCTCGCTGGTGAAAAGAAAAACCACCCTGGCGCCCAATACGCAAACCGCCTCTCCCCGCGC
GTTGGCCGATTCATTAATGCAGCTGGCACGACAGGTTTCCCGACTGGAAAGCGGGCAGTGAG
CGCAACGCAATTAATGTGAGTTAGCTCACTCATTAGGCACCCCAGGCTTTACACTTTATGCT
TCCGGCTCGTATGTTGTGTGGAATTGTGAGCGGATAACAATTTCACACAGGAAACAGCTATG
ACCATGATTACGAATTCGAGCTCGGTACCCGGGGATCCTCTAGAGTCGACCTGCAGGCATGC
AAGCTTGGCACTGGCCGTCGTTTTACAACGTCGTGACTGGGAAAACCCTGGCGTTACCCAAC
TTAATCGCCTTGCAGCACATCCCCCTTTCGCCAGCTGGCGTAATAGCGAAGAGGCCCGCACC
GATCGCCCTTCCCAACAGTTGCGCAGCCTGAATGGCGAATGGCGCTTTGCCTGGTTTCCGGC
ACCAGAAGCGGTGCCGGAAAGCTGGCTGGAGTGCGATCTTCCTGAGGCCGATACGGTCGTCG
TCCCCTCAAACTGGCAGATGCACGGTTACGATGCGCCCATCTACACCAACGTAACCTATCCC
ATTACGGTCAATCCGCCGTTTGTTCCCACGGAGAATCCGACGGGTTGTTACTCGCTCACATT
TAATGTTGATGAAAGCTGGCTACAGGAAGGCCAGACGCGAATTATTTTTGATGGCGTTCCTA
TTGGTTAAAAAATGAGCTGATTTAACAAAAATTTAACGCGAATTTTAACAAAATATTAACGT
TTACAATTTAAATATTTGCTTATACAATCTTCCTGTTTTTGGGGCTTTTCTGATTATCAACC
GGGGTACATATGATTGACATGCTAGTTTTACGATTACCGTTCATCGATTCTCTTGTTTGCTC
CAGACTCTCAGGCAATGACCTGATAGCCTTTGTAGATCTCTCAAAAATAGCTACCCTCTCCG
GCATTAAT

IV.1.S3: staple sequences and characteristics

Table IV.1.S1: Staple sequences and characteristics to fold the 63-bp edge length tetrahedron from the 1000-nt scaffold.

NAME	SEQUENCE	%GC	TM (°C)
T63_1-212-E	GTGAAATTGTCGCCAGGGTGGTTATTTTTGTCTGTTTCCTGT	42.9	81.1
T63_1-191-E	AATTCCACACAGAGGCGGTTTGCGTATTGGGTATCCGCTCAC	52.4	85.6
T63_2-516-V	AAGATCGCACTTTTTTCCAGCCAGCTAATTCGTAATCTTTTTATGGTCATAGTAAATCAGCTCTTTTTATTTTTTAAC	30.8	81.6
T63_2-716-E	CCATCAAAAAGACGACCGTATCGGCCTCAGGCAATAGGAACG	52.4	85.1
T63_2-695-E	TGGCCTTCCTCATCTGCCAGTTTGAGGGGACTAATTCGCGTC	54.8	86.6
T63_3-398-E	CTATTACGGGGCGATCGGTGCGGGAGGTTACG	62.5	82.9
T63_3-587-E	TTGGTGTATTGACCGTAATGGGATCCTCTTCG	46.9	76.4
T63_3-390-E	CCAGCTGGCGCTGTTGGGAA	65	74.8
T63_4-453-V	TTCGCCATTCATTTTTGGCTGCGCAAAAAGGGGGATGTTTTTTGCTGCAAGGCGGCCAGTGCCTTTTTAAGCTTGCAT	47.4	94.9
T63_4-484-E	CTTCTGGTGCGATCCCCGGGTACCGAGCTCGTTCCGGCACCG	69	93.3
T63_4-463-E	CAAAGCGCCAGCCTGCAGGTCGACTCTAGAGCGGAAACCAGG	61.9	88.9
T63_5-632-V	TCCGTGGGAACTTTTTAAACGGCGGAGATGGGCGCATTTTTTCGTAACCGTGGTAGCCAGCTTTTTTTTCATCAACAT	44.9	92
T63_5-73-E	TCGTGCCACCCGCTTTCCAGTCGGACAACCCG	65.6	88.5
T63_5-640-E	TCGGATTCTAAATGTGAGCGAGTAGAAACCTG	43.8	73.3
T63_5-65-E	GCTGCATTAAGCGCTCACTG	55	66
T63_6-128-V	CTAACTCACATTTTTTTAATTGCGTTTGAATCGGCCATTTTTACGCGCGGGGAACATACGAGCTTTTTCGGAAGCATA	41	89.7
T63_6-325-E	CACGACGTGGGTAACGCCAGGGTTGTGCCTAA	59.4	83.1
T63_6-136-E	TGAGTGAGAAGTGTAAAGCCTGGGTTCCCAGT	50	76.3
T63_6-317-E	TGTAAAACGACGATTAAGTT	30	54

IV.1.S4. Control experiments

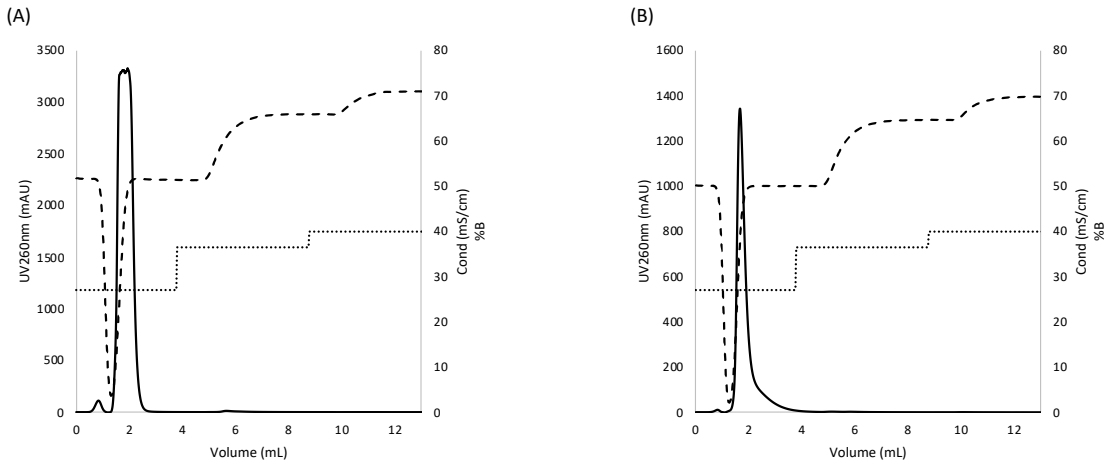

Figure IV.1.S1: Anion exchange chromatography of (A) dNTPs and (B) primers used in the production of ssDNA scaffolds by asymmetric PCR. A feed stream containing either the dNTPS or primers necessary for ten aPCR reactions was injected into a 1 mL Q-Sepharose pre-equilibrated with 540 mM NaCl buffer (27% buffer B, ≈49.5 mS/cm). Unbound material was washed with 2 CV of 27 %B, and stepwise elution was performed with 5 CV of 36.5% B (≈ 64 mS/cm) and 5 CV of 40% B (≈ 69.8 mS/cm). Continuous line: absorbance at 260 nm (mAU); dashed line: conductivity (mS/cm); dotted line: percentage of buffer B (%B).

IV.1.S5. Method reproducibility

(A) **Q-Sepharose**

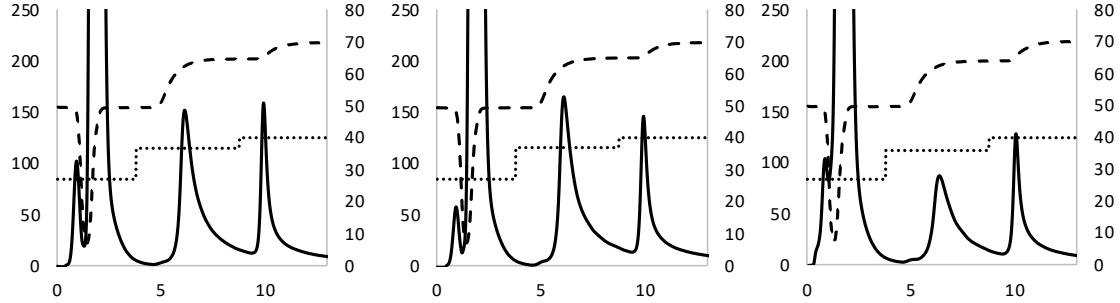

(B) **Capto Q**

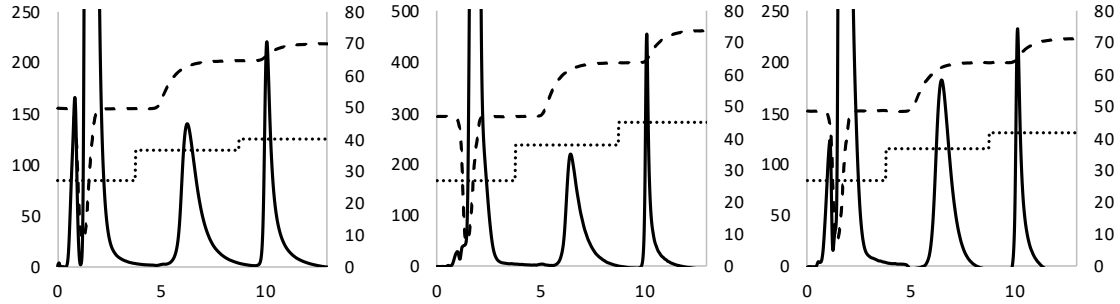

(C) **POROS XQ**

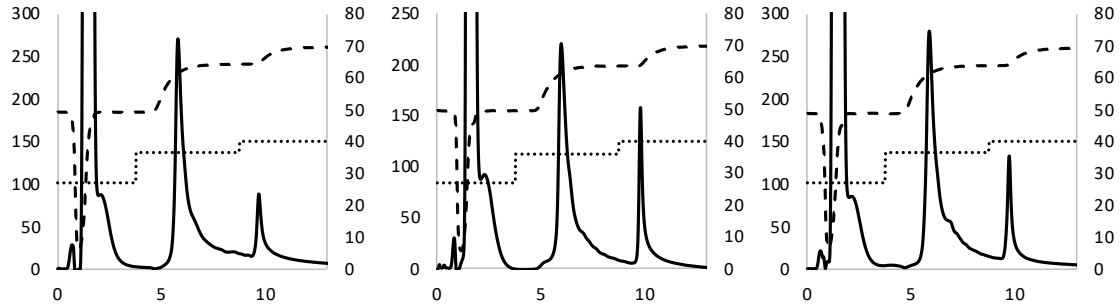

Figure IV.1.S13. Anion exchange chromatography purification of a 1000-nt ssDNA scaffold produced by aPCR from double stranded DNA, unspecific amplification products, dNTPs and excess primers. Independent replicates of a feed stream corresponding to a pool of ten aPCR reactions (500 μL) were injected into 1 mL (A) Q-Sepharose, (B) Capto Q ImpRes and (C) Poros XQ columns pre-equilibrated with 540 mM NaCl buffer (27% buffer B, ≈ 49.5 mS/cm). Unbound material was washed with 2 CV of 27 %B, and stepwise elution was performed with 5 CV of 36.5% B (≈ 64 mS/cm) and 5 CV of 40% B (≈ 69.8 mS/cm). Continuous line represented in the principal yy axis: absorbance at 260 nm (mAU); dashed line: conductivity (mS/cm) and dotted line: percentage of buffer B (%B) represented in the secondary yy axis. Xx axis corresponds to volume (mL).

IV.1.S6. Scale-up

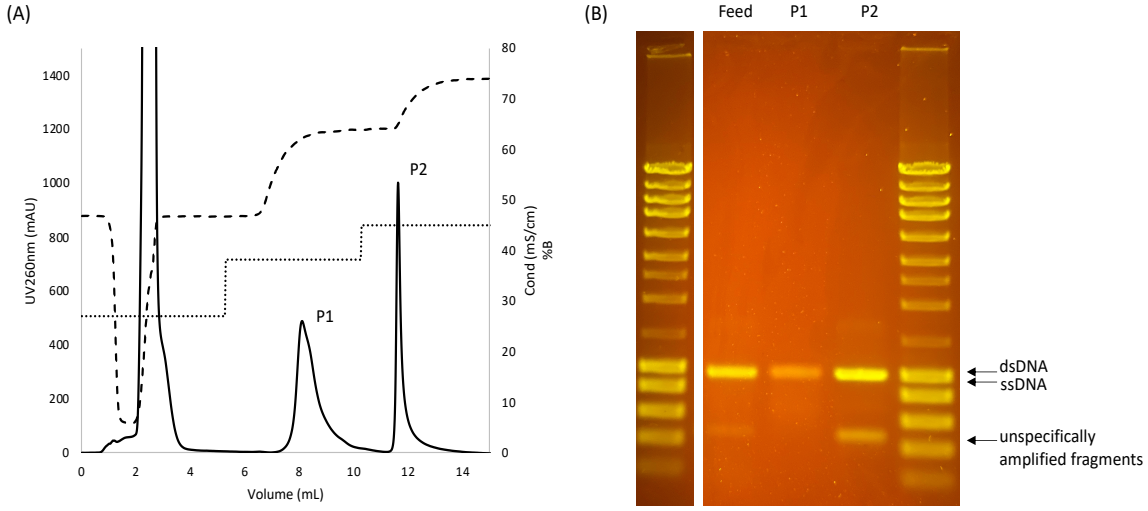

Figure IV.1.S3: Anion exchange purification *of a 1000-nt ssDNA scaffold produced by aPCR from double stranded DNA, unspecific amplification products, dNTPs and excess primers. A feed stream corresponding to a pool of twenty aPCR reactions (1 mL) was injected into 1 mL Capto Q ImpRes column pre-equilibrated with 540 mM NaCl buffer (27% buffer B, ≈49.5 mS/cm). Unbound material was washed with 2 CV of 27 %B, and stepwise elution was performed with 5 CV of 40 %B (≈64 mS/cm) and 5 CV of 45% B (≈ 75 mS/cm). Continuous line: absorbance at 260 nm (mAU); dashed line: conductivity (mS/cm); dotted line: percentage of buffer B (%B). (D) Agarose gel electrophoresis analysis of fractions collected during the chromatographic runs. Fractions collected during the chromatographic runs are marked P1 (step 1, correspondent to ssDNA) and P2 (step 2, correspondent to dsDNA). When excited with blue light illumination (497 nm) the SYBR dye makes it possible to discern between ssDNA (orange band) and dsDNA (yellow/green band).*

CHAPTER IV.2. – QUANTIFICATION OF SSDNA SCAFFOLD PRODUCTION BY ION-PAIR REVERSE PHASE CHROMATOGRAPHY

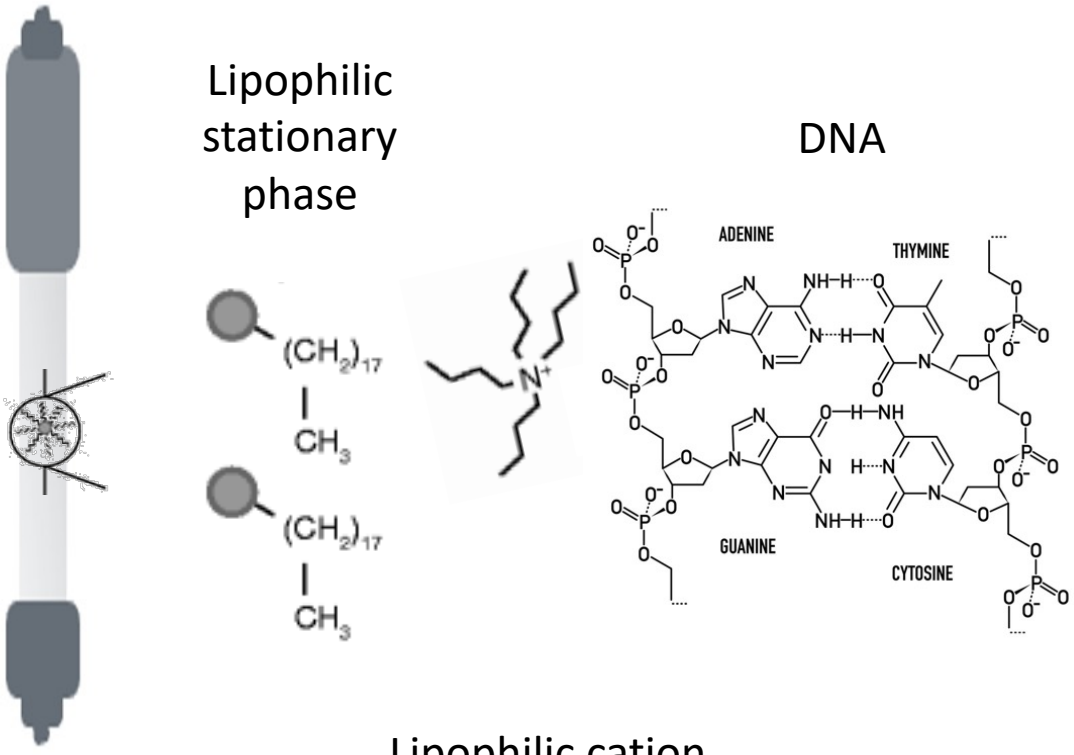

This chapter has been submitted for publishing as: Silva-Santos, A. R., Sousa Rosa, S., Marques, M.P.C., Azevedo, A.M., & Prazeres, D. M. F. Quantification of ssDNA scaffold production by ion-pair reverse phase chromatography.

Abstract

DNA origami is an emerging technology that can be used as a nanoscale platform in numerous applications ranging from drug delivery systems to biosensors. The DNA nanostructures are assembled from large single-stranded DNA (ssDNA) scaffolds, ranging from hundreds to thousands of nucleotides, and from short staple strands. Scaffolds are usually obtained by asymmetric PCR (aPCR) or *E. coli* infection/transformation with phages or phagemids. Scaffold quantification is typically based on agarose gel electrophoresis densitometry, for molecules obtained by aPCR, or by UV absorbance, in the case of scaffolds obtained by infection or transformation. Although these methods are well-established and easy-to-apply, the results obtained are often inaccurate due to the lack of selectivity and sensitivity in the presence of impurities. Herein, we present an HPLC method based on ion pair reverse-phase (IPC) chromatography to quantify DNA scaffolds.

Using IPC, ssDNA products (449 and 1000 nt) prepared by aPCR were separated from impurities and from the dsDNA by-product. Additionally, each type of DNA (ss and ds) was quantified with high accuracy. The Limit of Detection (LOD) and Limit of Quantitation (LOQ) were determined for both DNA species. The method was used to optimize the production of ssDNA by aPCR, by maximizing the ratio of ssDNA to dsDNA obtained. Moreover, ssDNA produced from phage infection was also quantified by IPC using commercial ssDNA from the M13mp18 phage as a standard.

Keywords: asymmetric PCR, DNA origami, HPLC, ion-pair reverse phase chromatography, phage infection, scaffold production

IV.2.1. Introduction

DNA nanotechnology explores the Watson-Crick base pairing to self-assemble nucleic acids into complex nanostructures [1]–[3]. In particular, a strategy denominated "scaffolded DNA origami" can be used where a long single stranded DNA (ssDNA) molecule (the scaffold) is folded into a target shape with the help of short oligonucleotides (the staples) [4]–[6]. Due to the high specificity of this technique, its use has been increasing over the years in a wide range of fields of study, like drug delivery systems [7], [8] and biosensors [9].

The production of scaffold DNA for DNA origami manufacturing is usually performed by (i) purification of phage-derived single-stranded genomic DNA [10], [11] or (ii) asymmetric PCR (aPCR) from DNA templates [5], [12]. Scaffold quantification is typically based on absorbance at 260 nm and/or on agarose gel electrophoresis densitometry. Although both methods are well-established and are easy-to-apply, the results obtained are often inaccurate due to a lack of selectivity and sensitivity of to the presence of impurities. When *E. coli*/phage systems are used to produce ssDNA, phage-derived impurities like proteins, and cell-derived impurities like genomic DNA and debris, will increase absorption at 260 nm, thus contributing to overestimate the scaffold concentration [13], [14]. On the other hand, the use of densitometry analysis of bands in agarose gels will typically underestimate the ssDNA concentration, since the commonly used dye molecules for gel staining intercalate less on ssDNA compared to dsDNA [15]. Different commercially available fluorescent dyes can be used quantify ssDNA with high sensitivity (1 ng/mL), nevertheless they lack sensibility and fluorescence enhancement when bound to double-stranded DNA (dsDNA) and RNA. To overcome these limitations, we present a method based on Ion-Pair Reverse-Phase (IP-RP) high performance liquid chromatography (HPLC) to quantify DNA scaffold production that can be applied throughout the biomanufacturing process.

Over the years, HPLC coupled with UV detection has been used as an analytical tool due to its high selectivity, sensitivity and reproducibility. Moreover, IP-RP is widely described for the separation of nucleic acids, namely DNA fragments [16], [17] and ssRNA [18]. To achieve separation, an ion-pair must be formed by quaternary ammonium compounds present in the mobile phase used with the negatively charged sugar-phosphate backbone of DNA. This ion-pair will then interact with the stationary phase of a reverse-phase chromatography column.

Elution of bound molecules is performed using a solvent, and the separation is dependent on the amount of sugar-backbone of each molecule.

In this work, IP-RP is explored as a methodology to separate and quantify ssDNA scaffolds (449 and 1000 nt long) and the corresponding dsDNA impurities obtained by aPCR. To characterize the method, several attributes are calculated, namely the limit of detection (LOD), limit of quantification (LOQ), decision limit (CCα) and detection capability (CCβ). The method is further employed to optimize the primer ratios that maximize the aPCR production of ssDNA relatively to dsDNA. In a second part of the work, the method was successfully used to quantify the ssDNA genome of the M13mp18 phage. This circular ssDNA molecule is widely used as a scaffold for the DNA-origami production of large objects [19], [20]. Overall, an analytical method that is selective and sensitive was implemented for the separation and quantification of ssDNA molecules, which can be used in multiple steps of the scaffold production process.

IV.2.2. Materials and Methods

IV.2.2.1. Materials

All chemicals and reagents were of analytical grade. Capto Q resin was from GE Healthcare (Uppsala, Sweden). The producer *E. coli* strain K12 ER2738, M13mp18 RF I DNA and M13mp18 ssDNA were from New England Biolabs (Massachusetts, USA). AccustartTM Taq DNA Polymerase Hifi was from Quantabio (Massachusetts, USA). Primers and oligonucleotides were from StabVida (Caparica, Portugal). DNAPac RP column and X2 DNAPacRP guard column were from ThermoFisher (Massachusetts, USA).

IV.2.2.2. Scaffold production

IV.2.2.2.1. M13mp18 ssDNA

M13mp18 ssDNA was produced according to [21]. Briefly, after *E. coli* K12 ER2738 transformation with M13mp18 RFI DNA (GenBank: X02513.1) a blue plaque was selected and used for infection of an *E. coli* pre-culture at an optical density of 0.5 in 5 mL 2xYT medium supplemented with 10 μg/mL tetracycline. After 2h at 37 °C, 250 rpm, cells were transferred

to 750 mL 2xYT supplemented with 10 ug/mL tetracycline and phage expansion occurred overnight in the same conditions. Phage purification and genomic ssDNA extraction were performed according to [11].

IV.2.2.2.2. aPCR mixtures

The target 449 and 1000-nt ssDNA scaffolds were synthesized by aPCR with different ratios of forward to reverse primers. The reaction conditions used were in accordance with [12], [21]. Briefly, a forward primer with a concentration ranging between 4 μM and 500 nM (GTCGTCGTCCCCTCAAACT for 449 nt and GTCTCGCTGGTGAAAAGAAA for 1000 nt), a reverse primer with a concentration ranging between 20 and 500 nM (ATTAATGCCGGAGAGGGTAG), 30 ng of purified M13 ssDNA template, 200 nM deoxynucleotide triphosphates (dNTPs) and 1 unit of Accustart Taq DNA polymerase were mixed in a final volume of 50 μL. The aPCR program consisted of an initial denaturation of 1 min at 94 °C and 35 thermal cycles of (i) 94 °C, 20 s, (ii) 55 °C, 30 s, (iii) 68 °C, 60 s per kilobase amplification.

IV.2.2.3. HPLC

DNA was quantified using IP-RP HPLC. A 2.1 x 100 nm DNAPac RP column and a guard column (3 x 10 nm) (ThermoFisher, USA) were used in a HPLC equipped with a column heater. 15 μL of sample diluted with 1 M of TEAA to a concentration of 0.1 M were injected in a column pre-equilibrated with 0.1 M Triethylamine Acetate (TEAA) (ThermoFisher). Elution was performed using 0.1 M TEAA (ThermoFisher) with 0.25% (v/v) acetonitrile (Fisher). Runs were performed at 60 °C and the absorbance was monitored at 260 nm. The run conditions are presented in the Supplementary Table IV.2.S1. M13mp18 ssDNA standards were prepared with commercially available ssDNA from New England Biolabs and used to construct a calibration curve in the 1 to 4 μg/mL range [18]. Products of 20 pooled aPCR reactions purified according to the method described in [16] were used to construct calibration curves ranging between 0.2 and 20 μg/mL, and 0.2 and 25 μg/mL for ssDNA and dsDNA, respectively. Calibration curves and standard chromatographic profiles for each of the pure samples are shown in supplementary material.

IV.2.2.4. Statistical analysis

Validation of the method was performed by calculating the limit of detection (LOD), limit of quantification (LOQ), the decision limit (CCα) and the detection capability (CCβ), according to the European Union regulation 2002/657/EC guidelines [22]. The limits were calculated based on the standard error of the intercept (σ) and the slope (S) of the calibration curves at a signal-to-noise ratio of 3.3 (LOD) and 10 (LOQ) according to:

$$LOD = \frac{3.3\sigma}{S} \quad (1)$$

$$LOQ = \frac{10\sigma}{S} \quad (2)$$

Calibration curves were performed twice with independent replicates.

CCα and CCβ were calculated considering a 2.33 factor, which corresponds to 1% of false positive risk, and a 1.64 factor, which corresponds to a 5% false negative risk with regards to CCα [22], [23], respectively.

$$CC_\alpha = \frac{2.33\sigma}{S} \quad (3)$$

$$CC_\beta = CC_\alpha + \frac{1.64\sigma}{S} \quad (4)$$

IV.2.3. Results and Discussion

An Ion-pair Reverse Phase Chromatography analytical method was developed for the quantification of DNA scaffolds. Using this method, ssDNA scaffolds (449 nt and 1000 nt) were quantified directly from samples collected from aPCR reaction mixtures. Typical chromatograms (Figure IV.2.1.a) display a flowthrough peak that contains process-related impurities, as demonstrated by injecting control samples with polymerase and dNTPs (result not shown). Upon elution with increased acetonitrile concentration, two peaks with ill-defined shape emerge at 12-15 minutes (see top inset of Figure IV.2.1.a) and at 18-22 minutes (see top inset of Figure IV.2.1.a). Chromatograms were similar whether aPCR mixtures contained ssDNA scaffolds with 449 nt (Figure IV.2.1.a left) or 1000 nt (Figure IV.2.1.a right), albeit residence times varied slightly. To determine the identity of the molecules in the elution peaks, ssDNA scaffolds and the corresponding dsDNA impurities were first isolated from aPCR

mixtures by anion exchange chromatography [24], analyzed by agarose gel electrophoresis (Figure IV.2.1.b) and then injected in the IP-RP column. Results show that the first peak corresponds to ssDNA scaffolds, whereas the second peak to dsDNA.

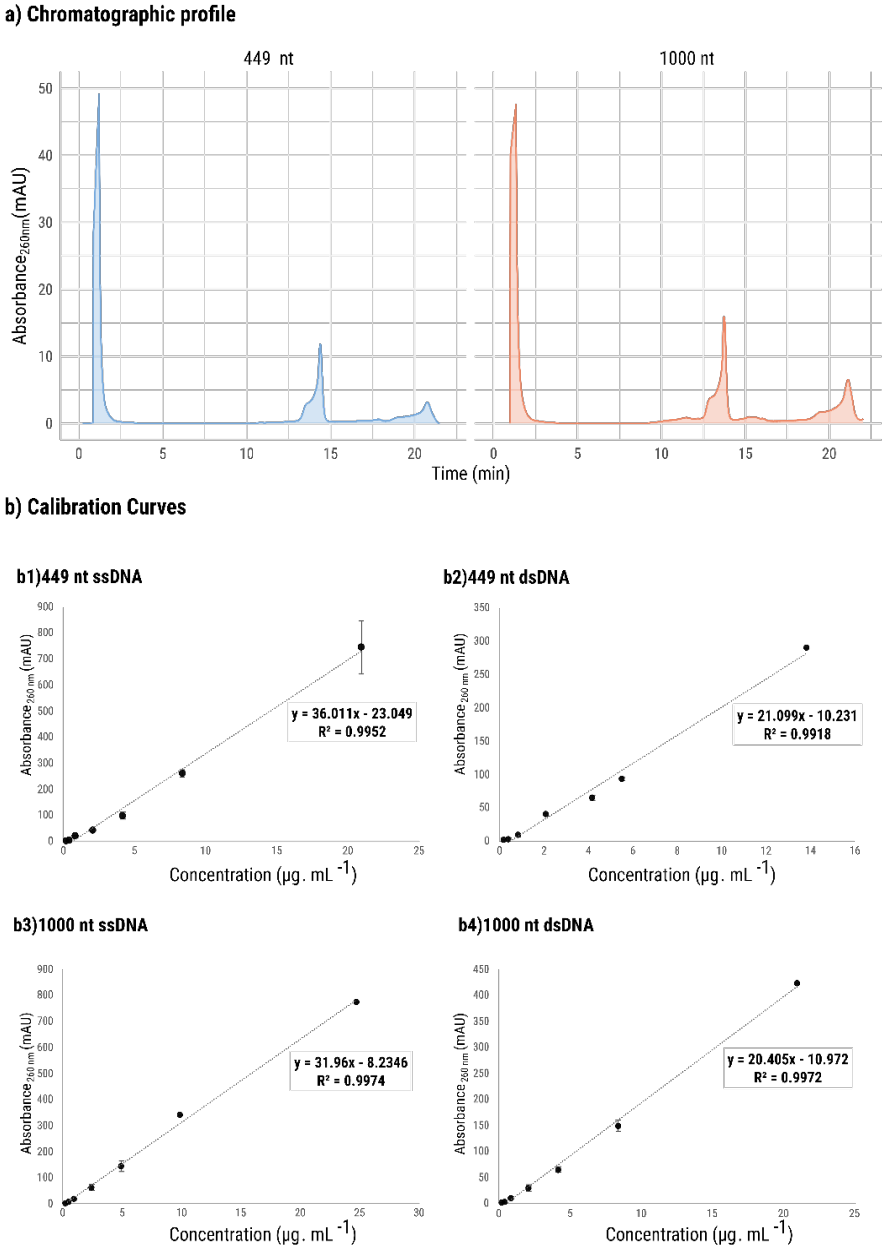

Figure IV.2.14. a) Representative ion-pair reverse phase chromatograms of samples collected from aPCR reaction mixtures used to produce 449 and 1000 nt ssDNA scaffolds. b) Calibration curves and the respective equation calculated for: b1) 449 nt ssDNA; b2) 449 bp dsDNA; b3) 1000 nt ssDNA; b4) 1000 bp dsDNA.

IP-RP chromatography is a well described technique that explores differences in hydrophobicity and is widely used in the separation of nucleic acids [25]. Optimization of the eluent gradient and column temperature are considered the key factors for the separation of dsDNA and ssDNA. Temperature seems to be an important factor on the separation as it can

affect the physical properties of the DNA [26]. For DNA molecules to form an ion-pair with a cationic ion-pair reagent (IPR) such as TEAA, phosphate groups in the backbone must be exposed. Then, the carbon atoms of the alkyl chains of the IP will form a hydrophobic bond with the stationary phase [27]. Exposure of the phosphate groups is facilitated if one interferes with the secondary structure of the DNA, for example by performing the separation at a temperature of 60 °C. Since dsDNA contains twice the number of phosphate groups when comparing with the corresponding ssDNA, the binding with the solid phase will be stronger. Concomitantly, a higher concentration of acetonitrile is required for elution, as observed in Figure IV.2.1.a.

To validate the analytical chromatography method proposed, a number of attributes were calculated, namely the LOD, LOQ, CCα and CCβ. The LOD corresponds to the smallest concentration of analyte that can be confidently quantified by the method, while the LOQ is the smallest concentration that can be quantified with a given level of confidence [28]. The results for both 449 and 1000 bp scaffolds are shown in Table IV.2.1. Although the TEAA buffer used is known to suppress the absorbance signal [29], the method presents LODs of 0.89 μg/mL (ssDNA) and 0.79 μg/mL (dsDNA) for the 449 nt scaffold, and 0.78 μg/mL (ssDNA) and 0.68 μg/mL (dsDNA) for the 1000 nt scaffold. The difference in the LOD observed between the different length scaffolds and between single stranded or double stranded DNA can be correlated with the molecule's mass. Higher mass will require less sample concentration to be detected, which in this case means that dsDNA with 1000 bp has the lowest LOD observed.

Table IV.2.2. HPLC attributes for the 449 and 1000 bp scaffolds, single and double stranded, in terms of limit of detection (LOD), limit of quantification (LOQ), the decision limit (CCα) and the detection capability (CCβ).

	449 nt/bp		1000 nt/bp	
	ss	ds	ss	ds
LOD (µg/mL)	0.89	0.79	0.78	0.68
LOQ (µg/mL)	2.70	2.40	2.36	2.07
CCα (µg/mL)	0.63	0.56	0.55	0.48
CCß (µg/mL)	1.07	0.95	0.94	0.82

The CCα and CCβ are described by the European Commission Decision 2002/657/EC as the limit at and above which the sample is considered to be non-compliant, with an error probability of α; and the smallest analyte quantity that may be detected, identified or quantified with an error probability of β, respectively [22]. The CCβ and CCα values for both ss and dsDNA can be found in Table IV.2.1. As previously observed, it seems that higher mass molecules, in this case 449 and 1000 nt dsDNA, present lower values for CCα and CCβ.

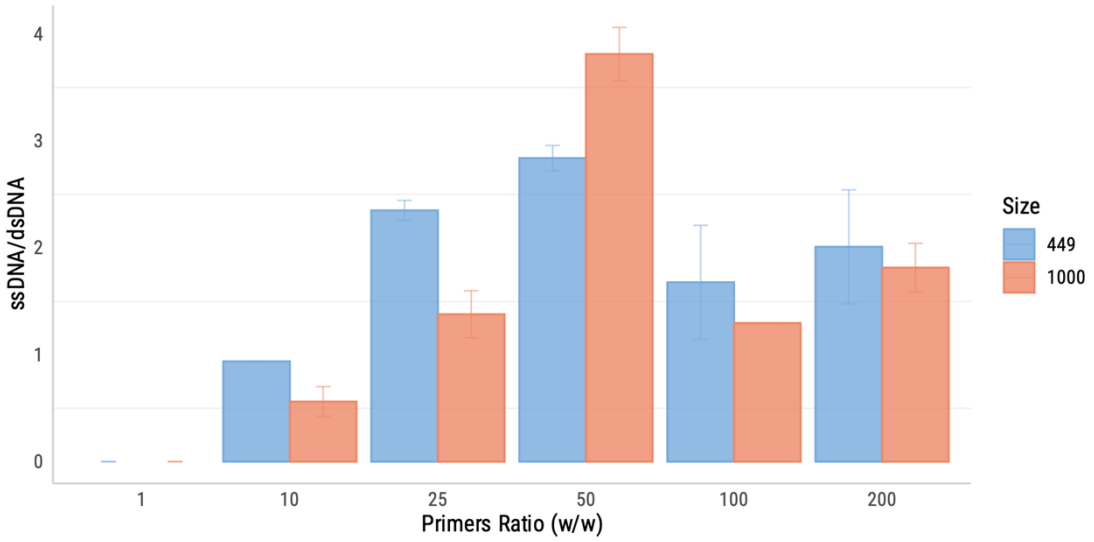

Figure IV.2.2. Optimization of the aPCR reaction in terms of ssDNA/dsDNA ratio. Optimization was performed so that the highest yield possible of ssDNA is obtained relatively to the dsDNA production. The ssDNA/dsDNA ratio was determined using the IP-RP chromatography method described.

The IP-RP HPLC method was used next to optimize the production of ssDNA scaffolds by aPCR, an amplification method that uses a molar excess of the forward primer over the reverse primer [12], [30]. The optimization was performed by varying the molar ratio between the reverse and forward primers from 1 to 200 (w/w) and then evaluating the ratio of mass of ssDNA to mass of dsDNA produced. The results are presented in Figure IV.2.2. The highest amount of ssDNA is obtained with a 50-molar excess of forward primer for both DNA sizes, 2.84 ± 0.08 ratio for 449 bp and 3.81 ± 0.18 for 1000 bp. Increasing the primers ratio above 50 negatively impact the aPCR yield. These results are in line with the results obtained by Veneziano *et al* [12], determined on the basis of gel electrophoresis analysis.

The IP-RP method was also evaluated to quantify M13mp18 ssDNA. A calibration curve was prepared using standards of commercial M13mp18 ssDNA at concentrations varying

from 1 to 40 μg/mL. A typical chromatogram of a standard (see Figure IV.2.S2, supplementary material) displays a peak with ill-defined shape eluting at 13-15 minutes. The method was again validated by calculating LOD, LOQ, CCα and CCβ. As observed in Figure IV.2.3(b), a LOD and LOQ of 1.45 and 4.4 μg/mL were obtained, respectively. In the case of CCα and CCβ, the values obtained were 1.03 and 1.75 μg/mL.

a) Chromatographic profile

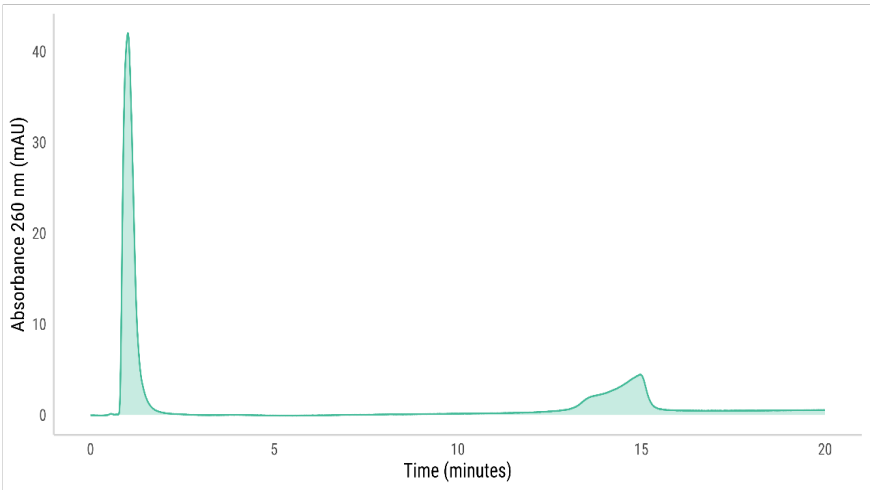

b) Attributes

LOD (µg/mL)	LOQ (µg/mL)	CCα (µg/mL)	CCß (µg/mL)
1.45	4.40	1.03	1.75

c) Calibration curve

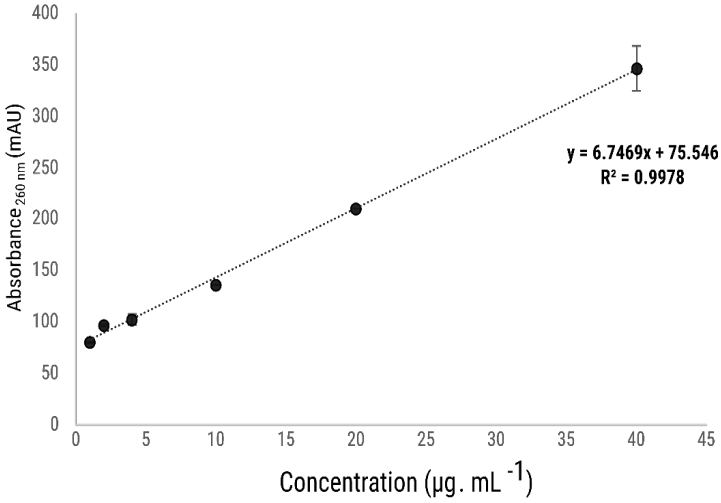

Figure IV.2.3. a) Representative ion-pair reverse phase chromatography profile of the M13mp18 ssDNA extracted from M13 phage. b) Attributes for the M13mp18 ssDNA extracted from M13 phage, in terms of limit of detection (LOD), limit of quantification (LOQ), the decision limit (CCα) and the detection capability (CCβ). C) Calibration Curve for the M13mp18 ssDNA.

The method was then used to quantify M13mp18 ssDNA extracted from M13 phage. A concentration of 126.25 $\pm$ 8.60 μg/mL was obtained. This value is lower than the one obtained when performing quantitation by UV absorbance at 260 nm (198.15 $\pm$ 2.95 μg/mL). Nevertheless, this difference is expected due to the lack of specificity presented by spectrophotometric techniques, which means that impurities can increase the obtained signal.

IV.2.4. Conclusions

DNA scaffold production is a crucial step for DNA-origami technology. However, current quantification methods rely on the use of techniques that are neither specific or sensitive enough, leading to erroneous estimations of the actual scaffold quantities produced and therefore, of the amount of DNA-origami nanostructures that can be produced. In this work, a HPLC method based on IP-RP was used to quantify different size scaffolds produced either by aPCR techniques or by infecting *E. coli* cells with the M13 phage. The method is sensitive, accurate and specific and delivers reliable titer measurements, making it a powerful tool for quantification of ssDNA scaffolds no matter the production system used.

IV.2.5. References

[1] N. C. Seeman and H. F. Sleiman, “DNA nanotechnology,” *Nat. Rev. Mater.*, vol. 3, 2017.
[2] P. W. K. Rothemund, “Folding DNA to create nanoscale shapes and patterns,” *Nature*, vol. 440, no. 7082, pp. 297–302, 2006.
[3] F. Zhang, J. Nangreave, Y. Liu, and H. Yan, “Structural DNA nanotechnology: State of the art and future perspective,” *J. Am. Chem. Soc.*, vol. 136, no. 32, pp. 11198–11211, 2014.
[4] W. M. Shih, J. D. Quispe, and G. F. Joyce, “A 1.7-kilobase single-stranded DNA that folds into a nanoscale octahedron,” *Nature*, vol. 427, no. 6975, pp. 618–621, 2004.
[5] R. Veneziano *et al.*, “Designer nanoscale DNA assemblies programmed from the top down,” *Science*, vol. 352, no. 6293, 2016.
[6] C. E. Castro *et al.*, “A primer to scaffolded DNA origami,” *Nat. Methods*, vol. 8, no. 3, pp. 221–229, 2011.
[7] S. M. Douglas, I. Bachelet, and G. M. Church, “A Logic-Gated Nanorobot for Targeted Transport of Molecular Payloads,” *Science*, vol. 335, no. February, pp. 831–834, 2012.
[8] J. Yan, C. Hu, X. Liu, J. Zhong, G. Sun, and D. He, “Recent Developments of New DNA Origami Nanostructures for Drug Delivery,” *Curr. Pharm. Des.*, vol. 21, no. 22, pp. 3181–3190, 2015.

[9] H. Pei *et al.*, "A DNA Nanostructure-based Biomolecular Probe Carrier Platform for Electrochemical Biosensing," *Adv. Mater.*, vol. 22, no. 42, pp. 4754–4758, 2010.

[10] F. Praetorius, B. Kick, K. L. Behler, M. N. Honemann, D. Weuster-Botz, and H. Dietz, "Biotechnological mass production of DNA origami," *Nature*, vol. 552, no. 7683, pp. 84–87, 2017.

[11] B. Kick, K. L. Behler, T. S. Severin, and D. Weuster-Botz, "Chemostat studies of bacteriophage M13 infected Escherichia coli JM109 for continuous ssDNA production," *J. Biotechnol.*, vol. 258, no. January, pp. 92–100, 2017.

[12] R. Veneziano, T. R. Shepherd, S. Ratanalert, L. Bellou, C. Tao, and M. Bathe, "In vitro synthesis of gene-length single-stranded DNA," *Sci. Rep.*, vol. 8, no. 1, pp. 1–7, 2018.

[13] C.-H. Shen, "Detection and Analysis of Nucleic Acids," *Diagnostic Mol. Biol.*, pp. 167–185, 2019.

[14] K. L. Behler, M. N. Honemann, A. R. Silva-Santos, H. Dietz, and D. Weuster-Botz, "Phage-free production of artificial ssDNA with Escherichia coli," *Biotechnol. Bioeng.*, no. January, pp. 1–12, 2022.

[15] M. R. Green and J. Sambrook, "Analysis of DNA by agarose gel electrophoresis," *Cold Spring Harb. Protoc.*, vol. 2019, no. 1, pp. 6–15, 2019.

[16] S. Eriksson, G. Glad, P. Å. Pernemalm, and E. Westman, "Separation of DNA restriction fragments by ion-pair chromatography," *J. Chromatogr. A*, vol. 359, no. C, pp. 265–274, 1986.

[17] C. G. Huber, G. K. Bonn, and P. J. Oefner, "Rapid and Accurate Sizing of DNA Fragments by Ion-Pair Chromatography on Alkylated Nonporous Poly(Styrene-Divinylbenzene) Particles," *Anal. Chem.*, vol. 67, no. 3, pp. 578–585, 1995.

[18] K. Karikó, H. Muramatsu, J. Ludwig, and D. Weissman, "Generating the optimal mRNA for therapy: HPLC purification eliminates immune activation and improves translation of nucleoside-modified, protein-encoding mRNA," *Nucleic Acids Res.*, vol. 39, no. 21, pp. 1–10, 2011.

[19] B. Kick, F. Praetorius, H. Dietz, and D. Weuster-Botz, "Efficient Production of Single-Stranded Phage DNA as Scaffolds for DNA Origami," *Nano Lett.*, vol. 15, no. 7, pp. 4672–4676, 2015.

[20] S. M. Douglas, H. Dietz, T. Liedl, B. Högberg, F. Graf, and W. M. Shih, "Self-assembly of DNA into nanoscale three-dimensional shapes," *Nature*, vol. 459, no. 7245, pp. 414–418, 2009.

[21] A. Rita Silva-Santos, R. Oliveira-Silva, S. Sousa Rosa, P. M. R. Paulo, and D. Miguel F. Prazeres, "Affinity-Based Magnetic Particles for the Purification of Single-Stranded DNA Scaffolds for Biomanufacturing DNA-Origami Nanostructures," *ACS Appl. Nano Mater.*, vol. 4, no. 12, pp. 14169–14177, Nov. 2021.

[22] E. Commission, "Commission Decision 2002/657/EC of 12 August 2002 implementing Council Directive 96/23/EC concerning the performance of analytical methods and the interpretation of results," *Off. J. Eur. Communities*, vol. 50, pp. 8–36, 2002.

[23] J. Van Loco, A. Jànosi, S. Impens, S. Fraselle, V. Cornet, and J. M. Degroodt, "Calculation of the decision limit (CCα) and the detection capability (CCβ) for banned substances: The imperfect marriage between the quantitative and the qualitative criteria," *Anal. Chim. Acta*, vol. 586, no. 1-2 SPEC. ISS., pp. 8–12, 2007.

[24] A. R. Silva-Santos, P. M. R. Paulo, and D. M. F. Prazeres, "Scalable purification of single stranded DNA scaffolds for biomanufacturing DNA-origami nanostructures: exploring

anion-exchange and multimodal chromatography," *Sep. Purif. Technol.*, p. 121623, 2022.

[25] A. Premstaller, H. Oberacher, and C. G. Huber, "High-performance liquid chromatography-electrospray ionization mass spectrometry of single- and double-stranded nucleic acids using monolithic capillary columns," *Anal. Chem.*, vol. 72, no. 18, pp. 4386–4393, 2000.

[26] J. M. Devaney, J. E. Girard, and M. A. Marino, "DNA microsatellite analysis using ion-pair reversed-phase high- performance liquid chromatography," *Anal. Chem.*, vol. 72, no. 4, pp. 858–864, 2000.

[27] A. Kaczmarkiewicz, Ł. Nuckowski, S. Studzińska, and B. Buszewski, "Analysis of Antisense Oligonucleotides and Their Metabolites with the Use of Ion Pair Reversed-Phase Liquid Chromatography Coupled with Mass Spectrometry," *Crit. Rev. Anal. Chem.*, vol. 49, no. 3, pp. 256–270, 2019.

[28] J. Vial and A. Jardy, "Experimental comparison of the different approaches to estimate LOD and LOQ of an HPLC method," *Anal. Chem.*, vol. 71, no. 14, pp. 2672–2677, 1999.

[29] M. Gilar, K. J. Fountain, Y. Budman, J. L. Holyoke, H. Davoudi, and J. C. Gebler, "Characterization of Therapeutic Oligonucleotides Using Liquid Chromatography with On-line Mass Spectrometry Detection," *Oligonucleotides*, vol. 13, no. 4, pp. 229–243, 2003.

[30] C. I. Wooddell and R. R. Burgess, "Use of asymmetric PCR to generate long primers and single-stranded DNA for incorporating cross-linking analogs into specific sites in a DNA probe," *Genome Res.*, vol. 6, no. 9, pp. 886–892, 1996.

Supplementary Material

IV.2.S1. IP-RP HPLC gradient method

Table IV.2.S1. IP-RP HPLC gradient method. Binding buffer: 0.1M TEAA. Elution buffer: 0.1 M TEAA, 25% acetonitrile (v/v).

Time (min)	Binding buffer (%)	Elution buffer (%)
0	65	35
18.0	45	55
19.2	0	100
22.0	0	100
22.2	65	35
30	65	35

IV.2.S2. IP-RP HPLC chromatograms of pure samples

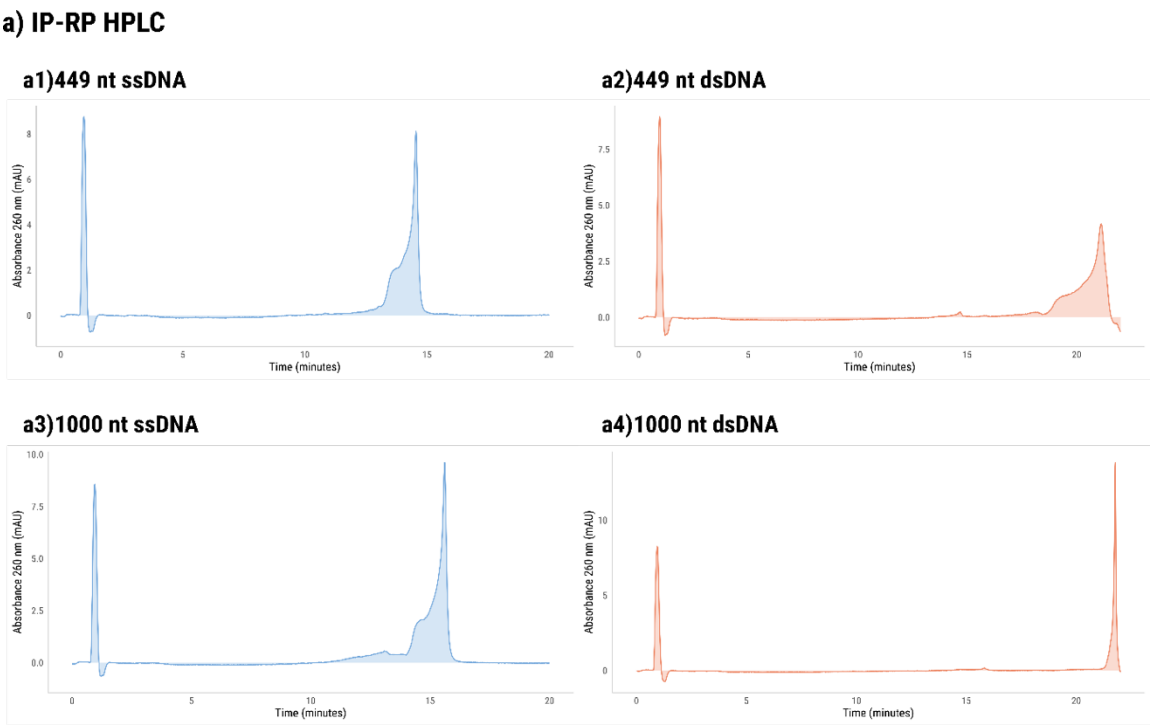

Figure IV.2.S1. a) IP-RP HPLC chromatograms of: a1) pure 449 nt ssDNA; a2) pure 449 bp dsDNA; a3) pure 1000 nt ssDNA; a4) pure 1000 bp dsDNA. b) Agarose Gel Electrophoresis of the 449 nt and 1000 nt samples.

IV.2.S2. IP-RP HPLC chromatograms of commercial M13mp18 ssDNA

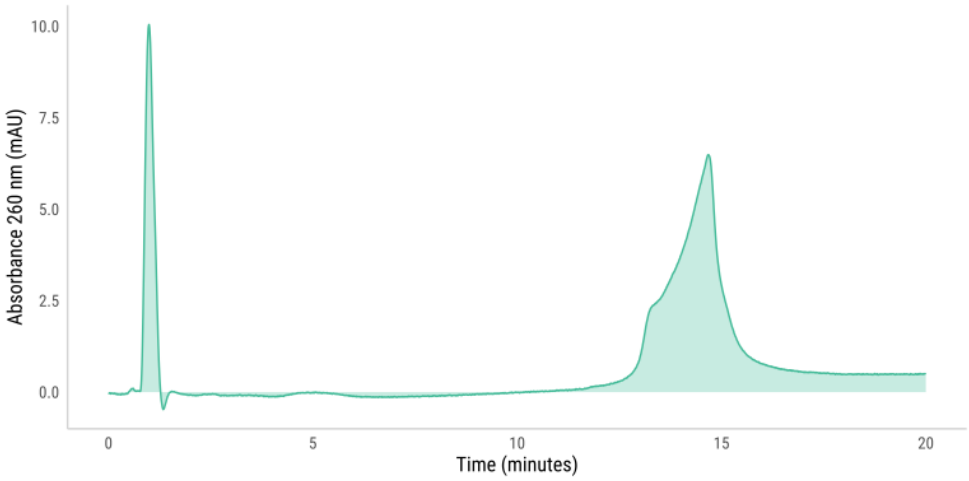

Figure IV.2.S2. IP-RP HPLC chromatogram of ssDNA from M13mp18 phage (New England Biolabs).

CHAPTER V – FLUORESCENTLY-LABELLED DNA-ORIGAMI NANOSTRUCTURES FOR BIO-IMAGING AND DRUG DELIVERY APPLICATIONS

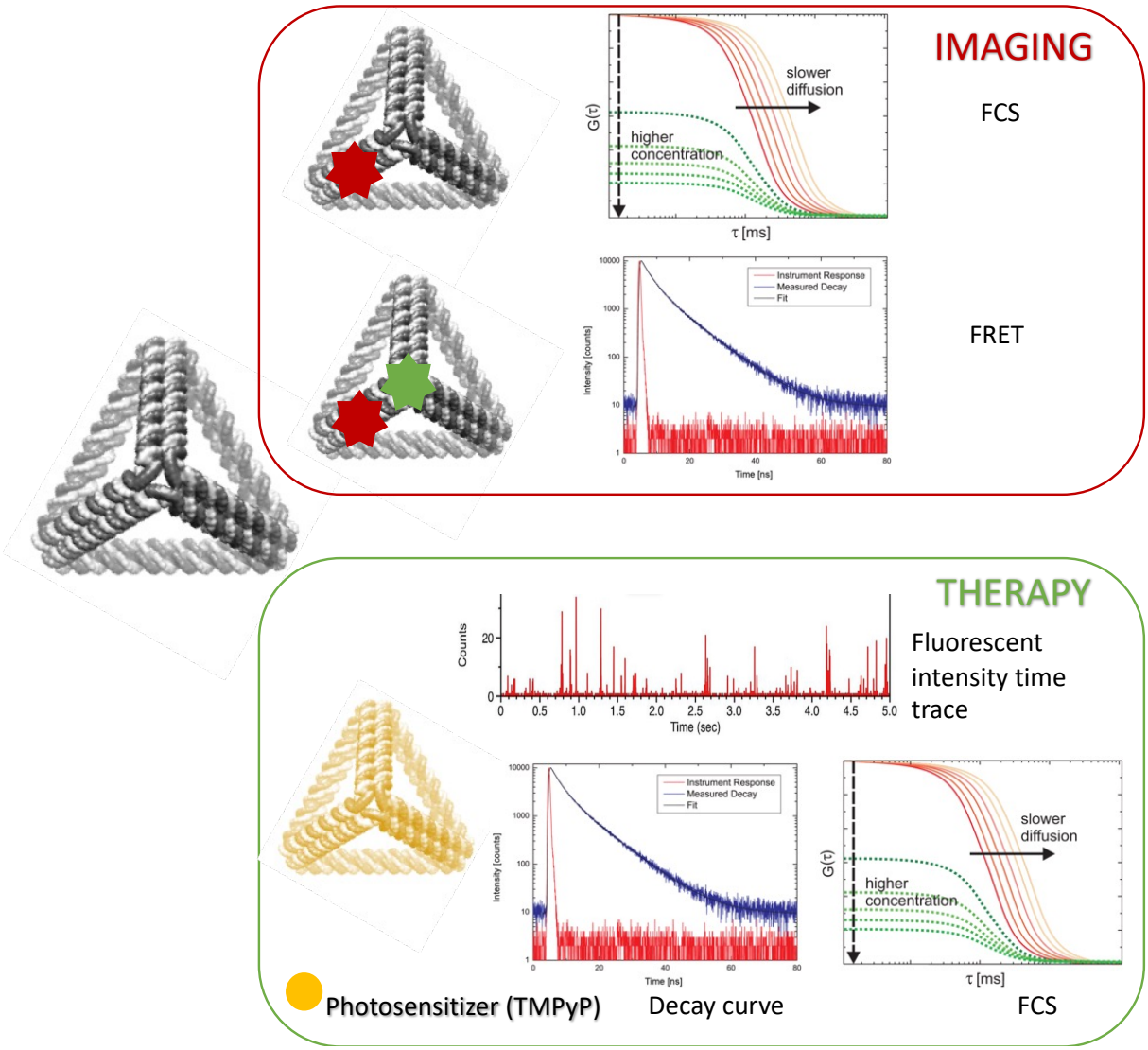

Abstract

DNA origami is an emerging technology in several fields of study due to its reproducibility, flexibility, scalability, and biocompatibility. Moreover, since a conformational change can be induced upon specific interaction, the possibility of drug release or production of a physical signal makes it a powerful tool to be explored for drug delivery or as a contrast agent. Even though the most common approach to evaluate the folding quality of the final product is through microscopy techniques, such as transmission electron microscopy or atomic force microscopy, the use of smaller structures requires alternatives. Here, 31 and 63-base pair edge length tetrahedrons were used as model for the development of indirect methods to address DNA-origami folding quality. Also, the possibility of intercalating a photosensitizer intended for photodynamic therapy into its structure was evaluated.

In a first step, a single-labelled DNA-origami tetrahedron was analyzed by fluorescence correlation spectroscopy. A comparison of the diffusion coefficient of the scaffolds and folded tetrahedrons confirmed that the diffusion coefficient decreases as the size of the structure increases. Also, single-molecule analysis of the labelled tetrahedra was performed and the on-off signal was evaluated. Next, the folding reaction was followed by real-time PCR using FAM-ROX as FRET pair since as folding takes place it opens a channel for energy transfer, thereby increasing the fluorescent signal of the acceptor dye. Then, an agarose gel electrophoresis was performed to determine band sharpness and migration distance, allowing the distinction between the correct folded structure and multimers, misfolded and/or partially assembled intermediates. Finally, intercalation of a photosensitizer (TMPyP) into the tetrahedron was accomplished by comparing the decay time of the free TMPyP with that intercalated into the DNA-origami.

Keywords: DNA-origami, bioimaging, fluorescence correlation spectroscopy, Förster resonance energy transfer, photodynamic therapy.

V.1. Introduction

DNA nanostructures formed by hybridization of DNA strands via Watson-Crick base pairing are finding applications in innumerous fields of research due to their versatility, biocompatibility and biostability [1]–[3]. Two different approaches have been used for the design of these nanostructures: either by promoting the hybridization of four short single-stranded DNA (ssDNA) [4] or through the "scaffolded DNA-origami" technique, where a long ssDNA molecule (the scaffold) is folded into the desired shape with the help of several short oligonucleotides (the staples) [2]. Even though the first approach offers structural simplicity and rigidity, problems of instability, unwanted by-products and low yield led to a growing interest in DNA-origami strategies. Moreover, DNA-origami offers the possibility of constructing larger structures, the underlying scaffold strand has a heterogenous sequence and each staple strand can be used for the placement of accessory molecules at virtually any site in the structure with nanometer precision [5].

A key aspect on the use of DNA-origami technology is its structural integrity. Although it is strongly dependent on the surrounding environment conditions, including metal ion concentrations, pH, enzyme components, and covalent linkages, previous studies have shown the stability of these structures for years *in vitro* under low temperatures and for 24h *in vivo* [6], [7] which makes DNA-origami a powerful tool for bioimaging and/or drug delivery systems.

Regarding bioimaging applications, DNA-origami nanostructures allow the incorporation of various non-DNA nano-objects like fluorescent dyes, quantum dots (QD) or radionuclides with a nanometer precision [3]. Even though vesicles or polymer micelles have been reported as hosts of imaging components through encapsulation, there are detrimental side-effects such as fluorescence self-quenching [8]. On the other hand, DNA-origami nanostructures can deliberately induce or avoid quenching by precisely arranging fluorophores and/or quenchers at controlled distances [3]. An example of this is the work developed by Schmied *et al.* were a rectangle, bundles and a nanopillar DNA-origami were used as nanoscopic rulers for calibration of super-resolution fluorescence microscopes [9]. Moreover, modified-DNA probes can also be incorporated. For example, the work from Wei *et al.* showed that Förster resonance energy transfer (FRET) can be used to visualize the structure folding path [10].

Considering *in vivo* applications, even though QDs present a poor cellular internalization and cytotoxicity, its loading onto gold nanoparticles functionalized with DNA-origami and cell-penetrating peptides resulted in lower cytotoxicity, strong fluorescence visualization and improved uptake into human glioblastoma cells [11]. Another example was the use of a tubular DNA-origami nanostructure combined with carbazole-based biscyanine, a molecular probe which has the characteristic property of emission recovery by restriction of intramolecular rotation. Upon loading the probe molecules, the DNA-origami structures displayed strong fluorescence emission allowing them to be easily tracked *in vivo*. Further, intracellular imaging could be used to deduce the total time necessary for DNA-origami to enter breast cancer cells and for complete degradation of the structures [12].

Regarding the use of DNA-origami nanostructures as drug delivery systems a lot of work has been done in the field. On a first approach, the use of these objects allow control over the amount of loaded drug and promote the cellular internalization of drug molecules, which may normally struggle to accumulate in cells [3]. Douglas *et al.* achieved a controlled release of antibody fragments using a DNA nanorobot capable of logic gate operation, molecular recognition and sensing, and smart release of payloads [13]. A similar device was developed by Burns *et al.*, where a DNA-origami cube could recognize target sites and release protein under acidic conditions using a reversible open and close lid [14].

Another approach is the administration of DNA intercalator drugs such as doxorubicin and daunorubicin [3]. Zhao *et al.* fabricated DNA-origami nanotubes for tunable release of doxorubicin. This was achieved by introducing different degrees of global twist and structural relaxation into the design since the more tightly-twisted DNA nanotube exhibited greater cytotoxicity and a lower rate of intracellular elimination compared to free doxorubicin when applied in breast cell cancer lines [15]. Similarly, Jiang *et al.* loaded doxorubicin onto a DNA-origami triangle and a tube with an efficiency of 60-70%. Both designs exhibited dramatically higher rates of death for drug resistant cells due to higher doxorubicin internalization when compared to free doxorubicin and doxorubicin-loaded double-stranded M13 DNA [16].

Like doxorubicin, daunorubicin, an anthracycline for which drug resistance has widely spread, was loaded with high efficiency onto a rod-like DNA-origami. This increased uptake and retention of the drug, helping overcome daunorubicin resistance in leukemia cells. When

compared with the behavior of free daunorubicin, its intercalation onto the origami increased the amount of drug delivered intracellularly, prevented drug efflux, and therefore circumvented efflux-pump-mediated drug resistance [17].

To improve cellular uptake, drug delivery, and administration of DNA-origami, various targeting ligands can be attached to the DNA-origami structure. One example is the incorporation of aptamers, a class of artificial nucleic acids, onto DNA-origami. These aptamers can recognize membrane receptors, induce aptamer-receptor mediated endocytosis in HeLa cells, a human cervical carcinoma cell line, and significantly enhance doxorubicin delivery efficiency [18], [19]. Another alternative is the incorporation of small molecules, as shown with the design developed by Ge et al. In this case, a six helix bundle DNA-origami was modified with a ligand 2-[3-(1,3-dicarboxyl propyl)-ureido] pentanedioic acid against prostate-specific membrane antigen, to serve as the antibody for drug conjugation in antibody-drug conjugate-like carrier for targeted prostate cancer therapy. The internalization efficiency for ligand-modified DNA-origami was highest in prostate-specific membrane antigen positive tumor cells due to the specific binding of targeting ligands and antigens [20].

Drug delivery via DNA-origami technologies have also been reported *in vivo*, namely by Zhang *et al.*, who used a triangle-shaped DNA-origami nanostructure to deliver doxorubicin to breast tumor cells, demonstrating a high passive tumor targeting accumulation without system toxicity [21]. Another example was the use of an autonomous DNA nanorobot to deliver a protein for therapeutic effects. The outside surface of this robot was functionalized with a DNA aptamer that, when in contact with the target nucleolin, triggered the structure to open and expose conjugated thrombin within its inner cavity, therefore prompting coagulation, necrosis and inhibition of tumor growth *in vivo* [22].

Another alternative for drug delivery using DNA-origami nanostructures is through the use of photothermal and photodynamic therapies, which are physical stimuli-responsive treatments triggered by light induced energy conversion [3]. Jiang *et. al* demonstrated that the use of a DNA-origami/gold nanorod complex exhibited enhanced cellular uptake and photothermolysis when administered to tumor-bearing nude mice. Along with efficient intracellular accumulation both *in vitro* and *in vivo*, the use of thermal imaging and near-

infrared laser irradiation revealed that this complex could burn and damage tumors more effectively than gold nanorods or DNA-origami alone [23]. Moreover, the same group demonstrated that these photothermal gold nanorods could be combined with doxorubicin delivery since near-infrared laser irradiation-stimulation could down-regulate a multidrug resistance pump protein and enhance the chemotherapy effect [24]. Photosensitizers, such as 6-bis[2-(1-methylpyridinium) ethynyl]-9-pentylcarbazole diiodide (BMEPC), could also be useful for photodynamic therapy, but their poor solubility in water limits their biomedical applications. To overcome this, BMEPC molecules were intercalated into DNA-origami nanostructures, and as a result, DNA-origami structures demonstrated fluorescence for imaging and generated free radicals under near-infrared light excitation to induce tumor cell apoptosis [25].

In this work, 31 and 63-bp edge length tetrahedrons were used as models for bioimaging and as a photosensitizer carrier for photodynamic therapy. In a first approach, the diffusion time and hydrodynamic radius of single-labelled DNA tetrahedrons were assessed by fluorescence correlation spectroscopy (FCS). Also, single-molecule fluorescence measurements were performed, and the decay times and on-off behavior of individual fluorophore was evaluated. Next, the tetrahedrons were dual-labelled with a FRET pair in order to observe energy transfer as the folding process takes place. Finally, the possibility of intercalating the cationic porphyrin meso-tetra(4-N-methylpyridyl)porphine (TMPyP), as a photosensitizer used in photodynamic therapy, was assessed (Fig. V.1). TMPyP has already showed some potential on achieving anti-tumor effects and reduce resistance to therapy [26], [27].

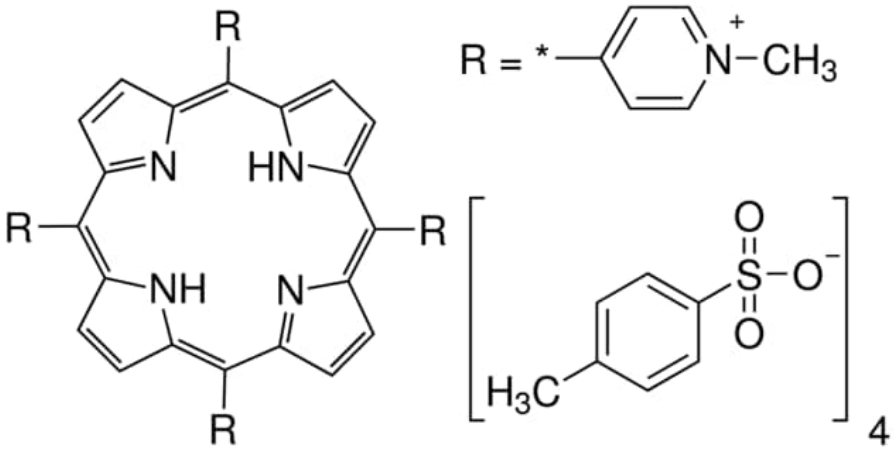

Figure V.1. Chemical structure of the TMPyP used in intercalation experiments.

V.2. Materials and Methods

V.2.1. Materials

All salts used were of analytical grade. Oligonucleotides were obtained from Stab Vida (Caparica, Portugal). Cy5 dye was obtained from Lumiprobe (USA).

V.2.2. Design, folding and purification of DNA-origami objects

Design of staple strands to fold 31 and 63-bp edge length tetrahedrons was performed with the DAEDALUS [28] software by inputting the sequences of the 449 and 1000-nt ssDNA scaffolds obtained according to [29]. DNA-origami assembly and purification was performed by slightly adapting the methods described in [28], [30]. Unless stated otherwise, 20 nM scaffold strand was mixed with 100 nM of a mix of staple strands in 50 μL of FoB15 buffer (15 mM $MgCl_2$, 5 mM NaCl, 1 mM EDTA, 5 mM Tris). Annealing was performed in a thermal cycler and a temperature ramp was performed between 60 and 40 °C at a rate of 1 °C/h. The final tetrahedra solution was purified with an Amicon Ultra-0.5 mL centrifugal filter with a molecular weight cut-off of 100 kDa by diafiltrating 5 times with FoB5 buffer (5 mM $MgCl_2$, 5 mM NaCl, 1 mM EDTA, 5 mM Tris) to remove excess staple strands. Scaffolds and staple sequences are in Supplementary Material.

V.2.3. Time-resolved fluorescence microscopy: FCS and FLIM

Fluorescence microscopy was performed on a Microtime 200 setup from PicoQuant GmbH (Germany). The excitation source used were pulsed diode lasers emitting at 482 nm or 639 nm with a repetition rate of 20 MHz (LDH-P-C-485 or LDH-635-b, PicoQuant GmbH). In FCS measurements, the laser beam was focused 10 μm inside the sample by means of a water immersion objective of N.A. 1.2 (UPlanSApo 60x, Olympus). Fluorescence emission was collected by the same objective and cleaned by a dichroic filter (485DRLP, Omega) and by a bandpass filter with transmission range between ca. 528 and 562 nm (545AF35, Omega). Out-of-focus light was rejected by means of a 50 μm pinhole. The collected emission was detected by single-photon avalanche diode detectors (SPCM-AQR-13, Perkin Elmer).

For FRET experiments two channels were used with transmission ranges between ca. 528 and 562 nm (545AF35, Omega) and ca. 640 and 750 nm (695AF55, Omega).

Fluorescence lifetime image scans (FLIM) were performed over an area of 20x20 μm^2, which consist of 256x256 pixels with a resolution of 0.078 μm/pixel. The integration time was 0.6 ms/pixel and the energy used was 1.1 kW/cm^2 at an excitation of 640 nm.

V.2.4. Data analysis

Data acquisition and preliminary analysis were performed on SymPhoTime software (PicoQuant GmbH).

The calculation of the fluorescence intensity time traces (MCS), time-correlated single photon counting histograms (TCSPC) and intensity correlation functions (FCS) from the measured data (TTTR file format) was performed on SymPhoTime. From the data analysis, it was possible to extract fluorescence intensity fluctuations, emission lifetimes and molecular diffusion coefficients.

From fitting the intensity correlation function with a model for free Brownian diffusion in 3D space, it was possible to extract from the diffusion time, τ_D, which is related to the diffusion coefficient *D* through,

$$\tau_D = \frac{w_0^2}{4D} \tag{V.1}$$

where w_0 is the distance from the center of the excitation volume in the radial direction and determined through calibration of the confocal volume with the appropriate dye. Since the rate of diffusion depends on the size of the molecule and its interactions with other molecules, FCS can be used to determine the hydrodynamic radius R_h of the fluorophore-labeled species via the Stokes-Einstein relation:

$$D = \frac{kT}{6\pi\eta R_h} \tag{V.2}$$

where *k* is the Boltzmann constant, *T* the temperature and η the viscosity of the solvent.

Decay fitting on FRET experiments was performed by reconvolution of the model with the experimental instrument response function (IRF) using a nonlinear least-squares procedure

based on the Marquardt algorithm. The quality of the fittings was judged by visual inspection of the weighted residuals and autocorrelation function. Average lifetimes $\langle\tau\rangle$ were calculated from:

$$\langle\tau\rangle = \frac{A_1\tau_1^2 + A_2\tau_2^2}{A_1\tau_1 + A_2\tau_2} \quad \text{(V.3)}$$

where τ_i is the individual decay lifetime, and A_i its respective normalized amplitude.

FRET distance (r) can then be calculated by:

$$k_{ET} = \frac{1}{\tau_{DA}} - \frac{1}{\tau_D^0} = \frac{1}{\tau_D^0}\left(\frac{R_0}{r}\right)^6 \quad \text{(V.4)}$$

where k_{ET} is the rate of the energy transfer from a donor to an acceptor, $\tau_D{}^0$ is the decay time of the donor in the absence of acceptor and R_0 is the Förster radius.

V.2.5. Real-Time PCR

Real-time PCR experiments were performed in a QuantStudio 5 Real-Time PCR System (Applied Biosystems, Massachusetts, USA). A concentration of 20 nM of the scaffold strand was mixed with 10 nM of a mix of staple strands in 25 μL of FoB15 buffer. Folding reactions were pipetted into 96-well plates, each sealed using appropriate sealing film. Raw intensity fluorescence measurements were acquired at an excitation of 470±15 nm, corresponding to the maximum absorption of FAM dye, and emission of 623±14 nm, which corresponds to the maximum emission of ROX.

V.2.6. Gel electrophoresis

Agarose gel electrophoresis was performed in 2% agarose gels containing 0.5x Tris-Borate EDTA (TBE) buffer (10x TBE, Invitrogen, Massachusetts, USA) and 5.5 mM $MgCl_2$ pre-stained with ethidium bromide. The working voltage was 90 V for 2 hours. The gels were imaged using a Axygen Gel Documentation System (Axygen Inc, Union City, USA). Ladder was NZYDNA ladder III (NZYTech, Lisbon, Portugal). Gels were loaded with samples pre-mixed with a 6× loading buffer (40% (w/v) sucrose, 0.25 %(w/v) bromophenol blue).

V.3. Results and Discussion

V.3.1. Single-labelled covalently nanostructures

V.3.1.1. Fluorescence Correlation Spectroscopy

On a first approach, in order to evaluate the correct folding of 31 and 63-bp edge lengths tetrahedrons, FCS measurements were performed. For this purpose, the scaffolds were labelled with Cy5 dye using a forward primer modified with Cy5 in the aPCR reaction. Using this strategy, it is expected that all single-stranded scaffolds are labelled covalently with the desired fluorophore, and, after chromatographic purification, the ssDNA recovered fraction was measured by FCS. To measure the tetrahedrons, non-labelled ssDNA scaffolds were mixed with the corresponding oligonucleotide mix that contained an oligonucleotide staple corresponding to one edge labeled with Cy5. This labelling procedure makes this approach more versatile since any of the oligonucleotides present in the folding mix can be modified and the assembly can be performed without further preparation processes.

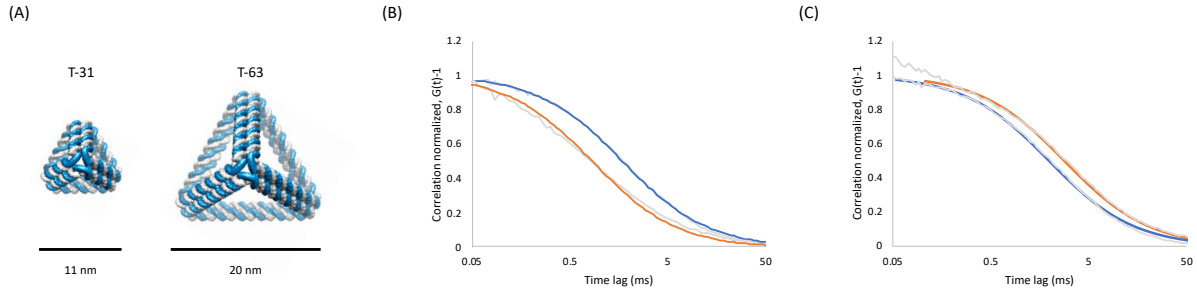

Figure V.2. (A) Atomic models of the folded 31 (T-31) and 63 (T-63) edge length tetrahedra. Fluorescence correlation spectroscopy analysis of the (B) 449-nt scaffold (blue) and T-31 tetrahedron (orange) and (C) 1000-nt scaffold (blue) and T-63 tetrahedron in aqueous medium.

FCS allows the observation of molecules in aqueous medium by measuring temporal fluctuations of the fluorescence intensity in a microscopic detection volume of about 10 fL (or less) defined by a highly focused laser beam and a confocal aperture. Fluctuations in fluorescence intensity in a small open region arise from the motion of fluorescent species in and out of this region, which allows for the determination of physical and chemical parameters of the sample under study, like diffusion coefficients [31].

The diffusion coefficient measured for 449-nt scaffold (Figure V.2(B)) was 28.6 $\mu m^2/s$, which corresponds to a hydrodynamic radius of 8.6 nm, and for the 1000-nt scaffold (Figure V.2(C))

25.1 $\mu m^2/s$, which corresponds to a hydrodynamic radius of 9.8 nm. Both values are in accordance with the literature that defines the hydrodynamic radius of a 449-nt ssDNA between 4.1 and 8.5 nm and for a 1000-nt ssDNA between 6.1 and 12.6 nm [32]. Regarding the folded tetrahedrons, the measured diffusion coefficient for T-31 was 52.4 $\mu m^2/s$, which corresponds to a hydrodynamic radius of 4.8 nm, which is in accordance with the simulated structure provided by the design software used (Figure V.2(A)). Moreover, the diffusion coefficient measure for T-63 (18.5 $\mu m^2/s$, 13.3 nm) is lower than the one obtained for the 1000-nt scaffold. The decrease of the diffusion coefficient between the folded tetrahedron and the scaffold is consistent with the Stokes-Einstein equation that shows that the diffusion coefficient is inversely related with the size of the molecules in the case of T-63. Regarding T-31, the hypothesis is that the folding of the tetrahedron leads the ssDNA scaffold to a state even more coiled than when it is in a free state, increasing its diffusion coefficient and decreasing the hydrodynamic radius.

V.3.1.2. Single-molecule fluorescence

For a better understanding of the behavior of the DNA-origami structures under study, single molecule fluorescence of 31 and 63-bp edge lengths tetrahedrons single-labelled with Cy5 was measured by FLIM. The labelling was performed by using a modified edge primer in the oligonucleotide mix during assembly. FLIM relies on differences in the excited-state lifetime of fluorophores to determine their spatial distribution in microscopic samples, thus fluorescence lifetime is used as a contrast mechanism for imaging [31]. For single-molecule analysis, a solution of tetrahedrons in 1 % polyvinyl alcohol (PVA) was used to deposit an appropriate density of dye molecules by spin-coating onto a clean glass coverslip [33]. The fluorescent intensity time traces, the decay time and the “on” and “off” histograms for T-31 and T-63 are presented in Figures V.3 and V.4, respectively. Regarding the fluorescent intensity time traces, the presented behavior is consistent with what is reported in the literature for Cy5, with an on-off blinking due to cis-trans isomerization [34], [35]. Moreover, the decay time is the range of 1.85 and 2.05 ns for the T-31 and 1.59 and 1.95 ns for the T-63, which is also consistent with what is reported [33], [36]. Regarding the distribution of “on” and “off” times, the exponential decay times are in the range of 0.95 and 1.81 ms (“on” times)

and 7.15 and 16.06 ms (“off” times) for T-31, and between 0.61 and 1.09 ms (“on” times) and 11 and 20 ms (“off” times) for T-63.

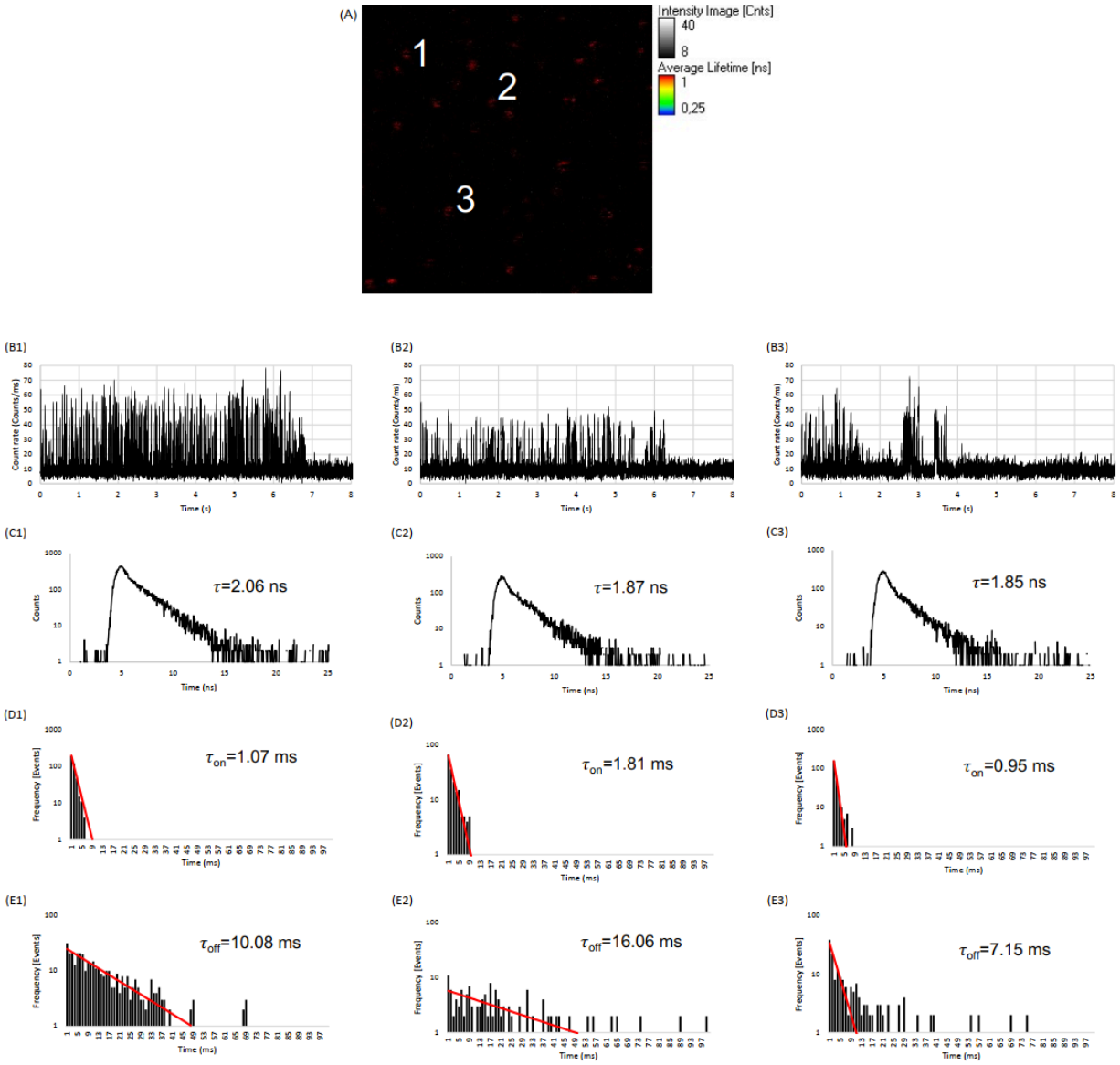

Figure V.3. (A) FLIM image of T-31 tetrahedron. (B) Fluorescent intensity time traces. (C) Decay time. (D) “on” histogram and (E) “off” histogram fitted with mono-exponential decay functions (red line), of three individual molecules (1,2,3).

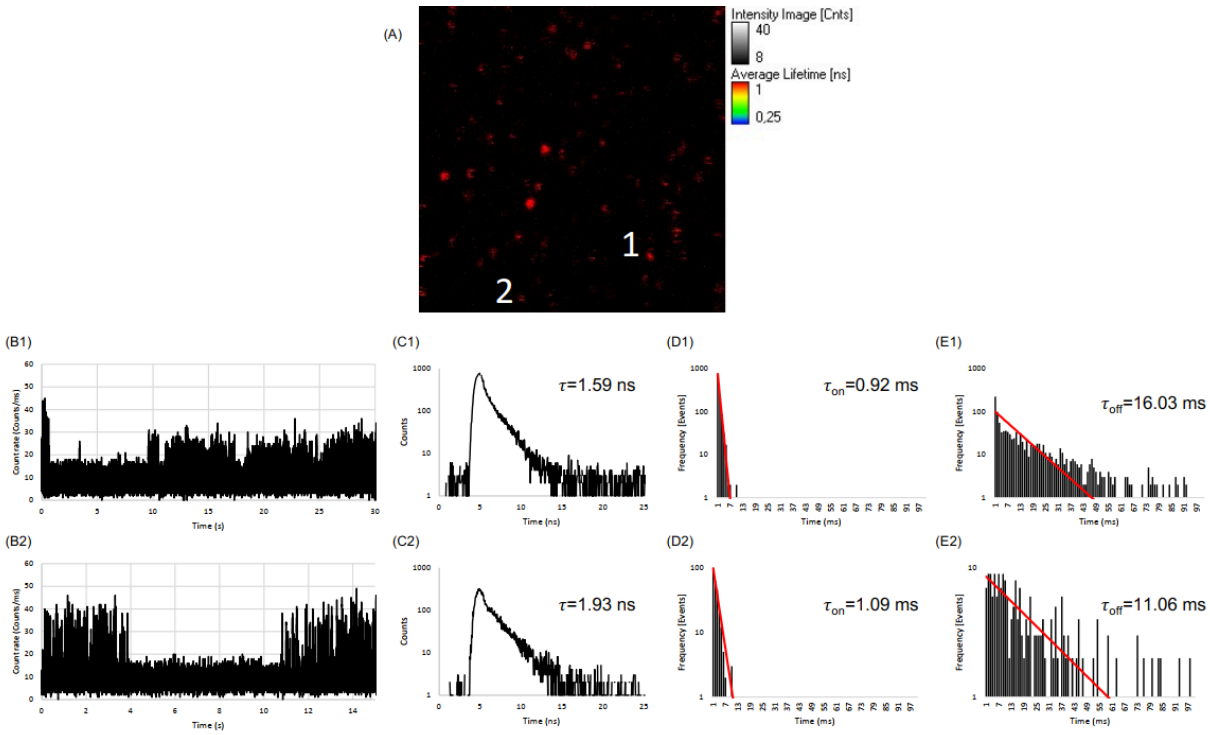

Figure V.4. (A) FLIM image of T-63 tetrahedron. (B) Fluorescent intensity time traces. (C) Decay time. (D) "on" histogram. (E) "off" histogram fitted with mono-exponential decay functions (red line), of two individual molecules (1,2).

In the follow-up, an FCS analysis of the modified edge oligonucleotide and the commercial Cy5 dye was performed using excitation energies ranging between 1.3 and 64.5 kW/cm^2. The results are present in Figure V.5. As can be seen by the correlation curves from FCS analysis, a major relaxation process occurs, which can be mainly attributed to translational diffusion that preceded by a minor relaxation component at short times that is attributed to trans-cis isomerization. Even though it is not possible to take further conclusions regarding dynamics of excited-state populations of Cy5 molecule at different excitation intensities, the isomerization phenomena observed is in accordance with literature [36].

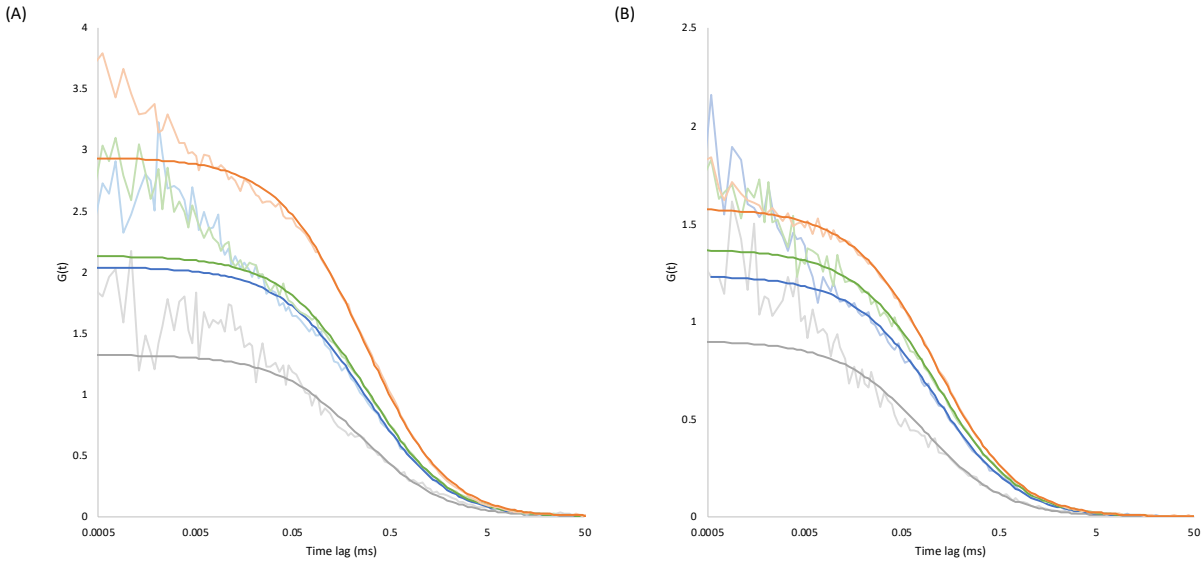

Figure V.5. Fluorescence correlation spectroscopy analysis of (A) edge oligonucleotide modified with Cy5 and (B) pure Cy5 at different energies: 1.291 kW/cm² (grey), 6.453 kW/cm² (blue), 12.906 kW/cm²,(green), and 64.532 kW/cm² (orange).

V.3.2. Dual-labelled covalently

V.3.2.1. Real-time PCR

To evaluate the correct folding of the DNA-origami tetrahedrons an approach based on real-time FRET was tested. FRET occurs between a donor molecule in the excited state and an acceptor molecule in the ground state. Energy transfer is the result of long-range dipole-dipole interactions and its efficiency is inversely proportional to the sixth power of the distance between donor and acceptor, making FRET extremely sensitive to small changes in distance [31]. To evaluate this hypothesis, the folding process of T-31 DNA-origami was followed by real-time PCR. Three different pairs of donor-acceptor were tested using FAM, as donor, and ROX, as acceptor, as FRET pair: V-E5, V-E3 and V-E2. The locations and distances of the three pairs are represented in Figure V.6.(A).

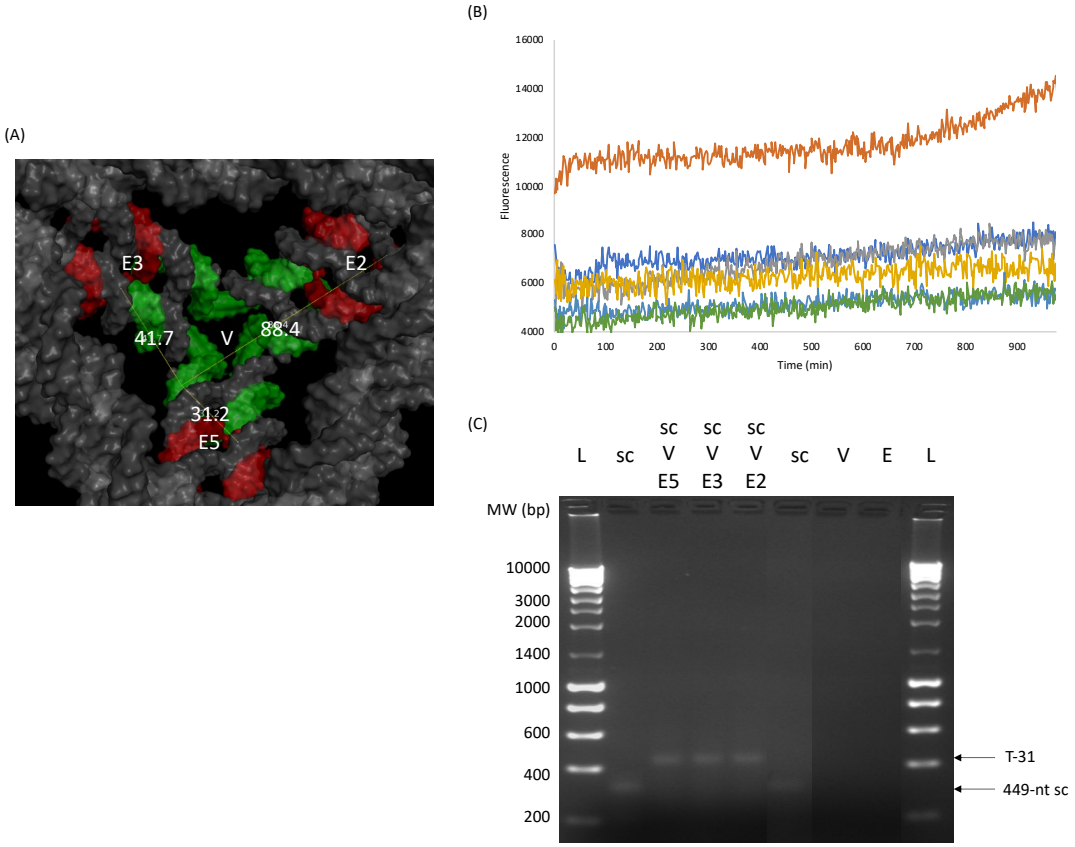

Figure V.6. (A) Overview on the location of the donor (FAM, V) and acceptors (ROX, E5, E3, E2) on T-31. Distances are in Angström. (B) Raw fluorescent data of folding reactions. Orange: V-E5, Dark blue: V-E2, Grey: V-E3, Yellow: scaffold only, Light blue: donor only, Green: acceptor only. (C) Agarose gel electrophoresis analysis of the folding reactions after real-time PCR.

Figure V.6.(B) represents the fluorescence of the folding reaction mix along the reaction time. It is possible to observe that for the pair V-E5 the fluorescence increases as the reaction proceeds indicating an energy transfer between the donor and the acceptor possible due to the proximity of the staples during the folding process. On the case of the other two pairs, it is not possible to see any differences, even though the absolute fluorescence value is higher than the controls, indicating that there is some energy transfer. Even though the concentration of staple strands were set to half the concentration of scaffold to reduce the background fluorescence of fluorescently labelled oligonucleotides, an agarose gel electrophoresis analysis reveals the correct folding of the scaffold into the target structure. Moreover, only one, well-defined band can be observed (Figure V.6(C)), that migrates less than the scaffold, suggesting an overall good folding quality.

V.3.2.2. Fluorescence Correlation Spectroscopy

The occurrence of FRET between a donor and an acceptor can also be evaluated by the FCS technique. For this purpose, the FRET pair of FAM-ROX was used with the donor located at one vertex of the T-31 and the acceptor on the edge corresponding to E5, since this was the combination that produced better results in real-time PCR. Also, according to simulation it has a shorter donor-acceptor distance. For DNA-origami assembly, it was used the double of concentration in acceptor-containing oligonucleotides to ensure that all the folded tetrahedrons contained ROX. Figure V.7. shows the result of the experimental curve and fitted rise and decay components of T-31 labelled with donor FAM and acceptor ROX.

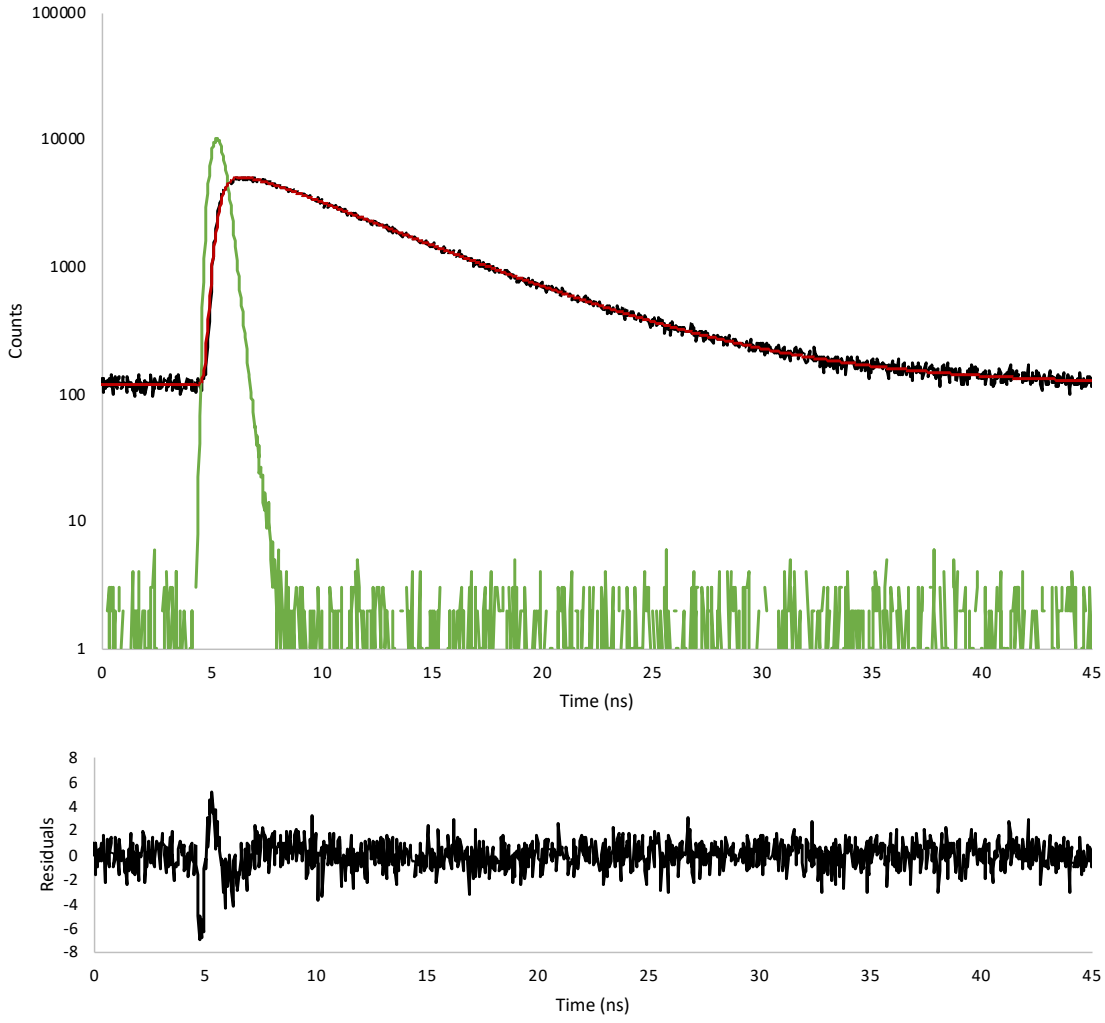

Figure V.7. Fluorescence lifetime with corresponding negative and positive amplitudes characterize the time-resolved fluorescence of the acceptor upon donor excitation (top). The time dependance of experimental (black) and fitted (red) fluorescence intensity of T-31 with FAM (donor) and ROX (acceptor). Experimental instrument response function is represented in green. (bottom) The weighted residuals between experimental and fitted curves.

Fitting the experimental curve using an expression containing a single rise time (with negative amplitude) and a single decay time (with positive amplitude) affords a reasonable description of the experimental data, because the χ^2 criterion is close to the limiting value of 1 (1.435) and the weighted residuals randomly fluctuate around zero. In this case, the rise time is 1.257 ns (A_2 = -1624.25) and the decay time is 5.968 ns (A_1 = 6893.08). The negative pre-exponential component reflects a time-dependent increase (rise) of the excited-state acceptor population due to energy transfer from donor to acceptor [37]. Moreover, the rate of energy transfer can be calculated through the difference between the fluorescence decay rate of a donor in the presence of an acceptor, or equivalently the rise time of acceptor fluorescence ($1/\tau_{DA}$), and the donor fluorescence lifetime in the absence of acceptor ($1/\tau_D$), allowing the estimation of a distance between donor and acceptor. In this case, considering a Förster radius of 64.5 Å, determined using the PhotoChemCad software for the FAM-ROX pair [38], and a decay time of the donor in the absence of the acceptor as 3.78 ns, measured by FCS, a distance of 5.7 nm was calculated. Even though the value obtained is higher than the simulated distance (3.1 nm), it is within an acceptable margin of uncertainty, in particular, considering the fact that there are spacers between the oligonucleotides and the fluorophores (that are not being taken into account in the distance from the simulated structure), and the fact that the theoretical Förster radius is calculated for the free fluorophores with a random orientation of their transition dipoles, i.e. this calculation does not take into account specific interactions with DNA. Overall, this result gives some confidence on the correct folding of the target tetrahedron via DNA-origami techniques.

V.3.3. Single-labelled non-covalently model drug delivery system

TMPyP is a water-soluble porphyrin that is pharmacologically inactive but, when exposed to visible light (e.g. sunlight), it produces reactive oxygen species, mainly singlet oxygen, resulting in the induction of cell death. For this reason, its use as a photosensitizer in photodynamic therapy is very promising [26]. The possibility of intercalating TMPyP into T-31 and T-63 DNA-origami nanostructures was evaluated by FCS at different TMPyP concentrations ranging between 10 nM and 2 μM. The results obtained regarding the pre-exponential factors and

lifetime values fitted to the fluorescence decays are presented in Table V.1. Decay curves are represented in supplementary material V.S4.

Table V.1. Pre-exponential and lifetime values fitted to the fluorescence decays of T-31, T-63 and free TMPyP at TMPyP concentrations ranging between 10 nM and 2 μm.

		[TMPyP] (nM)							
		10	**20**	**50**	**100**	**200**	**500**	**1000**	**20000**
T-31	A_1	91.78	177.95	225.24	397.18	462.74	2469.64	6543.57	17716.28
	τ_1 (ns)	7.29	8.023	10.585	10.848	10.35	9.941	9.504	7.837
	A_2	-	-	85.63	167.1	180.9	1758.14	8894.44	69684.79
	τ_2 (ns)	-	-	2.457	2.977	2.603	3.268	4.986	4.732
	A_3	-	-	-	-	-	-	2872.85	14168.26
	τ_3 (ns)	-	-	-	-	-	-	1.603	1.699
	$\langle\tau\rangle$ (ns)	7.29	8.02	9.93	10.03	9.66	8.68	7.37	5.46
	χ^2	0.997	0.998	1.126	1.024	0.985	1.023	1.067	1.265
T-63	A_1	628.32	430.34	1455.77		1677.76	2474.97	3206.77	5100.43
	τ_1 (ns)	9.986	10.237	10.584		10.003	10.098	9.517	7.605
	A_2	479.6	526.6	1219.64		1207.95	2967.58	4528.37	8432.1
	τ_2 (ns)	2.007	1.9	3.02		2.619	4.376	4.278	3.453
	A_3	-	-	-		-	1435.46	2364.59	3436.9
	τ_3 (ns)	-	-	-		-	1.443	1.39	1.219
	$\langle\tau\rangle$ (ns)	8.92	8.69	9.12		8.83	7.8	7.11	5.57
	χ^2	1.061	1.047	1.061		1.05	1.046	1.081	1.053
Free TMPyP	A_1	81.38	486.63	2233.12	2727.01	4874.33	20764.82	15778.16	36178.76
	τ_1 (ns)	8.032	10.469	9.714	10.231	10.162	8.228	7.682	7.168
	A_2	38.95	196.55	842.9	1115.98	4169.34	38898.87	59970.2	120867.2
	τ_2 (ns)	0.924	2.943	2.571	2.921	5.502	4.549	4.794	4.675
	A_3	-	-	-	-	1413.25	6141.88	9975.66	20181.3
	τ_3 (ns)	-	-	-	-	1.268	1.385	1.689	1.597
	$\langle\tau\rangle$ (ns)	7.66	9.7	9.07	9.47	8.51	6.61	5.49	5.31
	χ^2	1.007	0.996	1.033	1.026	0.986	1.186	1.296	1.481

Overall, it is possible to observe that the number of components needed to describe the observed fluorescence decay observed increases with the increase of TMPyP concentration in the sample. Fluorescence decays are bi- or tri-exponential with a major component between 7 and 10 ns, a second one between 3 and 5 ns in the case of tri-exponential fits, and a last one around 1.5 ns. Average lifetime of TMPyP intercalated with T-31 and T-63 increases from free

TMPyP between 50 to 1000 nM of TMPyP. Literature reveals an expected biexponential decay with a major component of about 5 ns and a second one around 1 ns [39] for free TMPyP in water and of 10 ns and 5 ns when interacting with biological systems [40]. Discrepancies observed for lower concentrations of TMPyP might be due to EDTA present in the buffer solution since EDTA is negatively charged molecule which can electrostatically interact with TMPyP, increasing the lifetime of the free form. For concentrations above 200 nM, the average lifetime starts to decrease again until a value of 5 ns, which is the expected value for the free TMPyP in water, indicating that the amount of free TMPyP is so high that masks the signal of the intercalated one.

In order to have a better understanding of the system, FCS curves were analyzed. It was observed that above 200 nM no FCS could be observed in all three samples studied (results not shown). However, below 200 nM of TMPyP, FCS could be observed for T-63. The results obtained are presented in Figure V.8. for the limiting cases of 200 and 10 nM.

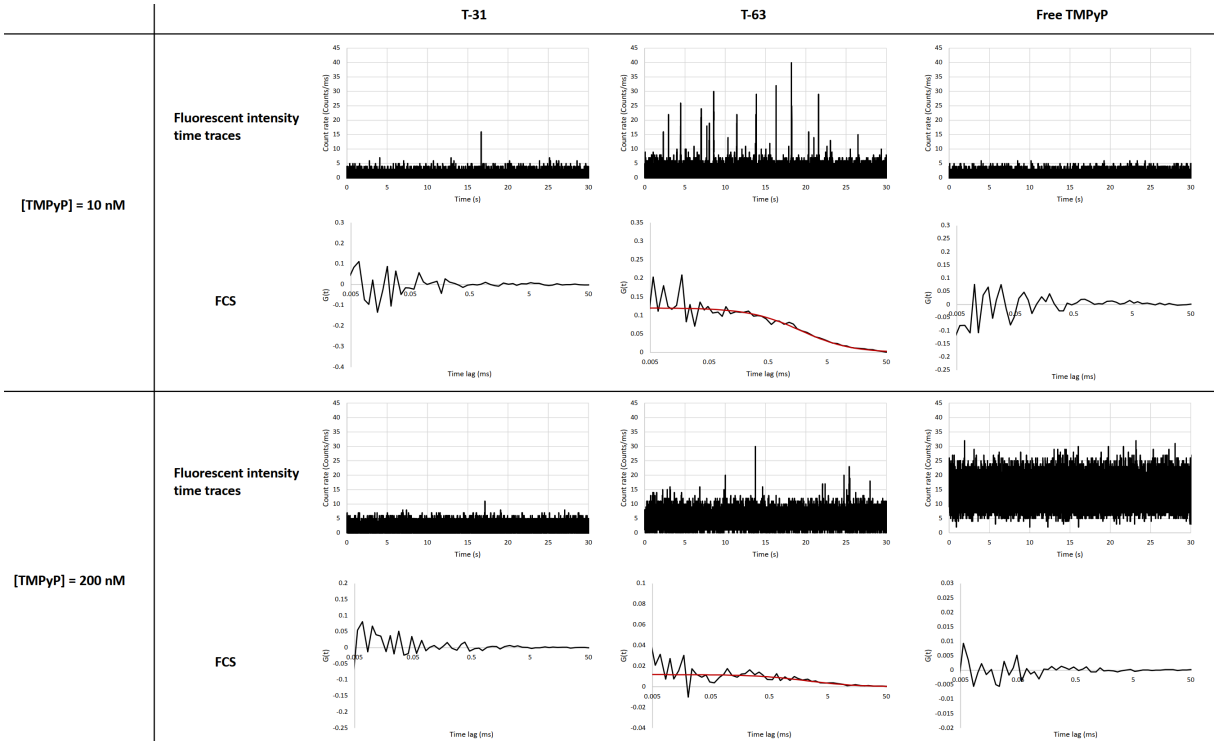

Figure V.8. Fluorescent intensity time traces and FCS analysis of T-31, T-63 and free TMPyP at the limiting situations at which FCS can be observed: 10 and 200 nM TMPyP. Red line represents the fit of the FCS curves.

As Figure V.8 shows, it is only possible to observe an FCS curve for T-63. Even though this was expected for the free TMPyP, in the case of T-31 it is not possible to conclude anything about the intercalation of TMPyP into the tetrahedron probably because it is very small and for this reason it does not have enough binding sites to afford a bright single nanostructure due to

collective TMPyP emission. In the case of T-63, it was possible to determine a diffusion coefficient of 20.2 $\mu m^2/s$ for the 200 nM and 24.9 $\mu m^2/s$ for the 10 nM, which corresponds to hydrodynamic radius of 12.1 and 9.9 nm, respectively. These values are in accordance with the expected size of T-63, allowing the conclusion that the intercalation was possible and efficient in this range of TMPyP concentrations. Moreover, an analysis of the fluorescent decay was performed (see Supplementary Material, Figure V.S2) above and below a threshold in the fluorescent intensity time trace that isolated the background from the bursts observed for T-63 at both 200 and 10 nM. This was an attempt to isolate the free TMPyP from the T-63 that contained intercalator, however, the mean value for lifetime do not allow to take any conclusions since they contain a long component at 10 ns and a short at 2 ns in all the cases evaluated.

V.4. Conclusion

In this exploratory work, the possibility of using spectroscopic techniques to evaluate the folding and application of tetrahedral DNA-origami nanostructures was evaluated. In a first approach, FCS analysis revealed diffusion coefficients and hydrodynamic radius coherent with the simulated size for tetrahedrons with 31 and 63-bp edge length. Single-molecule fluorescence was also measured, and it allowed the characterization by means of fluorescence decays and on-off histograms of Cy5 labelled T-31 and T-63. Next, the folding reaction of T-31 was followed by real-time PCR using FAM-ROX as FRET pair, which allowed the conclusion that, in fact, as expected from the origami assembly over the time, the two different labelled staple oligonucleotides came closer, eventually, reaching a point where there is energy transfer, indicating the folding of the structure. An FCS analysis was also performed for this FRET pair in the DNA-origami. A rise-time component was observed, i.e. a negative pre-exponential indicative of energy transfer, which allowed the determination of a distance between the donor-acceptor labelled staples of 5.7 nm. Finally, the possibility of intercalating a photosensitizer molecule into the DNA-origami nanostructure was evaluated. Preliminary results show the possibility of using TMPyP at a concentration below 200 nM to intercalate T-63 with a calculated diffusion coefficient and hydrodynamic radius, in accordance with the simulated structure.

V.5. References

[1] N. C. Seeman and H. F. Sleiman, "DNA nanotechnology," *Nat. Rev. Mater.*, vol. 3, 2017.

[2] P. W. K. Rothemund, "Folding DNA to create nanoscale shapes and patterns," *Nature*, vol. 440, no. 7082, pp. 297–302, 2006.

[3] Y. Zeng, R. L. Nixon, W. Liu, and R. Wang, "The applications of functionalized DNA nanostructures in bioimaging and cancer therapy," *Biomaterials*, vol. 268, no. November 2020, p. 120560, 2021.

[4] R. P. Goodman *et al.*, "Rapid chiral assembly of rigid DNA building blocks for molecular nanofabrication," *Science*, vol. 310, no. 5754, pp. 1661–1665, 2005.

[5] D. M. Smith, V. Schüller, C. Forthmann, R. Schreiber, P. Tinnefeld, and T. Liedl, "A structurally variable hinged tetrahedron framework from DNA origami," *J. Nucleic Acids*, vol. 2011, 2011.

[6] S. Ramakrishnan, H. Ijäs, V. Linko, and A. Keller, "Structural stability of DNA origami nanostructures under application-specific conditions," *Comput. Struct. Biotechnol. J.*, vol. 16, pp. 342–349, 2018.

[7] S. Manuguri, M. Nguyen, J. Loo, A. K. Natarajan, and A. Kuzyk, "Advancing the Utility of DNA Origami Technique through Enhanced Stability of DNA-Origami-Based Assemblies," *Bioconjugate Chem.*, 2022.

[8] A. Reisch and A. S. Klymchenko, "Fluorescent Polymer Nanoparticles Based on Dyes: Seeking Brighter Tools for Bioimaging," *Small*, vol. 12, no. 15, pp. 1968–1992, 2016.

[9] J. J. Schmied *et al.*, "DNA origami-based standards for quantitative fluorescence microscopy," *Nat. Protoc.*, vol. 9, no. 6, pp. 1367–1391, 2014.

[10] X. Wei, J. Nangreave, S. Jiang, H. Yan, and Y. Liu, "Mapping the thermal behavior of DNA origami nanostructures," *J. Am. Chem. Soc.*, vol. 135, no. 16, pp. 6165–6176, 2013.

[11] J. Yan *et al.*, "Growth and Origami Folding of DNA on Nanoparticles for High-Efficiency Molecular Transport in Cellular Imaging and Drug Delivery," *Angew. Chemie*, vol. 127, no. 8, pp. 2461–2465, 2015.

[12] X. Shen *et al.*, "Visualization of the intracellular location and stability of DNA origami with a label-free fluorescent probe," *Chem. Commun.*, vol. 48, no. 92, pp. 11301–11303, 2012.

[13] S. M. Douglas, I. Bachelet, and G. M. Church, "A Logic-Gated Nanorobot for Targeted Transport of Molecular Payloads," *Science*, vol. 335, no. February, pp. 831–834, 2012.

[14] J. R. Burns, B. Lamarre, A. L. B. Pyne, J. E. Noble, and M. G. Ryadnov, "DNA Origami Inside-Out Viruses," *ACS Synth. Biol.*, vol. 7, no. 3, pp. 767–773, 2018.

[15] Y. X. Zhao, A. Shaw, X. Zeng, E. Benson, A. M. Nyström, and B. Högberg, "DNA origami delivery system for cancer therapy with tunable release properties," *ACS Nano*, vol. 6, no. 10, pp. 8684–8691, 2012.

[16] Q. Jiang *et al.*, "DNA origami as a carrier for circumvention of drug resistance," *J. Am. Chem. Soc.*, vol. 134, no. 32, pp. 13396–13403, 2012.

[17] P. D. Halley *et al.*, "Daunorubicin-Loaded DNA Origami Nanostructures Circumvent Drug-Resistance Mechanisms in a Leukemia Model," *Small*, vol. 12, no. 3, pp. 308–320, 2016.

[18] M. Cao *et al.*, "Multivalent Aptamer-modified DNA Origami as Drug Delivery System for Targeted Cancer Therapy," *Chem. Res. Chinese Univ.*, vol. 36, no. 2, pp. 254–260, 2020.

[19] K. Liu, C. Xu, and J. Liu, "Regulation of cell binding and entry by DNA origami mediated

spatial distribution of aptamers," *J. Mater. Chem. B*, vol. 8, no. 31, pp. 6802–6809, 2020.
[20] Z. Ge *et al.*, "DNA Origami-Enabled Engineering of Ligand–Drug Conjugates for Targeted Drug Delivery," *Small*, vol. 16, no. 16, pp. 6–11, 2020.
[21] Q. Zhang *et al.*, "DNA origami as an in vivo drug delivery vehicle for cancer therapy," *ACS Nano*, vol. 8, no. 7, pp. 6633–6643, 2014.
[22] S. Li *et al.*, "A DNA nanorobot functions as a cancer therapeutic in response to a molecular trigger in vivo," *Nat. Biotechnol.*, vol. 36, no. 3, pp. 258–264, 2018.
[23] Q. Jiang *et al.*, "A Self-Assembled DNA Origami-Gold Nanorod Complex for Cancer Theranostics," *Small*, vol. 11, no. 38, pp. 5134–5141, 2015.
[24] L. Song *et al.*, "DNA origami/gold nanorod hybrid nanostructures for the circumvention of drug resistance," *Nanoscale*, vol. 9, no. 23, pp. 7750–7754, 2017.
[25] X. Zhuang *et al.*, "A Photosensitizer-Loaded DNA Origami Nanosystem for Photodynamic Therapy," *ACS Nano*, vol. 10, no. 3, pp. 3486–3495, 2016.
[26] A. Garcia-Sampedro, A. Tabero, I. Mahamed, and P. Acedo, "Multimodal use of the porphyrin TMPyP: From cancer therapy to antimicrobial applications," *Porphyr. Sci. By Women (In 3 Vol.*, no. ii, pp. 11–27, 2020.
[27] L. Žárská *et al.*, "The effect of two porphyrine photosensitizers TMPyP and ZnTPPS4 for application in photodynamic therapy of cancer cells in vitro," *Photodiagnosis Photodyn. Ther.*, vol. 34, no. November 2020, 2021.
[28] R. Veneziano *et al.*, "Designer nanoscale DNA assemblies programmed from the top down," *Science*, vol. 352, no. 6293, 2016.
[29] A. R. Silva-Santos, P. M. R. Paulo, D. Miguel, and F. Prazeres, "Scalable purification of single stranded DNA scaffolds for biomanufacturing DNA-origami nanostructures : Exploring anion-exchange and multimodal chromatography," *Sep. Purif. Technol.*, vol. 298, no. June, p. 121623, 2022.
[30] K. F. Wagenbauer *et al.*, "How We Make DNA Origami," *ChemBioChem*, vol. 18, no. 19, pp. 1873–1885, 2017.
[31] J. R. Lakowicz, *Principles of fluorescence spectroscopy*. 2006.
[32] B. Tinland, A. Pluen, J. Sturm, and G. Weill, "Persistence length of single-stranded DNA," *Macromolecules*, vol. 30, no. 19, pp. 5763–5765, 1997.
[33] M. K. Singh, "Time-resolved single molecule fluorescence spectroscopy of Cy5-dCTP: Influence of the immobilization strategy," *Phys. Chem. Chem. Phys.*, vol. 11, no. 33, pp. 7225–7230, 2009.
[34] Z. Huang *et al.*, "Spectral identification of specific photophysics of Cy5 by means of ensemble and single molecule measurements," *J. Phys. Chem. A*, vol. 110, no. 1, pp. 45-50, 2006.
[35] Z. Huang, D. Ji, and A. Xia, "Fluorescence intensity and lifetime fluctuations of single Cy5 molecules immobilized on the glass surface," *Colloids Surfaces A Physicochem. Eng. Asp.*, vol. 257–258, pp. 203–209, 2005.
[36] J. Widengren and P. SchwiÏle, "Characterization of photoinduced isomerization and back-isomerization of the cyanine dye cy5 by fluorescence correlation spectroscopy," *J. Phys. Chem. A*, vol. 104, no. 27, pp. 6416–6428, 2000.
[37] S. Lindhoud, A. H. Westphal, C. P. M. Van Mierlo, A. J. W. G. Visser, and J. W. Borst, "Rise-time of FRET-acceptor fluorescence tracks protein folding," *Int. J. Mol. Sci.*, vol. 15, no. 12, pp. 23836–23850, 2014.
[38] H. Du, R. C. A. Fuh, J. Li, L. A. Corkan, and J. S. Lindsey, "PhotochemCAD++: A Computer-

Aided Design and Research Tool in Photochemistry," *Photochem. Photobiol.*, vol. 68, no. 2, pp. 141–142, 1998.

[39] P. M. R. Paulo and S. M. B. Costa, "Interactions in noncovalent PAMAM/TMPyP systems studied by fluorescence spectroscopy," *J. Phys. Chem. B*, vol. 109, no. 29, pp. 13928–13940, 2005.

[40] R. Teixeira, V. V. Serra, P. M. R. Paulo, S. M. Andrade, and S. M. B. Costa, "Encapsulation of photoactive porphyrinoids in polyelectrolyte hollow microcapsules viewed by fluorescence lifetime imaging microscopy (FLIM)," *RSC Adv.*, vol. 5, no. 96, pp. 79050–79060, 2015.

Supplementary Material

Sequences of scaffolds

The sequences of the two scaffolds synthesized by asymmetric PCR are shown below.

V.S1: 449-nt scaffold sequence (5'->3')

GTCGTCGTCCCCTCAAACTGGCAGATGCACGGTTACGATGCGCCCATCTACACCAACGTAAC
CTATCCCATTACGGTCAATCCGCCGTTTGTTCCCACGGAGAATCCGACGGGTTGTTACTCGC
TCACATTTAATGTTGATGAAAGCTGGCTACAGGAAGGCCAGACGCGAATTATTTTTGATGGC
GTTCCTATTGGTTAAAAAATGAGCTGATTTAACAAAAATTTAACGCGAATTTTAACAAAATA
TTAACGTTTACAATTTAAATATTTGCTTATACAATCTTCCTGTTTTTGGGGCTTTTCTGATT
ATCAACCGGGGTACATATGATTGACATGCTAGTTTTACGATTACCGTTCATCGATTCTCTTG
TTTGCTCCAGACTCTCAGGCAATGACCTGATAGCCTTTGTAGATCTCTCAAAAATAGCTACC
CTCTCCGGCATTAAT

V.S2: 1000-nt scaffold sequence (5'->3')

GTCTCGCTGGTGAAAAGAAAAACCACCCTGGCGCCCAATACGCAAACCGCCTCTCCCCGCGC
GTTGGCCGATTCATTAATGCAGCTGGCACGACAGGTTTCCCGACTGGAAAGCGGGCAGTGAG
CGCAACGCAATTAATGTGAGTTAGCTCACTCATTAGGCACCCCAGGCTTTACACTTTATGCT
TCCGGCTCGTATGTTGTGTGGAATTGTGAGCGGATAACAATTTCACACAGGAAACAGCTATG
ACCATGATTACGAATTCGAGCTCGGTACCCGGGGATCCTCTAGAGTCGACCTGCAGGCATGC
AAGCTTGGCACTGGCCGTCGTTTTACAACGTCGTGACTGGGAAAACCCTGGCGTTACCCAAC
TTAATCGCCTTGCAGCACATCCCCCTTTCGCCAGCTGGCGTAATAGCGAAGAGGCCCGCACC
GATCGCCCTTCCCAACAGTTGCGCAGCCTGAATGGCGAATGGCGCTTTGCCTGGTTTCCGGC
ACCAGAAGCGGTGCCGGAAAGCTGGCTGGAGTGCGATCTTCCTGAGGCCGATACGGTCGTCG
TCCCCTCAAACTGGCAGATGCACGGTTACGATGCGCCCATCTACACCAACGTAACCTATCCC
ATTACGGTCAATCCGCCGTTTGTTCCCACGGAGAATCCGACGGGTTGTTACTCGCTCACATT
TAATGTTGATGAAAGCTGGCTACAGGAAGGCCAGACGCGAATTATTTTTGATGGCGTTCCTA
TTGGTTAAAAAATGAGCTGATTTAACAAAAATTTAACGCGAATTTTAACAAAATATTAACGT
TTACAATTTAAATATTTGCTTATACAATCTTCCTGTTTTTGGGGCTTTTCTGATTATCAACC
GGGGTACATATGATTGACATGCTAGTTTTACGATTACCGTTCATCGATTCTCTTGTTTGCTC
CAGACTCTCAGGCAATGACCTGATAGCCTTTGTAGATCTCTCAAAAATAGCTACCCTCTCCG
GCATTAAT

V.S3: staple sequences and characteristics

Table V.S1: Staple sequences and characteristics to fold the 31-bp edge length tetrahedron from the 449-nt scaffold.

NAME	SEQUENCE	%GC	TM (°C)
T31_1-98-E	ACAACCCGTCCTGCCCCTGA	65	73.3
T31_2-237-V	AACGTTTTTTTAATATTTTGAACATTAAATGTTTTTTGAGCGAGTAGAGTCTGGAGCTTTTTAAACAAGAGAATTGTA	26.9	80
T31_2-346-E	ATCGATGAACAAATATTTAA	20	51.3
T31_3-284-E	AAAGCTTTTTGCTCACCCAA	40	63.5
T31_4-206-V	ATTTTTTTTTTGTTAAATCATAACCAATAGGTTTTTAACGCCATCAGCGTCTGGCCTTTTTTTCCTGTAGCCCGTTAA	34.6	85.5
T31_4-222-E	TTAAAATTCGAGCTTTCATC	30	56.1
T31_5-299-V	CGGTTTTTTTGATAATCAGAAAACAGGAAGATTTTTTTGTATAAGCGGTAATCGTAATTTTTAACTAGCATGGTACCC	30	56.1
T31_5-315-E	TCAATTAGATTGGTGCATAT	30	54.5
T31_6-51-V	TGGGATTTTTTAGGTTACGTGGGCGCATCGTTTTTTAACCGTGCATGGATTCTCCGTTTTTTGGGAACAAACCCGTAA	43.6	91.5
T31_6-67-E	GGCGGAATTCAAAATATTGA	35	61.2

Table V.S2: Staple sequences and characteristics to fold the 63-bp edge length tetrahedron from the 1000-nt scaffold.

NAME	SEQUENCE	%GC	TM (°C)
T63_1-212-E	GTGAAATTGTCGCCAGGGTGGTTATTTTTGTCTGTTTCCTGT	42.9	81.1
T63_1-191-E	AATTCCACACAGAGGCGGTTTGCGTATTGGGTATCCGCTCAC	52.4	85.6
T63_2-516-V	AAGATCGCACTTTTTTCCAGCCAGCTAATTCGTAATCTTTTTATGGTCATAGTAAATCAGCTCTTTTTATTTTTTAAC	30.8	81.6
T63_2-716-E	CCATCAAAAAGACGACCGTATCGGCCTCAGGCAATAGGAACG	52.4	85.1
T63_2-695-E	TGGCCTTCCTCATCTGCCAGTTTGAGGGGACTAATTCGCGTC	54.8	86.6
T63_3-398-E	CTATTACGGGGCGATCGGTGCGGGAGGTTACG	62.5	82.9
T63_3-587-E	TTGGTGTATTGACCGTAATGGGATCCTCTTCG	46.9	76.4
T63_3-390-E	CCAGCTGGCGCTGTTGGGAA	65	74.8
T63_4-453-V	TTCGCCATTCATTTTTGGCTGCGCAAAAAGGGGGATGTTTTTTGCTGCAAGGCGGCCAGTGCCTTTTTAAGCTTGCAT	47.4	94.9
T63_4-484-E	CTTCTGGTGCGATCCCCGGGTACCGAGCTCGTTCCGGCACCG	69	93.3
T63_4-463-E	CAAAGCGCCAGCCTGCAGGTCGACTCTAGAGCGGAAACCAGG	61.9	88.9
T63_5-632-V	TCCGTGGGAACTTTTTAAACGGCGGAGATGGGCGCATTTTTTCGTAACCGTGGTAGCCAGCTTTTTTTTCATCAACAT	44.9	92
T63_5-73-E	TCGTGCCACCCGCTTTCCAGTCGGACAACCCG	65.6	88.5
T63_5-640-E	TCGGATTCTAAATGTGAGCGAGTAGAAACCTG	43.8	73.3
T63_5-65-E	GCTGCATTAAGCGCTCACTG	55	66
T63_6-128-V	CTAACTCACATTTTTTTAATTGCGTTTGAATCGGCCATTTTTACGCGCGGGGAACATACGAGCTTTTTCGGAAGCATA	41	89.7
T63_6-325-E	CACGACGTGGGTAACGCCAGGGTTGTGCCTAA	59.4	83.1
T63_6-136-E	TGAGTGAGAAGTGTAAAGCCTGGGTTCCCAGT	50	76.3
T63_6-317-E	TGTAAAACGACGATTAAGTT	30	54

V.S4: Decay curves at different TMPyP concentrations

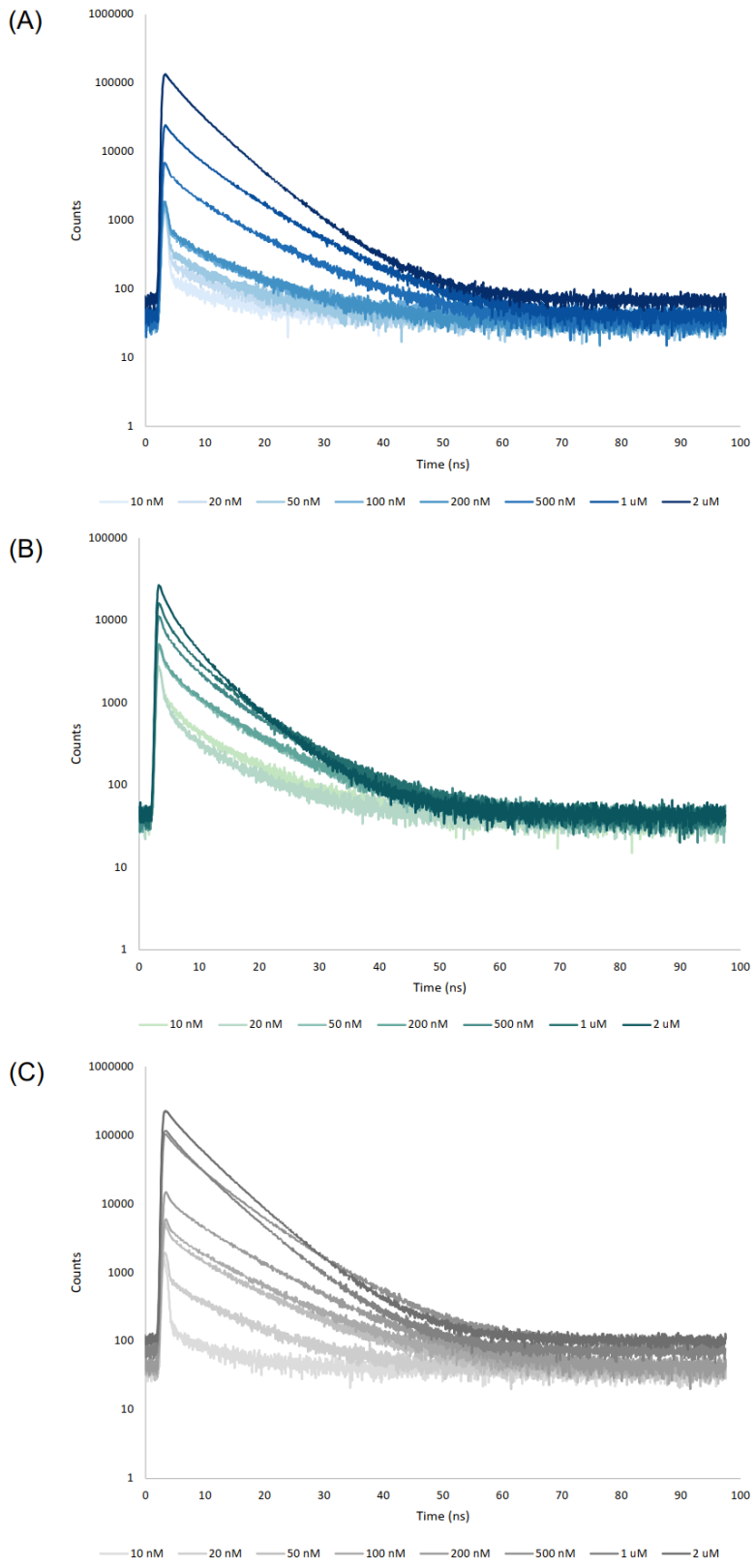

Figure V.S1. Fluorescence decays of (A) T-31, (B) T-63 and (C) Free TMPyP under TMPyP concentrations ranging between 10 nM and 2 μM.

V.S5: Decay curves above and below the count threshold

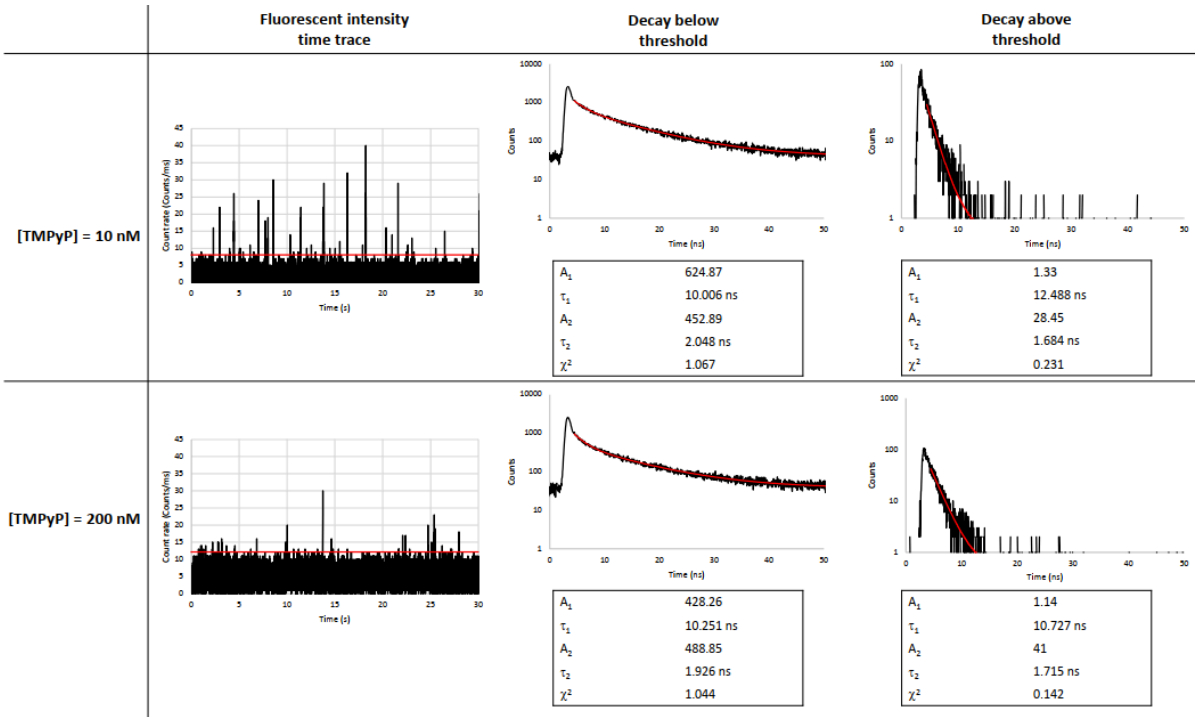

Figure V.S2. Fluorescent intensity time traces and fluorescent decay analysis of T-63 at the limiting situations at which FCS can be observed: 10 and 200 nM TMPyP. Red line in fluorescent intensity time traces represents the threshold above which the fluorescent bursts were considered T-63 that intercalated TMPyP. Red line in fluorescent decays represent the tail fit for which lifetimes and pre-exponential parameters were calculated.

CHAPTER VI – CONCLUSIONS AND FUTURE CHALLENGES

DNA-origami nanostructures are emerging as components of nanomachines, nanopores, drug delivery systems and biosensors. Current state of the art relies on scaffolds purification by (i) extraction of phage genomic DNA, produced in *E. coli*, which has sequence limitations and raises safety concerns regarding contamination of following cultures, preventing the scalability potential of the technique and its applications, or (ii) by agarose gel extraction, which is a laborious, time consuming, limited and not scalable technique that presents low recovery, delivers low-quality products, and requires specific equipment, making it not suitable for pharmaceutical or analytical applications. In this thesis, several crucial aspects of DNA-origami manufacturing were addressed.

Looking at the upstream, ssDNA scaffolds were produced using phages and phagemid particles. Even though the use of phages is the most straightforward approach for the biotechnological mass production of ssDNA molecules, safety issues, like possible cross-contamination of large reactors, and the desire for having user-defined sequence scaffolds, make its use limited. Having this in mind, reverse infection method was developed and allowed the efficient and scalable production of artificial ssDNA with *E. coli*. In this method, the produced phagemid particles are unable to self-replicating even though they can infect *E. coli* cells that were previously transformed with a helper plasmid. Large scale production has been feasible at any contract manufacturer as remaining, unwanted phagemid particles after cleaning and sterilization are of no consequence to other following processes with *E. coli*. Moreover, this method showed to be more efficient and resulted in a 1.5 to 3-fold yield increase compared to the previous double transformation method. The produced ssDNA was free of contaminating DNA species that could interfere with downstream applications such as DNA-origami folding.

Future challenges rely essentially in two main points. First, the possibility of using this type of strategy to produce a fully user-defined sequence scaffold, eliminating the bacterial backbone and G3 protein sequence necessary for the assembly of the phagemid particle, present in the phagemid. Second, the development of a fully scalable downstream processing that does not involve ethanol precipitation, since its use as a large scale is not feasible. A possible strategy would be the use of tangential flow filtration in combination with chromatography processes, namely anion-exchange and multimodal chromatography.

Regarding the downstream processing, two different purification strategies were developed for the isolation of ssDNA scaffolds from aPCR mixtures. In a first approach, a process based on complementary oligonucleotide probes attached to magnetic beads was explored. A 20-nt oligo was coupled to carboxylate-modified magnetic beads allowing the hybridization between the beads and 449 and 1000-nt ssDNA scaffolds generated by aPCR. Following bead separation and elution, 550 ± 160 ng of 449-nt ssDNA and 890 ± 220 ng of 1000-nt ssDNA, virtually free from dsDNA contaminants, could be recovered per 50 µL aPCR reaction. Additionally, this method showed better results than the established agarose gel purification method. The purification process was complete in less than 1 hour, which is substantially less than the 3 hours required using the standard agarose gel electrophoresis extraction. Furthermore, the beads were re-used without loss of binding capacity for at least three cycles. Lastly, beads modified with a given probe, as shown here, can be used to purify ssDNA scaffolds with different lengths as long as they share the same 3' region. Purification of other scaffolds will require coupling different probes to the beads.

In an attempt to scale-up downstream processing of ssDNA scaffolds produced via aPCR, chromatographic methods based on anion-exchange and multimodal chromatography were also developed using stepwise gradients with increasing NaCl concentrations. In anion exchange chromatography, the less-charged ssDNA eluted before the dsDNA, whereas in multimodal chromatography, the elution pattern was reversed, highlighting the importance played by hydrophobicity. Both types of chromatography allowed the purification of between 8.4 µg and 10.7 µg of the 1000-nt ssDNA, homogeneous and impurity free.

Even though the use of chromatography is a scalable process *per se*, the use of aPCR to generate these small ssDNA scaffolds is not. An alternative would be to explore these strategies for ssDNA produced in *E. coli*, that deliver higher yields, but there is still the need to develop plasmids that deliver such small scaffolds, or the scale-out of the PCR method, like the one explored in this thesis.

A lack in quantification strategies for DNA-origami scaffolds, which currently relies on the use of techniques that are neither specific nor sensitive, like agarose gel densitometry of UV absorbance, and lead to erroneous estimations of the actual scaffold quantities, led to the development of an analytical method based on ion-pair reverse phase HPLC. This method was used to quantify different size scaffolds produced either by aPCR techniques or by infecting *E.*

coli cells with the M13 phage. The method proved to be sensitive, accurate, specific and to deliver reliable titer measurements, making it a powerful tool for quantification of ssDNA scaffolds no matter the production system used.

Finally, the possibility of using spectroscopic techniques to evaluate the folding and application of tetrahedral DNA-origami nanostructures was evaluated. In a first approach, FCS analysis revealed diffusion coefficients and hydrodynamic radius (4.8 and 13.3 nm, respectively) coherent with the simulated size for tetrahedrons with 31 and 63-bp edge length. Single-molecule measurements were also performed affording the fluorescence decays and on-off histograms of Cy5 labelled T-31 and T-63. Next, the folding reaction of T-31 was followed by real-time PCR using FAM-ROX as FRET pair, which corroborated that, in fact, over the time, the two different labelled staple oligonucleotides came closer, reaching a point where energy transfer becomes possible, thus, indicating the folding of the structure. An FCS analysis was also performed for this FRET pair in the DNA-origami. It afforded decay curves from the acceptor channel that display a rise-time component, i.e. a negative pre-exponential indicative of energy transfer, which allowed for the determination of a distance between the origami-assembled staples of 5.7 nm. Lastly, the possibility of intercalating a photosensitizer molecule into the DNA-origami nanostructure was tested. Preliminary results show the possibility of using TMPyP at a concentration below 200 nM to intercalate T-63 with a calculated diffusion coefficient and hydrodynamic radius in accordance with the simulated structure, showing great promise of using these structures in combination with a photosensitizer for photodynamic therapy. In the future, more concentrations, or even a different type of photosensitizer porphyrin, should be explored. Moreover, the possibility of delivery of these intercalated tetrahedrons into cancer cells should be tested.